Biomineralized Structural Materials with Functional Optical Properties

by

Ling Li

B. S., Materials Science and Engineering, National University of Singapore (2008)

Submitted to the Department of Materials Science and Engineering
in partial fulfillment of the requirements for the degree of
Doctor of Philosophy in Materials Science and Engineering
at the
MASSACHUSETTS INSTITUTE OF TECHNOLOGY
June 2014

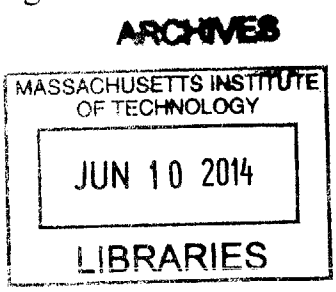

Signature redacted

Author.....
Department of Materials Science and Engineering
April 30, 2014

Signature redacted

Certified by.....
Christine Ortiz
Morris Cohen Professor of Materials Science and Engineering
Thesis Supervisor

Signature redacted

Accepted by.....
Gerbrand Ceder
R. P. Simmons Professor of Materials Science and Engineering
Chair, Departmental Committee on Graduate Students

Biomineralized Structural Materials with Functional Optical Properties

by

Ling Li

Submitted to the Department of Materials Science and Engineering
On April 30, 2014 in partial fulfillment of the
requirements for the degree of Doctor of Philosophy

ABSTRACT

Many biological structural materials exhibit "mechanical property amplification" through their intricate hierarchical composite designs. In the past several decades, significant progress has been achieved in elucidating the structure/mechanical property relationships of these materials. However, the design strategies of structural biomaterials with additional functional roles are still largely unexplored. This thesis, by selecting three unique mollusk shell model systems, explores the fundamental design strategies of multifunctional biomineralized materials with dual mechanical and optical functions: transparency, photonic coloration, and lens-mediated vision. The model systems are the bivalve *Placuna placenta*, the limpet *Patella pellucida*, and the chiton *Acanthopleura granulata*, respectively. By investigating the relationships between the mechanical and optical properties and the structural characteristics, this thesis uncovers novel design strategies used to integrate optical functions into mechanically-robust material systems. The high transmission property of the *P. placenta* shells (~99 wt% calcite), for example, is elucidated through experimental and theoretical analysis based on a light scattering model. This armor utilizes deformation twinning and additional mechanisms at the nanoscale to enhance the energy dissipation efficiency by almost an order of magnitude relative to abiotic calcite. 3D quantitative analysis of the damage zone resulting from high load indentations was performed via synchrotron X-ray micro-computed tomography, revealing the formation of a complex network of microcracks. A unique structural motif, screw dislocation-like connection centers, is identified to enable a high density of crack deflection and bridging. This thesis also leads to the discovery of a unique biomineralized photonic structure in the shell of the blue-rayed limpet *P. pellucida*. The photonic system consists of a calcite multilayer and underlying particles, which provide selective light reflection through constructive interference and contrast enhancement through light absorption, respectively. Lastly, this thesis presents a detailed investigation of the biomineralized lenses embedded in the armor plates of the chiton *A. granulata*. The image formation capability of these lenses is experimentally demonstrated for the first time. The optical performance of the eyes is studied via comprehensive ray-trace simulations that take into account the experimentally measured geometry and crystallography of the lens. Mechanical studies illustrate that trade-offs between protection and sensation are present in the plates.

Thesis Supervisor: Christine Ortiz
Title: Morris Cohen Professor of Materials Science and Engineering

ACKNOWLEDGMENTS

It would be impossible to draw this work to its conclusion with so much fun and enthusiasm without the kind support and friendship I have received from a number of people, to whom I am greatly indebted.

First of all, I would like to thank my advisor, Prof. Christine Ortiz. I still remember her energetic and encouraging voice when we first spoke over the phone before I came to MIT. Since I joined the group, with her enthusiasm and joyful wisdom, she has always encouraged me to be an independent researcher and given me the freedom to explore my ideas, no matter how crazy and naïve they were. Christine also encouraged me to participate many conferences (like the one in Hawaii) and to collaborate with other researchers, which have greatly broadened my knowledge and professional experience. Christine was also a wonderful role model for me who balances many aspects of academic career extremely well, not only in science, but also in management, communication, and social relations. I feel really fortunate to be part of her group and benefited from her invaluable guidance and supervision. Thank you, Christine!

I would like to express my sincere gratitude to my committee members, Prof. Mary Boyce and Prof. Silvija Gradecak. Their constant sources of inspiration and guidance have really made great contributions to my research! Their highly constructive and apt criticisms have been invaluable in clarifying my thoughts and sharpening my arguments.

I am deeply indebted to Prof. Mathias Kolle, who has been a great research mentor and an awesome personal friend. I feel so fortunate that I get to know Mathias through the collaborative work on the blue-rayed limpet since 2010, and I can always share with him, not only my achievement, but also any kind of frustration and disappointment. His profound knowledge, excellent hands-on skills and amiable personality always made the experience of working with him so inspiring, joyful, and fun. Every time I talked to him, I feel I have learned something, not just about science, but maybe something else as well, such as time management, or 3D rendering with Blender. Thank you, Mathias!

I would like to thank Prof. Joanna Aizenberg for her kind support and critical comments for our work on the blue-rayed limpet. Her enthusiasm and passion in science had been a constant driving force for me to excel in research.

Part of the work presented in this thesis results from collaborative work with excellent researchers, to whom I would like to express my deep gratitude. In particular, I would like to thank Dr. James Weaver, who has been the go-to person whenever I have questions related with imaging techniques. His broad knowledge of different biological organisms could always surprise me. I would also thank Stephan Kolle and Grant England for their support on the blue-rayed limpet and the chiton eye projects, respectively.

Prof. Pete Vukusic, who provided excellent and in-depth advice to this thesis work, particularly the photonic effects in the blue-rayed limpet. Every Skype meeting with Pete has been a wonderful and inspiring experience, never hindered by the spatial distance by which we are separated.

Matthew Connors, I owe him a huge "thank you". I will never forget the relaxing and stimulating times when we had discussions about science or other topics in the Indian restaurant every other week. Matt has also been a great editor of my scientific writing, and he has proofread most of my papers including this thesis.

Prof. Lin Han for our general and fruitful discussions and for providing me the opportunities to conduct nanomechanical testing in your lab.

Dr. Steve Wang and Dr. Xianghui Xiao provided me great assistance and support for X-ray tomography experiments at Argonne National Laboratory, which had made every trip to Advanced Photon Source so productive and fun.

I would like to thank Dr. Alan Schwartzman at the MIT Nanolab, for all his technical support and general discussions regarding nanoindentation. He also taught me a lot about electron microscopy, and gave me his always-neatly-marked notes and books. Thank you, Alan!

Prof. Haimin Yao, for all his guidance and mentoring especially during the first year of my Ph.D. studies. I would also like to thank Dr. Juha Song for her support and general discussion on many topics. When I first joined the group, Juha's passion and energy in science had really set a standard for me follow.

I owe particular thanks to Eric Arndt for his great help in taking over the lead to coordinate lab relocation during the last several months when I was busy with writing this thesis. Thank you Eric!

I am grateful to all other colleagues in the Nanomechanics of Structural Biological Materials group. Ting Ting Chen, Ashley Browning, Swati Varshney, Hadi Nia, and Katia Zolotovsky, Erica Lin, you really have created a unique energetic and active atmosphere in the group. I also like to thank our group and department assistants, Jeremey Brittan, Bonnie MacEachern, Theresa Hayes, Jessica Landry, Elissa Haverty, and Angelita Mireles, for their kind assistance.

Dr. Ming Dao for the fruitful discussions on deformation twinning. Dr. Jie Yin and Dr. Lifeng Wang, thank you for all the great general discussions on the mechanical properties.

I would also like to thank the lab technicians from the CMSE research facility: Dr. Shiahn Chen, Dr. Yong Zhang, Patrick Bioisert, and Dr. Scott Speakman, for their constant support on the equipment training, experiment troubleshooting, and general discussions.

I would like to express my sincere gratitude to my undergraduate supervisor, Prof. Junmin Xue, for his constant support in both academic research and personal life. I would also like thank my colleagues and friends in Singapore: Shengqiu Sha, Guangxia Hu, Nina Bao, Xiaohui Li, Yang Sheng, Jiaquan Yuan, Xiaosheng Tang, for all your kind help and support when transferring from Singapore to United States.

Grandpa, Grandma, Dad, Mum, my brother and sister, and my family for their never-ending support, understanding, and patience all the time.

My wife, Miao, for the support and patience throughout the writing of this thesis and for all the joy and happiness that she brings to my life.

To my daughter Iris

TABLE OF CONTENTS

ACKNOWLEDGMENTS **3**
TABLE OF CONTENTS **6**
Chapter 1 Introduction **8**
Chapter 2 Background **11**
2.1 Biomineralized mollusk shells 11
2.1.1 Structural characteristics 11
2.1.2 Mechanical properties and deformation mechanisms 15
2.2 Light-tissue interactions in nature 18
2.2.1 Coloration 19
2.2.2 Transparency 19
2.2.3 Photoreception 20
2.3 Combining optics and mechanics: inherent materials conflicts 21
2.4 Model systems 22
Chapter 3 Materials design and optical properties of the shell of *P. placenta* **26**
3.1 Introduction 26
3.2 Methods 26
3.2.1 Experimental methods 26
3.2.2 Theoretical methods: light scattering model 27
3.3 Results 29
3.3.1 The hierarchical structural characteristics 29
3.3.2 The crystallographic texture 33
3.3.3 The multiscale structural model 35
3.3.4 Optical properties 37
3.4 Discussion and conclusion 40
Chapter 4 Pervasive nanoscale deformation twinning as a catalyst for efficient energy dissipation in *P. placenta* **42**
4.1 Introduction 42
4.2 Methods 43
4.3 Results 44
4.3.1 Summary of hierarchical structure 44
4.3.2 Quantitative mechanical properties 45
4.3.3 Nanoscale deformation twinning in *P. placenta* 50
4.3.4 Additional nanoscale deformation mechanisms in *P. placenta* 54
4.3.5 Nanoscale deformation mechanisms in calcite 56
4.4 Discussion and conclusion 58
Chapter 5 Macroscopic deformation behavior of *P. placenta* shell and its related ultrastructural features **64**
5.1 Introduction 64
5.2 Materials and Methods 65
5.3 Results 65
5.3.1 Screw dislocation-like connection centers 65

5.3.2 Large-scale deformation behavior via macroindentation 73
5.3.3 Theoretical analysis of interface fracture toughness 78
5.4 Discussion and conclusions 80
Chapter 6 Functional structural color in the mineralized shell of the blue-rayed limpet, *Patella pellucida* 84
6.1 Introduction 84
6.2 Methods 86
6.2.1 Experimental methods 86
6.2.2 Theoretical methods 87
6.3 Results 87
6.3.1 Ultrastructural features of the entire shell 87
6.3.2 Ultrastructure of the photonic components 88
6.3.3 Crystallographic characteristics of the photonic components 91
6.3.4 Optical properties of the photonic multilayer 94
6.3.5 Optical properties of the colloidal particles 97
6.4 Discussion and conclusions 100
Chapter 7 Multifunctional design of a biomineralized armor with an integrated visual system 105
7.1 Introduction 105
7.2 Materials and methods 106
7.2.1 Sample collection and preparation 106
7.2.2 Materials characterization 106
7.2.3 Optical measurements 108
7.2.4 Ray-trace simulations 109
7.2.5 Mechanical tests 109
7.3 Results 110
7.3.1 Geometrical features of the sensory system 110
7.3.2 Ultrastructural, compositional, and crystallographic features 113
7.3.3 Optical performance of the lenses 118
7.3.4 Mechanical properties 120
7.4 Discussion and conclusions 123
Chapter 8 Summary and future directions 124
8.1 Summary 124
8.2 Future directions 127
8.2.1 Theoretical study of deformation twinning at building block level of *P. placenta* ... 127
8.2.2 3D structural characterizations of photonic multi-layer in *P. pellucida* 127
REFERENCES 129
Appendix A. Additional supporting figures 144
Appendix B. List of supporting movies 149

Chapter 1 Introduction

Bio-inspired or biomimetic materials research is an emerging field that aims to develop advanced functional materials by utilizing the design principles learned from natural material systems[1–3]. Plants and animals, through hundreds of million years of evolution, have evolved a vast variety of biological materials to fulfill diverse needs[3]. These biological material systems are usually very different from those used by engineers as they usually exhibit complex designs in a hierarchical manner[4].

Biological structural materials has been one of the most active bio-inspired materials research fields[5], and nature provides a multitude of different structural materials with specific combinations of mechanical properties for a variety of biological functions, such as protection, predation, locomotion, and body support. Particularly, biomineralization is perhaps one of the most common strategies used to enhance mechanical properties, such as stiffness, strength, and toughness. The amplified mechanical properties of biomineralized materials, in comparison to their weak and brittle mineral constituents, are achieved through intricate hierarchical composite designs. During the last several decades, the biomineralized shells of mollusk have provide many insights into this "mechanical property amplification". Chapter 2 highlights the major deformation mechanisms of mollusk shells discovered recently. This research has already resulted in substantial progress in the development of artificial bio-inspired advanced structural materials[6,7].

Multifunctional structural materials with attributes beyond enhanced mechanical properties, such as electrical, magnetic, optical, and power generative properties, provide some immediate advantages such as size and weight reduction, cost and maintenance effectiveness, and possible self-healing capabilities[1]. In particular, protective materials incorporated with optical properties, such as transparency, photonic coloration, and photoreception, may find a wide range of applications, such as transparent armor, windows/walls with display functions, and self-sensing structural composites. Currently, this type of materials is still largely unexplored in engineering fields, as design of such multifunctional materials faces new questions and challenges as compared to conventional materials, in which a single primary function is usually considered. Engineering strategies for achieving specific mechanical and optical properties of a material system are usually exclusive from one another, which raises the barrier to establish effective structure-property-function relationships for such multifunctional materials. For example, the current design and fabrication of protective transparent materials "is done almost exclusively using empirical, trial-and-error and legacy approaches"[8]. Therefore, the development times of new transparent armor systems are long, the production costs are quite high and many shortcomings of the systems become apparent only after they have been used in the fields[8].

Can we, again, solve this complex problem by adopting strategies used in natural materials systems? Although biological materials are usually multifunctional so as to maximize organisms' overall fitness, it appears that mechanical protection and optical functionalities are also surprisingly exclusive from each other in natural world. As reviewed in Chapter 2, in nature, a high level of mechanical protection usually relies on heavily mineralized structures, whereas

optical functions, such as coloration, transparency, and photoreception, are usually achieved through soft organic-based materials. Some primary design strategies for mechanical robustness and optical functionality are inherently contradicting, such as presence of interfaces, degree of crystallographic misorientations, heterogeneity, and geometry. In addition to the rareness of appropriate model systems, other challenges, such as relationship and possible trade-offs between the structure/mechanical- and structure/optical-property relationships in identified systems, are largely unexplored.

In this thesis, by carefully selecting three exotic mollusk shell-based model systems, I explore the underlying design principles of multifunctional biomineralized materials with simultaneous mechanical and optical functions, including transparency, photonic coloration, and lens-mediated vision. The model systems are the bivalve *Placuna placenta*, the limpet *Patella pellucida*, and the chiton *Acanthopleura granulata*, respectively. By integrating the investigation of the mechanics and optics, this research aims to elucidate the fundamental material design strategies of multifunctional biomineralized materials. The strategies uncovered from this fundamental research could provide effective solutions for engineering structural materials integrated with similar optical functions. Moreover, by studying the multiple aspects of these structural biomaterials, we may gain a more complete understanding of the evolutionary development of these materials. It is well known that trade-off situations are often resulted from the need of organisms to perform multiple tasks that contribute to their fitness. These trade-offs have traditionally been discussed in the context of phenotype morphologies, e.g. the beak size and shape of Darwin's finches. This thesis is focused on the multifunctional performance of individual systems that could potentially test the hypothesis that trade-off situations are also fundamentally present at the materials level in order to achieve multiple functions. As shown in the following chapters, the results of this thesis support the validity of this hypothesis.

This thesis is organized according to the three model systems, i.e. *P. placenta, P. pellucida*, and *A. granulata*, whose optical properties are optical transparency, photonic coloration, and lens-mediated vision, respectively. Each model system is treated as an integrated materials system, in which the mechanical and optical properties are intimately related together to their corresponding multiscale structural characteristics.

Chapter 2 provides some relevant background information of this thesis. A brief summary of the general characteristics of mollusk shell microstructures and their mechanical behavior are first presented. This is followed by a literature review of our current knowledge of the multiscale deformation mechanisms present in these protective systems. Additionally, as this thesis deals with structural materials with functional optical properties, three common light-tissue interactions in nature (coloration, transparency, and photoreception) are briefly reviewed with emphasis on their biological functions, physical principles, and materials involved. Lastly, information about the biology of the three study models is provided.

Chapters 3, 4, and 5 explore the structural, optical, and mechanical characteristics of the transparent armor of *P. placenta*. In Chapter 3, the multiscale structural design of the shell is first elucidated through a number of materials characterization techniques. Its unique high optical transmission capability is then investigated through both experimental and theoretical approaches, through which we demonstrate that *P. placenta* shells have special structural features at multiple length scales to reduce light absorption and scattering. Chapter 4 presents a detailed study of the nanoscale deformation behavior of *P. placenta* through instrumented nanoindentation and electron microscopy. Pervasive nanoscale deformation twinning and

additional nanoscale deformation mechanisms work synergistically to enhance the energy dissipation efficiency by almost of an order of magnitude as compared to the shell's main constituent, calcite. Chapter 5 focuses on the large scale deformation behavior of *P. placenta* shell via macroindentation tests. Direct 3D visualization and quantitative analysis of the damage zone is achieved through synchrotron X-ray micro-computed tomography. The outstanding damage localization capability at macroscopic level is shown to be related to a unique structural motif, i.e. screw dislocation-like connection centers, which enables a high density of crack deflection and bridging within the damage zone.

Chapter 6 focuses on the structural origin of the bright blue stripes found in the shell of the blue-rayed limpet *P. pellucida*. Using a combination of material characterization techniques, we, for the first time, discovered a biomineralized photonic structure in nature. The photonic system consists of a calcite-based multilayer and an array of underlying colloidal particles, which provide selective light reflection through constructive interference and contrast enhancement through absorption of the transmitted light. The synergistic combination of these two optical elements results in distinct stripe patterns along the limpet shell, which ensures the organism's visibility and conspicuousness with a large range of observation directions. Its unique structural architecture and optical performance strongly suggest that these blue stripes have evolved to serve a biological function, which is expanded upon in the chapter.

In Chapter 7, I present a comprehensive investigation of the third biological structural armor, *A. granulata*, which contains hundreds of mineralized-lens eyes. First, the ultrastructural, geometrical, and crystallographic characteristics of the mineralized lenses are investigated through a combination of materials characterization techniques. I then provide a detailed investigation of the optical performance of these eyes through both computational and experimental approaches, which confirmed the image formation capability of the mineralized lenses. The mechanical performance of the lenses in comparison to other sensory and non-sensory structures in this protective armor is studied via multiscale indentation tests. Through this combinational study, I show that as the size, complexity, and functionality of the integrated sensory elements increases, the local mechanical performance of the armor decreases.

The last section of this thesis Chapter 8 summarizes the key findings for each model systems with emphasis on the common design principles and their implications to design of engineering multifunctional materials. Finally, several potential research directions are suggested and their significance is briefly discussed.

Chapter 2 Background

In Section 2.1, the general structural and mechanical characteristics of mollusk shells are summarized. Emphasis is placed on recent developments in our understanding of mechanical deformation mechanisms at multiple length scales. In Section 2.2, I briefly introduce the three main forms of light-tissue interactions found in nature, coloration, transparency, and photoreception. The physical principles, biological functions, and materials involved in these interactions are discussed. In Section 2.3, the model systems used in this thesis are introduced.

2.1 Biomineralized mollusk shells

2.1.1 Structural characteristics

The phylum Mollusca comprises around 70,000 species, most of which have a very soft body and a hard external shell for protection from predators[9]. The natural habitats of mollusks are extremely diverse, including both terrestrial and aquatic environments. Mollusk shells are mainly composed of calcium carbonate, usually in the form of calcite or aragonite, and also contain a small amount of organic material[10]. Over million years of evolution, mollusks have evolved to produce strong yet tough protective shells with a vast diversity of microstructural architectures, including nacreous, foliated, prismatic, crossed-lamellar, and granular structures[11,12].

Nacreous structures (**Figure 2-1a-b**), or mother-of-pearl, consist of aragonite tablets assembled in a "brick-and-mortar" manner. Tablets are generally arranged in a random or column fashion (commonly referred to as sheet or columnar nacre, respectively). An organic "mortar" phase holds the tablets together.

Prismatic structures (**Figure 2-1c**) consist of large elongated column-shaped aragonite or calcite crystals. The cross sections of the prismatic structures usually exhibit a polygonal arrangement. Calcitic prismatic structures are commonly found in the outer layers of shells.

Crossed-lamellar structures (**Figure 2-1d,e**) have a lamellate arrangement with at least three orders of hierarchy, which are made of aragonite.

Foliated structures (**Figure 2-1f,g**) consist of thin elongated calcitic crystals arranged in a mosaic-like manner.

Granular structures (**Figure 2-1g**) consist of very small (~1 μm) aragonite crystals, and usually found in the regions of muscle-shell interfaces as well as in the outer layer of chiton plates.

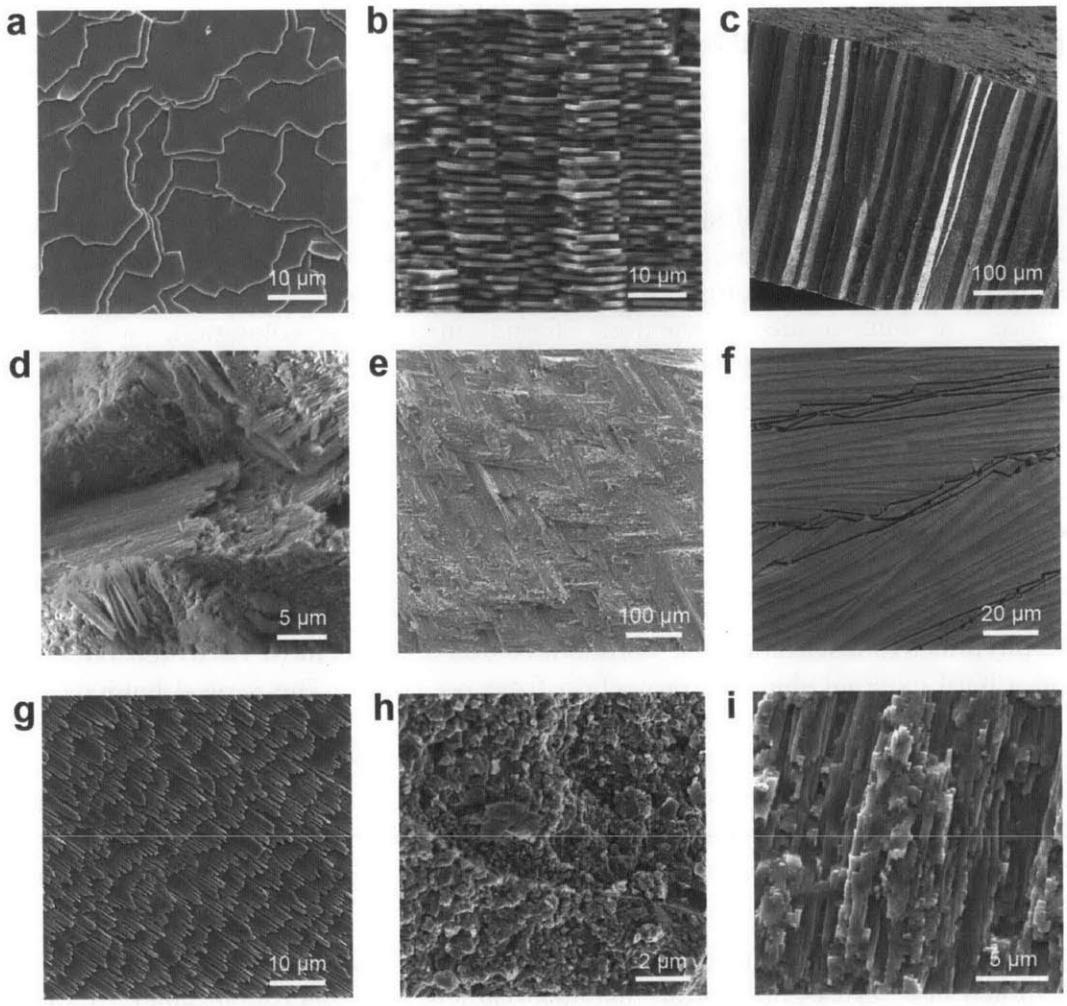

Figure 2-1| A variety of microstructures observed in mollusk shells. (**a**) Top-viewed and (**b**) cross section-viewed nacreous structure in the abalone *Haliotis rufescens*. **c**, Prismatic structure of *Atrina rigida*. (**d**) Cross lamellar and (**e**) complex cross lamellar structure found in the limpet *Cellana testudinaria*. Foliated microstructure of (**f**) the bivalve *Placuna placenta* and (**g**) the limpet *Cellana testudinaria* (slightly demineralized). **h**, Granular structure found in the chiton *Acanthopleura granulate*. **i**, Irregular lamellar structure of *Cellana testudinaria*. (**b**) is adapted from ref. 13.

Regardless of their specific microstructural features, mollusk shells share three main structural and crystallographic characteristics: they are composites, hierarchical, and textured.

The composite nature

Mollusk shells are natural composites consisting of mineralized building blocks and organic materials[4,14]. The mineral content is usually very high (95-99 vol%), with few notable exceptions, such as the hydrothermal vent gastropod[15] and brachiopods with shells similar to bivalves (note that they are not mollusks)[16,17]. The minerals are usually polymorphs of calcium carbonates, primarily calcite, aragonite, or both. The organic materials distributed in biominerals are generally categorized as two types, inter- and intra-crystalline (**Figure 2-2**). Intercrystalline

organic materials are located along the interfaces of adjacent building blocks, e.g. the interfaces between adjacent aragonitic nacre tablets or calcitic prisms[18,19]. Intracrystalline organic materials (commonly referred to organic inclusions), on the other hand, refer to materials trapped within mineralized building blocks[19,20]. This composite nature of biominerals is one of the most significant characteristics in comparison abiotic minerals[14,21]. A large number of studies have shown that the organic materials play a critical role in controlling the formation of biominerals in terms of building block geometry and size, crystallographic phase and orientation, and other characteristics[22–24]. Moreover, the composite nature of mollusk shells is also the fundamental structural origin for their remarkable mechanical properties[4].

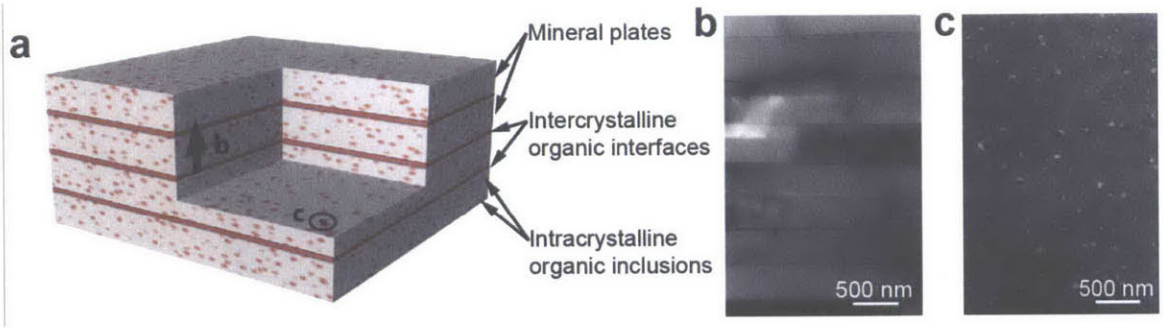

Figure 2-2| Inter- and intra-crystalline organic materials in mollusk shells. a, Schematic diagram showing both two types of organics in a generic layered microstructure. Transmission electron microscopy (TEM) images in (**b**) transverse and (**c**) horizontal cross sections of the bivalve *Placuna placenta*, showing intercrystalline organic interlayer and intracrystalline organic inclusions, respectively.

The hierarchical nature

The structural hierarchy from nanoscale to macroscale is perhaps the most prominent characteristics of biological structural materials, such as bones[4,25], sponges[26], crustacean exoskeletons[27], fish scales[28], and mollusk shells[29]. Mollusk shells are constructed with minerals and with small amount of organic materials in a hierarchical manner. Here I use nacre as an example to illustrate this feature. As shown in **Figure 2.3**, the heavily mineralized abalone shell consists of two macroscopic layers, which include a hard but more brittle calcite outer layer and a tough inner nacreous layer (**Figure 2.3b-c**). As the primary structural component, the inner nacreous layer provides compliance and toughness for the entire armor system. Mesolayers (thickness ~20 μm) consisting of organic materials are found in the nacreous structure with typical spacings of ~300 μm (**Figure 2-3d-e**)[30,31]. The basic building blocks of the nacreous structure are the micro-sized polygon-shaped aragonite tablets (**Figure 2-3f-g**), which have a diameter of ~10 μm and thickness of ~0.5-1.0 μm. These mineral tablets are closely packed together with thin organic interlayers between them, which results in a "brick-and-mortar" structure. On a smaller length scale, the surfaces of aragonite tablets contain nanoscale asperities and mineral bridges (**Figure 2-3h-i**)[32,33]. The organic materials, as discussed above, are in two forms, the intercrystalline interfacial layer (thickness ~20 nm) between aragonite tablets and intracrystalline inclusions (size, 30-40 nm)[19,34,35]. The crystalline lattice of aragonite is slightly distorted relative to abiotic forms[36], presumably resulted from the presence of intracrystalline organic materials[37,38]. This hierarchical structure design from the macroscopic to atomic level is

responsible for multiple strengthening and toughening mechanisms operating at different length scales, as discussed in next section.

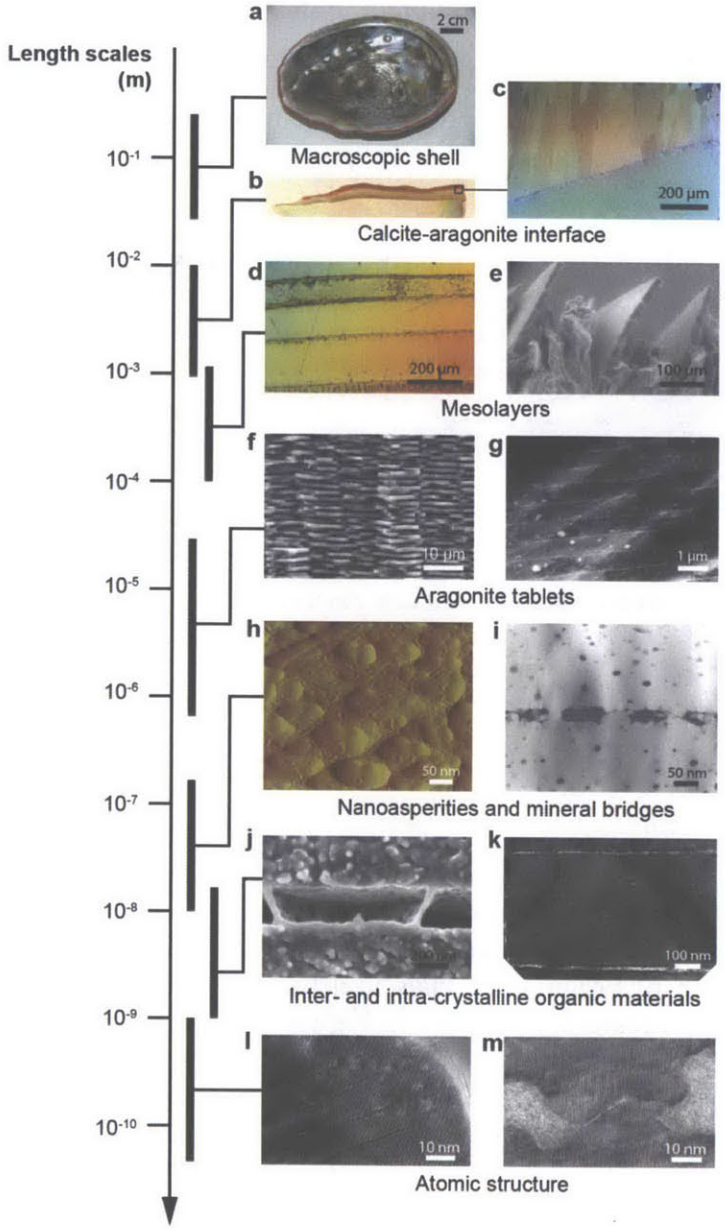

Figure 2-3| Hierarchical structure of nacre. **a**, Photo of an abalone shell *Haliotis rufescens*. (**b**) Photo and (**c**) light micrograph of the shell cross section showing the calcite-aragonite interface. **d**, Light micrograph of mesolayers. **e**, SEM image of the demineralized shell with protruding mesolayers. (**f**) Scanning electron microscopy (SEM) and (**g**) TEM images of aragonite tablets. **h**, Atomic force microscopy (AFM) image of nanoasperities on the aragonite tablets. **i**, Scanning transmission electron microscopy (STEM) image of mineral bridges. **j**, SEM of intercrystalline organic interfaces. **k**, TEM image of intracrystalline organic inclusions within tablets. High-resolution TEM (HRTEM) images of (**i**) aragonite tablets and (**m**) mineral bridges. Images in **a**, **c**, **f**, **g**, **h**, **j**, **k**, and **l** are adapted from ref. 13. **d** and **e** are adapted from ref. 30. **i** and **m** are adapted from ref. 33

The textured nature

The crystallographic characteristics of a variety of mollusk microstructures have been extensively studied via a number of different techniques, such as X-ray diffraction[39], electron backscattered diffraction[40–42], and X-ray photoelectron emission spectromicroscopy[43,44]. In general, the biomineralized structures of mollusk shells exhibit preferred global co-alignment of crystallographic orientations[39–42]. One example of this is found in the calcite-based foliated microstructure of the bivalve *Placuna placenta* (will be discussed in detail in Chapter 3). As shown in **Figure 2-4**, the calcite *c*-axes are tilted along the longitudinal directions of elongated building blocks by ~24°. Moreover, it appears that there is never a perfect alignment between adjacent building blocks[39–42]. The degree of crystallographic misalignment varies amongst different mollusk shells, and even among different locations in one specimen.

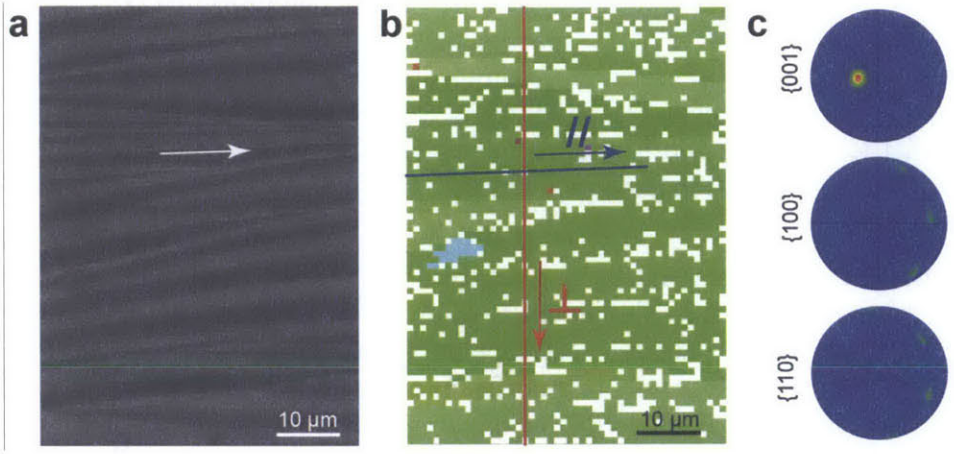

Figure 2-4| Observations of the crystallographic alignment of mollusk shells. a, An SEM image of the freshly cleaved shell surface mapped with electron backscattered diffraction (EBSD). The white arrow indicates the longitudinal direction of the elongated building blocks. **b**, A corresponding EBSD map with color coded for all the three Euler angles ($\varphi 1$, φ, $\varphi 2$). **c**, Pole density plots for the mapped region in (**a**).

2.1.2 Mechanical properties and deformation mechanisms

Since Currey's pioneering work in 1970s[12,45], the mechanical behavior of mollusk shells have been investigated through numerous testing methods, including tension[45,46], compression[46], three-point bending[12,46,47], four-point bending[47], and indentation[32,47]. Recent advances in experimental and modeling techniques have enabled significant progress in understanding the underlying deformation mechanisms. Here again, I take nacre, the most studied molluscan microstructure, as a model system to summarize the key deformation mechanisms which have been identified at multiple length scales and are responsible for its high toughness, stiffness and strength.

Typical mechanical parameters for nacre include elastic moduli of 60-80 GPa[12,45], tensile strength of 35-168 MPa[12,45,46], compressive strength of 100-540 GPa[48], modulus of rupture of ~270 MPa[2]. One key mechanical behavior of nacre is its significant amount of inelastic strain (~1%) with slight strain hardening before fracture in tension[47,49]. This characteristic has been

reported in numerous studies, although specific stress and strain values differ depending on species and testing conditions[49]. The capability to undergo large inelastic deformation is also observed in flexural bending tests, which closely resembles physiological loading condition[47]. This inelastic deformation behavior makes nacre mechanically robust and tough; it has been shown that nacre is orders of magnitude tougher than its main constituent, aragonite[5,50].

Considering its constituents, stiff but brittle ceramic tablets and soft but weak organics, the remarkable mechanical behavior of nacre has long fascinated scientists. There is a continuing effort to try to understand the underlying deformation mechanisms of nacre, with the aim of applying these design principles to engineering structural materials. As we discussed in the previous section, nacre has a hierarchical architecture with structural control from macroscopic to atomic level, which has direct and profound influence on the fundamental deformation mechanisms at multiple length scales (**Figure 2-5**). At a global level, it has been found that water plays an important role in plasticizing the organic phases[46] and residual stresses within the shell also affects energy dissipation[51]. At the macroscopic level, the development of diffuse whitening zones on the tensile tested samples, indicating significant inelastic deformations for energy dissipations[45,47]. This is directly resulted from microscopic deformation mechanisms at the individual tablet level (discussed in the next paragraph). At mesoscale, two primary toughening mechanisms are plastic buckling and crack deflection by mesolayers[48].

At nano- and microscale, a number of deformation mechanisms have been identified and proposed through experimental and/or theoretical approaches. Tablet pull-out and sliding were among the first mechanisms elucidated, which directly lead to the formation of the aforementioned whitening zones, corresponding to the process zones of inelastic deformation[47,49]. This process results in significant energy dissipation[49,52,53]. A number of energy dissipation mechanisms associated with this tablet-sliding process include crack deflection/stopping[47,54], viscoplastic deformation of the organic phase[55], crack bridging by ligaments of the organic phase[46], and unfolding of proteinaceous chains[56], fracture of mineral bridges[57], and frictional strengthening from nanoasperties[47,58]. In particular, the surface waviness at the individual tablet level has been identified as an effective mechanism that leads to hardening, spreading damage and dissipating energy over large areas[49,50,59]. Moreover, numerous studies have shown that the nano-/micro-sized aragonite tablets have optimal (length/thickness) aspect ratios, which permits the energy dissipation through tablet pull-out while still maintaining a high level of load transfer, leading to simultaneous high toughness and strength[60,61]. Based on both theoretical analysis and finite element simulations, Gao *et al.* suggest that the basic mineralized building blocks are flaw insensitive due to their nano-/microscopic sizes[62,63], although this mechanism remains controversial[64]. In addition, Li *et al.* through a number of studies, have demonstrated that the individual building blocks of nacre, albeit their apparent single crystal nature, consist of nanosized grains[65]. These nanograins enable plastic deformation of individual tablets for energy dissipation through nanograin rotation and reorientation[66,67]. The periodic variation of moduli in the microscopic multilayered structure of nacre has also been shown to be able to reduce the crack driving force[68]. At the atomic level, the anisotropic lattice distortion might also contribute to the intrinsic mechanical properties of aragonite[37,69].

The contribution of each specific mechanism summarized above is yet to be elucidated[54], which presumably depends on specific loading conditions. These mechanisms might work synergistically so as to achieve the outstanding combinations of strength, stiffness, and energy dissipation in nacreous structure. Most of the energy dissipation mechanisms, regardless of their

length scales, operate at the interfaces between mineral and organic materials, which are again intimately related to its hierarchical and composite nature. The intricate interface control is also found to lead enhanced toughness and resistance to crack propagation in other molluscan microstructures. For example, the aragonite-based cross-lamellar structure in the shell of the conch *Strombus gigas* is able to resist catastrophic failure with two energy-dissipating mechanisms: multiple microcracking in the outer layers at low mechanical loads, and crack bridging in the shell's tougher middle layers at higher loads[29,70–72].

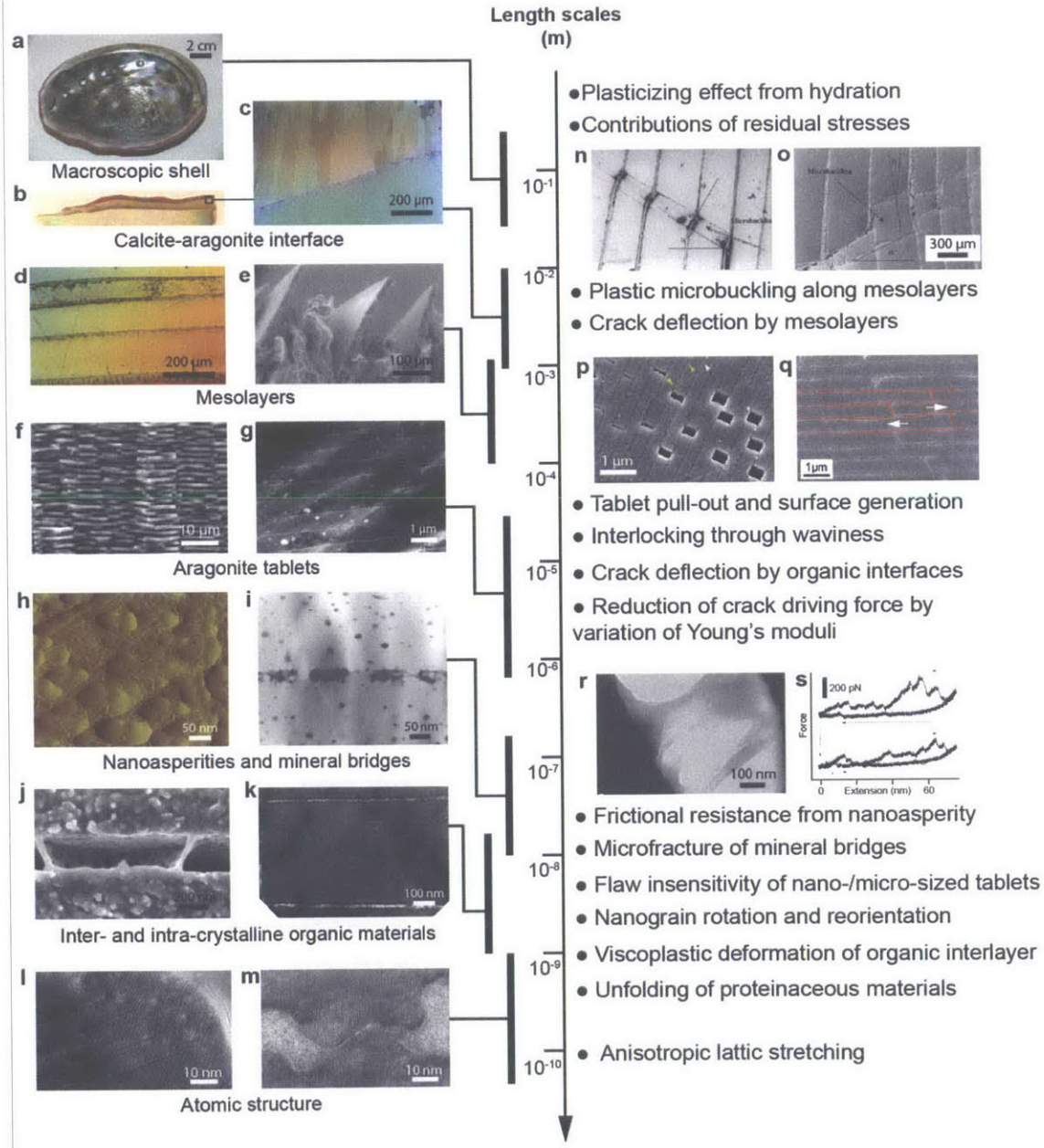

Figure 2-5| Summary of multiscale deformation mechanisms in nacre. Images in **a**, **c**, **f**, **g**, **h**, **j**, **k**, and **l** are adapted from ref. 13. **d** and **e** are adapted from ref. 30. **i** and **m** are adapted from ref. 33. **n** and **o** are adapted from ref. 48. **p** is taken from ref. 73. **q**: ref. 49. **r** is adapted from ref. 55. **s** is adapted from ref. 56.

2.2 Light-tissue interactions in nature

In addition to mechanical functions, a variety of biological material systems have also evolved to provide optical functions. Based on the physical principles involved, here we consider three main optical interactions between biological tissues and light, which include coloration (pigmentation[74,75], bioluminescence[76], and structural color[77]), transparency[78], and photoreception[79] (**Figure 2-6**). In this section, I present a brief overview and summary for each interaction form with emphasis on their physical principles, biological functions, and materials involved.

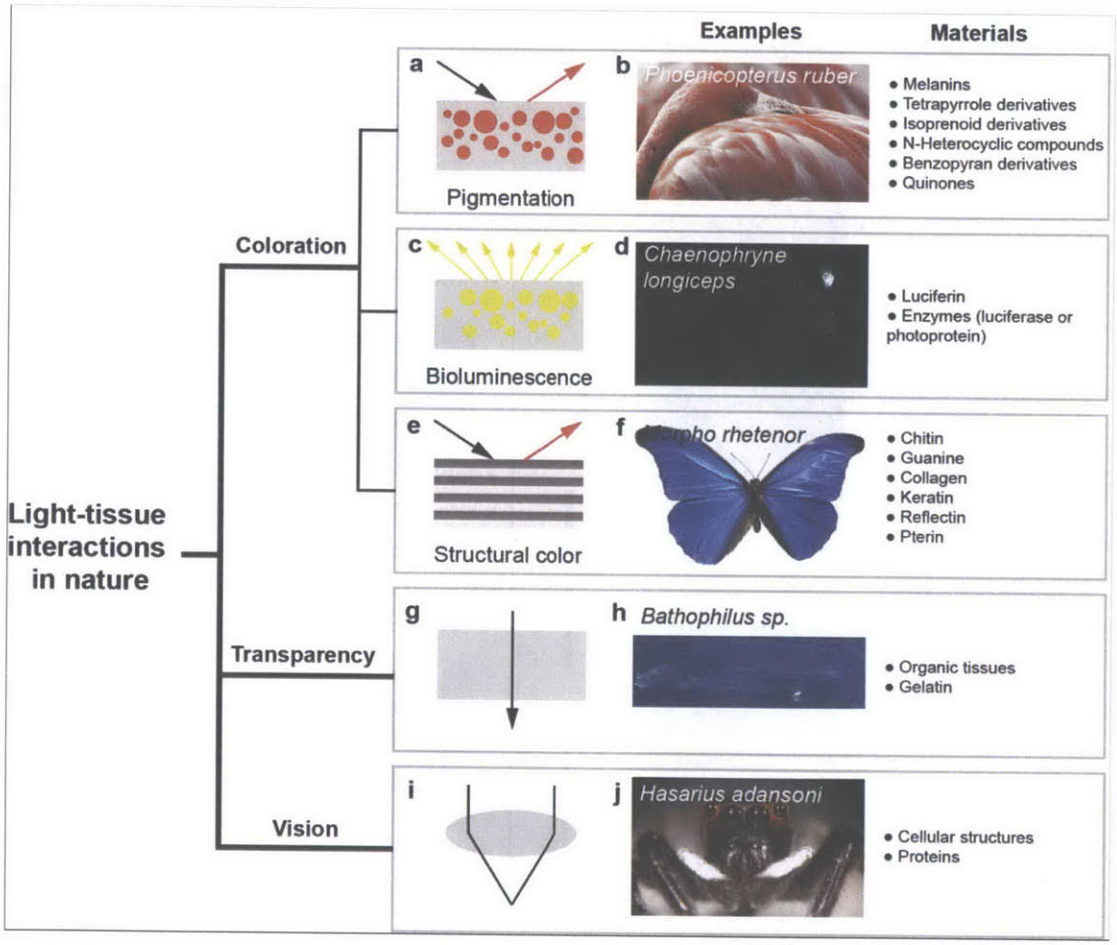

Figure 2-6| Light-tissue interactions in nature: coloration, transparency, and photoreception. **a**,**b**, Pigmentation. **b**, Pink coloration in the plumage of a flamingo (*Phoenicopterus ruber*) comes from its diet (adapted from ref. 80). **c**,**d**, Bioluminescence. **d**, Live photo of anglefish *Chaenophryne longiceps* with glowing bioluminescent bacteria inside its retractable lure (adapted from ref. 76). **e**,**f**, Structural color. **f**, Photo of a *Morpho rhetenor* with bright blue structural color (adapted from ref. 77). **g**,**h**, Transparency. **h**, Photo of the larva of deep-sea fish *Bathophilus sp.* (adapted from ref. 78) **i**,**j**, Photoreception via eyes with lens. **j**, Anterior view of the jumping spider, *Hasarius adansoni*, with four eyes (adapted from ref. 81). The materials involved in each light-tissue interaction forms are based on the following references: pigmentation: ref. 74, 75, 82; bioluminescence: ref. 76, 83, 84; structural color: ref. 85-91; transparency: ref. 78, 92, 93; photoreception: ref. 94-96.

2.2.1 Coloration

One of the most stunning aspects of living organisms is their vast diversity of color, from green leaves to vibrant flowers, fast color change in cephalopods, bright fireflies, and the brilliant blue *Morpho* butterfly, natural organisms have developed countless ingenious ways to interact with light in order to create unique visual displays for a variety of biological functions, such as camouflage, signaling, mimicry, and thermal regulation[84]. Here I discuss three principal mechanisms, i.e. pigmentation, bioluminescence, and structural coloration[97].

Pigmentation empowers air-borne, terrestrial, and aquatic creatures to display mostly red, orange, yellow, and more rarely green or blue hues in their skins, plumages, scales or shells[98–100]. Coloration is achieved through absorption of specific wavelength range of visible light through organic-based colored chemicals called pigments[74,75,82]. Pigments are able to capture incoming electromagnetic energy by exciting electrons from lower to higher energy states; the non-absorbed energy is then reflected and/or refracted which can be perceived by eyes as color. The fascinating camouflage and dynamic coloration control of cephalopods are also based on pigment-containing cells called chromatophores[101], which can dynamically change their size to vary the display of color.

Bioluminescence, similar to pigmentation-enabled coloration, is also based on organic chemicals, although dynamic chemical reactions are taking place during light production[76,83]. Bioluminescence might serve as a communication pathway with nearby animals, but it may be also utilized as tiny searchlights for feeding for some deepwater marine animals[84].

Nature's chromatic display does not end with chemicals, nano- and microscopic organic structural architectures have evolved to interfere with light in circumstances where strong metallic-like reflections and iridescent colorations are required or the pigmentation for a specific hue is unavailable[99,102,103]. Structural colors have been found in the feathers of peacocks and other birds[104–106], the wing scales of butterflies and moths[107–109], the exoskeletons of beetles[85,110], and even in the skins of birds and mammals[88], shedding light on a stunning diversity of structural coloration in biological organisms. Common light manipulation mechanisms involved in these structural colorations have been identified as scattering, multilayer interference, and diffraction[102,111]. Common structural morphologies include microporous scattering films, simple multilayers, and 3D photonic crystals[111,112]. The majority of these structurally diverse, functional biophotonic architectures of different organisms have been shown to be comprised of highly ordered organic materials, including cuticle[85], chitin[86], guanine[87], collagen[88], keratin[89,90], and proteins such as reflectin[91].

2.2.2 Transparency

In addition to coloration which requires manipulation of incoming light with materials through special chemicals and/or intricate structures, nature also explores another extreme of light-matter interaction, i.e. no interaction, transparency. Optical transparency has been shown to be a successful form of camouflage to visual predation based on experimental and theoretical studies in terrestrial, freshwater, and marine systems[78,113,114]. The phylogenetic distribution of transparent animals is surprisingly diverse and uneven, which is strongly affected by their habitats[65]. As summarized in his review paper, Johnson pointed out that most transparent animals are pelagic, where the open water has no surfaces to match or hide behind and transparency is

one of the few forms of camouflage possible[65]. Transparency in terrestrial species is extremely rare possibly due to the problem of reflections resulting from the low refractive index of air.

Transparency as a form of camouflage involves the entire body. Therefore, many or all the tissues and organs must be modified and specialized for transparency. This requirement even leads to special modifications of some organs that are inherently nontransparent, such as the extremely thin retina of the hyperiid *Cystisoma*[65]. From a physics point of view, high transparency requires low reflection, absorption, and scattering. Both absorption and scattering can be simultaneously reduced by decreasing the light path within an object, i.e. thickness. This strategy is utilized by many transparent animals, such as macroscopic cetid ctenophores, phylliroid nudibranchs, many freshwater cladocerans, hyperiid amphipods, and phyllosoma and stomatopod larvae[65]. An extreme example is the fish larva, leptocephalous, which are tens of centimeters long but only one or two millimeter thick (**Figure 2-6h**)[65].

As transparency typically involves the entire body, the materials involved are predominantly organic-based. Studies have shown special ultrastructural modifications of the organic tissues for the purpose of transparency, including anti-reflection through surface texture control and scattering reduction in the extracellular matrix through destructive interference[65]. Moreover, a large number of transparent animals are based on nonliving gelatinous materials which have very high water contents[92].

2.2.3 Photoreception

The two optical signatures of coloration and transparency as discussed in the two sections above are closely related to photoreception, which utilize optical sensory organs, that is, eyes or eyespots, to perceive the optical information from the environment both close up and far away[79]. Photoreception clearly provides significant advantages for the survibility and fitness of organisms. During the Cambrian explosion ~530 millions years ago, a rich fauna of macroscopic animals evolved, many of which had prominent eyes[79]. The evolutionary invention of vision-guided predation during late Precambrian may have generated a profound selection pressure on many prey species, triggering a great number of self-protective measures, such as producing protective armor with shells, avoiding exposure by deep burrowing, or developing good vision and mobility themselves. This visually-guided predation might have initiated the first stages of an arms race between predators and prey[79].

As the visual capabilities of different organisms are highly related to their specific behavioral requirements, there are vast varieties of eye designs. According to the level of visual performance, four classes of light-controlled behaviors exist[79]. Class 1 visual systems provide non-directional monitoring of ambient light. This can be achieved with non-directional photoreceptors, requiring one or a few photoreceptor cells. Visual systems from class 2 offer directional light sensitivity, which is achieved by adding screening pigment or partly shading the photoreceptor cells with other structures. Class 3 visual systems enable organisms with low spatial resolutions, which include motion detection, habitat selection, and orientation to coarse landmarks or major celestial objects such as the sun or moon. Visual systems within this class typically have resolution around 5-30°, which is achieved by simultaneously monitoring different directions with different photoreceptors. Class 4 visual systems are more advanced than Class 3 as they require much higher spatial resolutions, usually smaller than a few degrees. This high spatial resolution is achieved by equipping visual systems with special components, such as lens or other focusing optical elements. The stages of eye evolution also generally follow these

four levels of visual capability, from the simple unidirectional photoreception to advanced eyes with lenses.

As compared to other eye designs, addition of a lens clearly provides functional advantages, as it sharpens the images, maintains light intensity, and reduces the size needed for a given resolution. The primary function of the lens is to form a sharp focused image without distortion onto photoreceptors. Several material requirements have to be fulfilled, such as high transparency, refractive index control, and structural integrity. Animals develop extremely intricate lens microstructures so as to achieve desired optical performance[95]. Animal lenses are primarily made of fiberous cells (comprising more than 95 vol%), which are packed with high levels of proteins, known as crystalline[94]. Several significant structural characteristics emerge for this special optical element. First, nulcei and other light-scattering organelles from the cells within the lens are eliminated during the early stage of eye development[95,96]. Secondly, adhesive proteins, some of which are found only in lens, are sandwiched in between the fiber cells to minimize optical scattering[95,115]. Thirdly, scattering is further minimized by matching refractive indices between lens membranes and cytosol[95]. Lastly, complex suture-like structures are found at the surface of the lens fibers, which are believed to provide mechanical integrity during the change of lens geometries (so as to vary focusing power)[116].

Although most lenses are exclusively made of organic materials, nature also explores mineralized materials in constructing this demanding optical structure in a very few species. The classic example is the group of ancient arthropods called tribolites, which possess calcite-based compound eyes[117–120]. Another example of biomineral-based photoreception system is the calcitic lenses distributed across on the dorsal arm plates of brittlestars[121]. Both systems have been shown to possess controlled lens geometry and crystallographic orientation for better image formation performance[117,121]. The third example is the mineralized lens structures found in the two lineages of chitons, which possess hundreds of aragonite-based lens eyes embedded in their eight armor plates[122].

2.3 Combining optics and mechanics: inherent materials conflicts

As discussed in the previous two sections, prior knowledge has suggested that the biological tissues with mechanical protection and optical functions are highly exclusive, because the material requirements for these two types of functions are extremely conflicting from each other.

We can take the design of transparent structural materials as the first example to illustrate this conflict. Composite design with heterogeneous material phases (minerals and organic materials) with corresponding different mechanical properties is an effective strategy in order to achieve high stiffness, strength, and toughness, which have been found in many biological structural materials (as discussed in Section 2.1.1). The intricate interface control at multiple length scales directly governs the underlying deformation mechanisms for robust mechanical integrity and effective energy dissipation (as discussed in Section 2.1.2). However, introduction of multiple material phases and interfaces inevitably causes light absorption and scattering, which causes significant loss in light transmission. This is probably the underlying physical constraint why the majority of biological structural materials are opaque. The same physical constraint is also faced by us to design engineering transparent structural materials[8,123]. Homogeneous materials with low light scattering and absorption are excellent in providing high optical transparency; however, high mechanical performance can only be achieved with high intrinsic mechanical properties in these homogeneous materials, where all the extrinsic

strengthening and energy dissipation mechanisms are absent[124]. This is essentially impossible for biological materials as they are usually based on intrinsic weak organic and brittle ceramic materials.

Similar design conflict is also present for biological lens structures. As compared to organic-based lens, minerals pose several design barriers as resulted from their intrinsic material properties. First of all, many minerals, due to their crystalline structure, are optically anisotropic (such as calcite[125] and aragonite[126]), that is, the refractive indices are dependent on the angle of incident light relative to the crystallographic axes. This property leads to light scattering whenever light encounters an interface between two misaligned grains. Moreover, inorganic materials are rigid, which provides little accommodation capability for the lens to adjust the focus dynamically[79]. Other design barriers might be related to the biomineralization process for production of lens structures with optically desired geometries, as inorganic crystals usually tend to adopt their favorable shapes in order to achieve the lowest energy state.

2.4 Model systems

Despite the conflicts and constrains for achieving simultaneous mechanical and optical functions, Nature does provide a few unique model systems which incorporate optical functions with their mineralized protective armor materials. In this thesis, three model systems were chosen to investigate the use of biological ceramic-based (calcite or aragonite) armor systems with integrated optical functions of the three aforementioned light-tissue interaction forms. The systems include the bivalve *Placuna placenta* (transparency), the limpet *Patella pellucida* (structural color), and the chiton *Acanthopleura granulata* (photoreception), whose optical functions are transparency camouflage (hypothesized), biomimicry (hypothesized), and vision (experimentally demonstrated[127]), respectively (**Figure 2-7**). **Table 2-1** briefly summarizes some basic information about the three model systems, including taxonomy, geographic distribution, habitat, general morphology, and other related information.

Transparency: *Placuna placenta*

The bioceramic material system from *Placuna placenta* (Linnaeus, 1758; Mollusca: Bivalvia; commonly known as window pane oyster) has two highly light-transmissive, circular-shaped flat mineralized shells (**Figure 2-7h**). *P. placenta* lives unattached on the surfaces of muddy or sandy flats in shallow water (depth < 100 m) of the tropical Indo-West Pacific[128]. Due to the high optical transparency of their shells, *P. placenta* are widely collected and commercially cultured in large quantities for shellcrafts, and local people are known to use the shells as a substitute for window glass in houses[128]. While it is unclear whether or not the transparency plays a biological role such as transparency-enabled camouflage[78], the materials design strategies leading to a combination of mechanical robustness and optical transparency in a single system holds great potential for the development of bio-inspired engineering transparent structural materials. Previous study has only focused on the crystallographic texture of the shell[40], and the optical and mechanical properties are not reported in the literature.

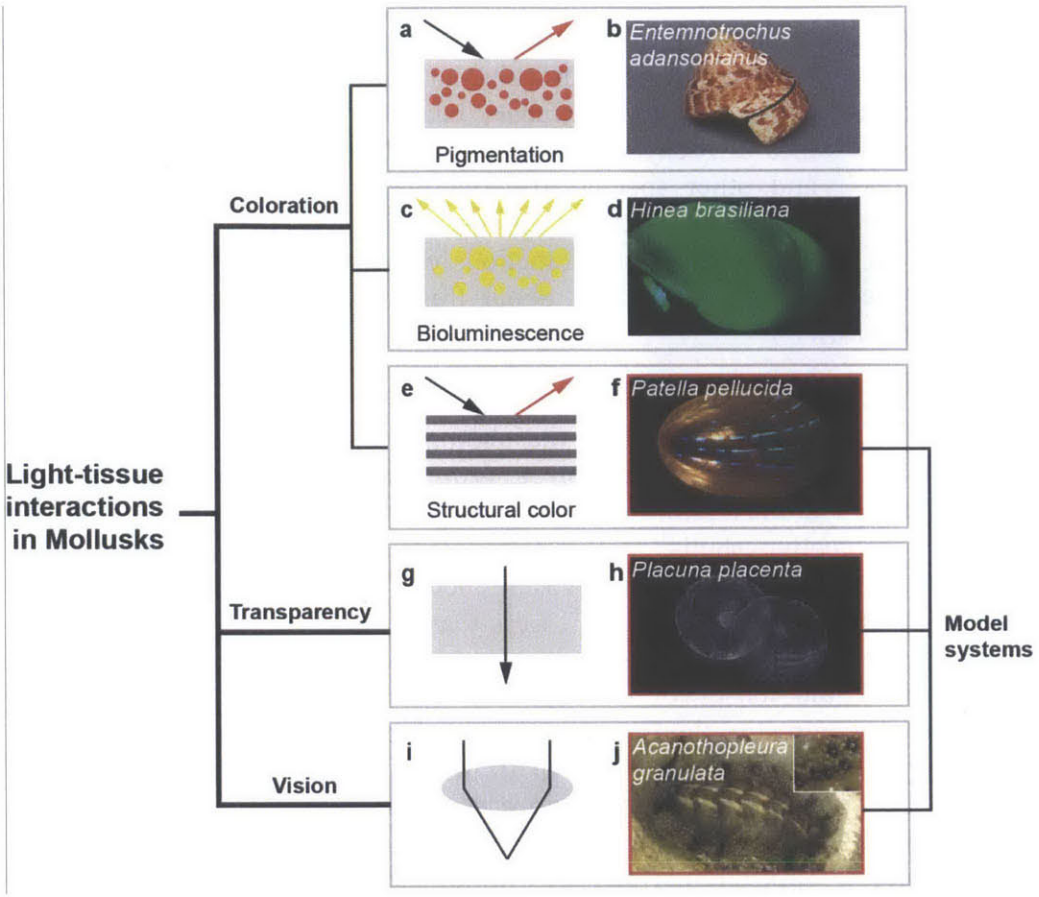

Figure 2-7| Light-tissue interactions in mollusks. **a**,**b**, Pigmentation. **b**, Pigment-based red colored pattern in the shell of *Entemnotrochus adansonianus adansonianus* (http://www.caledonianseashells.com/product.php?id_product=3370). **c**,**d**, Selective diffusive transmission of bioluminescent green light from the shell of *Hinea brasiliana*. **d**, adapted from ref. [129]. **e**,**f**, Structural color. **f**, iridescent blue stripes from the blue-rayed limpet *Patella pellucida*. **g**,**h**, Transparency. **h**, Highly translucent shells from the bivalve *Placuna placenta*. **i**,**j**, Photoreception via eyes with lens. **j**, Biomineralized lenses in the chiton *Acanthoperura granulata*.

Structural color: *Patella pellucida*

Although many mollusks are colored with beautiful patterns (**Figure 2-7b**), the majority of these colorations are resulted from pigment chemicals[130]. Very few mollusk species utilize structural coloration in their protective shells, presumably because of the hash marine environment, possible compromise of mechanical protection performance, and high energy cost to produce intricate photonic structures with biominerals. There are two previous reports on the study of the iridescent green/blue spots in the limpets of *Helcion pruinosus*[131] and *Patella grnatina*[132]. The authors have provided in-depth characterization of the optical performance of the iridescent spots of these limpets and attributed the observed coloration to the "thin-film stack" structures embedded in the shells[131,132]. Here in this thesis I will present a comprehensive investigation of a related species, i.e. the blue-rayed limpet *Patella pellucida*, which has a localized, highly sophisticated, structurally complex, but entirely mineralized localized photonic system embedded within the continuum of its translucent mollusk shell that lies at the origin of

the striking optical appearance (**Figure 2-7f**). This organism displays a dramatic array of thin bright blue stripes along the length of its translucent shell. Ranging from coastal Norway and Iceland south to Portugal and west to the Canary Islands[133,134], this species occupies the lower intertidal and subtidal zones of rocky shores (depth < 27 m), where it populates the fronds and stipes of *Laminaria*[177] and other species of large macroalgae. The limpets, occurring both solitarily and in groups, feed on the kelp leaving distinctive circular feeding marks[135]. It is unclear at this point about the biological functions of these blue stripe patterns; however, we have provided some in-depth discussions about this topic based on their intriguing optical performance (Chapter 6).

Photoreception: *Acanthopleura granulata*

The last model system is focused on the photoreception system of a chiton based on the biomineralized lens structures in the chiton *A. granulata* (**Figure 2-7j**). Chitons are the only known group of extant mollusks to have living tissue integrated within the outermost layer of their mineralized protective shells[136]. The tissue fills a complex network of channels that terminate dorsally as sensory organs known as aesthetes[137]. In two lineages, the aesthetes include hundreds of single chamber lens eyes[122,138]. Less than 10 million years old, the eyes of chitons are likely one of the most recently evolved animal eyes[136]. Unlike the protein-based lenses of most animal eyes[139], the lenses of chitons, like their shells, are principally composed of aragonite[127]. In stark contrast to the few other known eyes that contain calcium carbonate-based lenses, including those found in the shells of trilobites[140] and podocopid ostracodes[141 143], the eyes of chitons are integrated within the entire dorsal shell surface rather than localized to a specific shell region. Recent behavioral experiments found that the intertidal, eyed chiton *A. granulata* responded to dark circular targets with an angular size of 9° equally well in air and when submerged in seawater, but did not react to equivalent uniform decreases in illumination[127], suggesting that its eyes are capable of spatially resolving objects. However, the small size of chiton eyes[136], which range in diameter from ~25-75 μm in the genus *Acanothopleura*[144], and the large curvature of the lenses[145] have cast doubt on their ability to form images. Additionally, critical factors controlling image formation capacity, such as the 3D geometry and crystallography of the lens, are unknown, and the optical mechanism granting the eyes of *A. granulata* equal angular resolution in air and seawater is not well established. Moreover, the trade-offs in the design of mechanical robustness and optical sensation simultaneously in the same material system is not yet addressed previously. In this thesis, the structural, optical, and mechanical characteristics of this unique biomineralized material system will be studied in detail, and the interplay between these characteristics sheds light on the designs of multifunctional structural materials.

Table 2-1| Comparison of three model systems studied in this thesis, *Placuna placenta*, *Patella pellucida*, and *Acanthopleura granulata*.

		Placuna placenta	*Patella pellucida*	*Acanthopleura granulata*
Common names		Windowpane oysters	Blue-rayed limpet	West Indian fuzzy chiton
Taxonomy	**Kingdom**		Animalia	
	Phylum		Mollusca	
	Class	Bivalvia	Gastropod	Polyplacophora
	Order	Ostreoida	Patellogastropoda	Neoloricata
	Family	Placunidae	Patellidae	Chitonidae
	Genus	*Placuna*	*Patella*	*Acanthopleura*
	Species	*P. placenta*	*P. plellucida*	*A. granulata*
Origin		Indo-west Pacific[128]	Norway and Iceland south to Portugal and west to the Canary Islands[133,134]	Southern Florida to Mexico, south to Panama, West Indies
Habitat		Sandy, shallow waters (<100 m)[128]	the lower intertidal and subtidal zones of rocky shores (depth < 27 m), where it populates the fronds and stipes of *Laminaria* and other species of large macroalgae[177]	Intertidal zone, live on rock, a lot of sun
Light condition		Good	Good	Good
Morphology		Circular, flat	Cone	Eight plates, flexible
Optical features		High translucency	Iridescent blue stripes	Vision via lenses
Size		Up to 150 mm	Up to 15 mm	Up to 70 mm
Composition		Calcite	Calcite and aragonite	Aragonite
Mineral content		~99 wt%	>95 wt% (estimated)	> 95 wt% (estimated)
Locomotion		No	Little once settled	Slow movement

Chapter 3 Materials design and optical properties of the shell of *P. placenta*

This chapter was published as a regular article: Li, L. & Ortiz, C. Biological Design for Simultaneous Optical Transparency and Mechanical Robustness in the Shell of *Placuna placenta*, *Advanced Materials* **25**, 2344-2350 (2013)[146].

3.1 Introduction

The phenotype of biological systems can be represented by a space of traits, for example, macroscopic morphology, physiology, behavior, and, more recently, material properties, which are governed by natural selection through the adaptations to species-specific habitats in order to achieve multiple functions[147–149]. Biological exoskeletons, for example, need to simultaneously satisfy requirements of protection from predators, hydration and thermal regulation, locomotion, reproduction and etc. Such systems exhibit a hierarchical (length-scale dependent) set of structural features including molecular structure, chemical composition, and spatial distribution and crystallographic orientation of building blocks, which are coupled to larger length-scale morphology in order to achieve desired mechanical, optical, thermal, and other relevant properties[4,150,151]. A significant amount of research has focused on the structural origins of the unusual combination of superior mechanical properties of a variety of biological exoskeletal systems[15,26,28,32,151]. Recently, a number of mollusk species have been shown to possess shells that exhibit both mechanical and optical functions, including selective light diffusion[129], photonic coloration[131,132], and vision[127].

In this chapter, through a combination of experimental and theoretical methods, I investigate a highly mineralized biological exoskeleton, *Placuna placenta*, which simultaneously achieves high optical transparency and mechanical robustness. While it is unclear whether or not the transparency plays a biological role, the design leading to a combination of these characteristics in a single system holds great potential for the development of bio-inspired engineering transparent structural materials for both commercial and military applications, including, for example, soldier eye/face protection, windows and windshields, blast shields, and combat vehicle vision blocks[152–154].

3.2 Methods

3.2.1 Experimental methods

Samples: Edge-trimmed *P. placenta* shell specimens (diameter: ~50 mm) were purchased from Seashell World (FL, United States). Intact *P. placenta* shells were purchased from Conchology, Inc (Philippines).

Microscopy (optical microscopy, scanning electron microscopy, transmission electron microscopy and atomic force microscopy): Optical images were taken with a Nikon ECLIPSE LV100 microscope (Tokyo, Japan). Samples were imaged using Helios Nanolab 600 Dual Beam (FEI, OR) at the acceleration voltage of 5 keV and working distance of 4 mm. TEM observations were obtained using a JEOL 2011 operated at 80 and 120 keV, and a JEOL 2010F operated at 200 keV. The image magnification and camera constants were calibrated using a standard sample (MAG*I*CAL, Electron Microscopy Sciences, PA, USA). A Digital Instruments Multimode SPM IIIA (Veeco, Santa Barbara, CA) was used with AS-130 "JV" scanners. Tapping mode AFM (TMAFM) imaging was conducted with NANOSENSORS Si TMAFM cantilevers (PPP-NCHR-10).

Size measurement of intracrystalline inclusions: Top-viewed bright-field TEM images were used directly for the size measurement, and the relative frequency of inclusions in a certain size group counted in a unit area (f_A) was first obtained. The frequency of inclusions in a certain size groups counted in a unit volume (f_V) was then calculated from stereological correction, which is further fitted with the following log-normal distribution[155]:

$$f(r) = \frac{1}{\sqrt{2\pi}\sigma r_m e^{\frac{1}{2}\sigma^2}} e^{-\frac{(\ln r - \ln r_m)^2}{2\sigma^2}} \qquad \text{Equation 3-1}$$

Structural analysis: Powder X-ray diffraction spectrums were obtained using Rigaku powder diffractometers with a rotating anode generator and 180 mm Bragg-Brentano diffractormeter, operating at 250 kV and 50 mA between 20 and 90° (2θ). Electron backscattered diffraction analysis was carried out using a FEI Helios FIB/SEM system equipped with the HKL Technology "Channel 5" EBSD system.

Thermogravimetric analysis: The shells were first ground with a pestle and mortar. Samples were then vacuum dried at 110°C overnight to remove residual water. TGA was carried out from 100 to 500°C at 2.5°C/min on a TA Instruments TGA Q50 (New Castle, DE).

Total and in-line transmission and Microspectroscopy: Macroscopic optical in-line transmittance of samples with different thickness was measured using a Cary 5E UV-Vis-NIR Dual-Beam spectrophotometer in the wavelength range of 200-800 nm. The total forward transmission was measured using the spectrophotometer equipped with an integrating sphere. A modified Leica DMRX microscope was used to carry out parallel optical imaging and spectroscopic spatial optical mapping (reflection and transmission) at microscopic level.

3.2.2 Theoretical methods: light scattering model

The optical performance of *P. placenta* shells was investigated theoretically by modeling the light scattering which results from a combination of mechanisms[156,157]. Firstly, the in-line transmission (T, [-]) can be expressed by the Lambert-Beer Law:

$$T = (1-R)\exp(-C_{sca}t) \qquad \text{Equation 3-2}$$

where R is the reflection [-], C_{csa} [m^{-1}] is the effective scattering coefficient, and t [m] is the sample thickness.

Nanoscopic intracrystalline inclusions contribute to the light scattering, as the refractive index of organic inclusions and surrounding mineral matrix have different refractive indices. Additionally, calcite is a highly birefringent material, which means the refractive indices vary with the crystal orientations[125]. The misorientation of the calcitic building blocks leads to a discontinuity of the refractive indices, which further causes scattering of incident light. Thus the effective scattering coefficient is the sum of the scattering caused by the inclusions and by the birefringence:

$$C_{sca} = C_{incl} + C_{bire}. \qquad \text{Equation 3-3}$$

The scattering coefficient for the inclusions (C_{incl}) can be expressed as follows

$$C_{incl} = N_{incl} G_{incl} Q_{incl}, \qquad \text{Equation 3-4}$$

where N_{incl} is inclusion number density [m^{-3}], G_{incl} is the geometrical cross section of the inclusion ([m^2]; = πr^2; r is average radius of inclusions), and the Q_{incl} [-] is the scattering efficiency factor, which can be numerically calculated using classic Mie scattering theory[158]. The refractive index of proteinaceous inclusions was assumed to be 1.35[159,160].

The birefringent scattering model applied was developed by Apetz *et al.* and successfully used to predict the optical properties of polycrystalline transparent birefringent Al_2O_3[156]. The model approximates a polycrystalline material as a system with mono-sized spheres distributed in a homogeneous matrix such that the absolute refractive index difference between the spheres and the matrix (Δn) equals the average birefringence of the system. Similar to inclusion scattering, the birefringence scattering coefficient can thus be expressed as:

$$C_{bire} = N_{bire} G_{bire} Q_{bire}, \qquad \text{Equation 3-5}$$

where Q_{bire} [-], the birefringence scattering efficiency factor, can be expressed as

$$Q_{bire} = \frac{8\pi^2 r_{bire}^{\ 2}}{\lambda_m^{\ 2}} \left(\frac{\Delta n}{n} \right)^2, \qquad \text{Equation 3-6}$$

where r_{bire} [m] is the average radius of the grains (half of the thickness of calcitic building blocks was used), λ_m [m] is the wavelength of incident light in the medium, and n is the average refractive index of the matrix.

3.3 Results

3.3.1 The hierarchical structural characteristics

The natural transparent structural material system from *Placuna placenta* (Linnaeus, 1758; Mollusca: Bivalvia; commonly known as window pane oyster) has two highly transparent, circular-shaped flat mineralized valves (**Figure 3-1**). *P. placenta* lives unattached on the surfaces of muddy or sandy flats in shallow water (depth < 100 m) of the tropical Indo-West Pacific[128]. Due to the high optical transparency of their shells, *P. placenta* are widely collected and commercially cultured in large quantities for shellcrafts, and local people are known to use the shells as a substitute for window glass in houses[128]. The entire shell is highly transparent except the posterior adductor scar (PAS) regions (the whitish regions indicated by the red circles, **Figure 3-1b**), which are used for adductor muscle attachment.

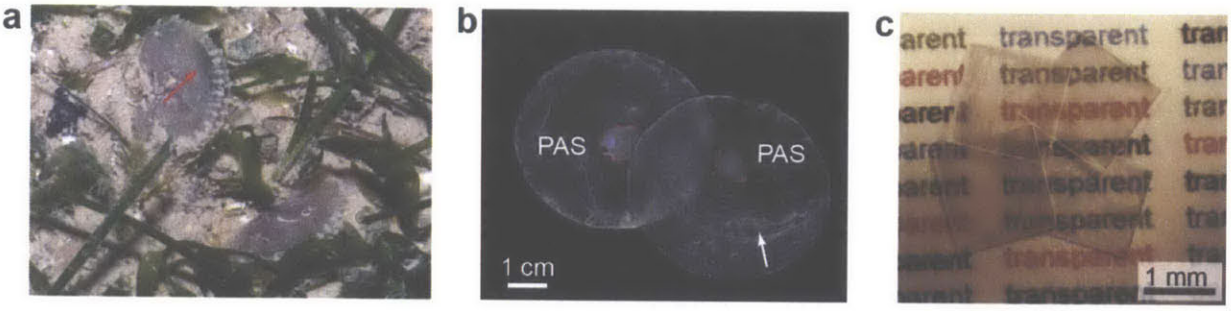

Figure 3-1| Highly transparent shells of *P. placenta*. a, Live *P. placenta* in their natural habitat (Kampong Pasir Ris, Singapore, May 2011). Green seaweed behind the shells can be seen (red arrow). Picture was used with permission from Ria Tan. **b**, *P. placenta* shell specimens with edges trimmed. "PAS" = posterior adductor scar (red circles). White arrow indicates the growth lines. **c**, Square-shaped tiles cut from *P. placenta* shell specimens.

With the exception of the PAS regions, where a thin layer (~20 μm) of a prismatic microstructure is present on the inner side of the shell, the entire shell is composed of the foliated microstructure (will be discussed in detail later), as both top and bottom shell surfaces exhibit similar elongated building blocks (**Figure 3-2**). This single-microstructure design is consistent with Taylor's hypothesis of the microstructural evolution trends in bivalves, where the outer prismatic layer is completely absent in Pectinacea, Limacea, and Anomiacea[161]. Additionally, unlike most other bivalves, no organic periostracum layer was found on the exterior side of the *P. placenta* shell. Detailed mapping of the entire cross-section of the shell reveals a relatively constant thickness profile of the foliated structure (294 ± 84 nm, n = 1748), although a slight decrease to ~50 nm towards the PAS prismatic/foliated interface was observed (**Figure 3-2d**). Tapping mode atomic force microscopic (TMAFM) imaging of finely polished shell cross sections (**Figure 3-2e**) and scanning electron microscopic (SEM) imaging of cryo-fractured surfaces (**Figure 3-2g**) showed that the *P. placenta* shell is composed of a mineralized lamellar microstructure with a crystallographic phase of calcite (as shown later).

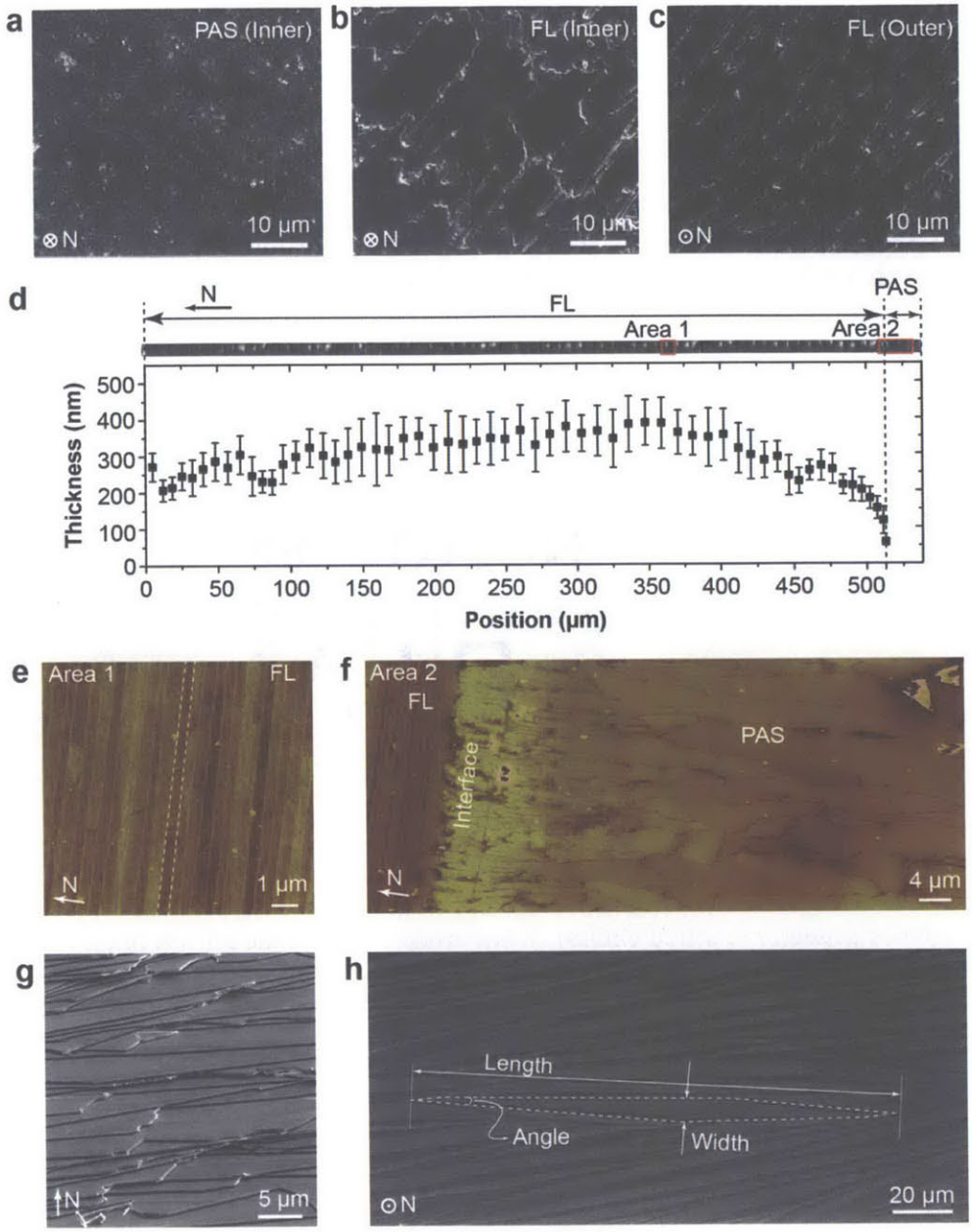

Figure 3-2| The foliated microstructure in the *P. placenta* shell. Scanning electron microscopy (SEM) images of (**a**) PAS area, (**b**) inner, and (**c**) outer surface of the foliated microstructure. **d**, Thickness mapping across the entire shell of *P. placenta*. Top, merged SEM images (~60 images). Bottom, corresponding thickness profile of the mineralized building blocks in the foliated microstructure. AFM images of (e) primary foliated layer and (**f**) the interface region between PAS and foliated structure. **g**, SEM image of a cyro-fractured surface, revealing the multilayer structure. **h**, A top-viewed SEM image of a freshly cleaved shell surface, revealing the elongated diamond-shaped building blocks of the foliated microstructure. Geometrical parameters, i.e., length, width and tip angle, are defined as indicated in the image.

Top-viewed SEM images of freshly cleaved samples reveal the mosaic-like organization of the elongated diamond-shaped building blocks, which have arrow-point endings and coalesce

laterally to form laminae or sheets (**Figure 3-2h**). This is the primary feature of the foliated microstructure commonly observed in bivalves and some limpets[40,162]. The characteristic length, width, and tip angle of the building blocks as defined in **Figure 3-2h** are 141.8 ± 43.4 μm (mean ± standard deviation, n = 40), 5.54 ± 1.36 μm (n = 49), and 10.45 ± 2.95° (n = 71), respectively.

Tapping mode atomic force microscopic analysis of freshly cleaved building block interfaces reveals a subtle surface tomographic feature: microridges with inclination angles of 1.4 ± 0.4° (**Figure 3-3a-c**). Imaging of the two opposed shell surfaces immediately after cleavage clearly shows that adjacent contacting mineral surfaces have conformal topologies (**Figure 3-3d-f**). This structural feature may enhance the shell's mechanical strength and toughness by restricting the sliding of building blocks upon deformation[59].

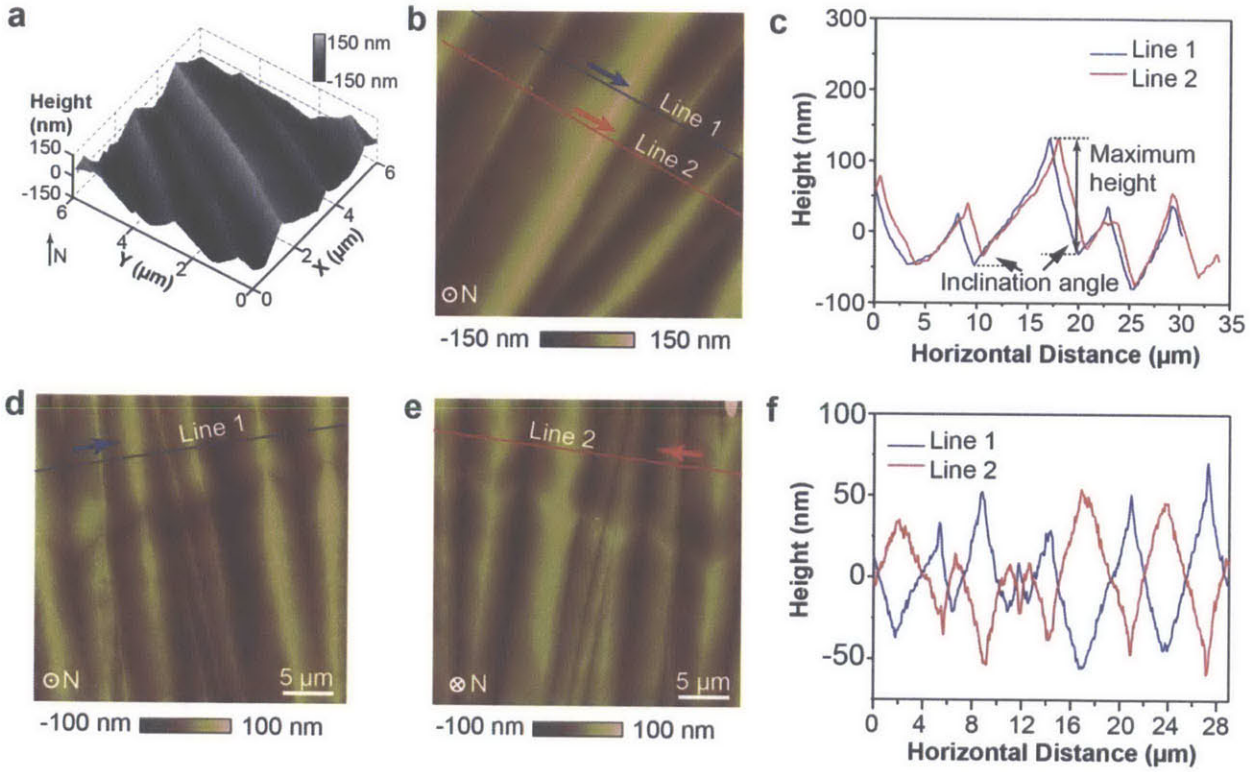

Figure 3-3| Microscale ridges at the surface of elongated diamond shaped building blocks. **a,b**, AFM height image of the surface topology of foliated microstructure, demonstrating the microridges of the building blocks. **c**, Height profiles along line 1 and 2 as indicated in (**b**). Inclination angle and maximum height are also indicated. **d,e,** AFM height images of two corresponding opposed surfaces of *P. placenta* shell immediately after cleavage, demonstrating conformal surface topologies. **f**, Height profiles along the two lines with the same location and orientation (as shown in (**d**) and (**e**), which further quantitatively shows the conformal surface topologies between two adjacent mineral layers.

Biological materials are usually composites consisting of biopolymers and minerals[4], as discussed in Chapter 2. Thermogravimetric analysis shows that the *P. placenta* shell is highly mineralized; its mineral content is 98.90 ± 0.19 wt% (n = 3, **Appendix A, Figure A-1**), which is higher than gastropod nacre, coral skeleton, and chiton plates.[22,23] Similar to nacreous structure, both inter- and intra-crystalline organics are present in the foliated microstructure of *P. placenta*

shell (**Figure 3-4a**). Both AFM and transmission electron microscopy (TEM) imaging were used to investigate the characteristics of the inter-crystalline organic materials, i.e. the organic interfaces between adjacent mineral layers (**Figure 3-4**). TEM cross-sectional examination of the foliated microstructure revealed ultra-thin organic interfaces (~2 nm, **Figure 3-4b-c**). Multi-mode AFM imaging shown in **Figure 3-4d-f** further shows the presence of organic materials after the shell was cleaved. The thickness of organic interfaces quantified from the height information is 1.19 ± 0.22 nm (n = 98). Moreover, nano-sized asperities similar to structures in nacre were observed at the surface of the calcite laths (**Figure 3-4d-e**).

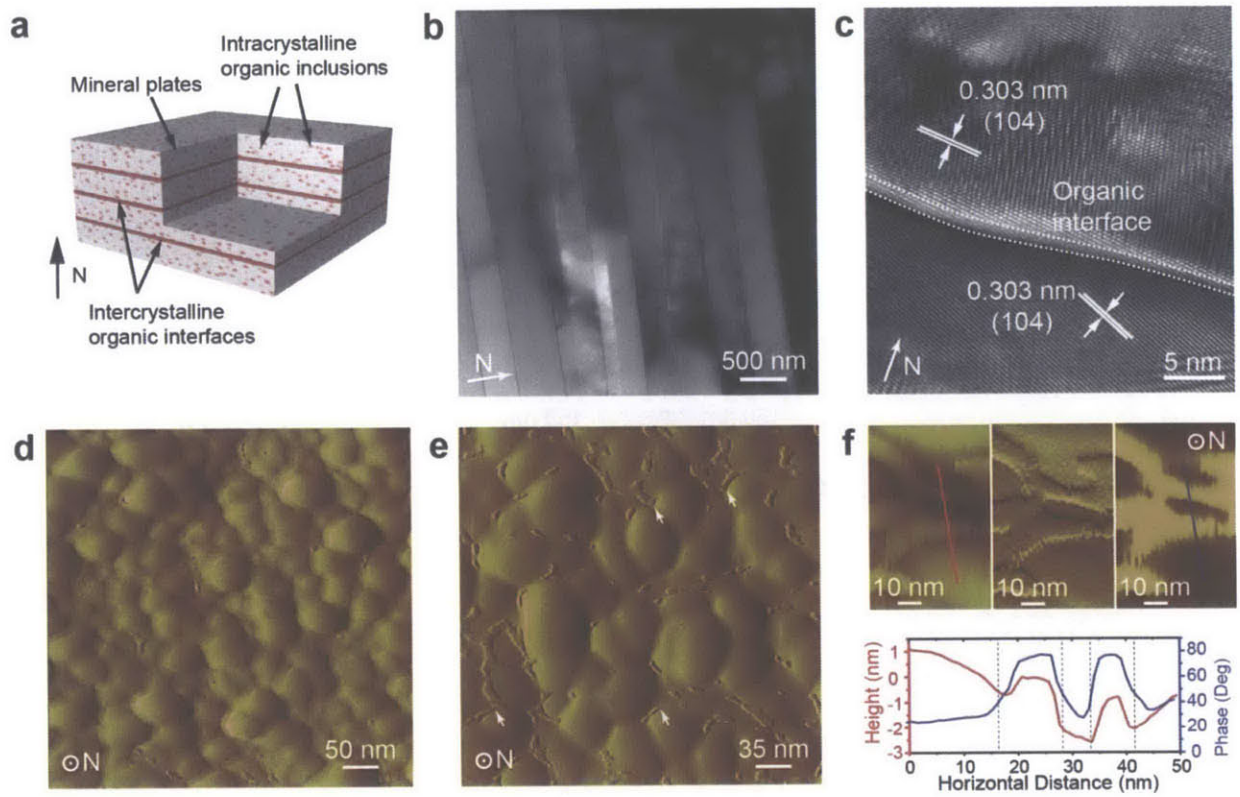

Figure 3-4| Inter-crystalline organic interfaces. a, Schematic diagram showing both intra- and inter-crystalline organics present in the mineralized foliated structure (not in scale). **b**, Cross-sectional TEM images of the foliated microstructure. **c**, High-resolution TEM image revealing the ultra-thin organic interfaces (~ 2 nm) between two adjacent mineral layers (marked by dotted lines). The lattice fringes match with {104} planes of calcite. **d,e**, Representative amplitude images of freshly-cleaved surface, showing the presence of organic materials. **f**, Top: height (left), amplitude (middle), and phase (right) images of the organic interface. Bottom: height and phase profiles across the organic along the lines as indicated in the height and phase images.

In addition to intercrystalline organic interfaces sandwiched between mineralized building blocks, nanoscopic intracrystalline inclusions are distributed within them (**Figure 3-5a**). These inclusions are believed to consist of organic macromolecules trapped during the biomineralization process, which is a common phenomenon observed in a variety of biogenic minerals, including nacre and sea urchin teeth and spines[34,163–165]. Through a quantitative dimension analysis using stereological correction methods[166], I determined the average diameter

and total volume fraction of the intracrystalline inclusions to be 25.2 nm and 0.45%, respectively (**Figure 3-5b**).

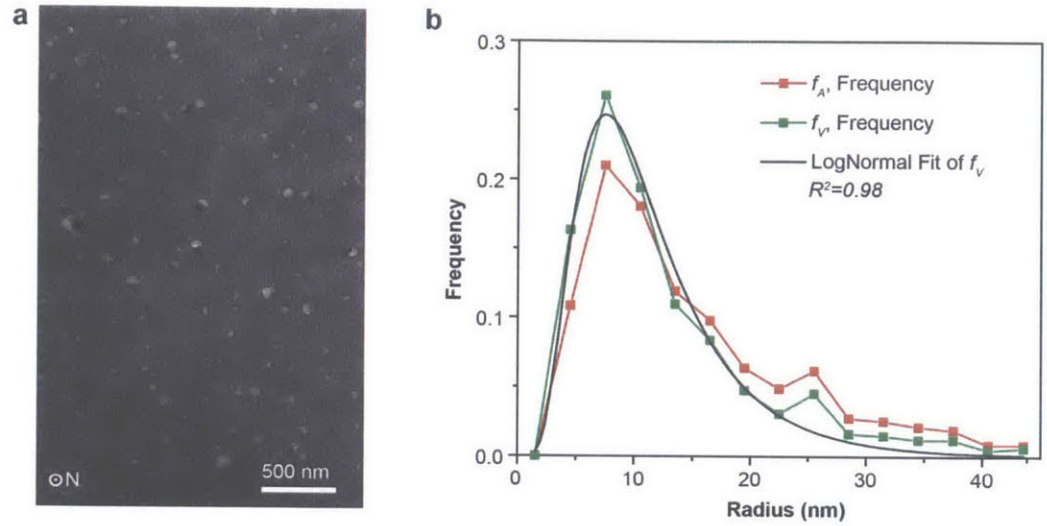

Figure 3-5| Intra-crystalline organic inclusions. a, A top-viewed TEM image of the intracrystalline nanoscopic inclusions within the mineralized building blocks. "N" = normal direction of shell. **b**, Quantitative analysis of the intracrystalline inclusion size through stereological correction[166]. f_A: the relative frequency of inclusions of a certain size group counted in a unit area based on TEM images; f_V: the calculated frequency of particles of a certain size groups counted in a unit volume from stereological correction, which is further fitted with a log-normal distribution (see methods)[155]:

3.3.2 The crystallographic texture

Determining the crystallographic organization of the calcitic building blocks is critical in order to understand the optical and mechanical performance of the shell due to the inherent anisotropic optical[125] and mechanical[167] properties of calcium carbonate. X-ray diffraction measurements of *P. placenta* shells show characteristic peaks corresponding to calcite (**Appendix A, Figure A-2**). Crystallographic orientation and distribution at the building block level were studied using electron backscattered diffraction (EBSD, **Figure 3-6**). **Figure 3-6a** displays an SEM image of an area in a freshly cleaved *P. placenta* shell which was mapped with EBSD. The similar green color in the corresponding Euler angle mapping in **Figure 3-6b** indicates that there is a strong crystallographic co-orientation among the calcitic building blocks (referenced to the hexagonal unit cell of calcite, a = 4.99 Å, c = 17.06 Å). The corresponding pole figures with well-defined diffraction spots further demonstrate the alignment (**Figure 3-6c**). The distribution of tilting angles of the calcite *c*-axes with respect to the shell normal extracted from the {001} pole figure is 24.43 ± 3.46° (**Figure 3-6d**). A similar result has been reported previously[40], and the top surface of the calcitic building blocks is close to {108} planes of calcite (the inter-planar angle between {108} and {001} planes is 26.27°). In addition, the tilting direction is towards the longitudinal direction of the building blocks, which is evident by the horizontal shift of {001} diffraction spot in its pole figure, consistent with the longitudinal direction of the building blocks in **Figure 3-6a**. The variation in *c*-axis tilting angles is mainly due to the crystallographic misalignment among different building blocks, as shown by the high

misorientation angles (typically > 5°) in the misorientation profile along the transverse direction of the building blocks (**Figure 3-6e**). In contrast, the profile along the longitudinal direction generally exhibits small misorientation angles (typically < 1°) due to its lower probability of crossing the boundaries of building blocks as compared to the transverse direction.

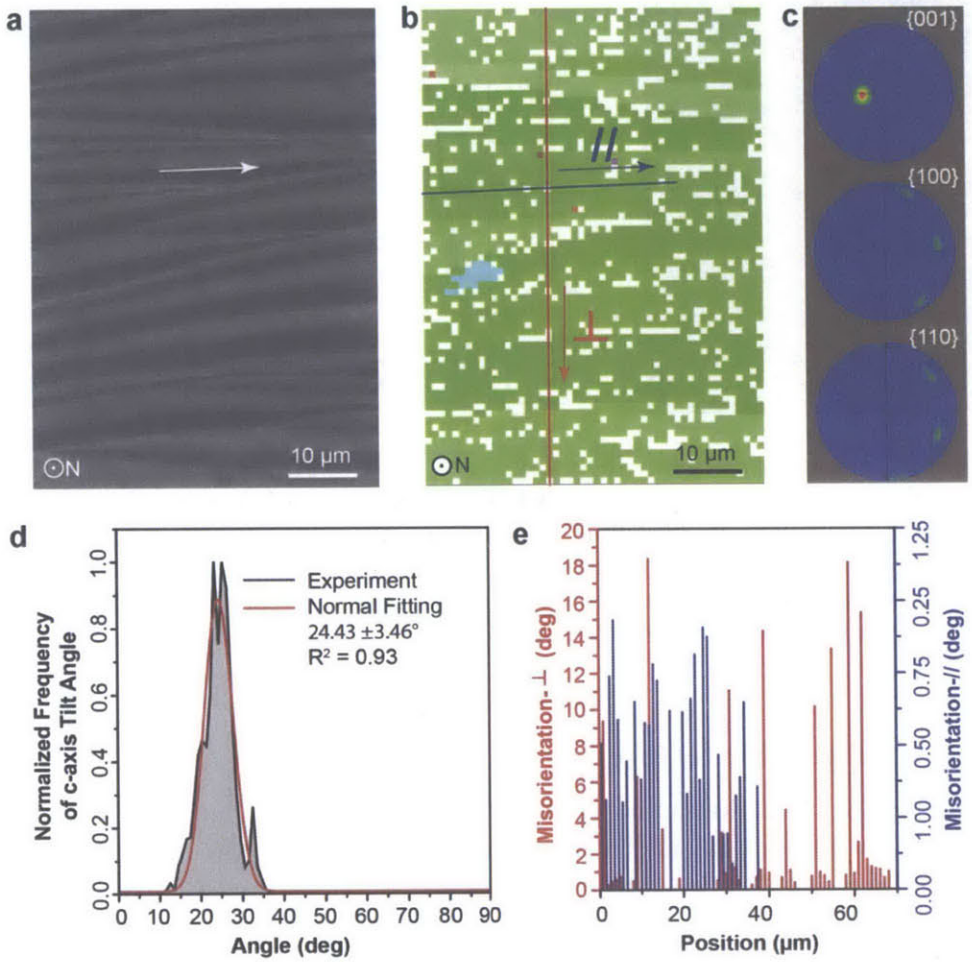

Figure 3-6| Crystallographic organization of the foliated microstructure in *P. placenta* at building block level. a, An SEM image of the freshly cleaved shell surface mapped with electron backscattered diffraction (EBSD). The white arrow indicates the longitudinal direction of the elongated building blocks. **b**, An corresponding EBSD map with color coded for all the three Euler angles ($\varphi 1$, φ, $\varphi 2$). The red and blue lines (perpendicular and parallel to the longitudinal direction of building blocks) are indicated for plotting the misorientation profiles along them as shown in (**e**). **c**, Pole density plots for the mapped region in (**a**). **d**, Distribution of tilt angle of the calcite *c*-axis with respect to the shell normal direction. The red curve represents a fit to a normal distribution to the data. **e**, Crystallographic misorientation profiles along the transverse (red line) and longitudinal (blue line) directions of the building blocks as shown in (**b**).

The misalignment among adjacent building blocks was further studied using selected area electron diffraction (SAED) in TEM (**Figure 3-7**). Diffraction patterns from two adjacent intact building blocks were indexed with calcite with the zone axis of $[1\bar{1}\bar{1}]$. The {110} diffraction spots are perpendicular to the corresponding longitudinal direction of the building blocks, which indicates that the *c*-axis is tilted in this direction, consistent with the EBSD results. The exact

tilting angle cannot be determined in this case since the angle between the top surface of the sample and the electron beam might not be exactly perpendicular. Moreover, the rotation angle between the two diffraction patterns for these two adjacent building blocks (6.9°) is consistent with the angle between their longitudinal axes (~6.0°).

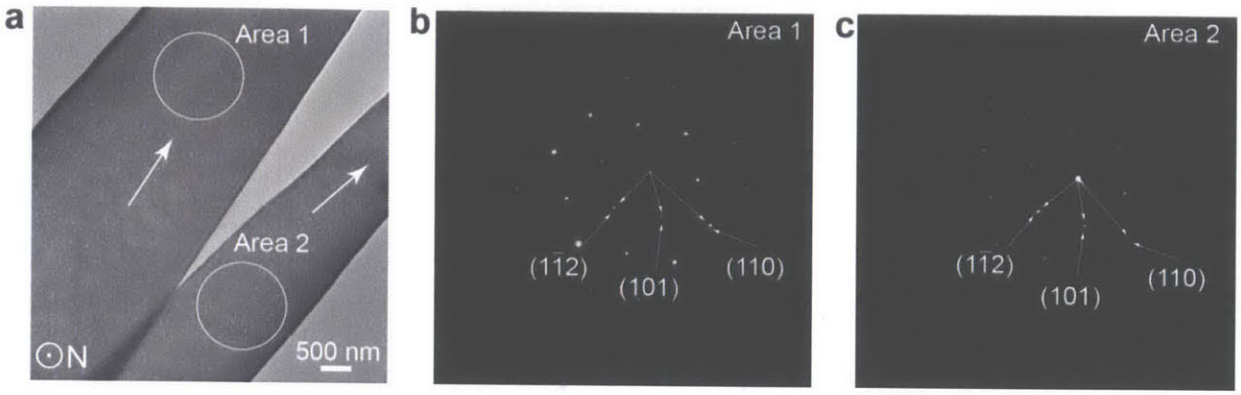

Figure 3-7| Electron diffraction at building block level. a, TEM image showing two adjacent intact building blocks. The longitudinal directions of the building blocks are indicated by the white arrows. Selected area electron diffraction (SAED) patterns corresponding to area (**b**) 1 and (**c**) 2 in (**a**). Zone axis = [1$\bar{1}\bar{1}$].

3.3.3 The multiscale structural model

The quantitative measurements of structural features of *P. placenta* shells at multiple length scales from mm to nm are summarized in **Table 3-1**. The hierarchical structural model is also schematically illustrated in **Figure 3-8**.Very briefly, the calcitic *P. placenta* shells are primarily composed of the foliated microstructure which has basic building blocks with elongated diamond geometries. The thickness of the mineral laths and inter-crystalline organic interfaces are ca. 300 and 2 nm, respectively. Similar to aragonitic nacre, each lath diffracts as a single crystal, although crystallographic misorientations are present among adjacent building blocks. the *c*-axis of these calcitic laths are tilted by 24.4 ± 3.5° relative to their surface normals, resulting in a lath surface close to the {108} planes of calcite. Nano-sized intra-crystalline organic inclusions are also distributed with the calcitic building blocks.

Table 3-1| Quantitative analysis of structural features of the *P. placenta* shell. Measurements are based on scanning electron microscopy (SEM), atomic force microscopy (AFM), transmission electron microscopy (TEM), thermogravimetric analysis (TGA), X-ray diffraction (XRD), and electron backscattered diffraction (EBSD). "N" = normal of the shell, "L" = longitudinal direction of the elongated diamond-shaped building blocks in the foliated structure.

Length Scale	Feature (orientation)	Mean ± Standard Deviation (n)	Technique
mm	Total Thickness (// to N)	~0.5 -1 mm	Micrometer and SEM
	Total number of layers (// to N)	~1500-3000	SEM
	Mineral content	98.93 ± 0.09 wt% (n=3)	TGA
	Crystallographic phase	Calcite	XRD, TEM, EBSD
µm	Length of foliated building blocks (⊥ to N)	141.8 ± 43.4 µm (n=40)	SEM
	Width of foliated building blocks (⊥ to N)	5.54 ± 1.36 µm (n=49)	SEM
	Tip angle of foliated building blocks (⊥ to N)	10.45 ± 2.95° (n=71)	SEM
	C-axis tilting angle (relative to N)	24.43 ± 3.46°	EBSD
	Crystal misorientation among adjacent building blocks	13.52 ± 6.63° (n=25)	EBSD
nm	Thickness of foliated building blocks (// to N)	294 ± 84 nm (n=1748)	SEM and AFM
	Maximum height of micro-ridges (// to N)	67.0 ± 37.2 nm (n=100)	AFM
	Inclination angle of micro-ridges (⊥ to N)	1.4 ± 0.4° (n=50)	AFM
	Diameter of the nano-asperities (⊥ to N)	54.8 ± 17.9 nm (n=71)	AFM
	Height of the nano-asperities (// to N)	4.3 ± 2.4 nm (n=71)	AFM
	Height of inter-crystalline organic interfaces (// to N)	1.2 ± 0.2 nm (n=98)	AFM
	Diameter of intra-crystalline organics inclusions (⊥ to N)	46.6 ± 24.7 nm (n=313)	TEM

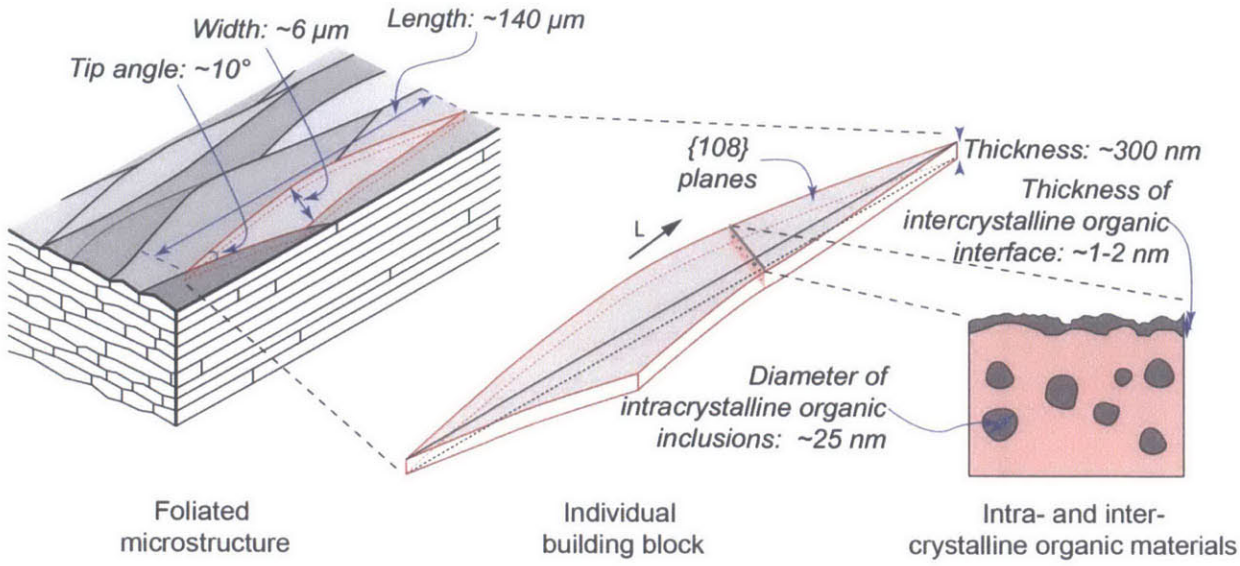

Figure 3-8| Schematic diagram (not in scale) of the foliated microstructure in *P. placenta*. Dimensions of structural features are also indicated. "*L*" refers to the longitudinal direction of the laths.

3.3.4 Optical properties

I performed a systematic investigation of the optical properties of *P. placenta* shells using both experimental and theoretical approaches. The macroscopic in-line transmissions (illumination area, ~1 mm^2, collection cone, ~2°) were measured via a double-beam spectrophotometer using wavelengths between 250-800 nm. The total forward transmission was also measured with the spectrophotometer by equipping it with an integration sphere. Typical transmission and reflection spectrums of the shells (thickness ~0.5 mm) are presented in **Figure 3-9a**. The shell exhibits high total transmission in the visible light range (up to ~80%), and summation of total transmission and reflection leads to ~95% of the incident light intensity, indicating this biocomposite absorbs a very small amount of visible light. The typical in-line transmission is about one half of the total transmission, and the positive correlation between the intensity and wavelength suggests the possible presence of light scattering. **Figure 3-9b** shows a series of photos of an intact *P. placenta* shell (thickness, ~0.5 mm) which was placed at different distances between the shell and the background. The shell is highly "transparent" when it is directly placed on top of the background, allowing to perceive the objects directly behind. However, due to the strong scattering of light, the degree of transparency dropped dramatically as the distance was increased between the shell and the background. Therefore, the shell is not intrinsically transparent, but translucent[123,168]. However, we should note that as the animal lives on sandy sea floor[128], this high translucency might already be enough in allowing successful transparency camouflage.

Interestingly, the in-line transmission intensity for the PAS area is very low (<5%) in comparison to the majority of the shell, which suggests that the single macroscopic layer with the same microstructure (foliated in this case) is beneficial for high optical transparency.

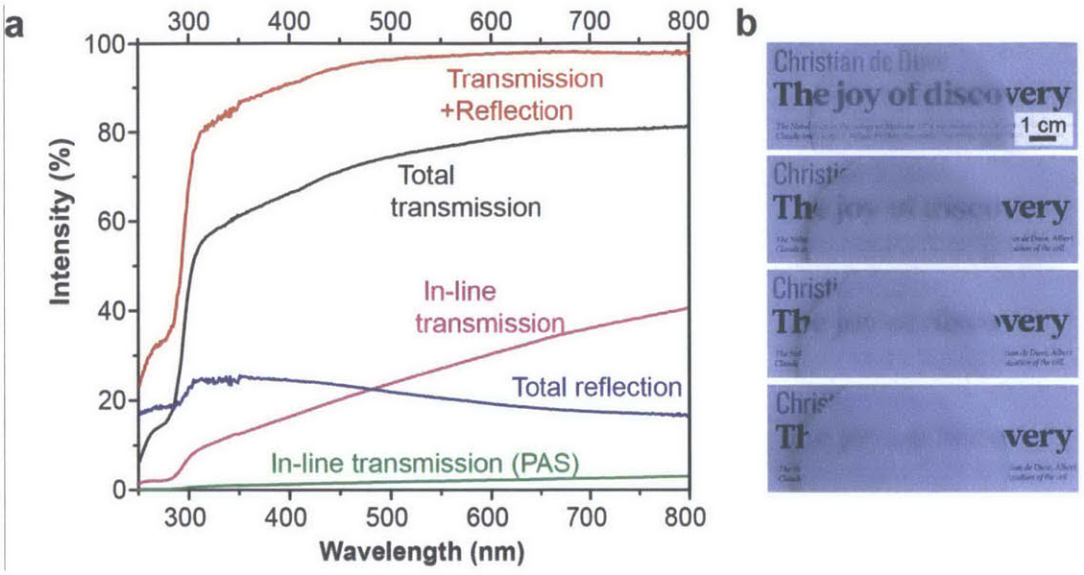

Figure 3-9| Macroscopic optical behavior of *P. placenta* shell. **a**, Macroscopic optical performance of the as-received *P. placenta* shell with thickness of ~0.5 mm. **a**, Photos of an intact *P. placenta* shell placed on top of background with increasing distance: 0 cm, 0.5 cm, 1.0 cm, 2.0 cm from top to bottom.

The microscopic optical performance of *P. placenta* shell at building block level was determined using a micro-spectrometer, through which the local transmission and reflection of samples was collected confocally via one of the microscope ports and guided through an optical fiber to a spectrometer (typical step size: 1 μm). The shell exhibits homogeneous transmission (~85%) and reflection (~13%) at the building block level (**Figure 3-10**).

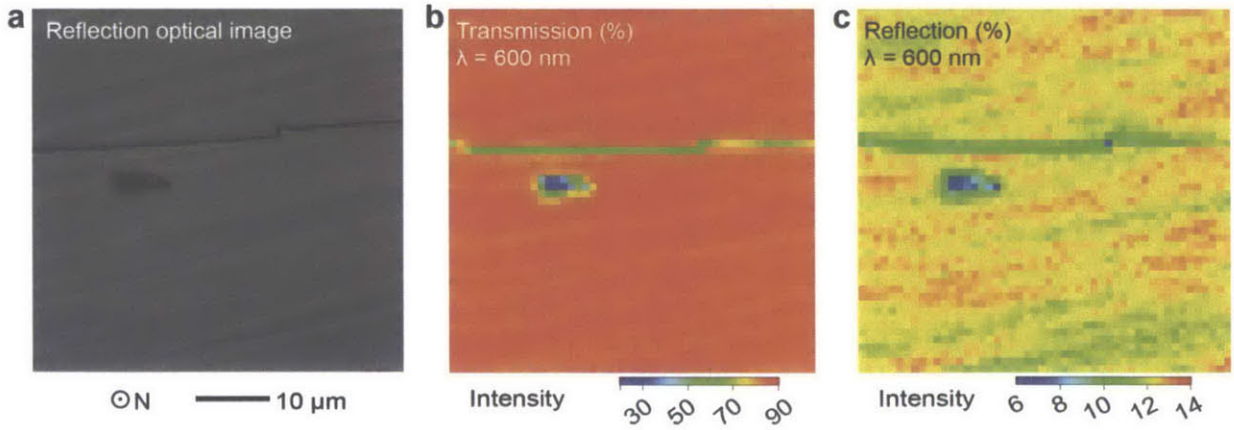

Figure 3-10| Microscopic optical behavior of *P. placenta* shell. Microscopic optical mappings at wavelength of 600 nm for transmission (**b**) and reflection (**c**) measured in the area of sample (thickness, ~ 100 μm) shown in the optical reflection image (**a**). The maps were generated from arrays of 50×50 individual spectrum measurements with a step size of 1 μm using a micro-spectrometer.

The experimentally measured in-line transmission intensities of samples with different thicknesses show good agreement with the predictions of the theoretical scattering model (**Figure 3-11a**). The decrease in transmission level with increasing sample thickness is a direct result of the Lambert-Beer Law. Using the measured size distribution of intracrystalline inclusions has a minimal effect in providing an improved prediction of the in-line transmission profiles as compared to the case of using the average inclusion size[155]. The scattering coefficients for both inclusion and birefringence scattering decrease with increasing wavelength (**Figure 3-11b**), which is responsible for the increase of in-line transmission with the wavelength. More importantly, the birefringence scattering dominates the scattering loss in the visible light range; the contribution of inclusion scattering ranges from 31% at 250 nm to 7% at 800 nm. Scattering losses from inclusions are low because their small sizes are just below the critical dimension (~100 nm) to cause significant scattering (**Figure 3-11c**). Parallel simulations (assuming the same volume fraction of inclusions) with the largest inclusions (~97 nm in diameter) only result in a scattering efficiency factor of ~0.02 at 600 nm, corresponding to the scattering coefficient ~0.14 mm^{-1} (~16.8% of total scattering). The low contribution of inclusion scattering is also due to the fact that calcite is a highly birefringent material. At wavelength of 600 nm, the refractive index is 1.6576 for the ordinary ray (polarization perpendicular to the *c*-axis) and 1.4858 for the extraordinary ray (polarization parallel to the *c*-axis), which results in a refractive index difference of 0.1718[125]. Using the distribution of crystallographic orientations measured from EBSD, the average refractive index difference (Δn) is typically 0.02-0.03 (full width at half maximum after fitting the distribution of refractive indices to a normal distribution), as compared to $\Delta n < 0.008$ (corresponding to ~2.8% of the birefringent scattering for calcite) for a typical engineering transparent birefringent material, polycrystalline Al_2O_3 (assuming the crystallographic orientation of each grain is random)[156].

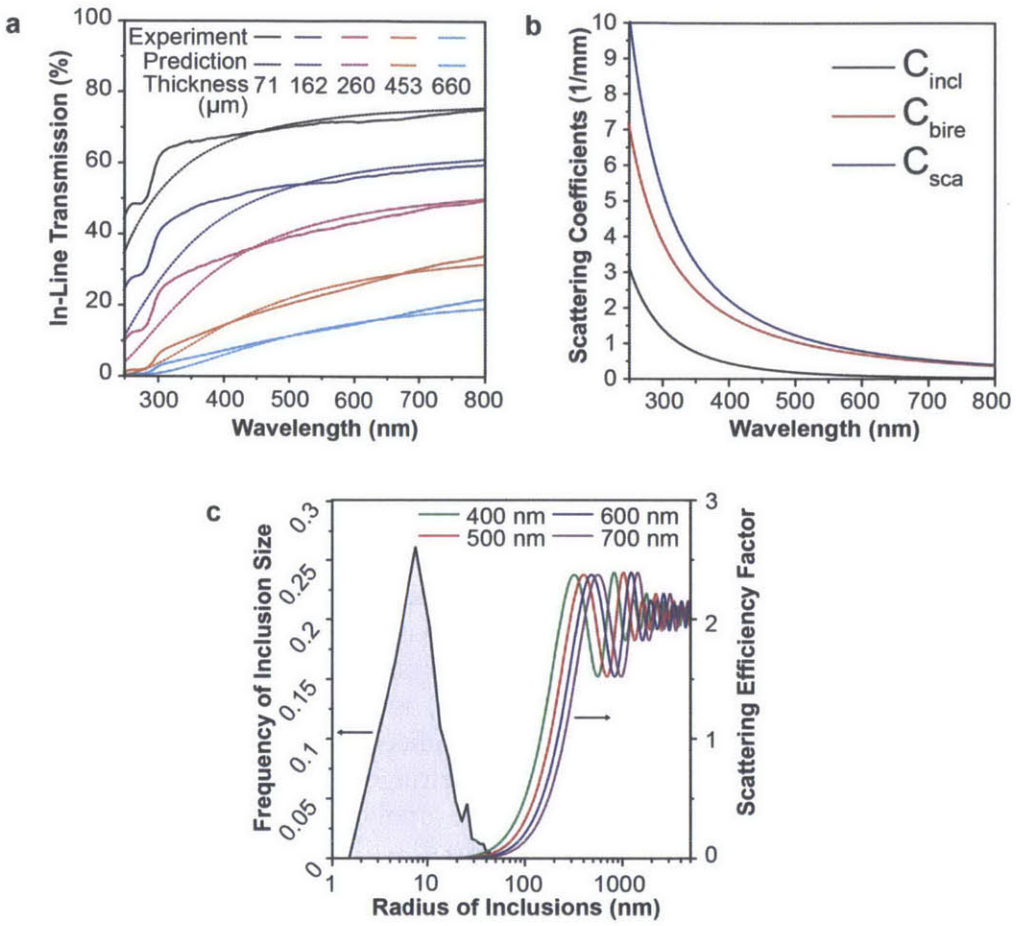

Figure 3-11| Theoretical analysis results of the optical performance of *P. placenta* shell. a, Predictions based on the light scattering model (dotted) and measurement (solid) of the in-line transmission intensities as a function of wavelength for samples with different thicknesses. **b**, Scattering coefficients of inclusion scattering (black), birefringence scattering (red), and total scattering (blue) as calculated from Equation 3-2, Equation 3-3, and Equation 3-4, respectively. **c**, Experimentally measured size distribution of the intracrystalline inclusions after stereological correction (black line), and the scattering efficiency factor for wavelengths of 400, 500, 600 and 700 nm as a function of inclusion sizes.

3.4 Discussion and conclusion

To the best of our knowledge, this work is the first detailed study that explicitly examines the optical performance and mechanical properties of a natural mineralized transparent structural material system in correlation with its microstructural and crystallographic features. The shell exhibits an intricate control of its structure at multiple length scales which allows it to simultaneously achieve high optical transparency and mechanical robustness. Macroscopically, the single foliated microstructure design leads to increased optical transparency relative to opaque mollusk shells which usually have multiple layers of mineralized microstructures in a single shell. Even an extra 20 μm thick prismatic layer in the PAS regions reduces the optical transmittance from ~40% to 5%. Moreover, the absence of a usually-pigmented, exterior

periostracum layer on *P. placenta* shells is also beneficial to transparency, although it is a common shell component in other bivalves[169,170]. The shells are also thin and flat, which enhances the transparency by reducing light scattering, absorption, and distortion. The nontransparent shells from a congeneric species, *Placuna ephippium* (Philipsson, 1788) are much thicker and highly curved (**Appendix A, Figure A-3**)[128]. It appears that the transparent *P. placenta* does not compromise its modulus and hardness to achieve the transparency as compared to the nontransparent *P. ephippium* at the length scale of the nanoindentation measurement (depth ~150 nm, **Appendix A, Figure A-3**). The geometric disadvantages of the shell of *P. placenta* are likely compensated by its high stiffness in order to maintain its rigidity upon potential predatory attacks[15]. Microscopically, the variation of crystallographic orientations of the calcitic building blocks is responsible for the majority loss of the in-line transmission due to the birefringence of calcite. This design, on the other hand, likely also contributes to the shell's remarkable capabilities of crack localization, damage tolerance, and multi-attack resistance as compared to its main constituent, calcite, possibly by disrupting dislocation motion and deflecting microcracks[171]. The presence of the nanoscopic organic inclusions is believed to improve the shell's fracture toughness and hardness relative to its pure mineral constituents possibly by preventing the dislocation of aligned slip planes[38,172], while still maintaining low light scattering due to their small sizes.

Mechanical protection is usually considered the primary task or function for mollusk shells, which are usually opaque. Although, at this point, we cannot fully rule out the possibility that the observed transparency may merely be a secondary consequence of the special microstructure of the mineralized shell in *P. placenta*, transparency as a camouflage strategy for anti-predation has been found in several pelagic mollusk groups, including pterotracheid and carinariid heteropods, pseudothecosomatous pteropods, and phylliroid nudibranchs[78], some of which exhibit miniaturized transparent calcium carbonate based shells (e.g., *Clio pyramidata* and *Limacina helicina*, unpublished data). Optical transparency has been shown to be a successful form of camouflage to visual predation based on experimental and theoretical studies in terrestrial, freshwater, and marine systems[78,113,114]. As discussed above, the highly mineralized shell of *P. placenta* displays an intricate control of the material system at multiple length scales in order to achieve both optical transparency and mechanical robustness. Optical transparency induced camouflage might act as another driving force in the evolutionary development of the materials/microstructures of this mollusk species in order to maximize the organism's survivability. The juvenile *P. placenta* shells are usually more transparent as compared to adult shells, and the transparency-induced camouflage might be more effective as compared to mechanical protection from the small and thin shells at this stage. However, we do not imply that being mechanically strong and optically transparent are the only desired functions for mollusks shells. Other possible functions include mobility[173], thermal protection[15], and other types of optical roles (e.g., biophotonic coloration[131,132], selective light diffusion[129], and vision[127]).

In conclusion, I have presented a detailed study of a highly mineralized mollusk shell that controls its microstructural/crystallographic features at multiple length scales in order to achieve high optical transparency as well as mechanical robustness. Whether or not this optical transparency is biologically utilized as camouflage, this biological structural material system represents an excellent example of nature's remarkable capability of engineering materials in order to achieve a desired set of diverse properties. In addition, the material design concepts reported here might lead to bio-inspired improvements in the design and application of engineering structural transparent materials.

Chapter 4 Pervasive nanoscale deformation twinning as a catalyst for efficient energy dissipation in *P. placenta*

This chapter was published as a regular article: Li, L. & Ortiz, C. Pervasive nanoscale deformation twinning as a catalyst for efficient energy dissipation in a bioceramic armor, *Nature Materials*, **13**, 501-507 (2014)[174].

4.1 Introduction

Biological exoskeletons achieve mechanical robustness and penetration resistance through exquisite and diverse structural designs that incorporate, for example, hierarchy, heterogeneity, multilayering, anisotropy, functionally graded interfaces, and sacrificial bonding[4,6,26,27,29,62,70,175,176]. While the energy dissipation mechanisms arising from these structural features are beginning to be elucidated with numerous studies, only recently has attention begun to focus on the simultaneous need for spatial localization of damage[28]. Generally, biological structural materials exhibit increased penetration resistance and energy dissipation with increased volume of deformation[29,49,70,177]. Conversely, deformation localization is essential to avoid degradation of the structural and mechanical integrity of the entire structure, in order to maintain multi-hit capability[28]. Particularly, in transparent armor systems, deformation over large areas increases light scattering and reduces visibility[152]. Biological exoskeletons offer important potential insights and designs for how to achieve multi-hit capability via increased energy dissipation density and damage localization – a key challenge in engineered armor materials, which are often made of ceramics and prone to radial cracking and catastrophic fracture[152]. In Chapter 3, the hierarchical structural features and optical performance of the *Placuna placenta* shells were studied in detail. Here in this chapter, I focused on the mechanical behavior of this fascinating nanocomposite bioceramic armor, in particular at nano- and micro-scale.

The specific goals of this study were: 1) to quantify of the penetration resistance of the shell of *P. placenta* relative to its mineral constituent calcite using instrumented nanoindentation, 2) to identify the detailed nanoscale deformation mechanisms in relation to the shell's unique crystallographic and micro-/nano-structural characteristics as compared to single crystal calcite through electron microscopy and 3) to explore how *P. placenta* balances spatially-driven energy dissipating deformation mechanisms with preservation of the structural, mechanical, and optical integrity of the overall system (providing multi-hit capability and visibility) via increased energy dissipation efficiency (per unit volume of material). Design of such penetration-resistant materials, which have amplified energy dissipation efficiency resulting in more localized deformation, hold great potential in the development of bio-inspired engineering structures with

improved multi-hit capability and preserved optical transparency under impact, which is desirable for a variety of both commercial and military applications[152,178].

4.2 Methods

Samples. Edge-trimmed and intact *P. placenta* shells were purchased from Seashell World (Florida, USA) and Conchology, Inc. (Philippines), respectively. Samples of single crystal geological calcite (origin, Mexico) were obtained from Pisces Trading Company, LLC. (Portland, USA).

Nanoindentation. *P. placenta* shells were cleaved using a razor blade and tested immediately. Single crystal calcite samples were sectioned using a diamond saw (Buehler, Isomet 5000 Lake Bluff, IL) along one of its {108} planes, and polished on a polishing wheel (South Bay Technology, Model 920) with aluminum oxide pads stepwise (15 μm, 6 μm, 3 μm, and 1 μm), and finally with 50 nm silica nanoparticles on a microcloth (South Bay Technology). Nanoindentation experiments were conducted in ambient conditions using a TriboIndenter (Hysitron, Inc., Minnesota, USA). Load-controlled nanoindentation was performed using Berkovich (trigonal pyramid, semi-angle = 65.3°) and conospherical (tip radius = ~1 μm, semi-angle = 30°) diamond probe tips. The piezoelectric transducer was first allowed to equilibrate for 105 s (the last 45 s with digital feedback) and another 40 s for calculating drift automatically prior to each indent. Typical load functions included loading (10 s), holding (20 s), and unloading (10 s). Maximum loads varied from 1 to 10 mN. The Oliver-Pharr (O-P) methodology was used to quantify material properties, i.e. indentation modulus ($E_{O\text{-}P}$) and hardness ($H_{O\text{-}P}$)[179]. The probe tip area function $A(h_c)$, which is the projected area of the indentation tip as a function of the contact depth h_c, and frame compliance were calibrated prior to each set of experiments using a fused quartz sample. Indentation experiments with maximum loads higher than 10 mN were carried out using a Micro Materials microindenter (Wrexham, UK).

Electron microscopy. Samples were coated with ultra-thin carbon to reduce charging effects prior SEM imaging. Samples were imaged using a Helios Nanolab 600 Dual Beam electron microscope (FEI, OR) at an acceleration voltage of 2 and 5 kV and a working distance of ~4 mm. Cross-sectional samples and TEM samples were prepared using ion beam milling with the same instrument. A detailed TEM sample preparation procedure is as follows: 1) A platinum protective layer (~0.5 μm) was first laid down on top of the desired region; 2) Another platinum protective layer (~1.5 μm) was further deposited on top of the region where the TEM slab was to be milled out; 3) Two trenches, one on each side of the platinum protective stripe, were milled by FIB, leaving the slab of specimen (thickness: ~1.5 μm); 4) The slab was then cut through by FIB and transferred to a copper TEM grid by an Omniprobe and welded securely with platinum deposition; 5) The lift-out lamellar of specimen was sequentially thinned by FIB at 30, 16, 5, and 2 kV ion beam voltages. Final cleaning at 2 kV and 28 pA is important to obtain a clean surface and minimize damage. TEM imaging with typical bright-field, dark-field, and SAED techniques was carried out using a JEOL 2011 operated at 120 kV. The image magnification and camera constants were calibrated using a standard sample (MAG*I*CAL, Electron Microscopy Sciences, PA, USA). HRTEM imaging was carried out using a field emission JEOL 2010F at 200 kV. A gold foil standard (Lattice plane resolution test-646, Pelco, USA) was first used to align the instrument prior to *P. placenta* and calcite samples. To

minimize electron beam damage, the correct zone axis was first found using areas away (~2-3 μm in distance) from the twin boundary but on the same lath using Kikuchi patterns, taking advantage of the fact that each lath in *P. placenta* diffracts as a single crystal. Once the correct zone axis was found and imaging conditions were optimized, the twin boundary was brought into the field of view with the beam spread. The beam was then focused and an image was taken immediately (typical exposure, ~0.5 s). Usually only two images could be taken at one boundary before the region was damaged.

Atomic force microscopy. Tapping mode AFM (TMAFM) imaging in ambient conditions was carried out using a Digital Instruments Multimode SPM IIIA (Veeco, Santa Barbara, CA) with an AS-130 "JV" scanner. TMAFM imaging was conducted with NANOSENSORS Si TMAFM cantilevers (PPP-NCHR-10). Typical scan speed was 1-5 μm/s; other parameters were optimized upon tuning.

Electron backscattered diffraction. The pre-cut square-shaped specimens from *P. placenta* shells were cleaved, fixed onto steel plates, and subsequently coated with ultra-thin carbon. EBSD analysis was carried out using a FEI Helios FIB/SEM system equipped with the HKL Technology "Channel 5" EBSD system. The sample was mounted on a 70° pre-tilted EBSD stage and the working distance was 6 mm. SEM images and EBSD patterns were generated using an accelerating voltage of 20 kV and a beam current of 2.7 nA. Typical scanning step size was 1 μm and EBSD patterns with a mean angular uncertainty of 1° and above were discarded. Scans with at least 80% of points indexed were further analyzed using HKL software.

4.3 Results

4.3.1 Summary of hierarchical structure

The shell of *P. placenta* (mineral content: 98.9 ± 0.1 wt%) possesses the unique optical property of ~80% total transmission of visible light which is enabled by its single foliated nano/microstructure composed of elongated diamond-shaped calcitic laths (thickness ~300 nm) arranged in a tiled assembly with ~2 nm organic interfaces (**Figure 4-1a**), small intracrystalline organic inclusions (~25 nm), a low overall shell thickness (0.5-1 mm) and curvature, and lack of an external organic periostracum[146]. Similar to aragonitic nacre, each calcite lath diffracts as a single crystal, although crystallographic misorientations are present among adjacent building blocks[146]. The *c*-axes of these calcitic laths are tilted by 24.4 ± 3.5° relative to their surface normal, which makes the surfaces of the laths close to the {108} planes of calcite (the angle between the {108} and {001} lattice planes is 26.3° in calcite, **Figure 4-1b-e**)[40,146].

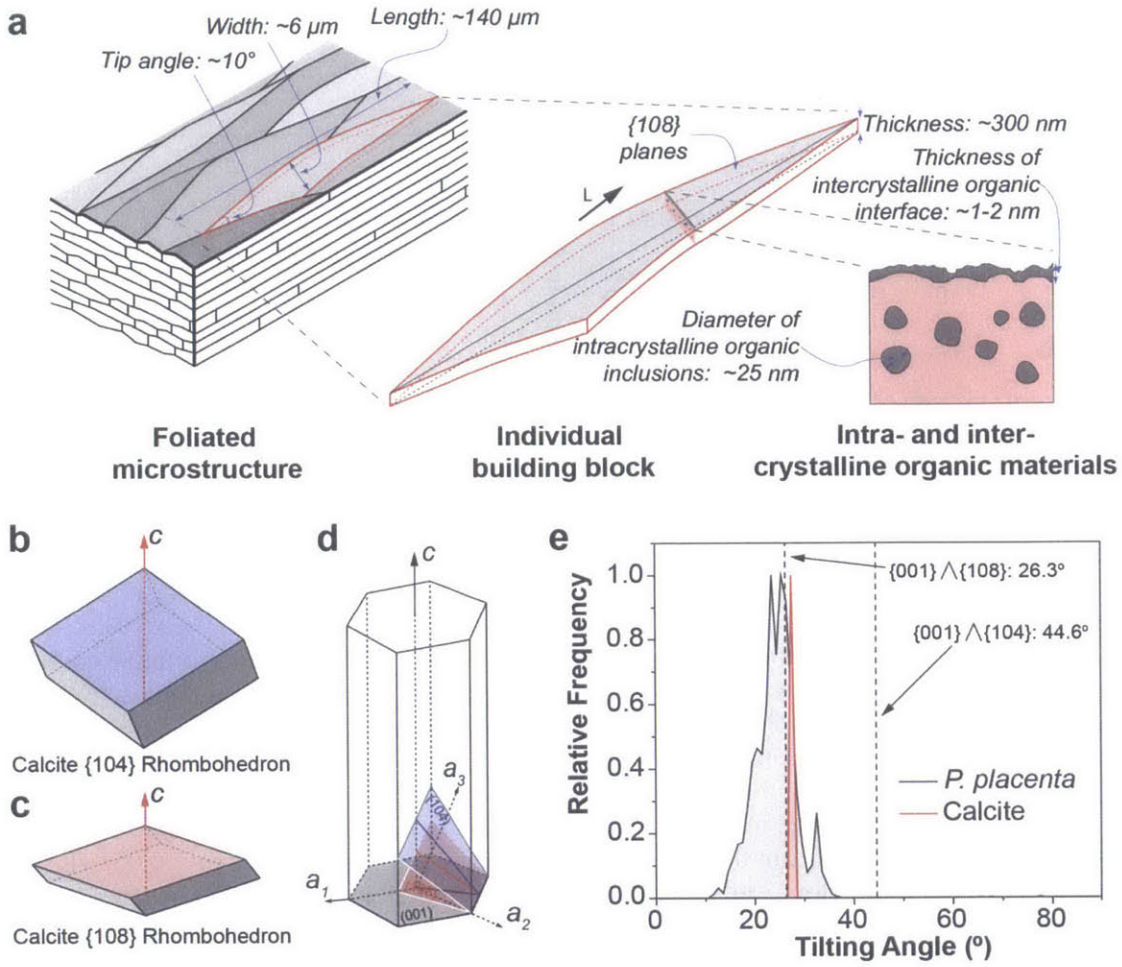

Figure 4-1| Microstructural/crystallographic features and mechanical behavior of biogenic calcite in *Placuna placenta* in comparison to single crystal geological calcite. a, Schematic diagram (not in scale) of the foliated microstructure in *P. placenta*. "*L*" refers the longitudinal direction of the laths. **b,c,** Rhombohedra enclosed by {104} and {108} planes of calcite, respectively. **d**, Schematic diagram showing the orientation of (104) and (108) planes in the calcite crystal structure. **e**, Tilting angles of *c*-axes of the calcitic laths with respect to the surface normal in the shell of *P. placenta* (black, as reported in ref. 14). A single crystal calcite sample was sectioned and polished along one of the {108} planes (red). Standard interplanar angles between {001} and {104}, and {001} and {108} planes in calcite are also indicated.

4.3.2 Quantitative mechanical properties

Quantification of the mechanical properties of freshly-cleaved *P. placenta* shells in comparison to single crystal geological calcite was carried out via instrumented nanoindentation with the loading axis perpendicular to their {108} planes (**see 4.2 Methods**). Using an obtuse Berkovich diamond tip, it was determined that *P. placenta* retains the modulus ($E_{o\text{-}p}$) of calcite (*P. placenta*: 71.1 ± 4.2 GPa, calcite: 73.4 ± 1.7 GPa), while its hardness ($H_{o\text{-}p}$) is increased by ~50% (*P. placenta*: 3.5 ± 0.3 GPa, calcite: 2.3 ± 0.1 GPa), demonstrating its enhanced resistance to plastic deformation (**Figure 4-2**)[179].

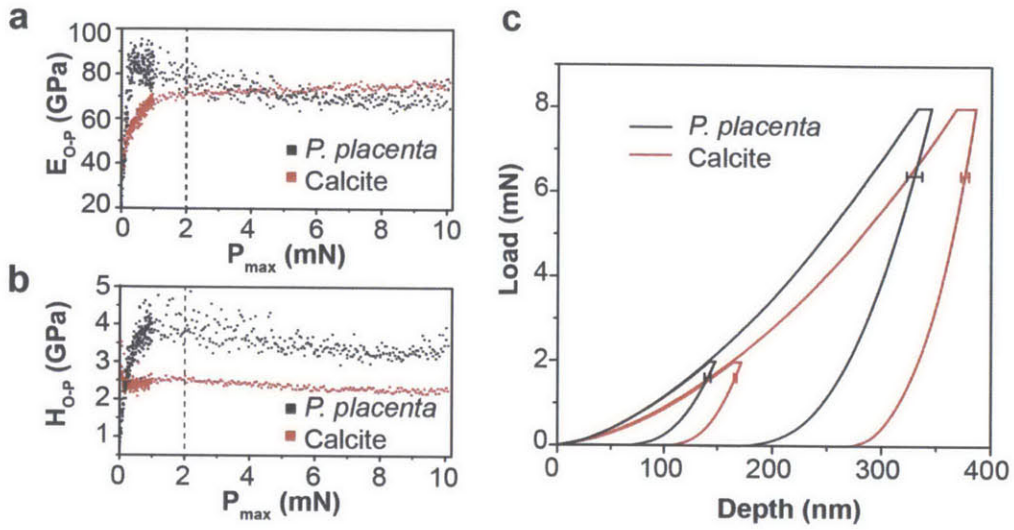

Figure 4-2| Quantification of the mechanical properties of *P. placenta* in comparison to calcite based on nanoindentation experiments (Berkovich tip). The calculated (**a**) modulus (E_{O-P}) and (**b**) hardness (H_{O-P}) based on Oliver-Pharr analysis as a function of maximum load (P_{max}) from 10 μN to 10 mN. Stable E_{O-P} and H_{O-P} are achieved when $P_{max} > 2$ mN, and the averaged values with P_{max} higher than 2 mN are obtained (E_{O-P}: 71.1 ± 4.2 GPa (*P. placenta*, n = 241), 73.4 ± 1.7 GPa (calcite, n = 159); H_{O-P}: 3.5 ± 0.3 GPa (*P. placenta*, n = 241), 2.3 ± 0.1 GPa (calcite, n = 159)). E_{O-P} and H_{O-P} for the two samples are statistically significant through non-parametric Mann-Whitney test ($p < 0.05$).The increase in E_{O-P} and H_{O-P} with P_{max} below 2 mN might be due to the imperfectness of tip geometry. **c**, Averaged indentation curves with maximum loads of 2 and 8 mN (n > 30 for each averaged curves).

Fracture and cracking was induced by indentation with a sharp axisymmetric conospherical diamond indenter, which also provides a better approximation of the geometry of predatory loading[180] and avoids potential complications due to the anisotropic mechanical response of single crystal calcite[181]. Load-depth curves of *P. placenta* and abiotic calcite using the conospherical indenter reveal displacement bursts with almost no increase in load ("pop-in" events) associated with discrete fracture events, although noticeable differences are present (**Figure 4-3**). Compared to calcite, the fractures of *P. placenta* are initiated at lower loads, F_i, (*P. placenta*: 2.10 ± 0.58 mN, calcite: 5.34 ± 1.35 mN, and depths, d_i, (*P. placenta*: 256.5 ± 72.6 nm, calcite: 675.2 ± 167.0 nm). However, the average "pop-in" depth, Δd, for *P. placenta* is much smaller than that for calcite (*P. placenta*: 38.7 ± 35.1 nm, calcite: 129.0 ± 192.1 nm), indicating that *P. placenta* fractures in a more graceful way. By integrating the area under load-depth hysteresis, the single crystal calcite was found to dissipate slightly higher total energy, ΔE_{diss}, relative to *P. placenta* during one indentation cycle (*P. placenta*: 6.04 ± 0.48 nJ, calcite: 8.77 ± 1.71 nJ)[32,182].

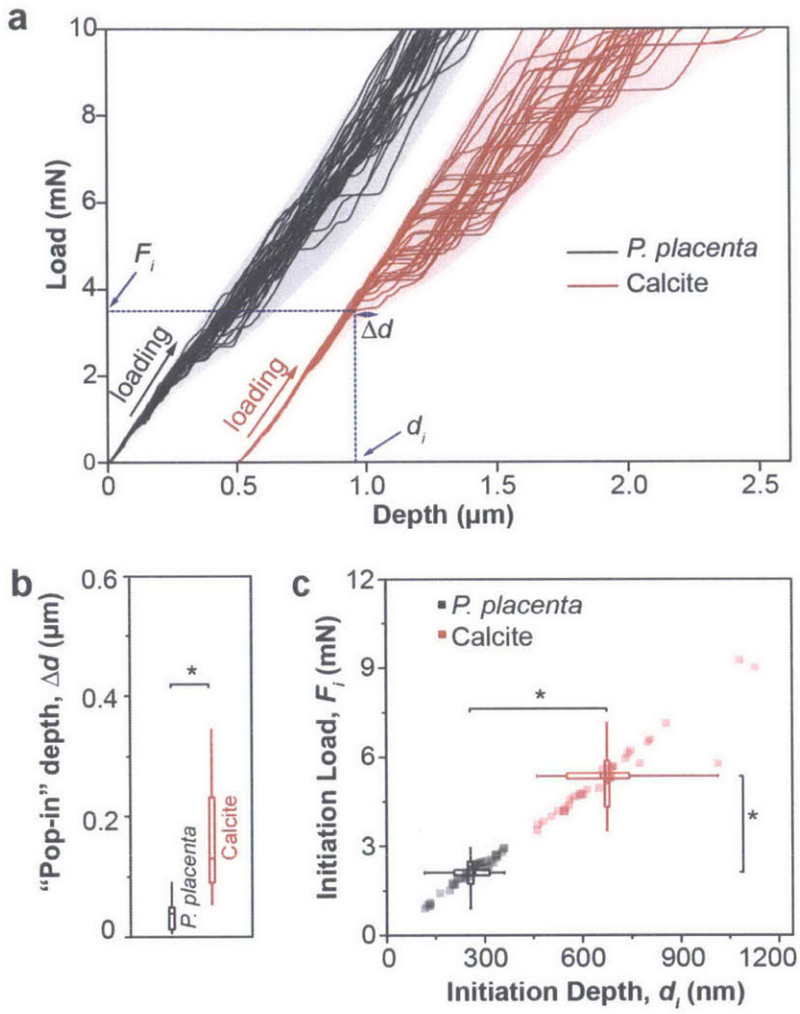

Figure 4-3| a, Loading portions of multiple individual load-depth curves (conospherical diamond tip, semi-angle = 30°, tip radius = ~1 μm, maximum load = 10 mN). F_i and d_i are the load and depth corresponding to the initial fracture event detected, and Δd represents "pop-in" depth. Distributions of Δd (**b**), F_i and d_i (**c**). Asterisks suggest statistical significance through non-parametric Mann-Whitney tests ($p < 0.05$).

Representative scanning electron microscopy (SEM) images of the indentation residues of the two samples are shown in **Figure 4-4a** (*P. placenta*) and **b** (single crystal calcite). The single crystal calcite shows an anisotropic distribution of large radial cracks and fractured regions, while the *P. placenta* shell exhibits a more isotropic, localized deformation with multiple small deflected cracks and nano-sized fractured pieces. Three parameters were defined in order to quantitatively compare their fracture patterns: R_i, the radius of inner indentation crater that was directly in contact with the tip during the test; R_o, the radius of the entire fracture pattern by fitting it with a smallest-possible circle; C, the distance between the centers of inner and outer circles (**Figure 4-4a**). Despite exhibiting similar R_i values (*P. placenta*: 1.11 ± 0.06 μm, calcite:

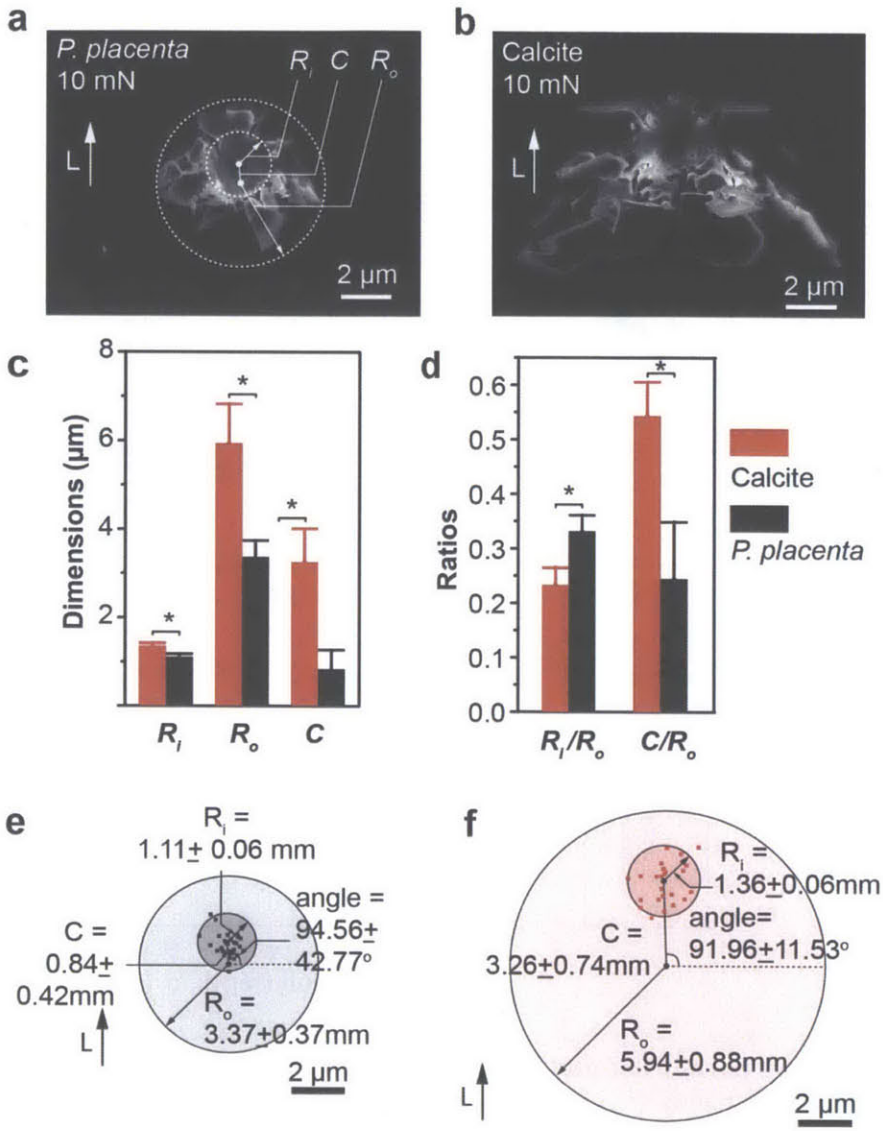

Figure 4-4| Quantitative measurement of the fracture patterns for *P. placenta* and single crystal calcite. SEM images of indentation residues of (**a**) *P. placenta* and (**b**) calcite. Three dimensional parameters are defined: R_i, radius of inner indentation crater; R_o, radius of entire fracture pattern by fitting it with a smallest circle; C, distance between the centers of two fitted circles. The indentation experiments were performed with a conospherical tip (tip radius = ~1 μm; semi-angle = 30°; maximum load = 10 mN). **c,d**, Quantitative dimensional measurement of the fracture patterns (calcite, n = 24; *P. placenta*, n = 28). All parameters for the two samples are statistically significant through non-parametric Mann-Whitney test ($p < 0.05$). Schematic diagrams of the averaged fracture patterns for (**e**) calcite and (**f**) *P. placenta*. The inner and outer circles are based on average values of R_i and R_o. The square-shaped data points represent the centers of R_i for each individual test. L represents the longitudinal direction of the calcitic laths.

1.36 ± 0.06 μm), *P. placenta* shows much smaller overall fracture size, R_o, (*P. placenta*: 3.37 ± 0.37 μm, calcite: 5.94 ± 0.88 μm), indicating its more localized deformation behavior (**Figure 4-4c**). In addition, the fracture patterns of *P. placenta* are more isotropic, indicated by its low C/R_o ratio (*P. placenta*: 0.24 ± 0.10, calcite: 0.54 ± 0.06, **Figure 4-4d**). For an ideally isotropic

material, the centers of the inner and outer circles should coincide; C, and hence C/R_o, approach to zero. **Figure 4-4e,f** schematically compare the averaged size and orientation of the fracture patterns of the two samples on the same scale.

Through cross-sectional transmission electron microscopy (TEM) analysis of the indentation zone (as discussed in detail later), it is possible to directly determine the depth to which the material has undergone permanent deformation (h_{def}, **Figure 4-5**). Hence, the total volume that was permanently deformed, V_{def}, can be estimated using $V_{def} = \pi R_o^2 h_{def}/3$, approximating the deformed volume as a conical shape. The energy dissipation density, e_{diss}, (i.e. energy dissipation per unit volume) can then be estimated for *P. placenta* as 0.290 ± 0.072 nJ/μm^3, which is approximately an order of magnitude higher than that of calcite (0.034 ± 0.013 nJ/μm^3, **Figure 4-5**). This finding indicates that *P. placenta*, although it only incorporates ~1 wt% of organic materials, is much more efficient in dissipating energy upon penetration as compared to its primary mineral constituent, calcite.

a

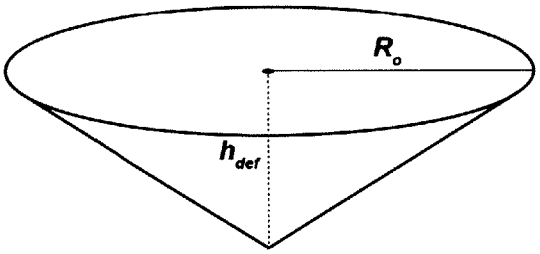

b

	Calcite	*P. placenta*
R_o	5.94 ± 0.88 μm (n = 24)	3.37 ± 0.37 μm (n = 28)
h_{def}	6.96 ± 1.29 μm (n = 3)	1.75 ± 0.20 μm (n = 5)
V_{def}	257.2 ± 94.2 μm^3 (Calculated)	20.8 ± 5.4 μm^3 (Calculated)
ΔE_{diss}	8.77 ± 1.71 nJ (n = 32)	6.04 ± 0.48 nJ (n = 36)
e_{diss}	0.034 ± 0.013 nJ/μm^3 (Calculated)	0.290 ± 0.072 nJ/μm^3 (Calculated)

Figure 4-5| Quantitative measurement of the permanent deformed depth (h_{def}) and volume (V_{def}). The permanently deformed volume is approximated as a cone with the radius of the base R_o and the height of h_{def}. The indentation was carried with a conospherical tip (semi-angle = 30°; tip radius = ~1 μm) with maximum load of 10 mN.

Figure 4-6 compares the key mechanical parameters of *P. placenta* and abiotic calcite by setting the values of calcite as the reference; it is observed that the biogenic calcite of *P. placenta* is mechanically superior in almost every aspect.

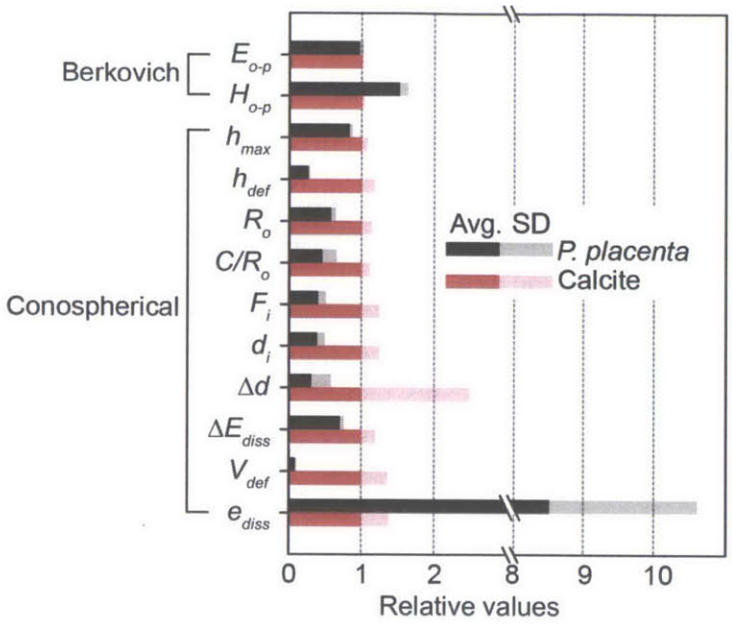

Figure 4-6| Comparison of the mechanical parameters of *P. placenta* and calcite. The values corresponding to calcite are normalized to 1. E_{O-P}, 1 = 73.42 ± 1.74 GPa; H_{O-P}, 1 = 2.34 ± 0.10 GPa; h_{max}, 1 = 1.53 ± 0.13 μm; h_{def}, 1 = 6.96 ± 1.29 μm; R_o, 1 = 5.94 ± 0.88 μm; C/R_o, 1 = 0.54 ± 0.06; F_i, 1 = 5.34 ± 1.35 mN; d_i, 1 = 675.2 ± 167.0 nm; Δd, 1 = 129.0 ± 192.1 nm; ΔE_{diss}, 1 = 8.77 ± 1.71 nJ; V_{def}, 1 = 257.2 ± 94.2 μm^3; e_{diss}, 1 = 0.034 ± 0.013 nJ/μm^3.

4.3.3 Nanoscale deformation twinning in *P. placenta*

In order to identify the underlying deformation mechanisms, cross-sectional TEM imaging of indentation residues of P. placenta was carried out (**Figure 4-7a** & **Appendix A, Figure A-4**, Methods). The permanently deformed region surrounding the indentation site can be clearly distinguished from the undamaged region (as marked by the dashed line) by image contrast and the disruption of the organic interfaces between adjacent laths (**Figure 4-7b**). This permanently deformed region also follows the V-shaped profile of the conospherical indenter with a semi-angle of ~60° and extends beyond the maximum indentation depth by ~0.4 μm (less than two mineral layers) without any vertical cracks. Close to the boundary of the inelastic deformation zone I observed planar defects with two closely-spaced parallel flat boundaries (**Figure 4-7b,c**). These defects were identified as deformation twins by electron microscopic imaging and diffraction as described below in detail. The twin bands are ~50 nm in width and propagate through the entire dimensions of each mineral lath at an angle of ~20-30° arrested by the organic interfaces (**Figure 4-7c**). The twin bands in the same mineral lath are typically parallel to each other due to their single crystal nature, while those from different laths are usually not parallel due to crystallographic misorientations. Additionally, local enlargement or opening of the organic interfaces without catastrophic delamination is usually observed at the terminations of twin bands due to displacement mismatch between adjacent laths (**Figure 4-7c**, white arrows). These local interface opening lead stretching deformation of inter-crystalline organic materials present in the interfaces, forming fibrillar structures (**Figure 4-7e-f**). Selected area electron diffraction (SAED) patterns obtained from the untwinned ("matrix") and the twinned regions clearly reveal e-type deformation twinning (twin boundaries: {018}) associated with the

rhombohedral crystal structure (space group, $R\bar{3}c$) of calcite (**Figure 4-7d**)[183,184]. Such twin bands are not observed in undeformed regions.

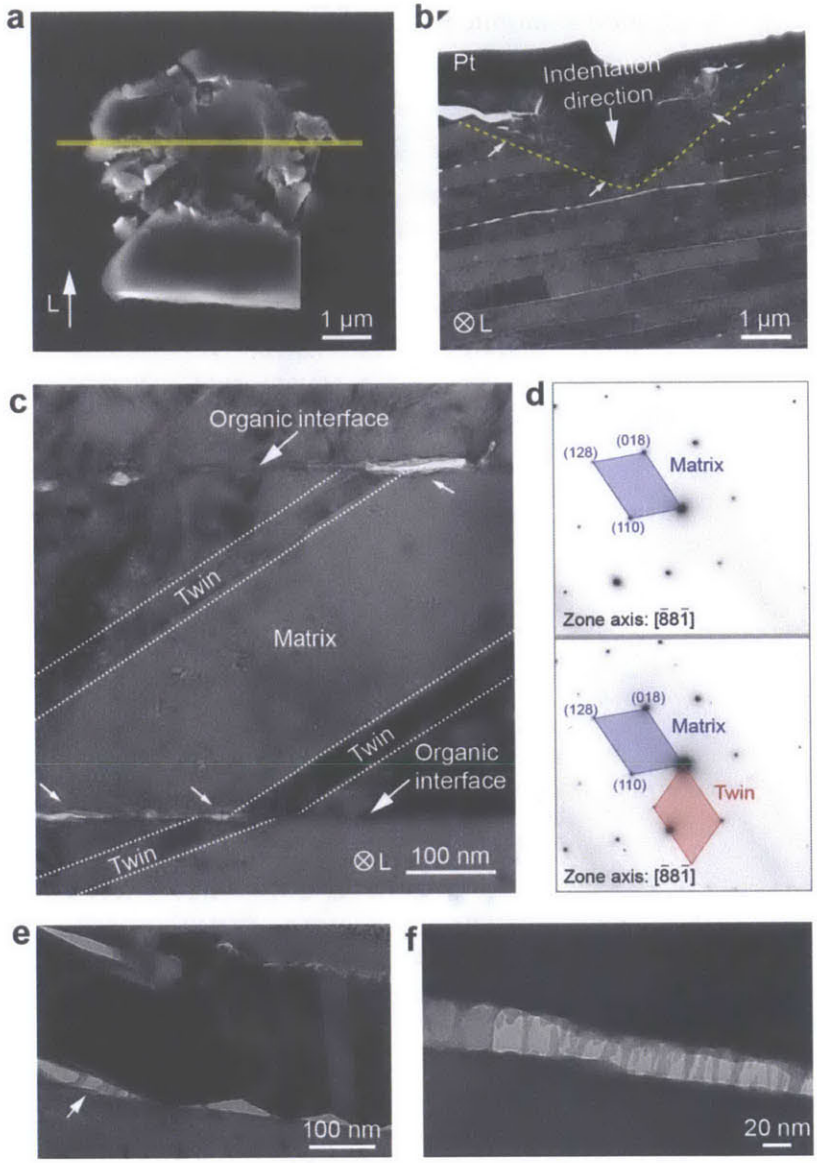

Figure 4-7| Nanoscale deformation twinning in *P. placenta*. **a,** top-viewed SEM image of the original indentation residue. The yellow solid line indicates the location and orientation of the TEM sample prepared by FIB. **b**, TEM image of the entire cross-section of the indentation zone (conospherical tip; semi-angle = 30°; tip radius = ~1 μm; maximum load = 10 mN). The yellow dashed line marks the boundary between the plastically deformed region close to the indentation tip and surrounding undeformed regions. White arrows indicate the location of deformation twins. **c**, TEM image showing deformation twinning bands with parallel boundaries running across the laths. White arrows indicate the interfacial openings associated with the twinning bands. **d**, Corresponding SAED patterns in the matrix (top) and twinned (bottom) regions with zone axis = $[\bar{8}8\bar{1}]$. "Matrix" in (**c,d**) refers to untwinned regions of the calcitic laths which maintain the original crystallographic orientation[19,20]. **e,f**, TEM image of *P. placenta* showing the stretching deformation of organic interfaces where the interface opening are generated due to the deformation twinning in the mineral layers. "Pt" in (**a**) refers the protective platinum layer. "*L*" refers the longitudinal direction of the laths.

Figure 4-8 shows a high-resolution TEM (HRTEM) image of a twinning boundary corresponding to the [$\bar{1}$00] zone axis and further illustrates the mirror symmetry between the twinned and the untwinned region at atomic resolution.

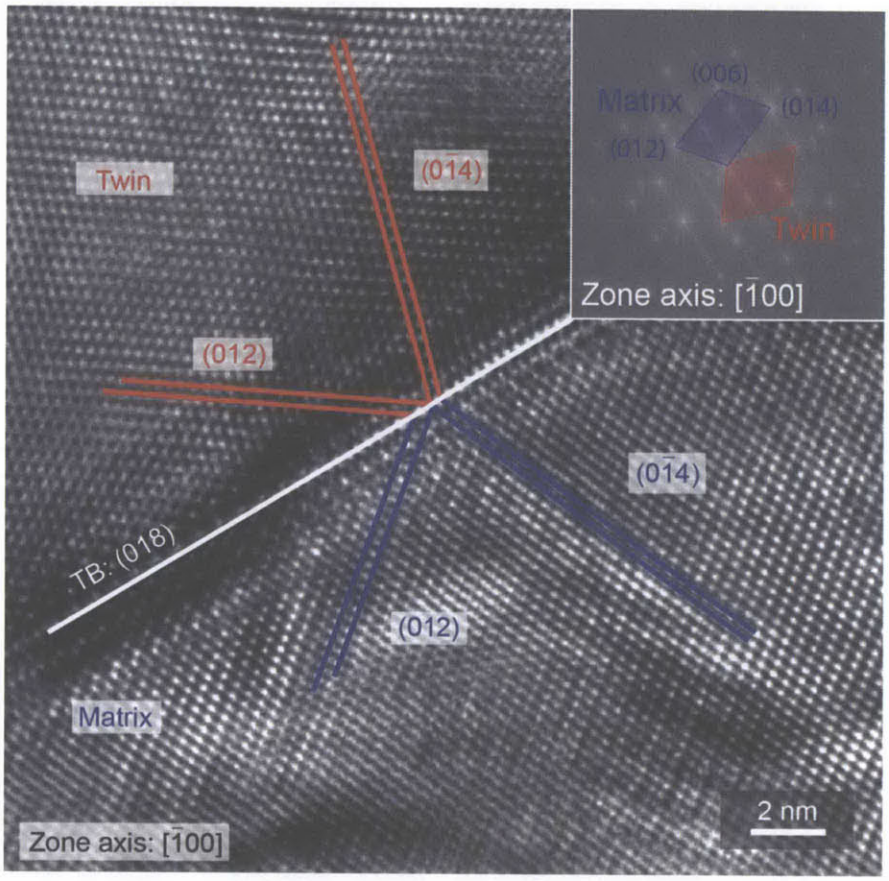

Figure 4-8| HRTEM image of the twinning boundary of {018}.

With the indentation loads increased to 500 mN and even 2.5 N, *P. placenta* is still able to confine the large inelastic deformation to a small volume without any radial cracks (**Figure 4-9**). TEM analysis of the deformed region again reveals a large population of {018} deformation twin bands that were present in the majority of calcite crystals (**Figure 4-9**) and which are believed to play a primary role in mitigating severe local deformation, especially in the region close to the tip of the indenter. The twinning-induced interface opening causes significant light scattering, thus reducing light transmission in the deformation region.

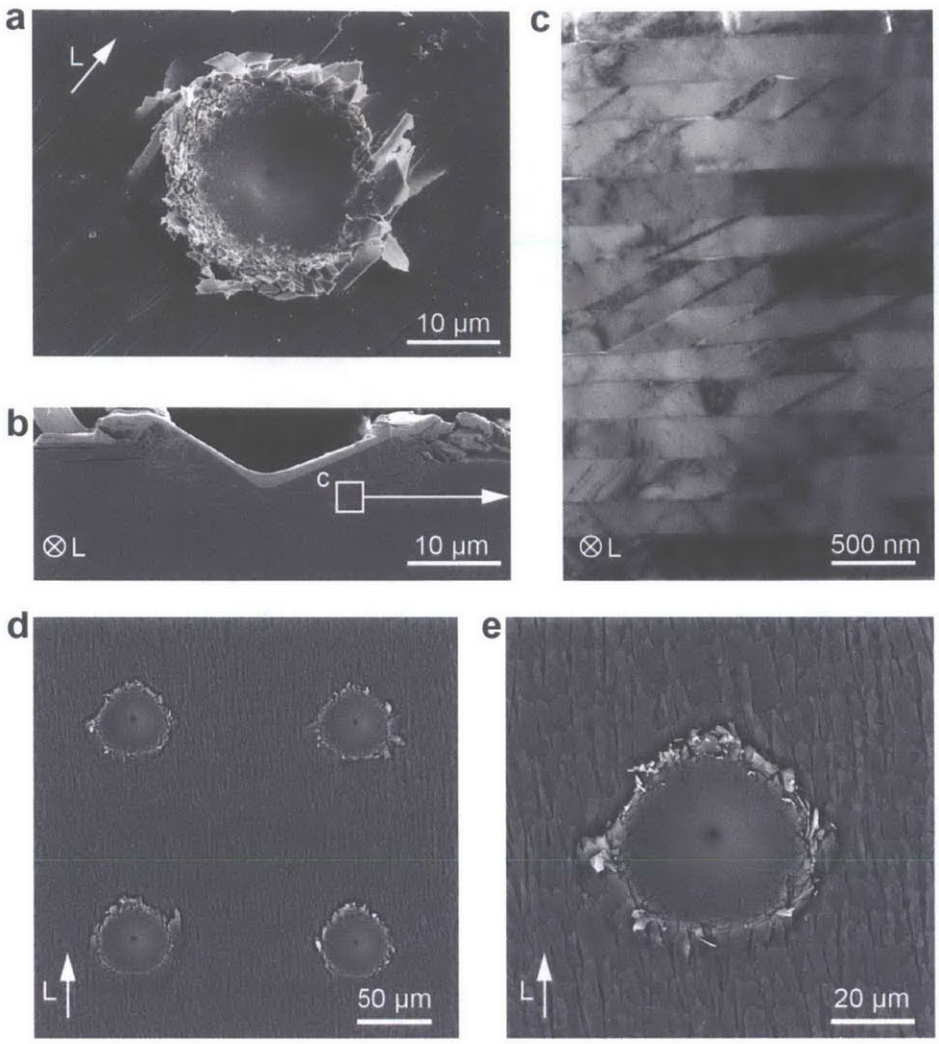

Figure 4-9| Damage localization through deformation twinning for higher indentation loads. Top-viewed (**a**) and cross-section viewed (**b**) SEM images of micro-indentation residue (conospherical tip; semi-angle = 30°; tip radius = 2 μm; maximum load = 500 mN). **c**, TEM image of multiple deformation twinning bands within the deformed zone shown in (**b**). **d,e,** SEM images of indentation residues at higher loads (conospherical tip; semi-angle = 30°; tip radius = 2 μm; maximum load = 2.5 N). "*L*" refers the longitudinal direction of the laths.

Manual grounding of the shell using a mortar and pestle can be also used to induce pervasive deformation twinning bands (**Figure 4-10**), which suggests that deformation twinning is not only induced by the high local stresses generated by an indenter tip[185]. Three equivalent twinning systems with twinning boundaries of $(1\,\bar{1}\,8)$, $(0\,1\,8)$, and $(\bar{1}\,0\,8)$ were observed, intersecting with the longitudinal direction of the laths by 0°, 42.6°, and 90°, respectively, as illustrated in the crystallographic configuration in **Figure 4-10**. With the TEM samples prepared perpendicular to the longitudinal direction of the laths, the twinning boundaries of $(0\,1\,8)$ and $(1\,\bar{1}\,8)$ create angles of 23.1° with the lath-organic interface, consistent with experimental observations (**Figure 4-10c**).

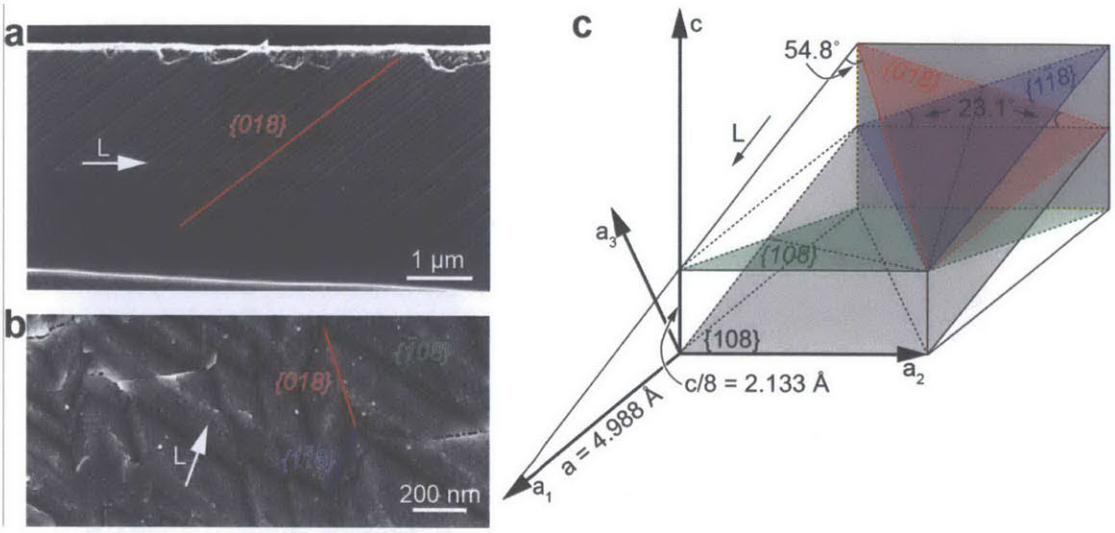

Figure 4-10| Multiple equivalent deformation twinning systems in *P. placenta*. a,b, SEM images of deformation twinnings in multiple orientations induced by manually compressing the shell with a mortar and pestle. **c**, Schematic model of the three crystallographically equivalent {018} twinning systems in calcite. "*L*" refers the longitudinal direction of the laths.

4.3.4 Additional nanoscale deformation mechanisms in *P. placenta*

In addition to deformation twinning, a series of other nanoscale inelastic deformation mechanisms at the building block level were observed (**Figure 4-11).** The bright-field TEM image of **Figure 4-11a** shows that the deformed zone (containing area "**b**") has a fractionated brightness, in stark contrast to the more homogeneous featureless brightness of the undeformed region (containing area "c"), suggesting the formation of nano-sized grains. SAED patterns reveal that the deformed and undeformed regions exhibit polycrystalline-like (**Figure 4-11b**) and single crystal like (**Figure 4-11c**) patterns, respectively. Thus, deformation induces the formation of nanograins with crystallographic misorientations. The dark-field TEM image of **Figure 4-11d**, obtained using selected diffraction spots from **Figure 4-11b** (indicated by the red circle), selectively lightens up some of the deformation-induced nanograins (~50 nm in diameter). The HRTEM image of **Figure 4-11e** further reveals misoriented nanoscopic grains, all of which were indexed to calcite, within the plastically deformed zone. Amorphous regions were also observed along the boundaries of grains or occasionally entirely encapsulated within grains, suggesting that individual calcite laths are capable of undergoing ductile deformation.

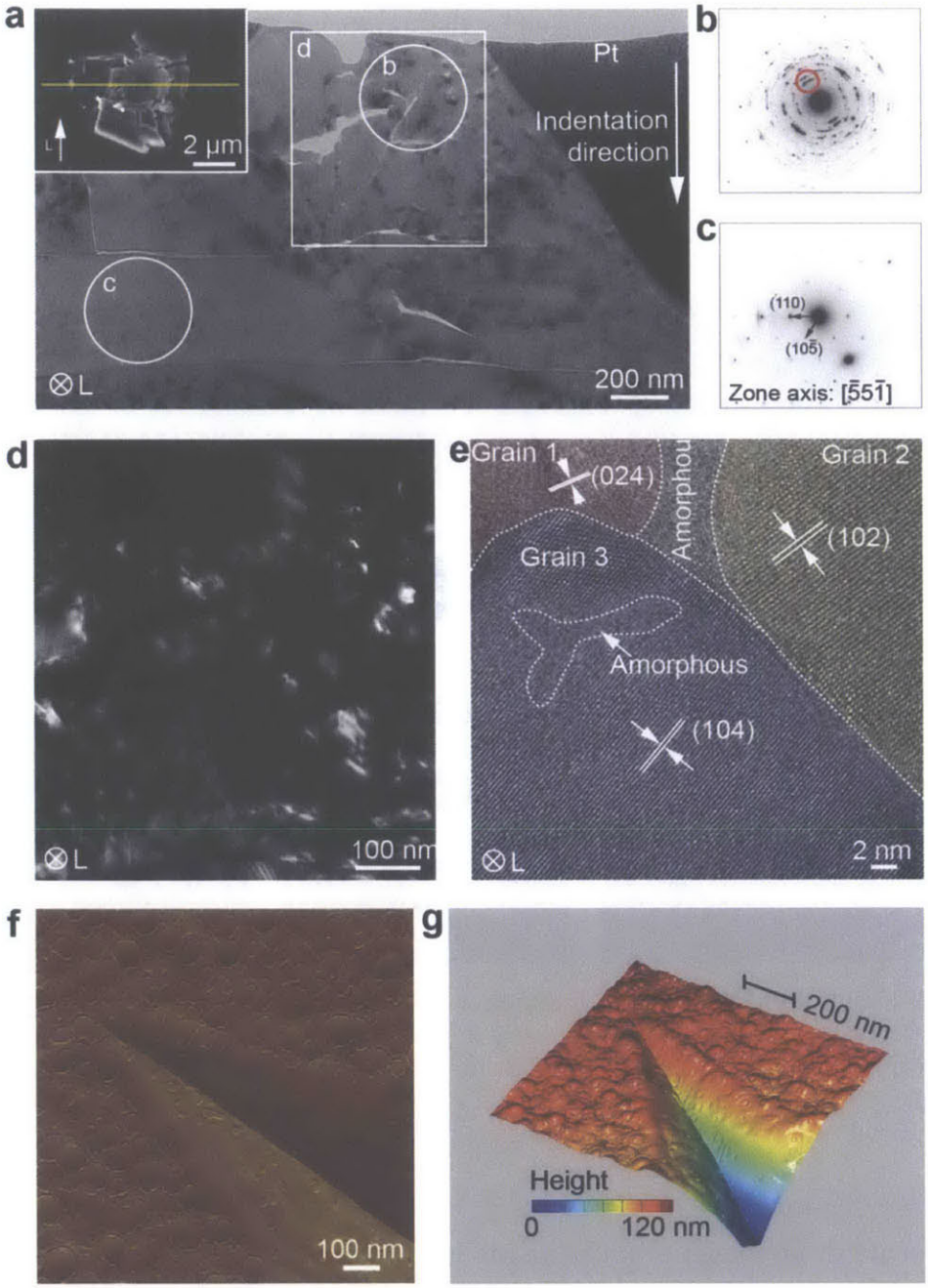

Figure 4-11| Nanoscopic inelastic deformation in individual calcitic layers of *P. placenta*. **a**, Bright-field TEM image of the permanently deformed region close to the indentation crater. Inset, top-viewed SEM image of the original indentation residue. The yellow line indicates the location and orientation of the TEM sample. SAED patterns acquired in the deformed (**b**) and surrounding undeformed (maintaining original single crystal structure, **c**) regions indicated by the circles in (**a**). **d**, Dark-field TEM image of the deformed region (corresponding to the region in the white box in (**a**)) with the corresponding selected diffraction spots indicated in (**c**) with the red circle. e, HRTEM image of misoriented calcite nanograins in the permanently deformed region. Tapping mode AFM amplitude (**f**) and height (**g**) image of an indent corner (Berkovich tip) showing the flattening of nanoscopic asperities within an indentation crater. "*L*" refers the longitudinal direction of the laths.

This capability is further demonstrated by the significant flattening of nanoscopic asperities within the residual indentation area (**Figure 4-11f,g**). In addition, crack deflections within individual building blocks were observed (**Figure 4-12**). These experimental results indicate that the calcite laths, despite their single crystal-like nature, do not fracture catastrophically, but rather dissipate considerable energy through a series of nanoscopic inelastic deformation processes[62,66].

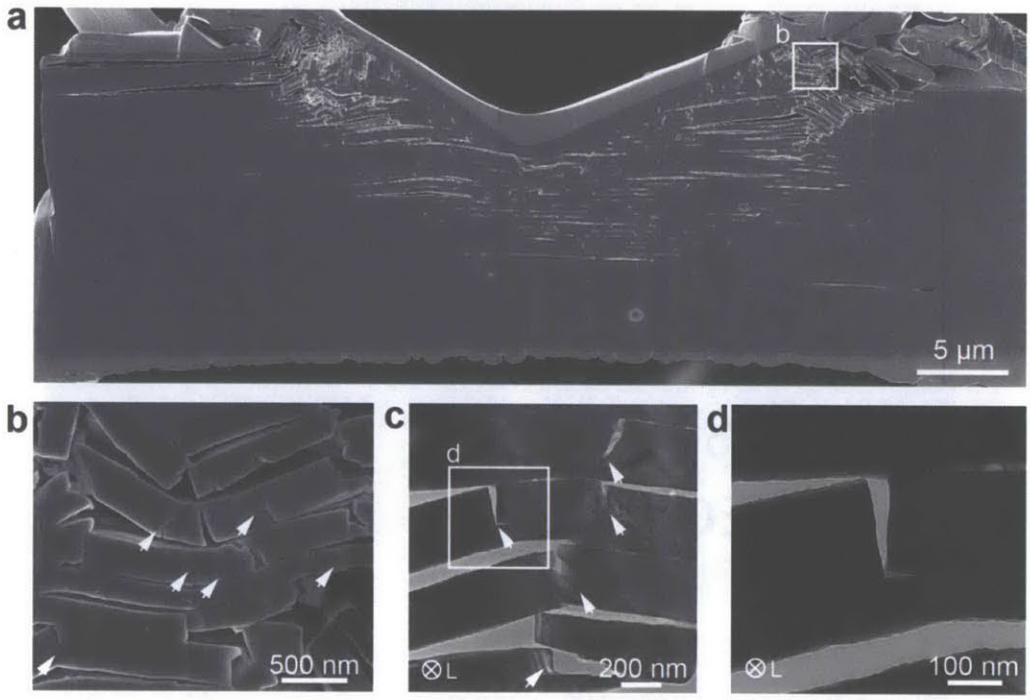

Figure 4-12| Crack deflection within individual building blocks. a, The SEM image of the FIB-milled cross-section of the indentation zone after *P. placenta* was microindented (conospherical tip; tip radius = 2 μm; semi-angle = 30°; maximum load = 500 mN). **b**, High-resolution SEM image of the deformed mineral laths, which shows multiple sites of crack deflection within individual layers (white arrows). **c-d**, Bright-field TEM images showing crack deflection within individual laths (white arrows).

4.3.5 Nanoscale deformation mechanisms in calcite

It has long been known that calcite deforms plastically via deformation twinning and slip primarily at elevated temperatures and confined hydrostatic pressures, whereas at room temperature and atmospheric pressure, calcite readily fractures upon compression, tension, and particularly indentation[183,184]. Bright-field and corresponding dark-field TEM imaging of the indentation zone of calcite samples, which had undergone the same indentation loading conditions as *P. placenta*, reveal large fractured pieces (size > 2 μm) and cracks (**Figure 4-13**), consistent with top-view SEM observations (**Figure 4-4b**). At the bottom of indentation craters, a primary vertical crack is produced downwards (~1-2 μm deep) and multiple lateral cracks are formed. As the load increases, the vertical cracks advance further downwards and the lateral cracks propagate nearly parallel to the surface to form large chipped pieces, similar to other brittle ceramic materials[186].

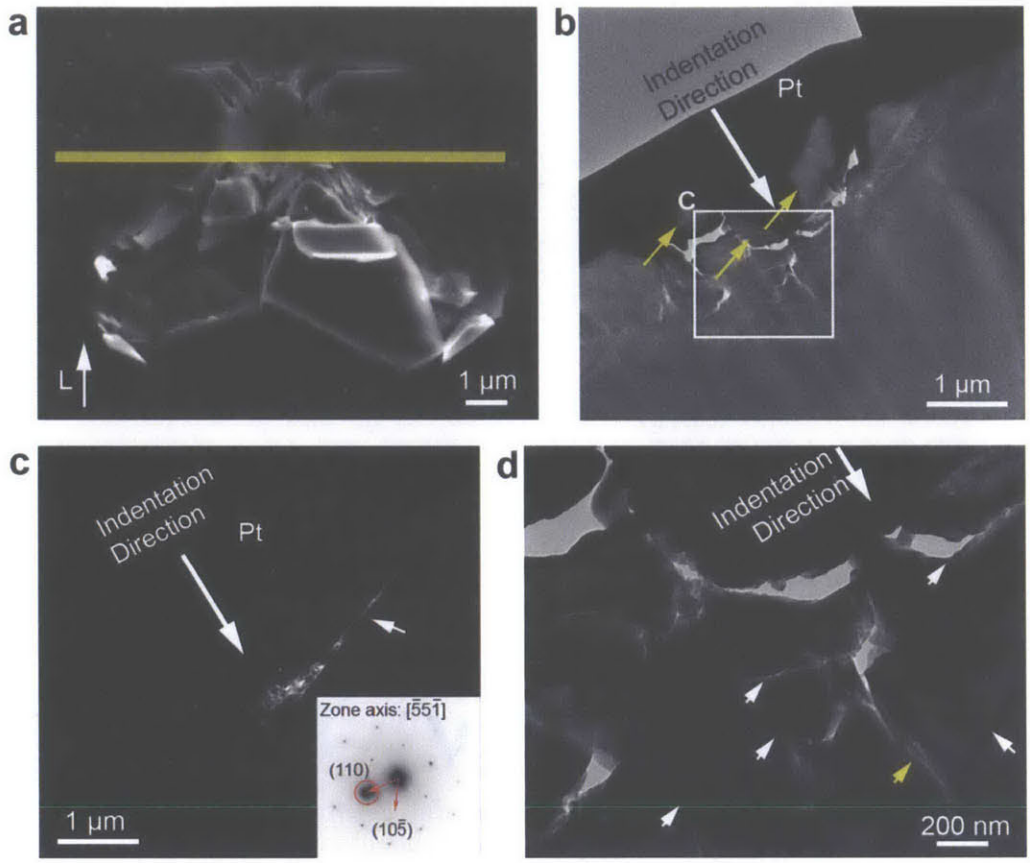

Figure 4-13| Formation of large microcracks in single crystal calcite after indentation tests (conospherical tip; tip radius = 1 μm; semi-angle = 30°; maximum load = 10 mN). **a**, Top-viewed SEM image of the original indentation residue. The yellow line indicates the location and orientation of the TEM sample prepared through FIB. **b**, Bright field TEM image of indentation zone, revealing multiple microcracks and micro-sized fractured pieces (yellow arrows). **c**, A corresponding dark field TEM image reveals the deformation-induced large-sized misoriented piece which propagates to the bulk surface with a very shallow orientation. Inset, the corresponding SAED pattern with the selected diffraction spot used for the dark field image in **c**. **d**, High-magnification bright field TEM image at the tip of the indentation residue. It reveals a vertical crack (yellow arrow) which is brunched with multiple lateral cracks propagating to the bulk surface (white arrows).

In contrast to *P. placenta*, extended dislocation arrays were also developed underneath indentation crater (**Figure 4-14b**). These events result in the large penetration depth (h_{def}), "pop-in" depth (Δd), fracture size (R_o), and volume of permanent deformation (V_{def}) observed (**Figure 4-6**). TEM samples prepared along the longitudinal direction reveal a very limited number of *e*-type deformation twins with only ($\bar{1}08$) twinning boundaries under this loading condition (**Figure 4-14**). The width of the twin bands (~200 nm) is usually much larger than those in *P. placenta*, inducing large cracks because of large local displacement incompatibilities. Due to the absence of effective crack arrestors and deflectors, such as the organic interfaces in *P. placenta*, these cracks propagate to the surface, generating large chipped blocks.

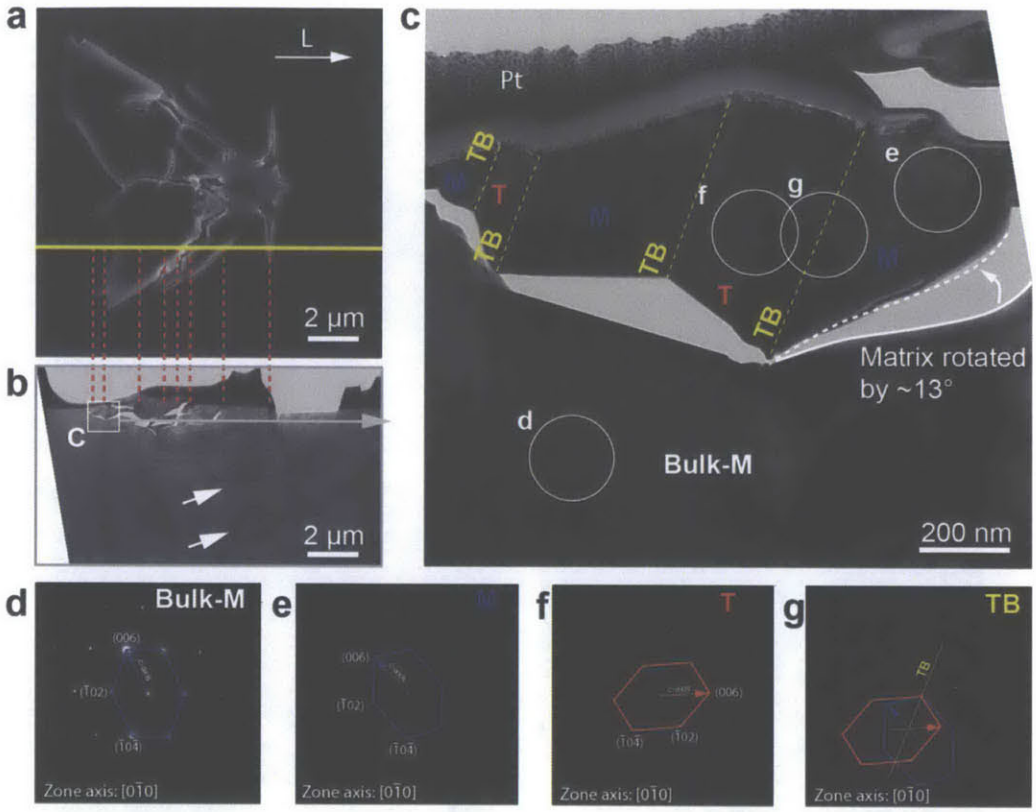

Figure 4-14| Deformation twinning in single-crystal calcite observed in the TEM sample prepared parallel to the longitudinal direction (conospherical tip; tip radius = 1 μm; semi-angle = 30°; maximum load = 10 mN). **a**, Top-viewed SEM image of the original fracture pattern. The yellow line indicates the location and orientation of the TEM sample prepared by FIB. **b**, Bright field TEM image of the entire cross-section of the deformation residue. The red dotted lines show one-to-one correspondence between the ridges and cracks from the top-viewed SEM image and corresponding twinning boundaries and cracks in the TEM cross-sections. The white arrows indicate the extended dislocation arrays generated from indentation deformation. **c**, Enlarged TEM image of the deformation twinning as shown in the area in (**b**). The twinning boundaries are marked by the yellow dashed lines. Matrix and twin regions are labeled by M and T. Note that the matrix was rotated (~ 13°) from the bulk matrix (Bulk-M) due to fracture (indicated by the white solid lines to the dotted lines). **d-f**, SAED patterns obtained in regions indicated in (**c**) (zone axes: [0$\bar{1}$0]). Note the mirror symmetry between the twin and matrix region with respect to the twin boundary (TB) of ($\bar{1}$08).

4.4 Discussion and conclusion

A summary of the entire progress of deformation mechanisms in *P. placenta* compared to those of single crystal calcite is provided in **Figure 4-15**. Upon indentation, the calcitic laths in *P. placenta* shells first undergo *e*-type twinning in all three crystallographically equivalent orientations [(018), (1$\bar{1}$8), and ($\bar{1}$08)], while only one orientation ($\bar{1}$08) is primarily activated in single crystal calcite (**Figure 4-15a-b**, **Figure 4-14**). This is possibly facilitated by the nanoscopic thickness of the calcitic laths in the shell. Such grain-size effects for deformation twinning have been observed in some metallic nanocrystalline materials, although further reducing the grain size below certain critical size may also lead to increased resistance to

deformation twinning[187,188]. Whether the thickness of the calcitic laths (~300 nm) is optimal to facilitate deformation twinning remains a question; further investigations, especially theoretical modeling, may provide more insights[189]. The nanoasperities on the surface of laths might also assist the initiation of multiple deformation twinning bands with nanoscale spacing due to roughness-induced stress concentrations during loading. The as-formed twin bands make inclination angles with the surface normal and longitudinal direction of the laths by 26°/43°, 26°/0°, and 52°/90° for (018), ($1\bar{1}8$), and ($\bar{1}08$) twin bands, respectively (**Figure 4-10**), which allows the biogenic calcite to mitigate stress concentrations more effectively in comparison to abiotic calcite, leading to a more isotropic deformation response (**Figure 4-15c, stage 1**). The variation of the thickness and crystal orientation of the calcitic laths allows a sequential activation of deformation twinning bands depending on the specific loading conditions, which is expected to result in a work hardening effect[190]. Unlike the growth twins, these deformation-induced twins only activate when and where they are needed, i.e., ahead of the impact region upon penetration. Moreover, deformation twinning in *P. placenta* is activated upon quasi-static deformation conditions, in contrast to the recently observed deformation twinning in aragonitic nacre under high strain rate deformations (~10^3 s^{-1})[176].The twin boundaries surrounding the penetration region act as effective barriers for dislocation motion and catastrophic crack propagation, leading to enhanced penetration resistance (**Figure 4-15c, stage 2**)[191]. While the twinning bands mainly act as barriers in the horizontal direction (**Figure 4-16**), the organic interfaces play a similar role in the vertical direction, resisting dislocation motion and crack propagation from one layer to another (**Figure 4-17**).

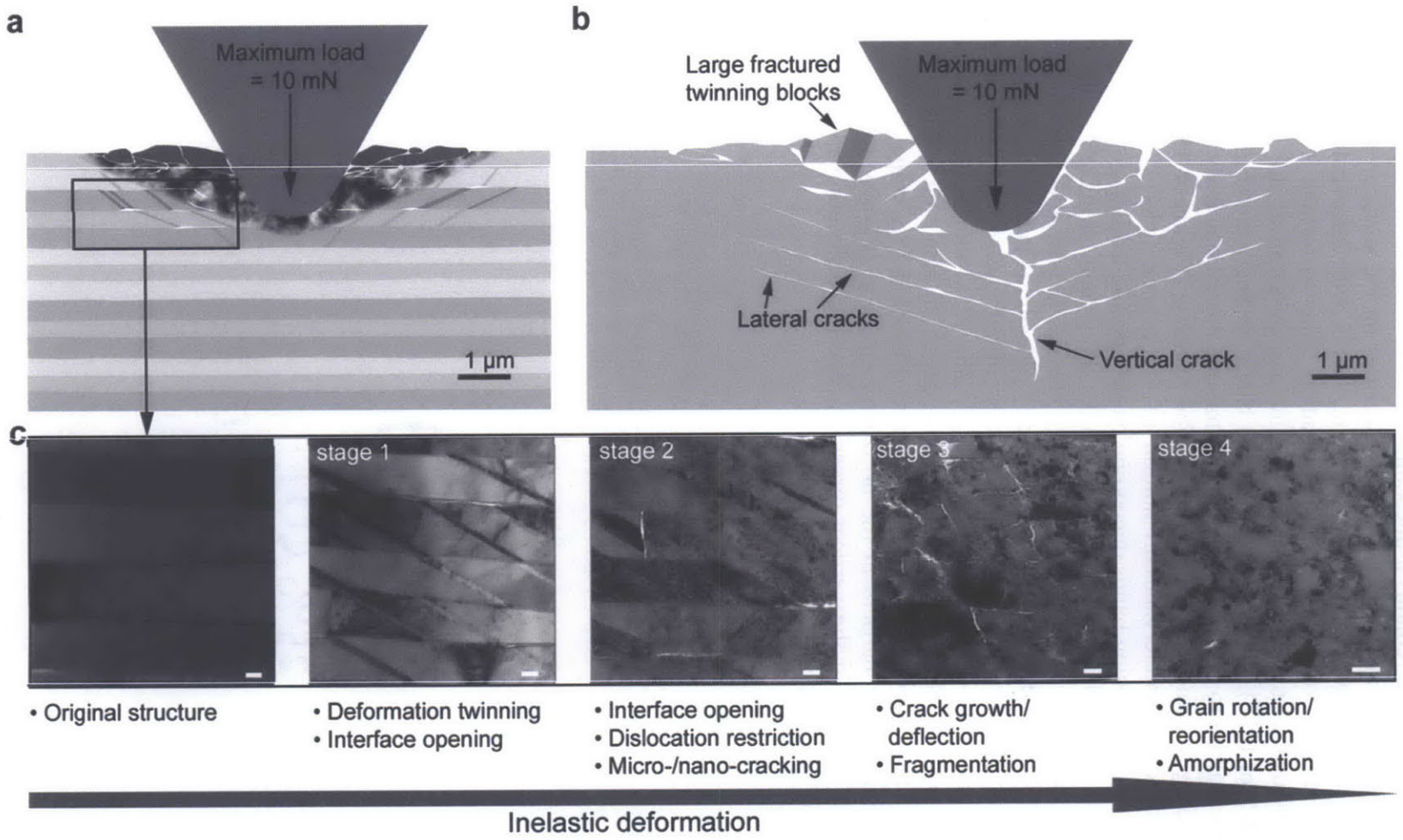

Figure 4-15| Nanoscale deformation mechanisms in *P. placenta* and single crystal calcite under indentation. **a**, Schematic of the deformation zone close to the indenter for (**a**) *P. placenta* and (**b**) single crystal calcite (conospherical tip; semi-angle = 30°; tip radius = ~1 µm; maximum load = 10 mN). The diagrams are drawn in scale based on microscopic dimensional measurement. Dislocation arrays in calcite are not shown in (**b**). **c**, TEM images illustrating the progression of nanoscale deformation mechanisms of *P. Placenta* (listed below the images) with decreasing distance from the indenter. All scale bars represent 100 nm.

The nanoscale twinning bands and organic interfaces increases energy dissipation density by acting as catalysts to promote other nanoscopic deformation mechanisms, including interfacial and intracrystalline nanocracking, organic viscoplastic stretching, as well as nanograin formation and reorientation. The relatively small amount of organic material (~1 wt%) present in the shell is expected to contribute to energy dissipation in a variety of ways. The nanoscopic openings associated with the ends of twin bands result in fibrillar viscoplastic stretching of intercrystalline organic material bridging neighboring calcite laths (**Figure 4-7**), leading to increased energy dissipation (**Figure 4-15c, stage 2**), which has been previously observed in nacre[56]. It is also hypothesized that the nanoscopic intracrystalline organic inclusions, in addition to twinning boundaries, contribute to deflecting and arresting intracrystalline cracks, which leads to fragmentation of the regular single-crystalline laths into irregular micro-/nano-sized pieces (**Figure 4-15c, stage 3**)[191]. Interactions between the accumulated dislocations and twinning boundaries might also contribute to this fragmentation process[190,191]. Further compressive deformation leads to formation and reorientation of nano-sized grains (in contrast to the observation of inherent nanograined structure in nacre[66]), and formation of amorphous regions. At this stage, the deformed material is transformed to an isotropic homogeneous nanocrystalline material, as the original laths and organic interfaces are destroyed (**Figure 4-15c, stage 4**).

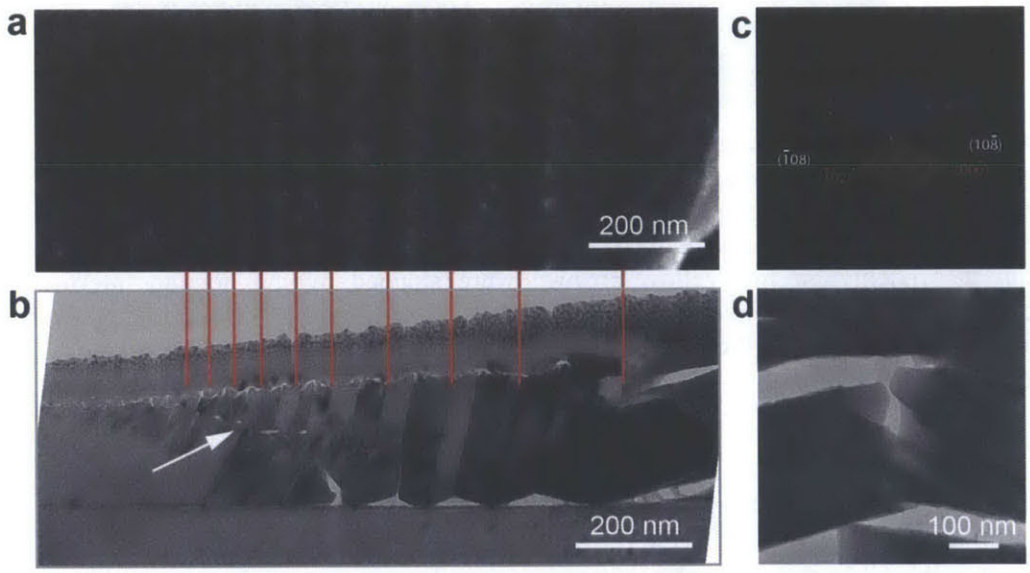

Figure 4-16| Crack deflection by twinning boundaries. a, SEM image of closely-spaced deformation twins in *P. placenta*. **b**, Corresponding cross-sectional TEM image of the same region which clearly shows the cracks were deflected multiple times at the twin boundaries. **c**, Corresponding SAED pattern in (**b**). **d**, TEM image showing a crack running across one mineral layer was deflected by the twinning boundaries.

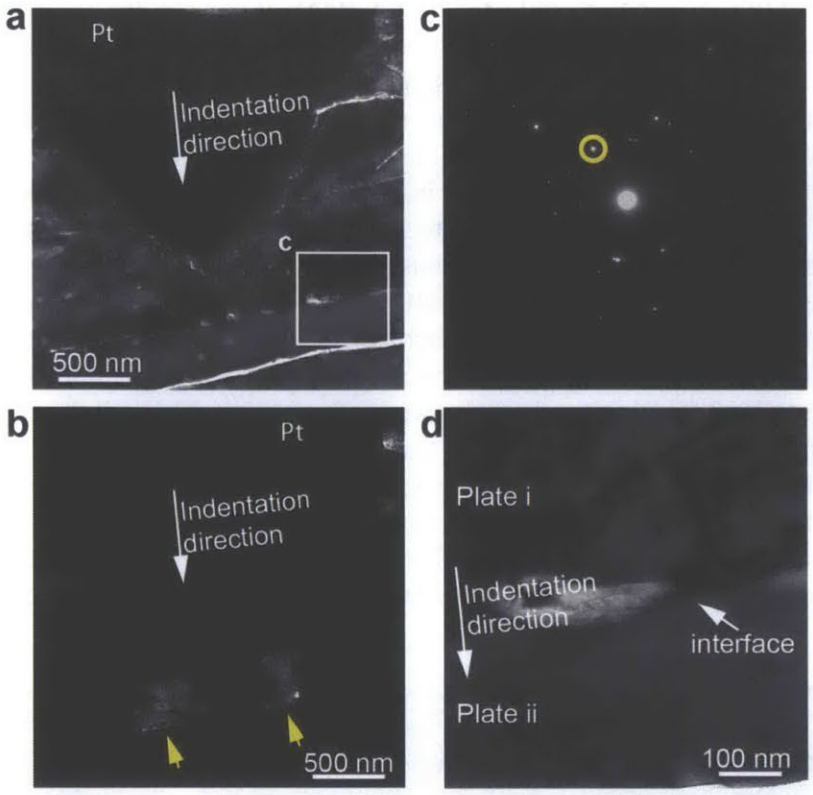

Figure 4-17| Deformation confinement by organic interfaces (conospherical tip; tip radius = 1 μm; semi-angle = 30°; maximum load = 10 mN). (**a**) Bright-field and (**b**) corresponding dark-field TEM image of the region close to the tip of the indentation residue. **c**, The SAED pattern with the diffraction spot selected for the dark-field image in (**b**). Two deformation-induced misoriented blocks of materials underneath the indentation tip (yellow arrows) were stopped by the organic interface. **d**, High-magnification TEM image showing high density of the dislocation developed in *Plate i* due to deformation was confined by the organic interface and the mineral layer underneath (*Plate ii*) was almost free of dislocations.

It is noted that the microscopic structural features responsible for pervasive nanoscale deformation twinning in *P. placenta* also exist in other calcitic bioceramic structural materials including other bivalve shells[40], brachiopod shells[192], and sea urchin spines and teeth[193,194]. Therefore, it is possible that this phenomenon may also play a similar role in these systems. In addition, some aragonite-based mollusk shells possess basic building blocks densely packed with nanoscale {110} growth twins[195,196]. These pre-existing twinning boundaries may play a similar role in constraining the dislocation motions and deflecting the propagation of micro-/nano-cracks[191]. However, the displacement incompatibilities resulted from the formation of deformation twinning bands will not be prevalent in aragonite structures with growth twins; therefore, they are not expected to effectively catalyze other nanoscopic energy dissipation processes in a fashion similar to *P. placenta*.

Energy dissipation enhancement resulting from spreading the deformation zone over a large area/volume has been observed in a variety of biological structural material systems through different mechanisms, such as the tablet interlocking of nacre[49], crack deflection and bridging of crossed-lamellar structure[29,70], and nanoscale heterogeneity of bone[177]. In addition to maximizing

the total energy dissipation upon deformation, maintaining the structural and mechanical integrity of the entire structure is also critical to the performance of biological exoskeletons during predatory attacks. Damage localization in the protective scales of a "living fossil" *Polypterus senegalus* is achieved through preferential circumferential cracking rather than more damaging radial cracking, which results from the complex quad-layered design of the scales[28]. In this work, I demonstrated that the bioceramic armor of *P. placenta*, despite its very high mineral content and relatively monolithic composition and structure, is able to achieve a great balance between energy dissipation and damage localization by efficient energy dissipation in a confined volume via pervasive nanoscale deformation twinning surrounding the deformation zone. A series of additional nanoscopic deformation mechanisms, including interface opening and viscoplastic stretching of organic materials, crack deflection within individual building blocks, fragmentation, nanograin formation and reorientation, and amorphization, work synergistically to increase the energy dissipation density by almost an order of magnitude relative to pure calcite. The nanoscale structural and crystallographic architecture in this biological nanocomposite determine the activation and control of these efficient energy dissipation mechanisms. Aside from deformation localization, which maintains the structural and mechanical integrity of the entire system (multi-hit capability), the optical properties (~80% total transmission of visible light) are also preserved at distances away from the penetration site. The findings in this work may provide design principles for engineering lightweight structural materials with efficient energy dissipation, in particular transparent armor, through control and design of the material systems at the nanometer scale.

Chapter 5 Macroscopic deformation behavior of *P. placenta* shell and its related ultrastructural features

5.1 Introduction

A diverse number of unique deformation mechanisms of biological structural materials have been discovered at a variety of length scales[4,197–200]. In particular, many previous studies have focused on the mechanical behavior at nanometer scale, primarily because the basic building blocks of most biomineralized structural materials are nanometer-sized. At this length scale, a variety of energy dissipation mechanisms have been identified, for example, viscoplastic stretching of organic materials in interfaces[55,56], nanograin rotation in nacre tablets[66], flaw insensitivity[62,63], and nanoscale deformation twinning as discussed in the Chapter 4 of this thesis.

These nanoscale deformation mechanisms are usually material specific, which hinders the potential transfer of design principles to bioinspired engineering structural materials. For example, the nanoscale deformation twinning discovered in *P. placenta* cannot be used as an energy dissipation mechanism for non-crystalline materials like glass, which is still the most common component of the majority of current transparent armor materials[8]. Additionally, understanding deformation mechanisms only at the nanometer scale does not give us the whole story since biological structural materials are, similar to engineering counterparts, also subject to large scale deformations with high loads during predatory attacks[10,180]. Study of deformation mechanisms at larger length scales is not only necessary to understand the biological materials' performance with respect to real-life threats, but also provides us with a direct comparison to engineering structural composite materials, in which deformation behavior above the nanometer scale usually plays a dominant role in energy dissipation and damage tolerance[201].

Due to the system-specific hierarchical structural designs in biological materials, it is experimentally challenging to directly link the structural features and deformation mechanisms at different length scales. Specific structural characterization and mechanical testing techniques with appropriate resolutions should be applied as an integrated approach.

In this chapter, I present a detailed analysis of a unique nanoscale structural motif, i.e. screw dislocation-like connection centers, and their distribution at the macroscopic level (~15 mm^2) in the foliated microstructure of *P. placenta*. Large scale deformation behavior was investigated through a customized macroindentation technique with loads high enough to penetrate intact shells, ~80 N. Moreover, the mm-sized three dimensional damage zone resulted from macroindentation tests was quantitatively studied via synchrotron X-ray μCT. Combining these results with high-resolution electron microscopy, I show that the connection centers act as anchoring centers for the formation of ligament bridges, which resist crack opening behind crack tips and retard crack propagation. Through this unique structural motif, the highly mineralized *P. placenta* shell is able to form an isotropic deformation zone, within which a three dimensional complex interconnected microcrack network is formed. In addition, in the vicinity of connection centers, nanoscale plastic deformation (as discussed in the previous chapter) is initiated due to

the local multi-axial loading conditions. This enhances the interface fracture toughness by almost two orders of magnitude, as evident from both a simple theoretical analysis and experiment-based calculations.

5.2 Materials and Methods

Samples. Edge-trimmed and intact *P. placenta* shells were purchased from Seashell World (Florida, USA) and Conchology, Inc. (Philippines), respectively. The specimens were stored in dry conditions prior to experiments.

Instrumented macroindentation. P. placenta shells were first cut into square-shaped samples (~2 cm in size) with a diamond saw. High load indentation experiments were performed on a Zwick Mechanical Tester (Zwick Z010, Zwick Roell, Germany), and the load-displacement curves were recorded. The indenter was a customized tungsten needle with a conical tip (full angle, ~31°; tip radius, ~ 21 μm; base diameter, 0.5 mm). All indentation experiments were conducted under displacement control (displacement rate: 0.02 mm/s).

Electron microscopy. Samples were coated with ultra-thin carbon prior to SEM observations. Samples were imaged using a Helios Nanolab 600 Dual Beam (FEI, OR) using acceleration voltages of 2 and 5 kV, and a working distance of 4 mm.

Atomic force microscopy. Tapping mode AFM (TMAFM) imaging in ambient conditions was carried out using a Digital Instruments Multimode SPM IIIA (Veeco, Santa Barbara, CA) with an AS-130 "JV" scanner. TMAFM imaging was conducted with NANOSENSORS Si TMAFM cantilevers (PPP-NCHR-10). Typical scan speeds were between 1-5 μm/s, and other parameters were optimized upon tuning. The imaging modes include height (i.e., Z-piezo movement), amplitude (i.e., cantilever oscillation amplitude), and phase (i.e., cantilever phase lag).

X-ray Micro-computed tomography. Pre-cut *P. placenta* shells (~3 mm in size) were first tested with macroindentation experiments as described above. Next, the indented shells were scanned with an energy of 18 keV and a resolution of 2.84 μm/voxel at beamline 2-BM of the Advanced Photon Source of Argonne National Laboratory. Mimics (Materialise, Belgium) was used for image segmentation and construction of three-dimensional triangulated surface meshes (binary STL format). The surface area of the interfaces generated by the indentations was measured using netfabb (www.netfabb.com). For generation of 3D illustrations and movies, STL meshes were directly imported into and rendered using Blender (www. blender.org).

5.3 Results

5.3.1 Screw dislocation-like connection centers

Examination of cleaved surfaces of *P. placenta* shell reveals one unique microstructural feature, i.e. the screw dislocation-like connection centers, as shown in **Figure 5-1**. These connection centers, similar to screw dislocations, join two adjacent mineral layers as an integrated structure (**Figure 5-1a**). In addition, connection centers with opposite signs, i.e. up and down (right-hand rule), were observed. AFM height images further reveal that the extra layers induced by connection centers are merged gradually so that there is no discontinuity between the additional and original mineral layers (**Figure 5-1b**). The additional layer associated with connection centers gradually increases its thickness to the normal value (~300 nm) in over

distance of ~3 μm. This leads to inclination angles of about 3° in the transition regions. The presence of connection centers can be also visualized through polished cross-sectional surfaces (**Figure 5-1c**), where extra interfaces are associated with insertion of additional mineral layers via connection centers.

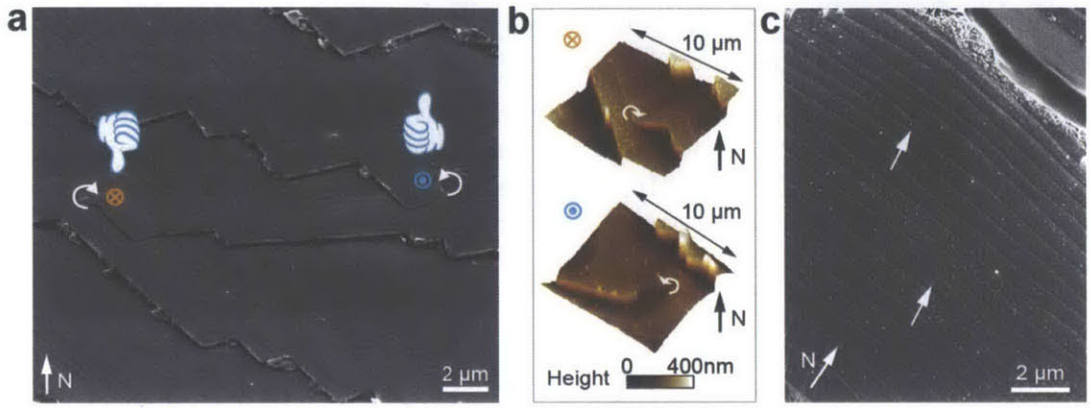

Figure 5-1| Screw dislocation-like connection centers in the foliated structure of *P. placenta*. **a**, SEM image showing two connection centers with opposite signs, i.e., up and down (defined according to the right-hand rule and indicated by the blue and orange markers, respectively). **b**, AFM height image of two connection centers with opposite signs. **c**, SEM image of a polished cross section showing two half-ended interfaces (indicated by white arrows), which are due to the presence of additional mineral layers resulted from connection centers.

Associated connection centers pairs with opposite signs which are located in the same mineral layer can be visualized through large-area imaging of cleaved surfaces, as shown in **Figure 5-2**. The two connection centers with opposite signs are linked through a common line of fractured interface in one mineral layer (top layer, **Figure 5-2a,b**). This line of fractured interface is denoted as the "fracture line" in following discussions. The formation process of fracture lines is as following: 1) a crack initiates via interface opening along the bottom layer; 2) interface opening is stopped by the connection centers; 3) the top mineral layer is fractured in between the two connection centers so that the crack can continue to propagate (**Figure 5-2e**). This interface cleavage technique thus provides us an effective method to expose connection centers over large areas.I also notice that the fracture line joining connection center pairs is roughly perpendicular to the longitudinal direction of building blocks.

The above interface cleavage technique was then used to prepare samples with large-area fracture surfaces, from which the distribution of connection centers over large length scales was investigated (**Figure 5-3**). As shown in the high-magnification representative region in **Figure 5-3a**, the fracture lines on the cleaved surface were manually traced and connection centers were marked with specific signs. **Figure 5-3b** shows a large area SEM image (~5.7 mm^2) with spatial resolution (~21 nm) high enough for identifying the fracture lines and connection centers. **Figure 5-3c** shows the traced fracture lines over the entire region. The colors represent different types of fracture lines according to their ending characteristics (**Figure 5-3f**):

Full (black): the fracture lines are completely within the mapped area, with both up- and down-signed connection centers at the two ends of lines.

Bottom (yellow): the bottom-right portions of the fracture lines are cut off by the bottom boundary of image, with only down-signed connection centers.

Top (green): the top-left portions of the fractured lines are cut off by the top boundary of image, with only up-signed connection centers.

Left (orange): the right portions of the fracture lines are cut off by the left boundary of image, with only up-signed connection centers.

Right (blue): the right portions of the fracture lines are cut off by the right boundary of image, with only down-signed connection centers.

Long (red): both left and right portions of the fracture lines are cut off by the image boundary, without any connection centers within the image.

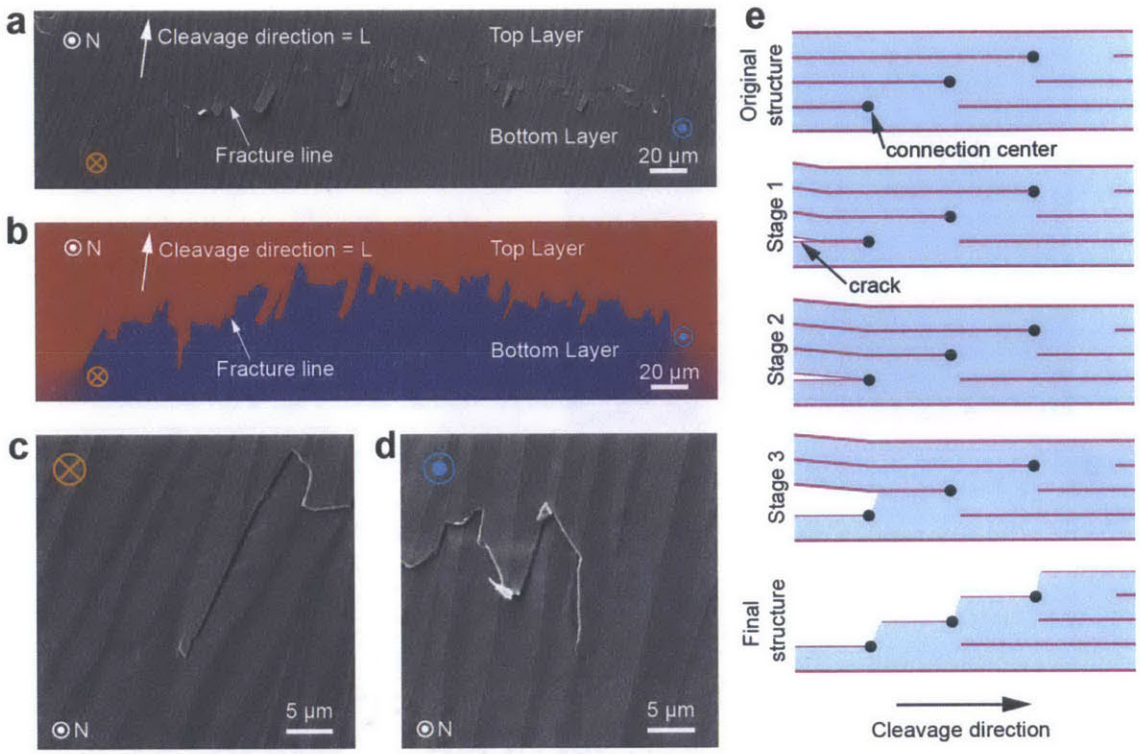

Figure 5-2| Associated connection centers with opposite signs. (**a**) SEM image and (**b**) corresponding schematic diagram of two associated connection centers with opposite signs located at the same mineral layer, which are linked through a common fracture line. **c,d**, High-magnification SEM images of the two associated connection centers. **e**, Formation process of fracture lines via connection centers. The blue and pink layers represent the mineral layers and organic interfaces, respectively.

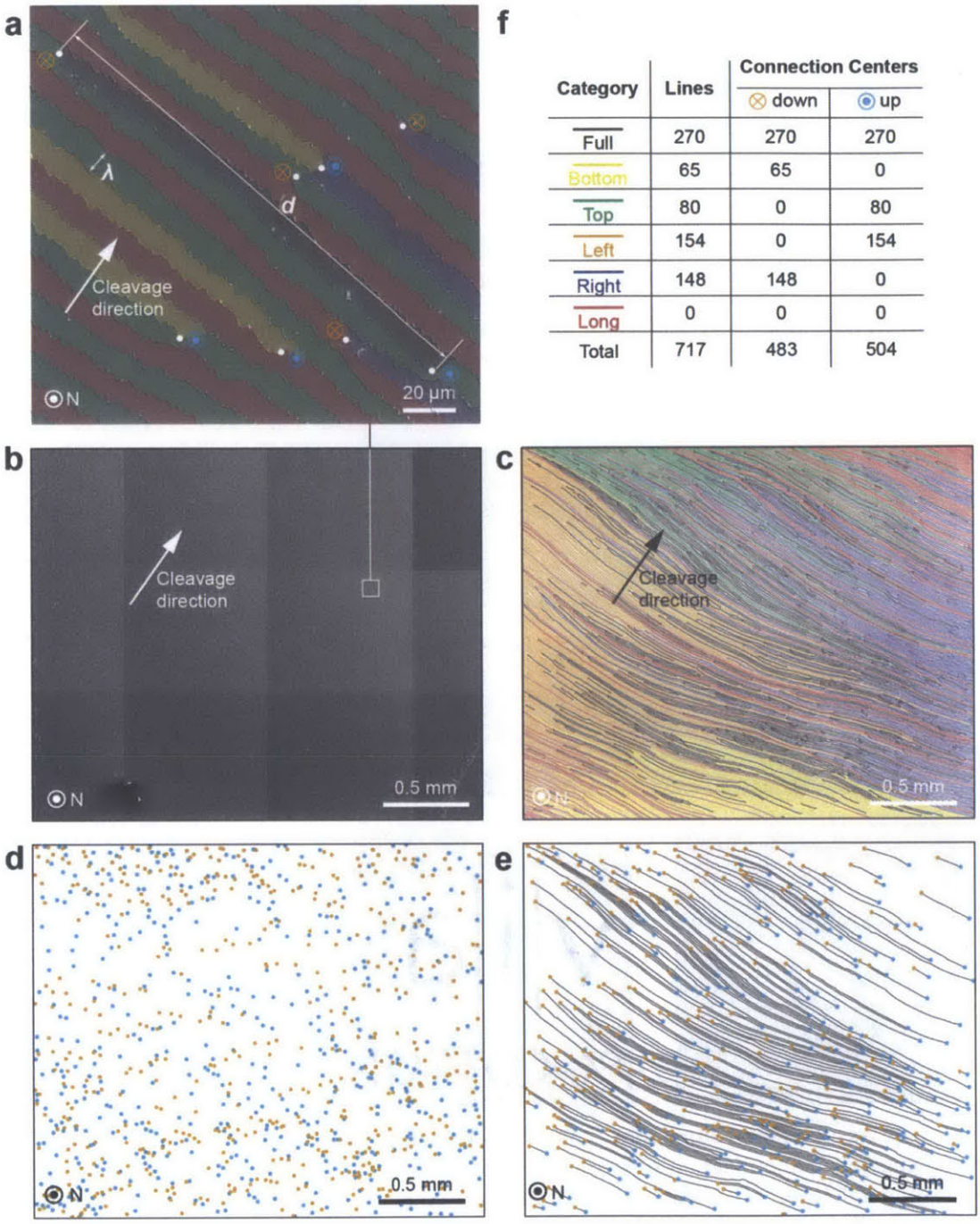

f

Category	Lines	Connection Centers	
		⊗ down	◉ up
Full	270	270	270
Bottom	65	65	0
Top	80	0	80
Left	154	0	154
Right	148	148	0
Long	0	0	0
Total	717	483	504

Figure 5-3| Large scale mapping of the distribution of connection centers. a, SEM image of a cleaved interface, from which fracture lines and connection centers are traced and marked, respectively. The image is artificially colored to further highlight adjacent mineral layers. Two dimensional parameters are defined: λ, the distance between two adjacent fractured lines; d, the distance between two associated connection centers with opposite signs. **b,** Large-area SEM image of a cleaved surface and corresponding images with traced fracture lines (**c**),connection centers marked (**d**), and full fracture lines with both opposite-signed connection centers located within image area (**e**). **f**, Quantitative measurements of the number of fracture lines and connection centers for the region shown in (**b-e**).

Figure 5-3d depicts the corresponding distribution of connection centers, which includes 483 down-signed and 504 up-signed connection centers. **Figure 5-3e** shows the traces of the full fracture lines with two associated opposite-signed connection centers in the analyzed region. As shown in (**Figure 5-3a**), two dimensional parameters were defined for further quantitative analysis: λ, the spacing between two adjacent fracture lines, and d, the distance between two associated opposite-signed connection centers.

Figure 5-4a plots the statistical distribution of the distance between an associated pair of opposite-signed connection centers (d). The distribution can be well fitted with the logarithmic distribution,

$$p = p_0 + Ae^{R_0 d}. \qquad \text{Equation 5-1}$$

55.9% of measurements of distance d were below 0.5 mm, and the average was 574 ± 509 μm (n = 270). Some fracture lines are longer than the entire mapped region (~2.4 mm). Note that this statistical distribution of d might be skewed towards the lower end, as there are long fracture lines which are not completely contained within the analysis region and are not counted in this statistical measurement. Hence, I expect that the actual average distance between two associated opposite-signed connection center pairs should be greater than the current value.

Moreover, I studied the relative positions of the connection centers along a given profile, as shown in **Figure 5-4b-d**. Crack propagation lines (line 1-3 in **Figure 5-4b**) are defined along the cleavage direction, which is perpendicular to the direction of fracture lines. Two distances were defined: l, the distance between the crack propagation line and connection centers on fracture lines encountered by the crack propagation line, and l', the distance between connection centers associated with two adjacent fracture lines (**Figure 5-4c**). The signs of these values are illustrated in **Figure 5-4c**. **Figure 5-4d** shows the profile of l and l' along three arbitrary crack propagation lines highlighted in **Figure 5-4b**. Both parameters exhibit an approximately equal number of positive and negative values within the range of ±2 mm. This indicates that, along a crack propagation line, the distance between adjacent connection center (l') is roughly 2 mm. In addition, the profiles of l periodically shift between two signs, which suggests that cracks propagating along organic interfaces must periodically shift to left and right to circumvent connection centers. This process inevitably increases the "sampling area" during crack propagation along interfaces, which increases interfacial strength and toughness.

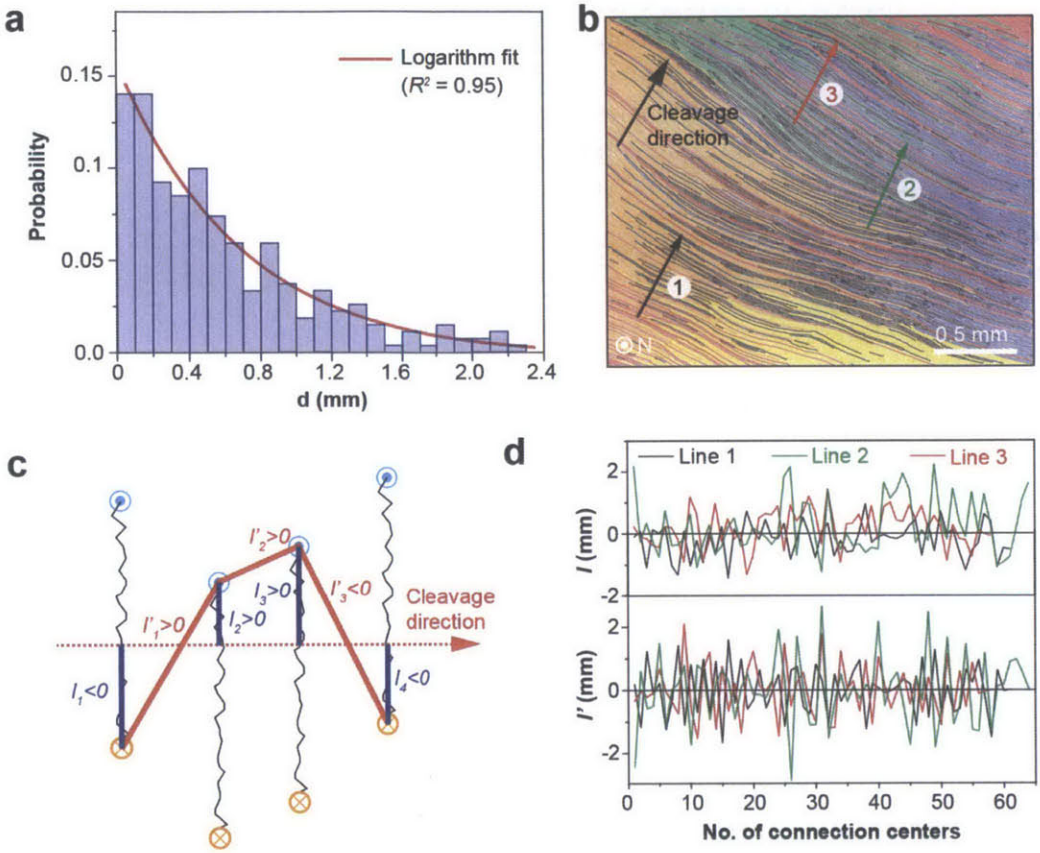

Figure 5-4| Further structural characteristics of connection centers. a, Distribution of the distance between one associated connection center pairs with opposite signs, as shown in Figure 5.3e. The red line represents a logarithmic fit ($p = p_0 + Ae^{R_0 d}$). **b**, Map with fractured lines traced. Lines 1-3 represent arbitrary crack propagation lines. **c**, Schematic diagram showing that the crack propagation line crosses four fracture lines. Two parameters are defined: l, the distance between the crack propagation line and connection centers; l', the distance between connection centers associated with two adjacent fracture lines along the crack propagation line. **d**, Profiles of l and l' along lines 1-3.

The density of connection centers was further investigated through a simple geometrical analysis. As shown in the schematic diagram in **Figure 5-5**, I define the thickness of mineral layers as t, and the length and width of an arbitrary area of the shell as a and b, respectively. The areal density of connection centers, ρ_{area}, which can be directly measured from experimental mapping as shown in **Figure 5-2**, is related to the volumetric density of connection centers (ρ_{volume}) by considering of the area and volume involved in the cleaved surface:

$$\rho_{area} = \left[2\lambda tb\left(\frac{a}{\lambda}\right)\rho_{volume} \right] / ab = 2t\rho_{volume}, \qquad \text{Equation 5-2}$$

where $2\lambda tb\left(\frac{a}{\lambda}\right)$ and ab are the volume and area associated with this cleaved surface.

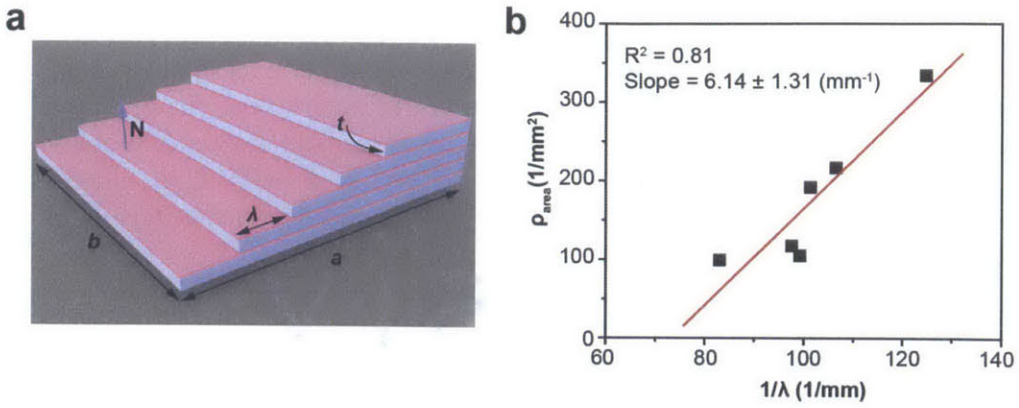

Figure 5-5| Relationship between the density of connection centers and spacing of fracture lines. **a**, Simplified schematic diagram showing the cleaved surface with fracture lines. The blue and pink layers represent the mineral layers and organic interfaces, respectively. *t*, thickness of mineral layers. **b**, The areal density of connection centers (ρ_{area}) as a function of the inverse of the fracture line spacing ($1/\lambda$).

From **Equation 5-1**, using the experimentally measured areal density (~100-400 mm^{-2}), I can estimate the volumetric density of connection centers, ρ_{volume}, to be between $1.7 - 6.7\times10^5$ mm^{-3}. The total volume of a typical *P. placenta* shell is about 4×10^3 mm^3 (circular shape; thickness, ~0.5 mm; diameter, ~10 cm). The total number of connection centers within the entire shell can then be estimated as $\sim2\times10^9$, which corresponds to $\sim10^6$ connection centers distributed within each mineral layer (~2000 layers throughout the entire shell). Through this large-area imaging analysis and the experiment-based calculations, I hypothesize that the foliated microstructure of *P. placenta* shell has, instead of a simple laminate structure with typical mineral-organic organization, a complex three dimensional integrated composite laminate structure, where all the mineral layers are connected together through screw dislocation-like connection centers.

Moreover, since the connection centers directly induce the formation of fracture lines, the number of fracture lines within an area is directly proportional to the number of connection centers. Therefore, we have

$$\rho_{area} \propto \frac{a}{\lambda} \propto \frac{1}{\lambda}. \qquad \text{Equation 5-3}$$

This inverse relationship is clearly supported by the linear fit between the density of connection centers and the spacing of fracture lines (**Figure 5.5b**).

In addition to integrating all mineral layers together to form a three dimensional interconnected nanocomposite, the specific distributions of connection centers are also able to control the orientation of building blocks within individual mineral layers. As we discussed in **Chapter 3**, the basic building blocks in the foliated microstructure of the shell of *P. placenta* are the elongated diamond-shaped laths, which are tiled together, forming layers. Since cracks usually propagate parallel to the longitudinal direction of laths, the fracture lines of each mineral layer are usually perpendicular to the longitudinal direction of laths. As shown in **Figure 5-6a-b**, the orientation of fracture lines varies in different regions. Close examination of the boundaries

between two misorientated regions reveal the presence of excessive connection centers with one particular sign (**Figure 5-6c-f**). As shown in **Figure 5-6c-d**, an excess of up-signed connection centers creates a clockwise rotation of the orientation of fracture lines (from blue to red). On the other hand, an excess of down-signed connection centers leads to a counter-clockwise rotation of the orientation of fracture lines (from blue to red, **Figure 5-6e-f**). High magnification SEM images shown in **Figure 5-6g-h** confirm that the corresponding orientations of building blocks rotate accordingly with the fracture lines.

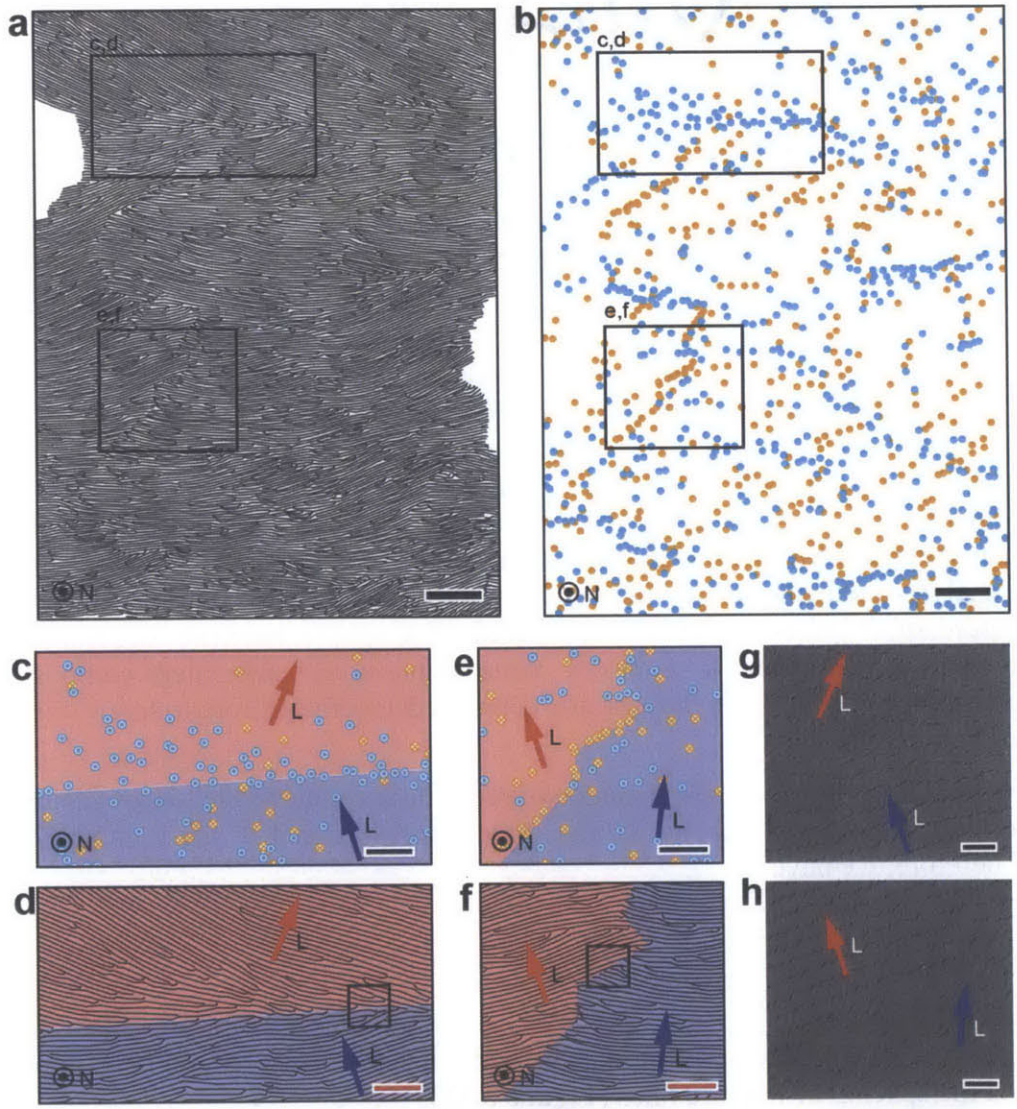

Figure 5-6| Distribution of connection centers as a pathway to control the orientation of building blocks. Traced fracture lines (**a**) and corresponding distribution of connection centers (**b**). Regions with an excess of up-signed (**c-d**) and down-signed (**e-f**) connection centers. The longitudinal orientations of building blocks (indicated by red and white arrows) change across the boundaries which are formed by an excess of connection centers with one particular sign. **g,h**, SEM images showing local variations of the orientations of building block and fracture lines. Scale bars: **a-b**, 200 μm; **c-f**, 100 μm; **g-h**, 20 μm.

5.3.2 Large-scale deformation behavior via macroindentation

I next investigated the mechanical behavior of *P. placenta* shells at large length scales to establish its relationship to the structural features discussed above. Intact shells were penetrated through their entire thickness using a customized indentation instrument with a tungsten tip and high load capabilities (**Figure 5-7a-c**). The as-obtained load-depth curves reveal two regimes (**Figure 5-7d**):

Regime 1: the indentation tip gradually indented into the shell until a maximum load (F_{max}) was reached when the shell was fractured (a single sound of "cracking" could be clearly heard);

Regime 2: this is the post-fracture penetration process during which the indentation tip continuously pushed out the fractured shell pieces and penetrated deeper until the load dropped to approximately zero.

Before F_{max} was reached, the nanocomposite underwent extremely localized deformation without any radial crack formation (**Figure 5-7e**). For shells with thicknesses of 0.68 ± 0.03 mm, the maximum fracture loads were 64.6 ± 12.3 N (n = 7). As a comparison, similar macroindentation experiments were performed on calcite samples with similar thicknesses (red profiles in **Figure 5-7d**), which exhibited brittle catastrophic fracture behavior without a post-fracture inelastic deformation regime as observed in *P. placenta*. Moreover, the maximum fracture loads for calcite (17.8 ± 6.6 N; thickness, 0.76 ± 0.09 mm; n = 4) were much lower compared to *P. placenta*, even though the average sample thickness was more than 10% greater The fractured pieces of calcite samples after indentation tests had little visible inelastic deformation close to the indentation site (**Figure 5-7i**). The bending deformation of the shells was very small (~0.5%) according to a finite element simulation analysis (**Appendix A, Figure A-5**) and its contribution to total displacement was therefore neglected.

The graceful penetration behavior exhibited by the shell of *P. placenta* maintained structural integrity even after multiple indentation experiments that fully penetrated the shell (**Figure 5-7e-g**). Thanks to the unique high optical transmission of the shell, the damage zone after indention tests can be directly visualized via optical microscopy in transmission mode (**Figure 5-7e, f, g**). The decrease in optical transmittance in the damaged zone results from the generation of interface openings and disruption of the original intact densely-packed structure, which causes light scattering and reduces transmission. The damage zone is isotropic and circular, which is dramatically different as compared to the brittle cleavage fracture of calcite. The localized damage behavior of the shell enables multi-hit capability without complete failure.

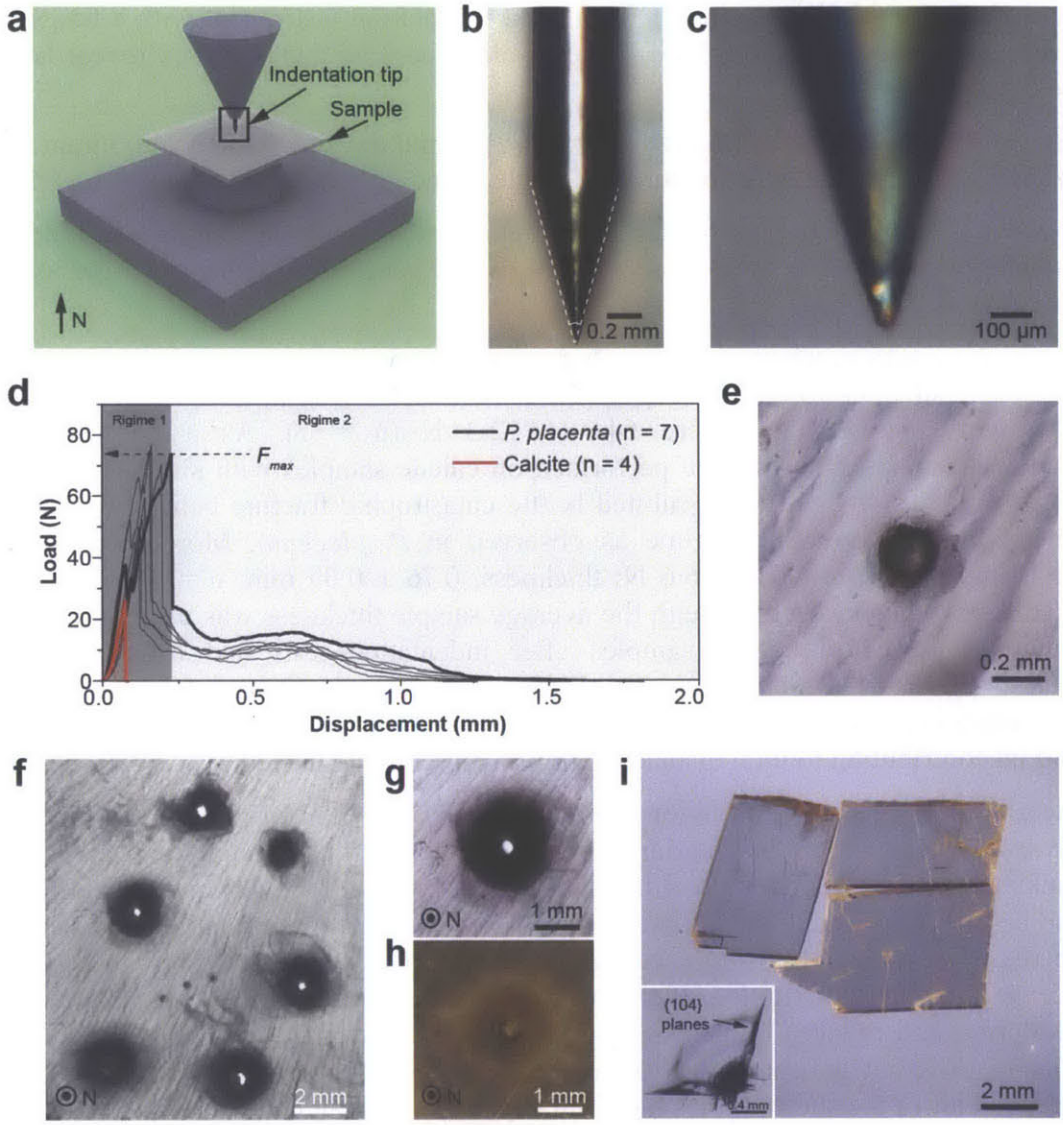

Figure 5-7| Macroindentation of *P. placenta* shells. a, Schematic diagram of experimental setup. The cylindrical substrate underneath the sample has a central hole (diameter, 5 mm) aligned with the indentation tip. **b-c**, Optical images of the tungsten indentation tip (full angle, ~31°; tip radius, ~22 µm). **d**, Representative macroindentation curves for *P. placenta* (thickness, 0.68 ± 0.03 mm; n = 7) and calcite (thickness, 0.76 ± 0.09 mm; n = 4). **e**, A residual indent in regime 1 before final fracture (maximum load, 30 N). **f**, A *P. placenta* shell after multiple macroindentation tests with complete penetration. **g-h**, optical images of one macroindentation residue in *P. placenta*. **i**, Multiple pieces resulting from brittle fracture of a calcite sample (thickness, ~ 0.8 mm) after an indentation test. Inset, an indentation residue of calcite before final fracture. Images in **e**, **f**, **g**, and **i** were taken in transmission mode. Image in **h** was taken in reflection mode.

The transmission optical images shown in **Figure 5-7e-g** allow us to visualize the damage zone after macroindentation tests in 2D; however, quantitative 3D information of the entire deformation zone cannot be obtained with this technique. In order to probe the resulted damage zone in 3D, so as to investigate the underlying deformation mechanisms which lead to damage localization and isotropy, high resolution synchrotron μCT was used (**Figure 5-8**). As shown in a typical three dimensional reconstruction with a transparency effect (**Figure 5-8a**), the entire indentation damage zone (dark regions) resembles a conical frustum geometry (please see **Movie 2 in Appendix** B for 3D visualization). The diameter of the top penetration hole of the conical frustum is ~0.5 mm, close to the base diameter of the tungsten indentation tip, and the diameter of the bottom of the conical frustum is ~1.5 mm, which results in the slant angle of the side edges close to 45°. **Figure 5-8b** shows a typical virtual slice of the indentation zone, which clearly reveals the complex interconnected networks of microcracks within the localized damage zone. Moreover, within the conical frustum damage zone, mineral layers have undergone shear failure with local breakages, and the resulting laminate orientation has rotated along the indentation direction. Please note that the three large horizontal cracks were generated during diamond saw cutting after indentation testing in order to fit the sample within the field of view of the synchrotron X-ray beam. **Figure 5-8c** shows a series of horizontal slices of the damage zone; the corresponding locations are indicated by the red dashed lines in **Figure 5-8b**. Small radial cracks originating from the central indentation hole are enclosed by multiple circumferential cracks, leading to confined damage behavior.

Figure 5-8d-e are three dimensional renderings of the microcrack network within the damage zone, corresponding the vertical section shown in **Figure 5-8a**. Note that the blue surface mesh is a negative of the indentation residue, i.e. it represents cracks between the mineral layers. A large number of microcracks were formed surrounding the central indentation hole, and they branched and linked together to form a complex three dimensional interconnected network. This allows enhanced energy dissipation via increased interface opening area within this confined volume. In addition, this complex interconnected network of microcracks also maintains the overall structural integrity of the shell by eliminating catastrophic large interface failures. Moreover, the orientation of microcracks was rotated away from the original horizontal direction by ~20° due to the large scale deformation. This rotational deformation of mineralized layers results in large amount of energy dissipation through local nanoscale inelastic deformations, as will be discussed later.

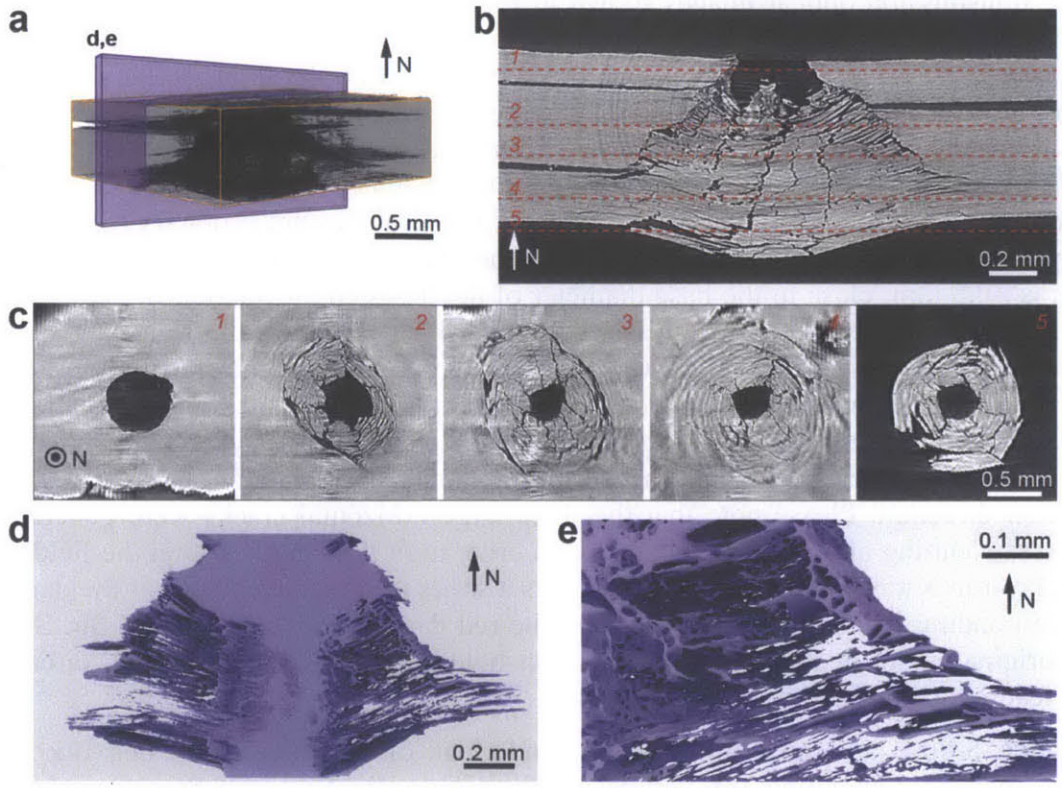

Figure 5-8| Three dimensional analysis of the macroindentation damage zone via μCT. a, 3D reconstruction of the entire damage zone using a transparency effect. **b**, A vertical slice of the damage zone with the orientation similar to the purple slice shown in (**a**). **c**, Five horizontal μ-CT slices of the damage zone from top to the bottom of the damage zone, as indicated by dashed lines 1-5 in (**b**). **d,e**, 3D negative rendering of the microcrack network generated within the damage zone.

I next provide direct experimental evidence of the formation mechanism of the complex interconnected microcrack network in the macroindentation damage zone. As shown in the μCT cross section of **Figure 5-9a**, multiple ligament-like bridges were formed along a crack. A representative three dimensional reconstruction of such ligament-like bridges shown in **Figure 5-9b** further demonstrates that these bridges are able to hold the two fractured pieces together even though the interface opening is greater than ~50 μm and the ligament itself undergoes local bending deformation. Since the resolution of μCT imaging (voxel size, ~2.84 μm) is much larger than the thickness of individual mineral layers, direct correlation of such bridge structures with connection centers is not possible. I then conducted electron microscopy imaging of finely polished cross sections of indentation residues to investigate this interface bridging mechanism at the building block level. **Figure 5-9c** and **d** show an SEM image of a horizontally propagated crack and corresponding schematic diagram with individual mineral layers highlighted. In this example, the crack was originally propagating horizontally from left to right along one organic interface. After encountering the connection center through which the two mineral layers are merged together, the crack was deflected to the top interface, forming a ligament-like bridge. Through this mechanism, the materials at the two sides of a propagating crack can be bridged together through this ligament. Clearly, the connection center plays a critical role in forming these ligament structures. We believe this is the primary mechanism responsible for forming the complex 3D interconnected microcrack network within the damage zone, which enables both

efficient energy dissipation through interface opening and maintains structural integrity of this highly mineralized bioceramic armor under large penetration loads.

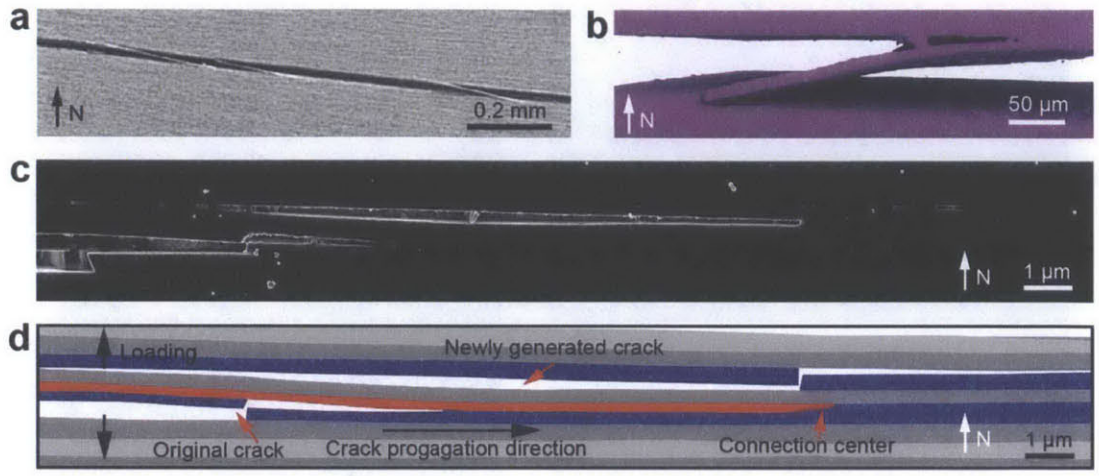

Figure 5-9| Crack bridging via connection centers. Vertical cross sectional μCT image (**a**) and 3D reconstruction based on μCT data (**b**) showing ligament-like bridge structures formed along cracks. SEM image (**c**) and corresponding schematic diagram (**d**) showing the crack was deflected by the presence of a connection center.

In addition to the formation of bridging ligament structures, the presence of connection centers also directly activates deformation mechanisms at smaller length scales, which are much more effective in energy dissipation relative to simple interface openings. As discussed in the previous chapter, *P. placenta* undergoes pervasive deformation twinning and other additional inelastic deformation mechanisms at the nanoscale, which results in a remarkably high energy dissipation per unit volume. As shown by a more commonly observed fracture surface (**Figure 5-10a-b**), many nanoscale inelastic deformations are observed along fracture lines, such as deformation twinning, nanocracking, and fragmentation. The crack front fractured the mineral building blocks once it encountered connection centers. This led to the formation of an inelastically deformed zone, which was characterized by its width, λ_{inel}, associated with each fracture line (**Figure 5-10c**). The multi-axial stress conditions surrounding the vicinity of the connection centers during crack propagation facilitates the generation of deformation twinning and promotes other nanoscopic energy dissipation deformation mechanisms. The cross sectional SEM image of the damaged zone clearly reveals a large number of deformation twinning bands (**Figure 5-10d**), which is also related to the rotation of mineral layers (**Figure 5-8**).

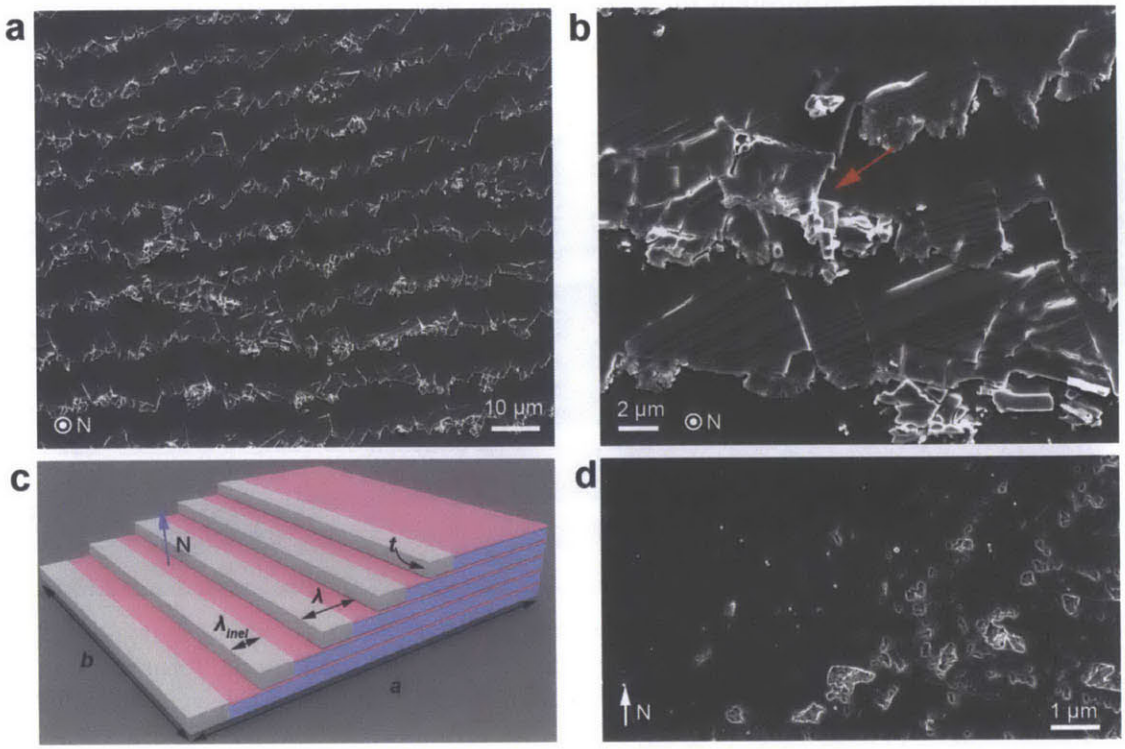

Figure 5-10| Nanoscale deformation mechanisms activated by connection centers. a, SEM image of a fractured surface where the fractured interfaces have regions which have undergone nanoscale deformations, such as nanocracking, fragmentation, and deformation twinnings. **b**, A high resolution SEM image showing nanoscale deformations surrounding a connection center (red arrow). **c**, Schematic diagram (revised from Figure 5.5a) including the nanoscale deformations associated with fractured layers. **d**, Deformation twinning bands observed in a polished cross section of a macroindentation residue.

5.3.3 Theoretical analysis of interface fracture toughness

A simple theoretical analysis of interface fracture toughness with the effects of connection centers can be formulated by considering the energy dissipation terms involved[202]. Here, I consider two laminate composite structures: 1) a simple laminate structure without connection centers, and 2) a modified laminate structure with connection centers. As illustrated in the schematic model in **Figure 5-10c**, the region of material which has undergone the permanent inelastic deformation has a characteristic width λ_{inel}. Other parameters are defined as following,

e_{int}: interface energy between two adjacent mineral layers (J/m^2);

e_{inel}: energy dissipation density of the mineral layers (J/m^3);

e_{cal}: surface energy along the cleavage plane of calcite (J/m^2);

For the simple laminate composite structure without connection centers, the interface fracture toughness is simply the interface energy between two adjacent mineral layers, i.e.

$$e_1 = e_{\text{int}}. \qquad \text{Equation 5-4}$$

For the laminate composite structure with connection centers, extra energy is dissipated through three additional mechanisms, 1) the inelastically deformed zone (λ_{inel}); 2) extra vertical surfaces generated along the fracture lines, and 3) extra interface opening associated with inelastically deformed zone. This can be represented as

$$e_2 = e_{int} + \frac{t\lambda_{inel}}{\lambda} e_{inel} + \frac{t}{\lambda} e_{cal} + \frac{\lambda_{inel}}{\lambda} e_{int}. \qquad \text{Equation 5-5}$$

By assuming $\lambda_{inel} \approx \lambda$ (**Figure 5-10a-b**), I can further approximate the interface fracture toughness of the laminate composite with connection centers as

$$e_2 = 2e_{int} + te_{inel} + \frac{t}{\lambda} e_{cal}. \qquad \text{Equation 5-6}$$

The magnitudes of the interface fracture toughness for the two composite structures can then be estimated with previously reported values of e_{int}, e_{cal}, and e_{inel}. The interface energy between two adjacent mineral layers (e_{int}) is approximated as that in nacreous structure (~1 J/m^2)[203], and the surface energy of calcite crystal along a cleavage plane is ~0.2 J/m^2 [204,205]. The energy dissipation density of the calcitic mineral layers is 0.29 ± 0.07 ×10^9 J/m^3 as determined in the previous chapter. The interface fracture toughness are then estimated as

$$e_1 = \sim 1 \text{ J/m}^2;$$
$$e_2 = \sim 100 \text{ J/m}^2.$$

Here we see that by incorporating the connection centers the highly mineralized shell of *P. placenta* is able to enhance the interface toughness by almost 30 times. We can roughly compare this number with the contribution from interface opening to the total energy dissipation. With the 3D information acquired from μCT data, we can estimate the total surface area generated through interface opening during one indentation cycle (**Table 5-1**). The total energy dissipation during one indentation cycle can be obtained by integrating the area under indentation curves. Thus, the contribution from interface opening for the total energy dissipation is about 0.5%. This number is broadly consistent with the theoretical estimations that the connection centers, through the activation of nanoscale deformation mechanisms with more efficient energy dissipation, are able to boost the total energy dissipation by ~100 times.

Table 5-1| Quantification of interface area generated and energy dissipation from macroindentation μCT data. "Total interface opening area generated" was calculated based on μCT data. "Interface energy" is taken from a literature value[203]. "Total energy dissipated by interface openings" is the product of "Total interface opening area generated" and "Interface energy". "Total energy dissipated" is calculated by integrating the area under the load-displacement curves of macroindentation experiment.

Parameters	Sample 1	Sample 2	Sample 3
Total interface opening area generated (mm^2)	51.3	73.7	88.8
Interface energy (J/m^2)	1	1	1
Total energy dissipated by interface openings (mJ)	0.05	0.07	0.09
Total energy dissipated (mJ)	13.96	13.96	13.96
Percentage of energy dissipated via interface opening (%)	0.37	0.53	0.64

5.4 Discussion and conclusions

The "brick-and-mortar" layered design consisting of nanoscale building blocks in the form of tablets, plates, and rods is one of the most common structural motifs of mollusk shells (e.g. the sheet and columnar nacreous, cross-lamellar, and foliated microstructures) [12]. A few studies also discovered out-of-plane interconnecting structures among adjacent mineral layers in some of these microstructures, including nanoscale mineral bridges[33] and screw dislocation-like structures in nacre[206–208].The mineral bridges, due to their small sizes (~10 nm in diameter), are proven to play a marginal role in the overall mechanical behavior of the shells[209]. The screw dislocation-like structures in nacre are believed to primarily function to provide biomineralization pathways for the formation of nacreous structures[206–208]. The screw dislocations allow the spiral growth of the orderly lamellar nacre and maintain the "levels of terraces of adjacent growth pyramids"[206] which leads the final closely packed lamellar structures. Yao *et al* suggested connection centers may contribute to the overall mechanical properties, although to date this hypothesis has not been tested[207]. We believe that the screw dislocation-like connection centers in nacre could play an important role in enhancing strength, but possibly not the fracture toughness. Due to the relatively small hexagon-shaped building blocks in nacre (~5-8 μm), cracks can simply bypass the connection centers by fracturing along the vertical boundaries of tablets without plastically deforming individual mineral tablets. In this process, only minimal extra energy is dissipated because the more efficient volumetric deformation mechanisms in the mineral tablets are not activated. This argument is supported by many electron microscopic images of the fractured surfaces of nacre, which are usually characterized by smooth and sharp vertical fracture surfaces along the boundary of adjacent tablets and little plastic deformation within mineral tablets[13,32].

In this work, I analyzed the large-scale distribution and mechanical behavior of the nanoscale screw dislocation-like connection centers in the highly optical transmissive shell of the bivalve *P. placenta*. Using electron microscopy mapping over large areas (~15 mm^2), I, for the first time, revealed that the foliated microstructure composed of calcitic elongated building blocks is integrated and reinforced as a three dimensionally interconnected architecture through screw dislocation-like connection centers. This result is in stark contrast to the previously assumed simple laminate structure of foliated microstructures like that of *P. placenta*. Moreover, associated pairs of connection centers with up and down signs were identified, and the distance (d) between them was fit well with a logarithmic distribution (number average: 574 ± 509 μm, n = 270, largest observed value ~3 mm).

Using a customized high load macroindentation experiment, I probed the mechanical behavior of the shell of *P. placenta* at the macroscopic scale, which provided deformation characteristics at an appropriate length scale to correlate with the distribution of connection centers. Synchrotron μCT scanning of the resulting damage zone demonstrated that the indentation residue was isotropic and circular without any radial cracking. This is a remarkable behavior for this biocomposite with fibrous building blocks (Chapter 3), because most of fiber-reinforced engineering composites typically exhibit anisotropic damage patterns directly related to their fiber orientations. This is true even when multiple laminae are stacked together with different directions to form the so-called plywood composites[201,210]. The μCT data clearly revealed that a complex 3D interconnected network of microcracks was formed within the isotropic damage zone, which not only produced a large area of interface opening for energy dissipation, but also maintained the structural integrity of the shell within the damage zone. This

process enabled effective damage localization and multi-hit capability. Moreover, both μCT and high resolution electron microscopy provided direct evidence that the interconnected network of microcracks was facilitated by the formation of micro-sized ligament bridges, which were directly associated with the screw dislocation-like connection centers.

Tablet pull-out has been identified as one of the key mechanisms which leads to the high toughness of the nacreous structure[49,50,53,61]. Theoretical analysis based on the shear force transfer from a continuous soft polymer matrix to the stiff tablets suggests that the aspect ratio between lateral dimension and vertical thickness, *s*, plays a critical role in determining the strength and toughness of the composites. Larger aspect ratios provide efficient load transfer to tablets and thus increase strength, while the fracture toughness may be reduced due to possible premature fracture of tablets. Therefore, aspect ratios slightly below the critical value as determine by $s_{critical} = \sigma_f/\tau_\gamma$ are considered to be optimal in providing both high strength and toughness. Indeed, structural measurements of various nacreous structures suggest a good agreement with this analysis[60]. Quantitative measurement of the building block geometry in *P. placenta* indicate that their aspect ratio is ~500, (length: ~140 μm; thickness: ~ 0.3 μm), which is more than one order of magnitude higher than the optimal value for the "pull-out" deformation mode ($s_{critical}$: ~25, σ_f: ~ 1 GPa; τ_γ: ~40 MPa). This analysis indicates that, unlike nacre, fiber pull-out is not the primary toughening mechanism of the foliated microstructure of *P. placenta*. Instead, the large aspect ratio of the building blocks, in conjunction with screw dislocation like connection centers, allow the formation of ligament bridges, which leads to high energy dissipation.

Considering both the nanoscale deformation mechanisms elucidated in Chapter 4 and the macroscopic deformation behavior in this chapter, we are now able to draw a full hierarchical picture of the mechanical behavior of the *P. placenta* shell. At macroscopic length scales (~mm), the laminate composite is able to form an interconnected complex network of microcracks surrounding the damage zone, which still maintains overall structural integrity while dissipating energy via a large amount of interface openings. Through these unique screw dislocation-like connection centers, the bioceramic armor is able to directly activate much more efficient pathways in dissipating energy at smaller length scales. As cracks have to fracture/break the mineral layers whenever crossing connection centers, local multi-axial stress fields are generated around the vicinity of connection centers. This initiates a series of nanoscale deformation mechanisms, such as deformation twinning, nanocracking, fragmentation, grain formation and reorientation, and amorphization. As suggested by our theoretical analysis, such direct activation of nanoscopic volumetric energy dissipation mechanisms via connection centers is able boost the interface fracture toughness by ~100 times. This is also broadly consistent with our surface area measurement-based energy dissipation analysis of the resulting macroindentation damage zone.

In-plane delamination failure along interfacial layers is one of the key issues for engineering laminate composite materials, which greatly affects the fracture energy adsorption capability and damage tolerance, particularly under out-of-plane impact loading conditions[202,211,212]. A number of interfacial control strategies have been proposed and developed to enhance fracture toughness while still maintaining a relatively high out-of-plane strength. In particular, placing reinforcement structures along the thickness direction of laminate composites, such as stitching fibers, steel wires, or whiskers, has been shown to improve the interfacial toughness and reduce delamination [212–214]. Moreover, improved out-of-plane strength can be also achieved with this three-dimensional composite structure. However, addition of these vertical delamination resistors

typically results in damage of the original laminate structure, entrapment of voids, and formation of regions with local stress concentrations [212].

Delamination is also one of the major problems of laminate-based transparent armor materials. Common low-velocity impacts and environment degradation often result in delamination.[8]. Moreover, reinforcement along the vertical direction through structures such as stitching fibers is simply impossible since most of transparent armors materials are made from brittle ceramic materials, for which drilling is generally not a good idea! Even if we succeeded in placing vertical reinforcement structures, optical transparency would certainly be compromised due to light scattering and/or absorption by the addition of secondary phases and generation of additional interfaces.

The unique screw dislocation-like connection centers discovered in this work provides an effective solution to minimize delamination by interconnecting the entire laminate structure in three dimensions. Unlike stitching with additional fibers or wires in a discrete manner, this type of out-of-plane reinforcement via connection centers utilizes the same material as the original laminate structure, minimizes local structural discontinuities, and introduces minimal structural modifications to the original layered structure. We believe this unique structural design principle is particularly relevant to transparent armor systems. With these connection centers, the anti-delamination performance can be improved while still maintaining high optical transparency with minimal alternation to the laminate structure.

In addition to delamination resistance, distribution of connection centers with specific densities and/or signs allows one to control the composite structure locally without sharp discontinuities. One possible application is related to edge delamination, which is induced by the 3D inter-laminar stresses developed at stress-free edges of discontinuities. Edge delamination is one of the main failure modes for ceramic coatings deposited on metal substrates due to their large thermal mismatch after cooling down to room temperature[215]. As shown in this work, the interface fracture toughness is directly related to the density of connection centers; therefore, it is possible to minimize edge delamination failure by placing more connection centers around edges. Another possible application of controlling density and signs of connection centers is local thickness control. Currently, variation of local thickness in laminate composite materials is usually achieved by simply removing lamina in the area of thickness reduction, so-called ply drop-off[211]. This configuration produces interface discontinuities which can further lead to edge delamination[211]. This problem can be potentially minimized by placing connection centers with specific signs so that the local thickness can be controlled without generating sharp interface discontinuities.

In this chapter, I presented a detailed investigation of a unique structural feature, i.e. screw dislocation-like connection centers, in the foliated structure of the *P. placenta* shell. Large area (~15 mm^2) mapping and analysis indicated that this structural motif integrates the entire laminate shell to form a 3D interconnected structure, as opposed to a simple laminate with discrete layers as was previously thought. Experiment-based analysis of the total interface fracture toughness showed that the connection centers are able to improve the interface fracture toughness by approximately two orders of magnitude as compared to simple laminates without connection centers. High-resolution synchrotron μCT scanning of macroindentation residues allowed us to visualize the damage zone in 3D. Combining these results with electron microscopy studies, we confirmed that connection centers play a critical role in bridging and deflecting microcracks, maintaining the entire structure as an integrated system and forming a complex 3D network of

microcracks to dissipate energy. Moreover, quantitative measurements of the surface area generated by the interface opening process allowed me to decouple the contributions of energy dissipation from two sources, interfacial energy dissipation via interface opening (debonding) and volumetric energy dissipation via plastic deformation. I found that ~1-5% of the total energy dissipation results from interface opening, which was consistent with my theoretical analysis. The total energy dissipation can be improved by up to ~100 times through connection centers distributed in interfaces. This two-order of magnitude enhancement results from the activation of nanoscale plastic deformation mechanisms, which are much more efficient in energy dissipation, as revealed in last chapter.

The direct linkage between the macroscopic and nanoscopic scales provides unique and effective pathways for toughness enhancement. As compared to nanoscale deformation mechanisms, the formation of interconnected microcrack network through ligament bridges via connection centers is more material-independent. The activated nanoscale deformation mechanisms certainly rely on the specific materials used in the system. Nevertheless, this design strategy can be potentially applied for novel composite structure designs, possibly future laminate-based transparent armor systems, to enhance fracture toughness and damage tolerance.

Chapter 6 Functional structural color in the mineralized shell of the blue-rayed limpet, *Patella pellucida*

This chapter is based on a collaborative work and is now under review for publication: Li, L.*, Kolle, S.*, Kolle, M., Weaver, J. C., Ortiz, C. & Aizenberg, J. Functional structural color in the mineralized shell of the blue-rayed limpet, *Patella pellucida*. (*Equal contribution).

6.1 Introduction

Through the course of evolution, many species have developed ingenious ways to interact with light in order to create unique visual displays[102,107,108,112,216,217]. Pigment-based spectrally selective absorption empowers air-borne, terrestrial, and aquatic creatures to display mostly red, orange, yellow, and more rarely green or blue hues in their skins, plumages, scales or shells[98–100]. In contrast, nano or micro-periodic organic structural architectures have evolved to interfere with light where strong metallic reflections and iridescent colorations are required or the pigmentation for a specific hue is unavailable[99,103]. Most natural occurrences of blue color, for example, are due to the interaction of light with such biological photonic systems. Structural colors have been found in the feathers of peacocks and other birds[104–106], the wing scales of butterflies and moths[107,108109], the exoskeletons of beetles[85,110], and even in the skins of birds and mammals[88], shedding light on a stunning diversity of biologically evolved light manipulation mechanisms.

Despite the fact that structural color is also extremely common in marine ecosystems, with representatives including algal, invertebrate, and vertebrate species, few examples have been well characterized, and in-depth investigations have been limited to metallic fish scales[87,218,219], the reflecting setae of crustaceans[220] and polychaetes[221,222] and, most notably, the camouflage and coloration control mechanisms of cephalopods that rely on the intriguing interplay of localized dynamic light-absorbing chromatophores, iridescent iridophores, and strongly scattering leucophores[101,223,224].

The majority of these structurally diverse, functional biophotonic architectures of different organisms have been shown to be comprised of highly ordered organic materials, including cuticle[85], chitin[86], guanine[87], collagen[88], keratin[89,90], and proteins such as reflectin[91]. Being the most prominent example of a biologically produced inorganic iridescent material, nacre's diverse color palette originates from light interference within its layered composite structure of microscopic aragonite tablets. The structural color is only apparent in the interior of the shell with little to no external visibility. Most likely mechanical robustness[45] is the primary biological purpose of this laminated microstructure.

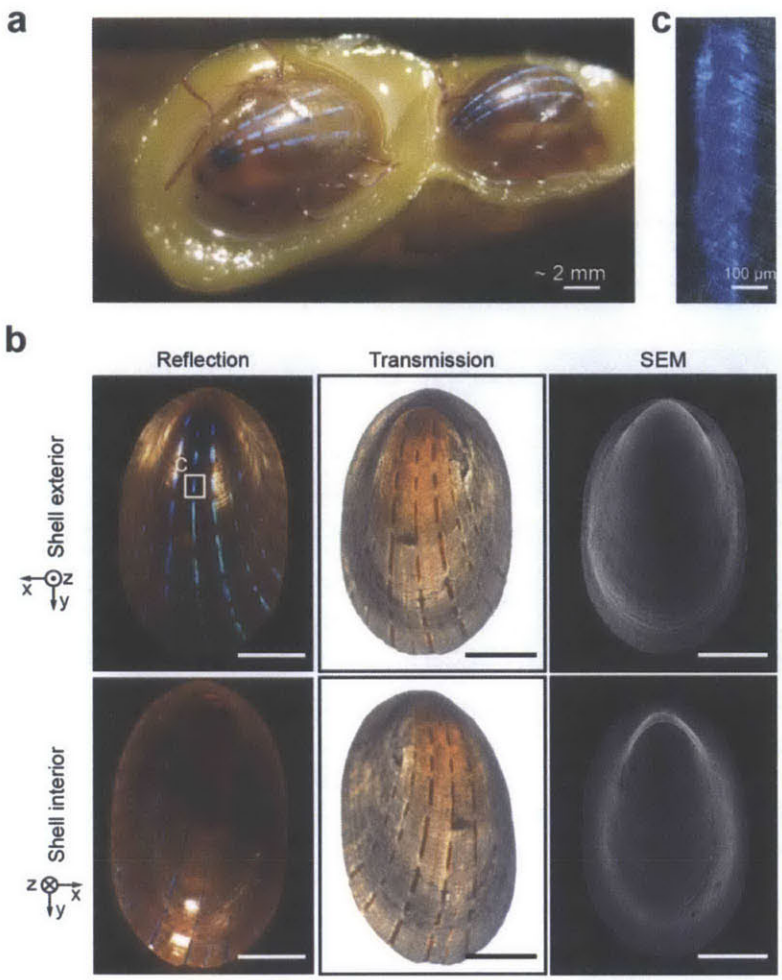

Figure 6-1| The blue-rayed limpet *Patella pellucida*. a, Two blue-rayed limpets in their natural habitat on the stipe of a macroalgae. The surrounding light-yellow regions show exposed algal tissue eaten away by the limpets. **b**, Optical (left and middle panels) and scanning electron micrographs (SEM, right panel) showing the reflection and transmission of light from the shell exterior and interior and the surface topography of the shell's exterior and interior. All the scale bars in (**b**) are 2 mm. **c**, Reflection optical micrograph of a single stripe.

In this chapter, I describe a localized, highly sophisticated, structurally complex, but entirely mineralized localized photonic system embedded within the continuum of a translucent mollusk shell that lies at the origin of the striking optical appearance of the blue-rayed limpet, *Patella pellucida*. This organism displays a dramatic array of thin bright blue stripes along the length of its translucent shell (**Figure 6-1a**). Ranging from coastal Norway and Iceland south to Portugal and west to the Canary Islands[133,134], this species occupies the lower intertidal and subtidal zones of rocky shores (depth < 27 m), where it populates the fronds and stipes of *Laminaria*[177] and other species of large macroalgae. The limpets, occurring both solitarily and in groups, feed on the kelp leaving distinctive circular feeding marks[135](**Figure 6-1a**). The blue stripes first appear as a spotty, interrupted pattern in juvenile limpets (shell length, ~2 mm), and become more continuous as the animal grows, although the width of the stripes remains relatively constant (0.1 - 0.2 mm, **Figure 6-1b-c**). The stripe patterns appear to be unique from limpet to limpet, and the

stripe color varies from deep blue to turquoise among different individuals. Scanning electron microscopy (SEM) analysis of the exterior and interior surfaces of the shell reveal no distinctive morphological features coinciding with the blue stripes, suggesting that the source of the color is subsurface (**Figure 6-1b**). Immersion of a mechanically partially damaged stripe in water or index-matching oil results in a variation of the color towards higher wavelengths or a complete disappearance or the reflected hue, respectively (**Figure 6-2**), indicating a color of structural origin.

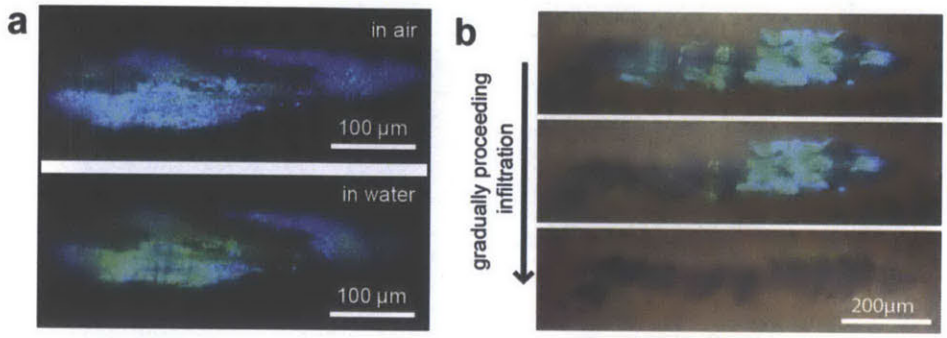

Figure 6-2| Experimental evidence indicating the structural origin for the blue stripes. a, A single, partially mechanically damaged stripe shows a pronounced variation of the reflected hue from blue in air towards green when immersed in water. **b**, Infiltration of index-matching oil into the interstitial spaces of the multilayer suppresses the blue reflection and reveals the underlying absorbing particles (*Experiments by Mathias Kolle*).

6.2 Methods

6.2.1 Experimental methods

Limpet specimens were collected along the coastlines of St. Abbs (Scotland), the Farnes Islands (North England), Rhosneigr, and Fishguard (Wales) in the United Kingdom and were stored under either dry conditions or in 40% ethanol.

For SEM studies using a Helios Nanolab 600 Dual Beam (FEI, OR), the shells were coated with an ultra-thin carbon layer to reduce charging effects prior to imaging. Cross-sectional samples and TEM samples were prepared using Focused Ion Beam (FIB) milling with the same system. Final polishing using the ion beam at 2 kV was critical for obtaining a clean surface with a minimum amount of damage. TEM imaging with typical bright-field, dark-field, and SAED techniques was carried out using a JEOL 2011 operated at 120 kV. High-resolution TEM imaging was performed on a JEOL 2010F operated at 200 kV.

AFM imaging was performed with a Digital Instruments Multimode SPM IIIA (Veeco, CA) (NANOSENSORS Si TMAFM cantilevers, PPP-NCHR-10).

X-ray nanotomography was performed at Beamline 32-ID (8.381 keV, APS, Argonne National Laboratory, US) with samples prepared from FIB cutting (~25×25×10 µm). The projection slices (pixel resolution, ~13.4 nm) were reconstructed using Xradia TXMReconstructor.

Spectrally resolved intensity maps were acquired for single stripes in a modified Leica DMRX optical microscope with a 20x objective where an additional photoport allowed for the collection of light reflected from the specimen into an optical fiber of 50μm diameter. Spectra were collected from a spot of 2 μm diameter with collection cone half angle of 33° and the corresponding maps were obtained by laterally scanning the sample in 2 μm steps while maintaining the specimen in constant focus.

Quantitative spectral measurements for the determination of the stripes reflectivity in water were performed by using a 63x water immersion objective with numerical aperture NA = 1.0 allowing for the collection of spectra from spots of ~ 2 μm diameter in a polar angular range of 0° to 50°.

Optical diffraction of the samples was studied using a modified Olympus BXFM microscope, where by incorporation of a Bertrand lens, scattering of a specimen under quasi-plane wave illumination, achieved via an additional photo-port, was analyzed by focusing on the backfocal plane of the objective. A high numerical aperture oil immersion objective (Leica PL APO 100 x / 1.4 - 0.7 OIL) was used to increase the observable angular range.

6.2.2 Theoretical methods

Theoretical calculations of the blue stripes' reflectivity were based on an iterative technique for the determination of the reflection coefficients of planar stratified media[225] implemented in a custom-made MatLab script. In order to account for the illumination and collection conditions resulting from the use of a water immersion lens with numerical aperture 1.0, for each of the 500 calculation runs we determined the average reflectivity $\langle R \rangle$ of non-polarized light as the weighted average $\langle R \rangle = \sum_{NA_i=0,\Delta NA=0.05}^{NA_{max}=1.0} \frac{{NA_i}^2-{NA_{i-1}}^2}{2\,{NA_{max}}^2} \cdot \left(R_{\parallel}(\theta(NA_i)) + R_{\perp}(\theta(NA_i))\right)$, with $\theta(NA_i) = \sin^{-1}\frac{NA_i}{n_{water}}$ and the reflectivities $R_{\parallel}$ of parallel and $R_{\perp}$ of perpendicularly polarized light. We also factored in the Gaussian intensity distribution of incident light in the back focal plane of the objective that we mapped prior to the spectroscopic experiments and calculations.

The reflection curve (shown in blue in **Figure 6-12a**) is the dataset re-plotted from **Figure 6-8d**. The absorption curve of water (black curve) was calculated from spectroscopic data reported in the literature (reference 54 in the paper). In **Figure 6-12b**, the spectral irradiance at sea level (0 m depth) is the ASTM standard, (ASTM G173 – 03, 2012). All other irradiance curves for lower depths were calculated based on this dataset taking into account the water absorption (black curve in **Figure 6-12a**). For each depth the reflected irradiance of the limpet's blue stripes was calculated by multiplying the corresponding incident irradiance data with the average reflectivity spectrum shown in **Figure 6-12a** (blue curve).

6.3 Results

6.3.1 Ultrastructural features of the entire shell

The *P. pellucida* shell consists of at least four different microstructural types in addition to the unique photonic multilayer as discussed in detail in the following sections (**Figure 6-3**). As shown in **Figure 6-3d**, on top of the photonic multilayer, an outer layer (~20-30 μm) composes of laminate-like structures with their boundaries much more irregular as compared to structures

like nacre and cross-lamellar structure. Below the photonic multilayer and colloidal particles, the majority of the shell is made of cross-lamellar layer (>100 μm, **Figure 6-3c,e**). As compared to typical cross-lamellar structures which have straight boundaries between corresponding hierarchical orders, the boundaries between regions with different crystal orientations are irregular in this case (**Figure 6-3c,e**). In addition, prismatic and complex cross-lamellar layers are observed further towards to the interior of the shells (**Figure 6-3c,f,g**).

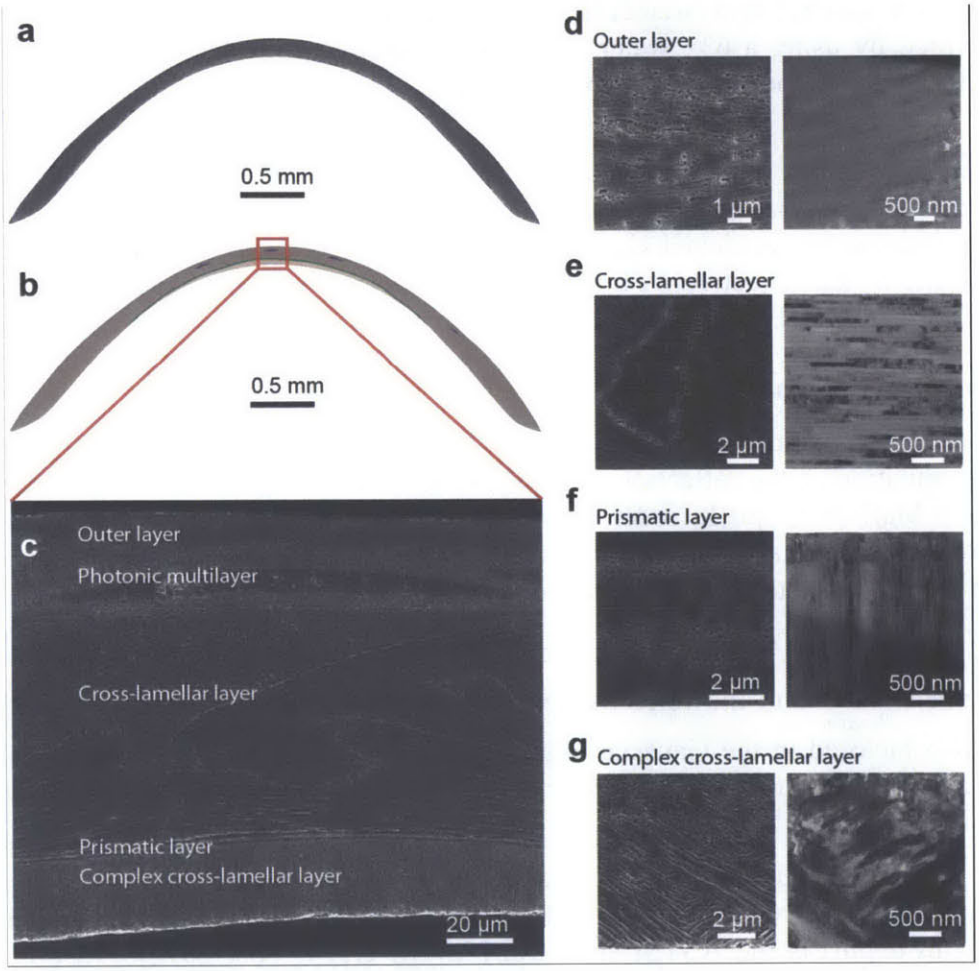

Figure 6-3| Microstructures observed in the shell of blue-rayed limpet. SEM image (**a**) and corresponding schematic diagram (**b**) of the entire shell cross-section. (**c**) Enlarged SEM image of the shell cross-section showing six observed microstructural types: from shell exterior to interior, irregular lamellar layer, photonic multilayer, colloidal particles, cross-lamellar layer, prismatic layer, and complex cross-lamellar layer. Corresponding high magnification SEM and TEM images for the four non-photonic microstructural types are shown in (**d-g**).

6.3.2 Ultrastructure of the photonic components

In the zones where blue stripes are present, a distinct multilayered structure (**Figure 6-4a,b**) with regular gap spacing between individual lamellae (**Figure 6-4c**) is located at a depth of 10–20 μm beneath the outer irregular lamellar layer, where the mineralized building blocks are closely packed without any detectable spacing. The maximum thickness of this multilayer region

is ca. 7–10 μm at the center (corresponding to 40–60 layers) and gradually decreases in thickness towards the edge of each stripe (**Figure 6-4a**). Beneath this multilayer region, a disordered array (~ 5 μm in thickness) of colloidal particles is observed (**Figure 6-4a-b and Figure 6-5**). Its lateral width (x-direction in the reference coordinate system) is found to be just short of matching that of the multilayer, leaving the stripe edges free of particles underneath. This distinctive combination of structural features specifically coincides with the location of the blue stripes and is clearly visible in SEM images of fractured shells prepared from freshly collected specimens, excluding the possibility that these features represent polishing-induced artifacts (**Figure 6-4d**). The width of the multilayer region (ca. 100 μm) is consistent with the width of the blue stripes observed in optical microscopy, further indicating that this is the structure responsible for the optical effects.

Transmission electron microscopy (TEM) imaging of thin sections from the multilayer structure prepared using focused ion beam milling (FIB) reveals that the individual lamellae in the multilayer microstructure have a thickness of 113 ± 11 nm (Average ± SD, n = 52) with the inter-lamella gap spacing measuring 53 ± 7 nm (n = 29) (**Figure 6-4c-e**). Under physiological conditions the space between lamella is likely occupied with water only or a low density heavily hydrated organic material. The constant thickness and spacing of the lamellae are maintained throughout the entire multilayer region. In particular, the thickness of the multilayer region decreases toward its edges by reducing the number of lamellae rather than the thickness of individual lamella or the spacing between them.

In general, the multilayer lamellae do not adopt a single global orientation parallel to the shell surface. Instead, the multilayer structure exhibits a complex zig-zag-like architecture with the multilayer surface normal spanning a polar angle θ' of about 16° - 18° with respect to the overall shell surface normal (**Figure 6-4b**, **Figure 6-9c-d** and explanations below). This is in contrast to most of the photonic multilayer systems found in nature, including the layered morphologies observed in jewel and scarab beetles[226–229]. When viewed in cross-section, the characteristic angle between lamellae forming the zig-zag pattern is 144.4° ± 3.0° (n = 52). Edge-dislocation-like interconnecting junctions and nanoscopic bridges linking adjacent lamellae observed within this complex zig-zag structure appear to reinforce the mechanical stability of this porous layered architecture (**Figure 6-4f,g**)[4,200]. Please see **Movie 2 in Appendix B** for the illustration of the hierarchical structure of the photonic multilayer.

Figure 6-4| The photonic architecture in the shell of the blue-rayed limpet. a,b, SEM images after sectioning and polishing along the white line of the limpet shell in the upper left inset (the center part of the polishing line marked in red represents the area of the cross-section shown in (**a**)). The two different structural components - a regular nanoscopic multilayer on top of a disordered array of colloidal particles (marked with the white dashed lines) - are embedded within the normal densely-packed lamellar microstructures (which lack the detectable gap spacing present in the multilayer region). The characteristic angle θ' between the local multilayer surface normal and the shell surface normal is marked in two positions (b). **c**, Transmission electron microscope (TEM) image showing the regularity in width and spacing of the mineralized lamellae in the multilayer region. **d**, SEM image of a fractured cross section of the multilayer structure. **e**, Distribution of calcite layer thickness and gap width within the photonic multilayer. TEM images of dislocation-like connections (**f**) and small inter-layer mineral

bridges, marked by white arrows (**g**), which might contribute to the structural integrity of the photonic multilayer architecture.

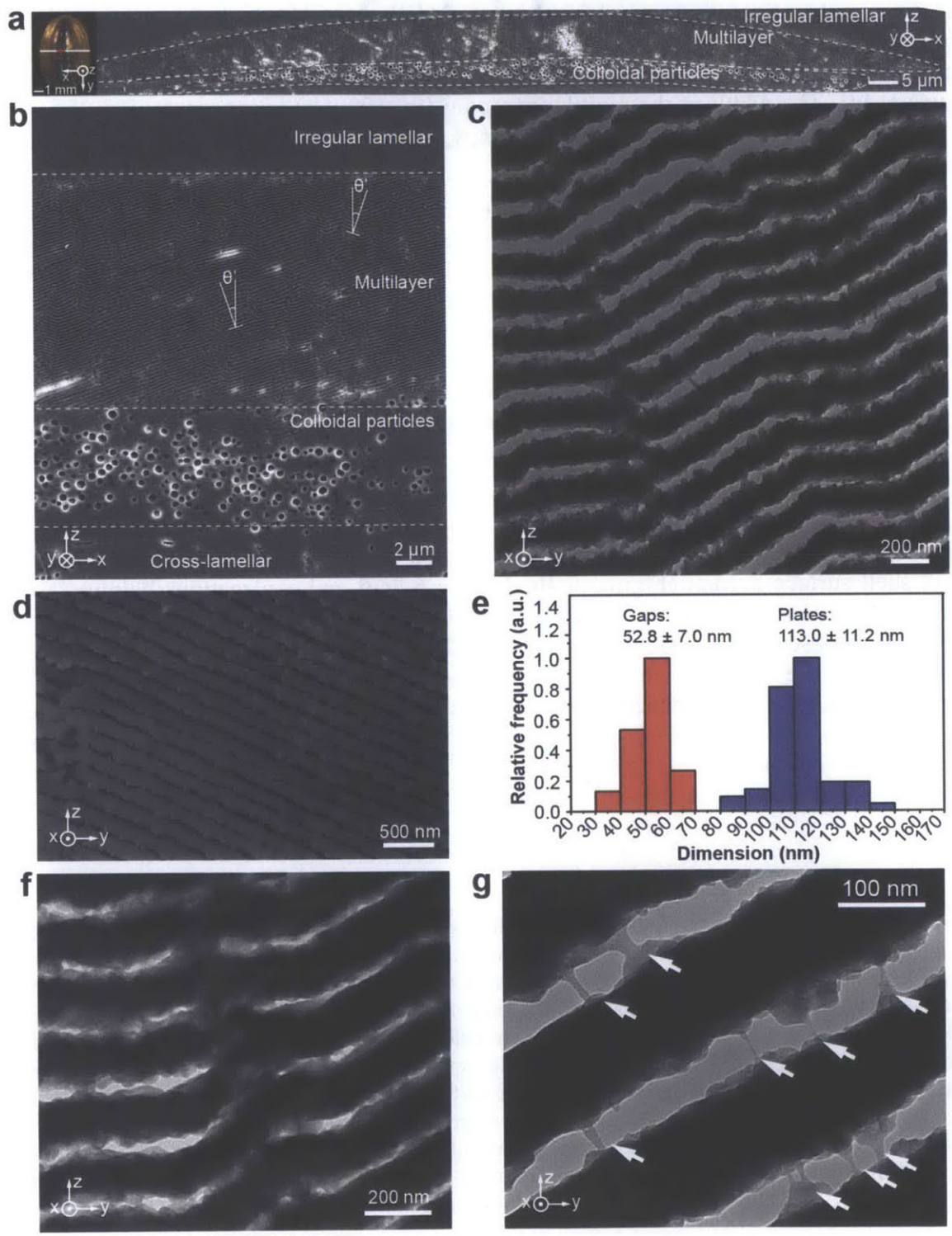

Please refer to page 89 for figure captions.

Another unique feature of the blue-rayed limpet's photonic system is the presence of disordered arrays of colloidal particles immediately beneath the multilayer structure (**Figure 6-4b, Figure 6-5**) with an average particle diameter of 300 ± 100 nm (n = 349, **Figure 6-5b**). Using X-ray nanotomographic reconstructions (see **Methods**), the colloidal particle array was segmented in the z-direction and the location of each colloidal particle was spatially mapped relative to its neighbor. Using this technique, a flattened z-stack that showed the plan view distribution of the colloidal particles suggested almost complete areal coverage (**Figure 6-5a**). Atomic force microscopy performed on intact colloidal particles in fractured shell cross-sections revealed a complex surface morphology, resembling the agglomeration of smaller granules (~50 nm in diameter, **Figure 6-5c**).

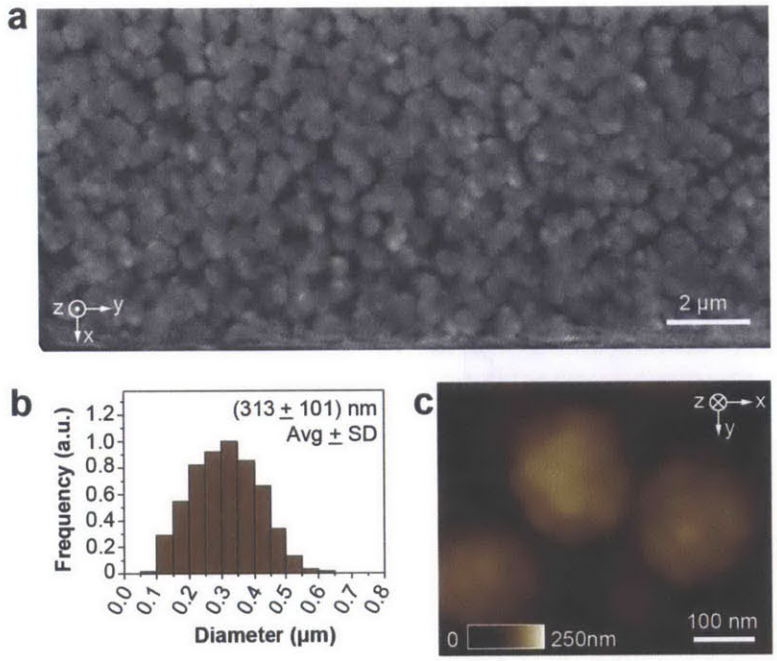

Figure 6-5| Morphology of colloidal particles underneath the photonic multilayer. a, Plan-view z-stack overlay showing the distribution of colloidal particles underneath the multilayer, based on X-ray nanotomography reconstructions. **b**, Size distribution of the colloidal particles. **c**, AFM height image of the intact colloidal particles, demonstrating the non-faceted fused-granules surface morphology.

6.3.3 Crystallographic characteristics of the photonic components

In most mollusk shells, crystalline calcium carbonate (either in the form of calcite, aragonite or a combination thereof) is the primary building material[4,24]. In particular, a variety of limpet species demonstrate the co-presence of both calcite and aragonite in their shells[230,231]. This is the case for the blue-rayed limpet as confirmed by whole shell powder X-ray diffraction (**Appendix A, Figure A-6**). Local crystallographic characteristics in the multilayer and surrounding regions were studied using selected-area electron diffraction (SAED) and high-resolution TEM imaging (**Figure 6-6 and Figure 6-7**). Diffraction patterns acquired from multiple adjacent multilayer

lamellae reveal well-defined single crystal-like diffraction patterns consistent with the calcite polymorph. Multiple closely-matched electron diffraction patterns acquired in the transition zone between the multilayer and the top irregular lamellar microstructure indicate that the photonic multilayer not only preserves the crystallographic phase but also the orientation from the surrounding non-photonic regions, despite the presence of 50 nm wide gaps in the multilayer and 300 nm sized particle beneath it (**Figure 6-6a,b**). This conservation of crystal orientation across multiple types of microstructures is known from other mollusk shells[39]; however, most of these microstructures are densely packed with the respective building blocks without such gap spacing or spherical particles being incorporated in the crystals.

Lattice imaging of the calcitic lamellae using high-resolution TEM further illustrates their crystalline nature (**Figure 6-6c**), and corresponding Fast Fourier Transforms (FFT, **Figure 6-6c, inset**) were indexed to the [010] zone axis of calcite. In some regions, a thin amorphous layer with thickness of ca. 10 nm was observed on the surface of the crystalline lamellae (**Figure 6-6c**), whereas in other areas, the lamellae are entirely crystalline (**Figure 6-6d,e**). High-resolution TEM images and corresponding FFT patterns obtained from two neighboring lamellae further confirm the local crystallographic co-alignment in the multilayer region (**Figure 6-6f,g**). This crystallographic continuity across lamellae is also manifested by the continuous lattice fringes running across the mineral bridges between adjacent lamellae (**Figure 6-6h**).

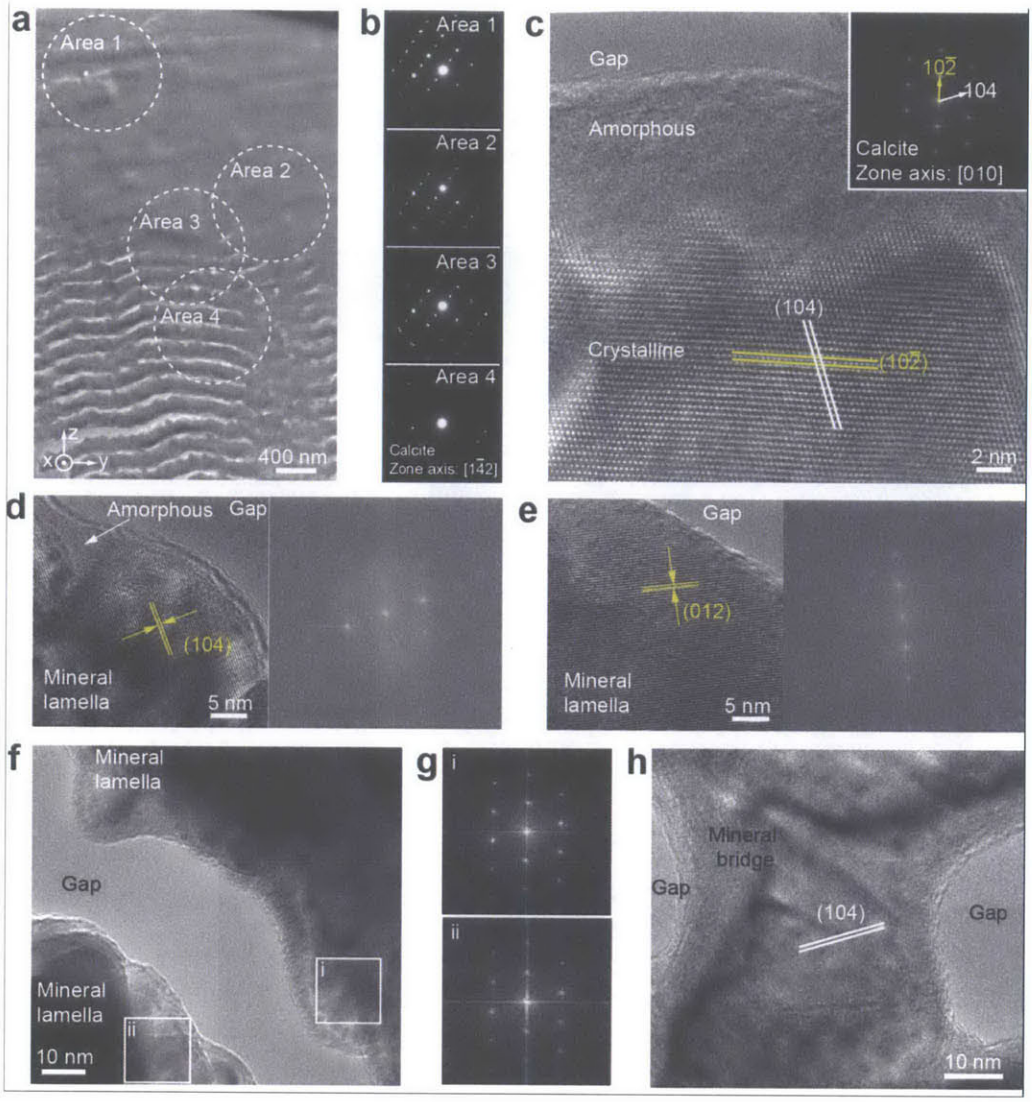

Figure 6-6| Crystallographic composition of the photonic architecture. a, TEM image of the upper transition zone between the dense lamellar matrix and the photonic multilayer. **b**, Selected area electron diffraction (SAED) patterns acquired from the areas marked in (**a**), which are all indexed to calcite with zone axis of [1$\bar{4}$2]. This demonstrates that both the crystallographic phase and orientation are conserved across the transition zone. **c**, High resolution TEM image of the calcite crystal lattice in a single lamella. The top ~10 nm of the lamella appears to be amorphous while the remainder is crystalline. The inset shows the corresponding Fast Fourier Transform (FFT) pattern of the crystalline region (calcite with zone axis, [010]). **d,e**, High-resolution TEM images and corresponding FFT patterns (insets) of the crystalline plates in the photonic multilayer structure, where the crystalline regions fully extend to the surface of the plates. A small amorphous region in A is indicated. **f**, Parts of two lamellae from the photonic multilayer that are separated by a gap. FFT patterns of the adjacent edges (i, ii) are displayed in the (**g**), showing that the crystal orientation is preserved across the gap. **h**, High resolution TEM image showing a mineral bridge connecting two lamellae within the photonic multilayer, with the crystal lattice translating from one lamella to the next via the connection.

The crystalline mineral phase continues to be conserved in the matrix surrounding the disordered array of particles beneath the multilayer structure (**Figure 6-7a,b**). In contrast, electron diffraction measurements on single colloidal particles reveal a characteristic amorphous diffraction halo, confirming their non-crystalline nature (**Figure 6-7a,c**).

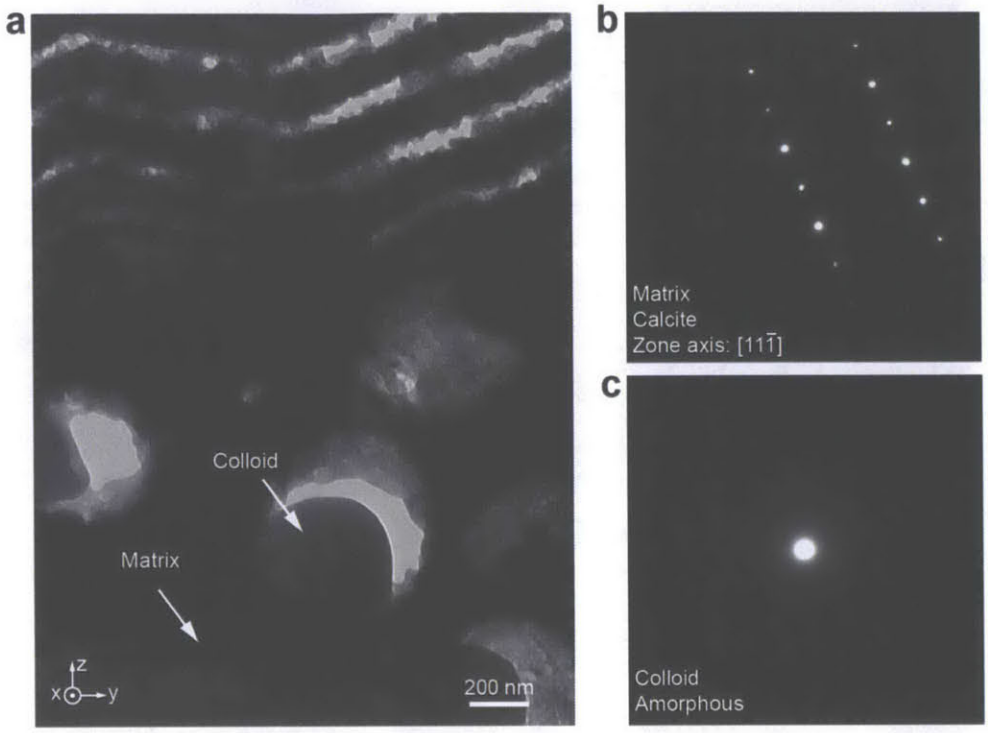

Figure 6-7| a, TEM image of the transition zone between multilayer and colloidal particle array. (**b** and **c**) SAED patterns of the surrounding crystalline matrix and amorphous colloids obtained from areas indicated in (**a**).

6.3.4 Optical properties of the photonic multilayer

To understand the optical interplay between the multilayer architecture and the underlying colloidal particle array, we investigated several blue stripes using optical microscopy, micro-spectroscopy, and diffraction microscopy. All optical measurements were performed with the shells being immersed and equilibrated in water to emulate the organisms' natural environment. The reflection of a typical stripe observed from the shell exterior was imaged and spectrally mapped with a resolution of 1 μm (**Figure 6-8a**). The stripe was strongly reflecting and very conspicuous in the wavelength range of 450–570 nm as compared to the surrounding region (**Figure 6-8a, middle**) and was indistinguishable from the neighboring areas at higher wavelengths (600–800 nm, **Figure 6-8a, right**).

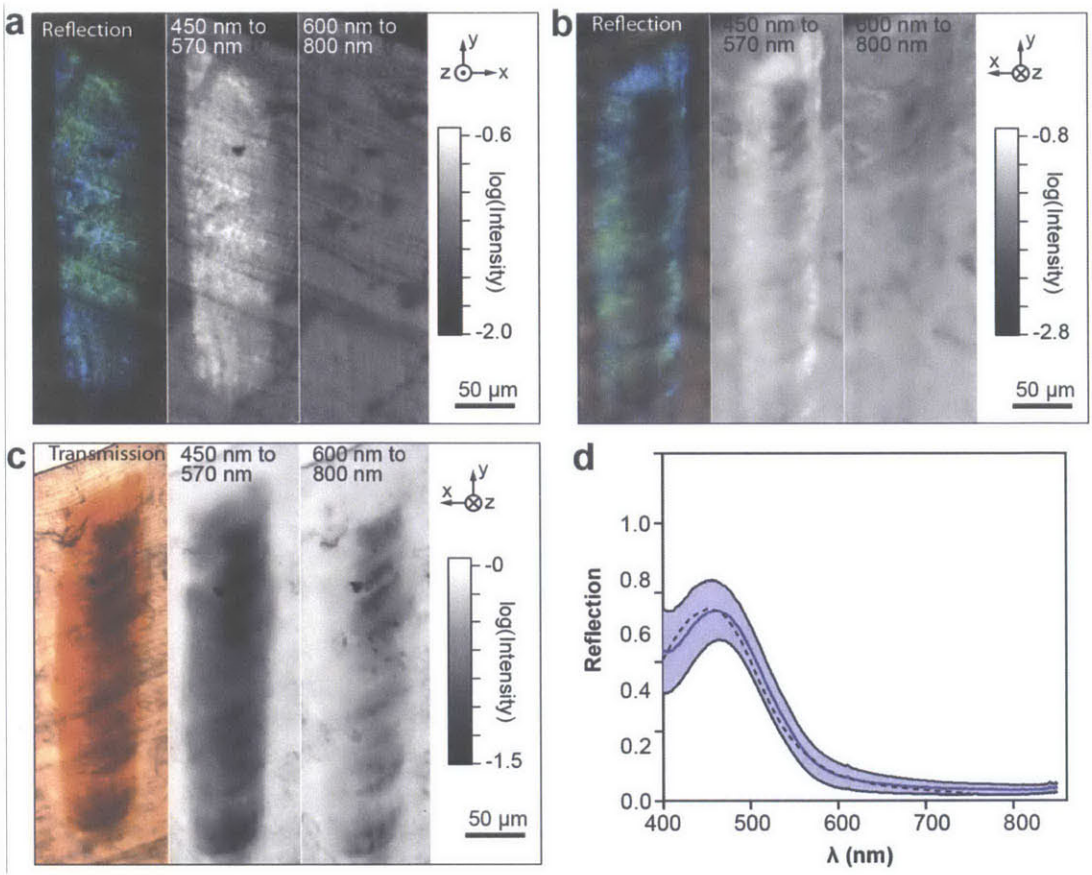

Figure 6-8| Optical properties of the photonic multilayer. a,b, Reflection optical micrograph of a single stripe (left) in comparison with two intensity maps of light reflected in the range of 450–570 nm (middle) and 600–800 nm (right) wavelength. The experiment was carried out from (**a**) the exterior and (**b**) interior side of the shell. **c**, Transmission optical micrograph of a single stripe (left) in comparison with two intensity maps of light transmitted in the range of 450–570 nm (middle) and 600–800 nm (right) wavelength. The experiment was carried out from the interior of the shell. **d**, Reflection spectrum of a stripe in water, referenced against a 97% reflective silver mirror. The blue line represents the average reflectivity with the standard deviation being visualized by the blue shaded area (7 limpets, 10–20 measurements on each). The black dashed curve represents theoretical calculations of the blue stripes' reflectivity that results from 500 calculation runs of a multilayer stack with 40 calcite lamellae (n = 1.59) and water filling the interstitial gaps (n = 1.33) with an average lamellae thickness of 113 ± 11 nm and a spacing of 53 ± 7 nm determined from TEM images

Under water, the reflectivity of the blue stripes amounts to 55% ± 10% (average and standard deviation, 7 limpets, 10–20 measurements on each, **Figure 6-8b**), as compared to a silver reflector (>97% reflectance in the spectral range of interest). The observed spectral distribution is very well correlated with the theoretical reflectivity calculations that were performed based on a multilayer consisting of calcite lamellae in water with the average thickness, spacing and standard variations experimentally measured in the limpet's layered architecture. This observation further supports the hypothesis that the main constituent in the multilayers interstitial space is aqueous. In extreme cases, a local reflectivity exceeding 75% could be observed.

The stripes scatter blue and green light over a broad angular range. Angle-dependence and wavelength-selectivity of the scattering was further elucidated by imaging a stripe's angular scattering profile under normal light incidence using diffraction microscopy (**Figure 6-9a**).

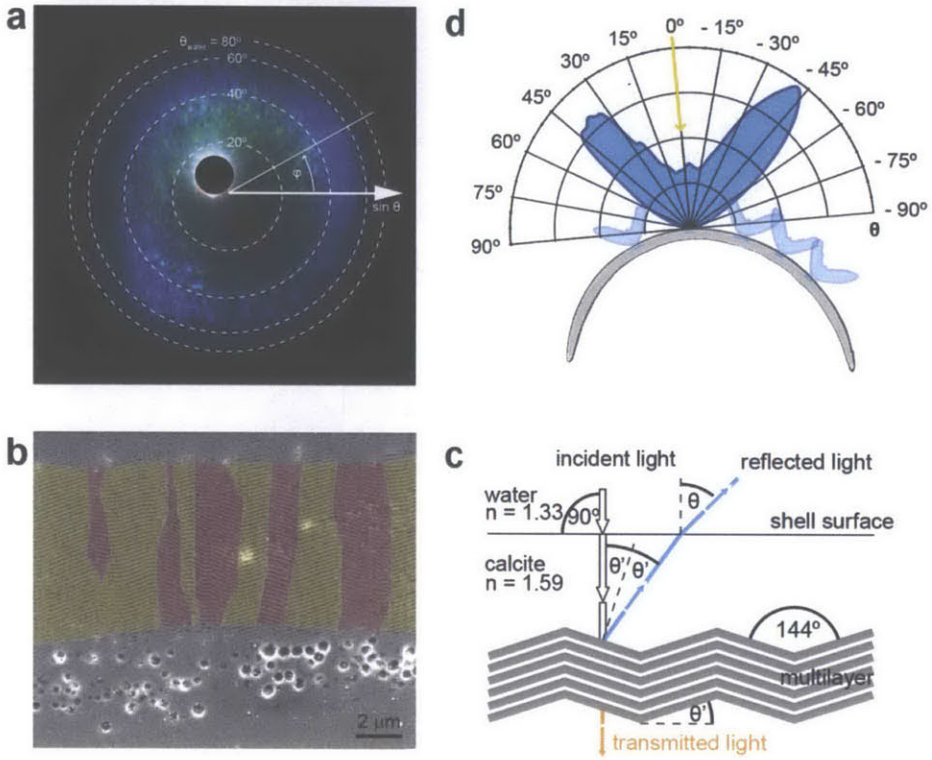

Figure 6-9| Optical properties of the photonic multilayer. a, Diffraction microscopy image visualizing the scattering upon light reflection from a single stripe, where each pixel represents the intensity of light as a function of its propagation direction after reflecting off the stripe as characterized by the polar angle θ (measured from the sample normal) and the azimuthal angle φ. **b**, Domains in the zig-zag multilayer architecture. Two different multilayer normal orientations of $\theta' \approx -16°$ (pink) and $\theta' \approx 16°$ (yellow) with respect to the shell normal surface are visualized in this scanning electron micrograph. **c**, Schematic representation of light reflection from the limpet's photonic zig-zag multilayer structure for light normally incident on the shell surface. According to Snell's law, the angle of highest reflectivity in water ($\theta \approx 40°$) corresponds to an angle of $\approx 32°$ (with respect to the incident light) in the calcite shell suggesting an inclination of the reflecting multilayer of $\theta' \approx 16°$ with respect to the shell surface, which matches well with the observed characteristic angle of around 144° between the multilayer lamellae. **d**, Polar plot of reflection intensity showing that each stripe reflects light in a broad angular range of up to more than 60° cone angle. Due to the different orientations of the stripes along the curved shell, part of the stripe pattern can be seen from almost any direction.

Each individual pixel in the resulting diffraction image captures the intensity and hue of reflected light that is observed from a specific direction defined by the polar angle θ (measured from the sample surface normal) and the azimuthal angle φ. Three different effects are apparent: (1) The rotational symmetry of the scattering pattern as characterized by the even intensity

distribution along φ; (2) an annulus of high reflection intensity corresponding to $\theta \approx 40°$; (3) the variation of hue with increasing θ.

The rotational symmetry in the stripes' diffraction pattern results from local in-plane rotational variations of the multilayer lamellae across the stripe, as will be discussed in detail later (**Figure 6-10e**). The annulus of higher intensity at polar angle $\theta \approx 40°$ in water suggests that the layered architecture has a predominant inclination of $\theta' = 1/2 \cdot \sin^{-1}\left(n_{water}/n_{CaCO_3} \cdot \sin\theta\right) \approx 16°$ with respect to the shell's surface normal (**Figure 6-9b-c**), which correlates very well with the major inclination observed in the zig-zag pattern. Overall, the observed scattering increases the visibility of each individual blue stripe in water, which can be perceived in a range of polar angles of up to more than 60° measured from the stripes' surface normal (**Figure 6-9d**). Taking into account the macroscopic curvature of the limpet's shell, at least a part of the blue stripe pattern can be seen from any direction on the top of the shells (see supporting movie M1).

The change of color with increasing polar angle θ is an effect inherent to reflection of light from a multilayer where the reflection peak wavelength depends on the angle of observation. This color variation is evident in a series of spectra obtained by micro-spectroscopy from a single stripe at increasingly larger collection angles using an oil immersion objective (**Appendix A, Figure A-7**).

6.3.5 Optical properties of the colloidal particles

Knowing that the mineralized multilayer in the stripe region serves as an optical interference filter to produce the strong blue reflection, we will now discuss the role of the disordered array of colloidal particles. Using optical transmission microscopy, we can identify the locations of high colloidal particle abundance, which corresponds to dark areas in the stripe micrographs (**Figure 6-10a**). The same regions also appear dark upon reflection of light from the shell interior (**Figure 6-10b**). A direct correlation of high-resolution optical images (**Figure 6-10c**) and scanning electron micrographs (**Figure 6-10d**) at the interior growth front of the stripe close to the shell edge reveals different morphological regions with distinct optical signatures: At the end of the stripe closest to the shell's growth edge, the emergence of the multilayer lamellae is observed ("M" in **Figure 6-10c, d, & e**). The gap spacing among adjacent lamellae can be clearly observed in the M region (**Figure 6-10e, inset**). The rotational variation in the planar orientation of the multilayer stacks (**Figure 6-10e**) is responsible for the rotation symmetry observed in the reflection pattern in **Figure 6-10c**. Further away from the growth edge (i.e. towards older regions of the shell), the lamellae appear to be covered by exposed colloidal particles ("C" in **Figure 6-10c, d, &f**) with a corresponding decrease in reflection intensity. Even further away from the growth edge, densely packed cross-lamellar structures cover the colloids ("CL" in **Figure 6-10c, d, &g**) and a very low reflection intensity is observed.

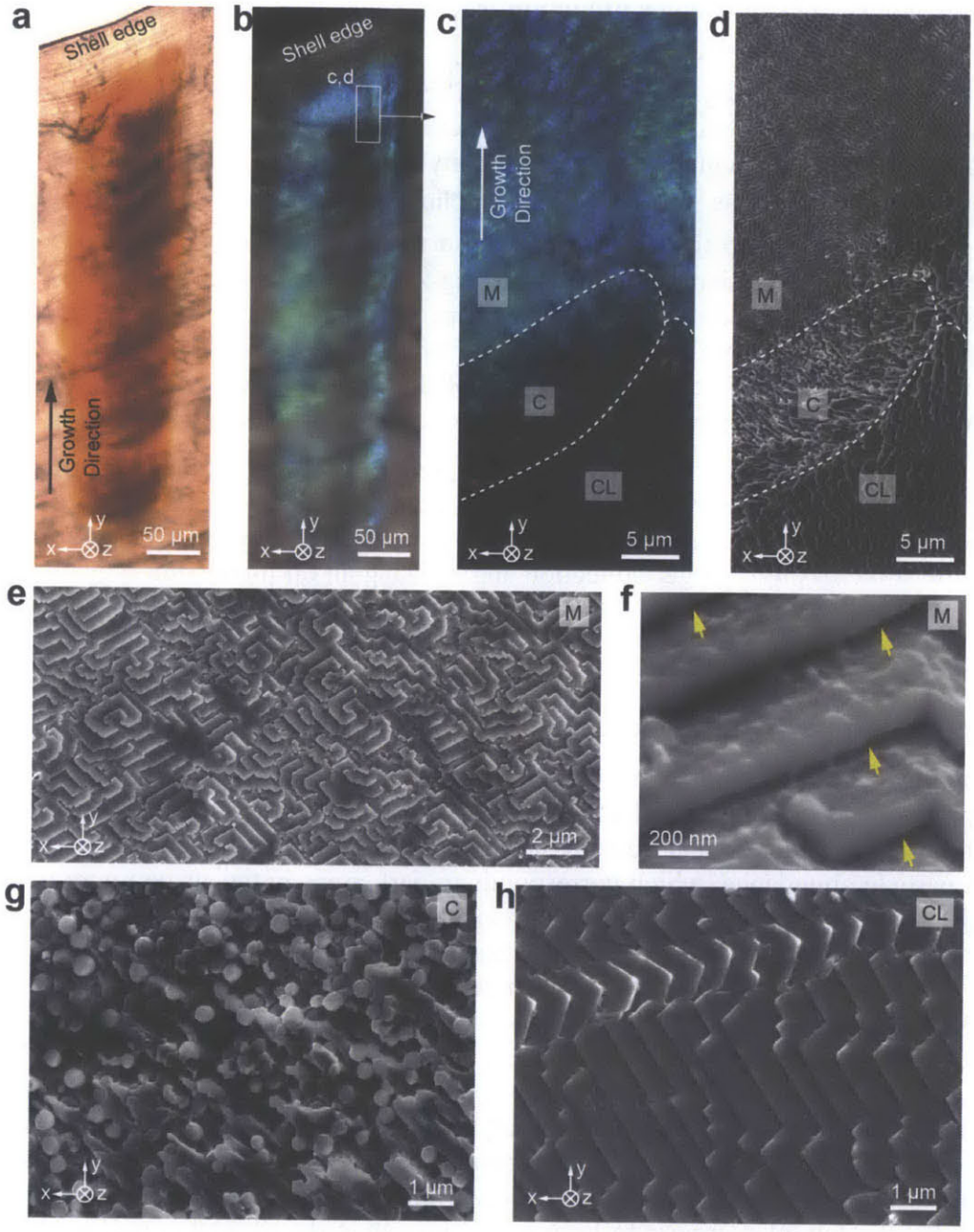

Figure 6-10| Micro-morphology at the growth edge. a,b, Transmission and corresponding reflection optical micrographs of a stripe at a shell's growth edge imaged from the shell interior. **c,d**, High-resolution optical micrograph and SEM image acquired in the transition zone (marked in (**b**)) between the blue reflecting and non-reflecting areas. Three different regions are apparent: the multilayer region with high blue reflection "M"; the region covered with colloidal particles with decreased reflection intensity "C"; a cross-lamellar region with very low reflection intensity "CL". (**e-h**) High magnification SEM images of regions of "M", "C", and "CL", respectively. **f** shows the gaps (yellow arrows) between the lamellae in region M.

The increase of colloidal particle density also leads to reductions in the transmission intensity across the edge of stripes (**Figure 6-11a**). This is further evident by the quantitative negative correlation between the density of colloidal particles (data deduced from FIB cross-sectional images from the stripe edge to its center) and the transmission intensity (**Figure 6-11b, c**).

While the attenuation of light of complimentary color transmitted through the multilayer in the regions of high colloidal particle abundance could in principle result from light scattering by the particles, our experiments reveal that it is primarily due to absorption. This becomes apparent when considering the limpet's shell with its underlying soft body together. The color of a live limpet's body is typically off-white. To imitate this natural situation during optical characterization, we partially painted the interior of a limpet shell white (**Figure 6-11d**). The blue stripes can be clearly seen in the unpainted part as well as the whitened part without any decrease in intensity or change in hue, which would be observed when placing a simple dielectric multilayer mirror on a white background. On a dark background (or with no background at all as is the case in the unpainted part), the reflection of a stripe appears bright blue (**Figure 6-11e**, the region with multilayer (M) is marked by the dashed line). Imaged with transmitted light, the stripe shows up in the complementary color (orange-red), and the dark areas correspond to the locations where the colloidal particles are present (**Figure 6-11f,** areas with colloidal particles underneath the multilayer (C) are marked with dotted lines). After the interior of the shell is painted, the blue reflection remains prominent only in regions with particles underneath the multilayer (**Figure 6-11g**, regions marked M+C). In areas deprived of colloidal particles (regions marked M), the light of complementary color is scattered by the white paint beneath the multilayer and recombines with the blue reflection, resulting in a drastic desaturation of the perceived color. We deduce therefore that when present underneath the multilayer, the colloidal particles, which absorb the majority of the transmitted light, provide enhanced contrast for the blue reflection against the white scattering soft limpet body below. Additionally, the arrangement of the colloidal particles appears to be optimized to ensure complete areal coverage beneath the majority of the multilayer, thus maximizing the absorption of transmitted light (**Figure 6-5a**). The size and separation of the colloidal particles are comparable to other systems that favor multiple scattering[232], which could increase the number of interactions of incident light with the absorbing colloidal particles through multiple scattering and thereby lead to an increased absorptivity[233] of the thin layer in which the particles are located. A similar interplay between photonic structure and absorbing particles has been observed in the feathers of birds[234].

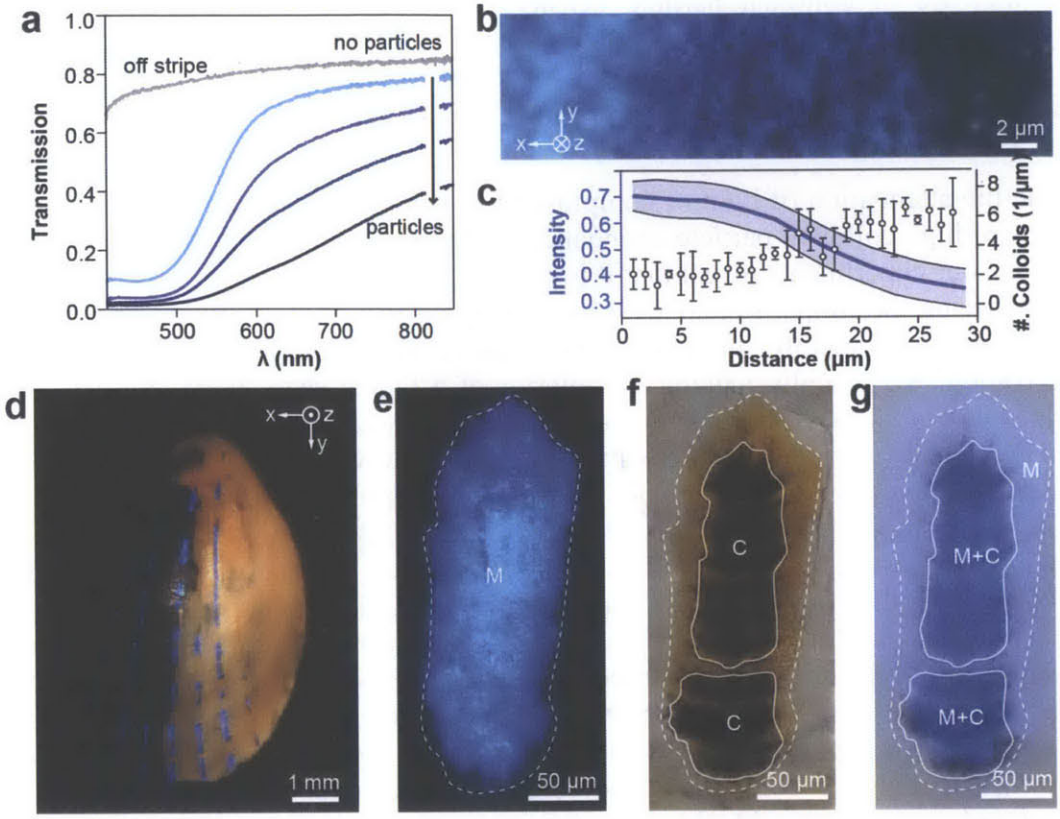

Figure 6-11| Optical function of the particles beneath the multilayer. a, Light transmission along a path from particle-free zones to particle-covered regions beneath a blue stripe. **b**, High-resolution optical micrograph acquired in reflection of the transition area from the edge of a blue stripe (no particles, left) towards the center (dense particle coverage, right). **c**, Correlation of transmitted light intensity averaged over the wavelength range of 400–750 nm and particle density deduced from SEM cross-sections along a path from left to right of (**b**). **d**, Optical image of a limpet shell with its right interior side painted white. **e,f,** Reflection and transmission optical image of a single stripe before paint application. The circumference of the stripe, i.e. the area where the multilayer (M) is located is marked with a white dashed line. The locations of colloidal particles (C) beneath the multilayer are marked with white solid lines. **g**, Reflection optical image of the same stripe after painting. The areas with multilayer and colloidal particles (M+C) maintain a strong blue coloration while areas where particles are missing below the multilayer (M) display only a faint blue.

6.4 Discussion and conclusions

The combination of two mineralized structural elements, i.e., the photonic multilayer and the light-absorbing colloidal particles in a calcite matrix beneath, that enables a strong blue reflection with enhanced color contrast, together with the macroscopic localization of those structures in the form of stripes along the shell, indicate that the photonic system in the blue-rayed limpet might have evolved to serve a purpose in visual communication. Individual stripes on a limpet shell reflect light in a cone of more than 120° opening angle. Due to the curvature of the shell, each stripe has a distinct orientation on the shell surface. Consequently, for most observation positions above the limpet's shell there is a set of stripes that can be clearly seen.

Besides the wide angular visibility range, the highest intensity of reflection from the stripes is found in the spectral domain that coincides with the absorption minimum of seawater (**Figure 6-12a**). Blue and green light travels farthest in seawater before being attenuated completely and therefore lends itself as the optimum color range for visual communication in the marine environment (**Figure 6-12b**). At water depths of 10m and 20m the intensity of blue light reflected from a limpet's stripes still amounts to 77% and 60% of its original value at the water surface respectively, providing a good color fidelity therefore allowing the organisms to appear highly conspicuous and identifiable even at deeper water levels within its habitat. A diver can see the blue color reflected by limpets on the kelp from over five meters distance. By contrast, other limpet species such as *Helcion pruinosus*[131] and *Patella granatina*[132] display only subtle hints of green iridescence on the exterior of their shells.

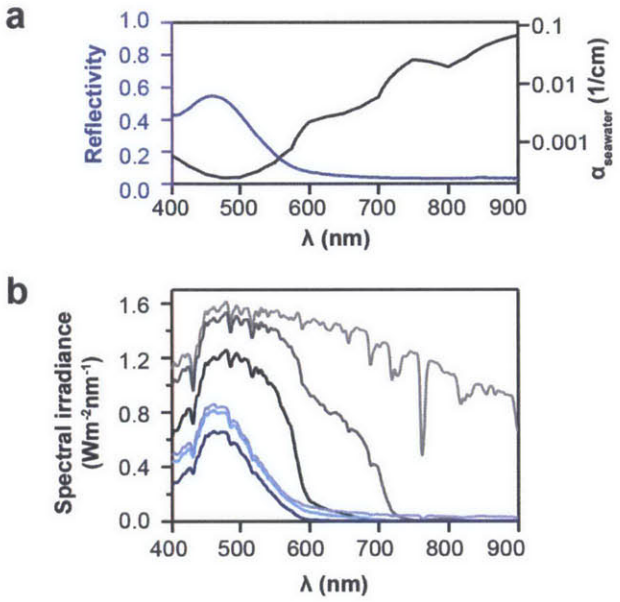

Figure 6-12| Optical performance of the blue stripes in seawater. a, The stripes' reflectivity (blue, dataset of Figure 6-8d) and the linear absorption coefficient of sea water (black, data adapted from ref. 235). **b**, Spectral irradiance at 0 m (ASTM G173-03, 2012), 2 m and 10 m depth below sea level before (light grey, grey and black) and after (light blue, blue and dark blue) light is reflected from a blue stripe.

The limpet *P. pellucida* occurs as two distinct morphotypes. Individuals found on the visually exposed parts of the host kelp, including the fronds and stipes, belong to the *pellucida* morph and display the bright blue stripes over the entire shell (**Figure 6-13a, top**). On the contrary, the *laevis* morph is usually found in concealed cavities of the kelp holdfast, where the environment is darker with low ambient light intensity and is full of visual obstructions. This morph has a stronger, non-transparent shell with pronounced growth lines (**Figure 6-13a,** bottom).

Provided the mineralized photonic structure has indeed evolved for visual communication, what would be the message and to whom would it be addressed? Intraspecific communication seems unlikely. The blue-rayed limpet has very primitive pit eyes just underneath the shell's apex[236], which are not well positioned or sufficiently well developed to recognize the blue stripes

of conspecifics. What about interspecific communication? For an herbivorous, slow-moving, largely exposed organism like the blue-rayed limpet that relies on reproduction through broadcast spawning, the largest benefit in interspecific communication would lie in preventing predation from other species. This can be achieved by either blending itself into the environment or hiding in concealment as observed for the *laevis* morph. Moreover, the *laevis* morph's thicker and stronger shell also provides further mechanical protection from potential predators. The thin colorful shell of the highly exposed *pellucida* morph found on the kelp fronds does not blend in at all and is clearly visible. We speculate that to protect the limpet from potential predators, the stripe patterns and color might serve to mimic toxic or otherwise distasteful organisms in its habitat that use similar visual features to advertise their unpalatability, a strategy known as *Batesian mimicry*[237]. Indeed, very similar bright blue features are found on toxic nudibranchs, including *Polycera elegans and Facelina auriculata* (**Figure 6-13b**) whose habitats overlap with the limpet distribution along the East Atlantic coast **Figure 6-13c**). Alternatively, instead of potentially enabling predator evasion through mimicry, the blue stripes could provide camouflage through disruptive contrast. The coloration of the limpet's non-striped body regions matches the appearance of its kelp habitat and the presence of bright blue stripes running across the shell could dramatically disrupt the limpet's body shape or outline to help it eluding predators. This type of camouflage through disruptive contrast has been observed in a vast variety of animals, and it has been shown that the presence of the contrasting patterns provides survival advantages[238]. In addition, from field studies, the *pellucida* morph seems to have developed effective means for keeping the shell surface above and in proximity of the stripes free from fouling so as to maintain the bright blue iridescence while the *laevis* morph usually appears to suffer substantial overgrowth from smaller organisms (compare the images in **Figure 6-13a**). The latter observation further highlights the potential importance of the unique photonic system for the survival of this small and highly conspicuous marine snail.

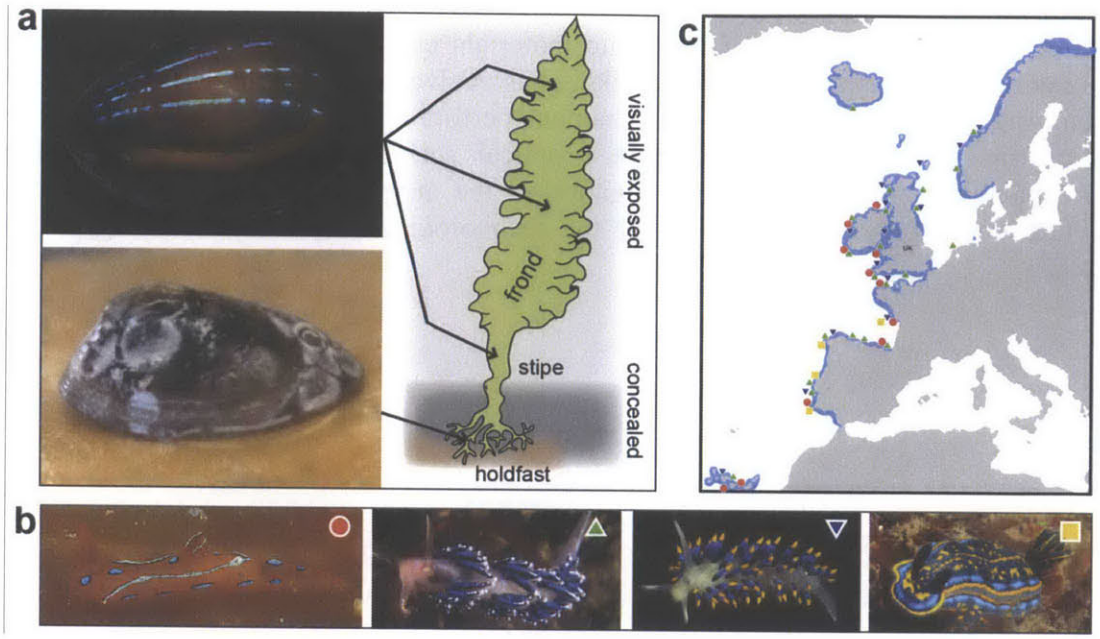

Figure 6-13| Hypothesis for the functional significance of the blue stripes. a, Comparison of the two morphotypes of *Patella pellucida*. Limpets of the *pellucida* morph (top left) live visually exposed on the kelp fronds, while members of the *laevis* morph (bottom left) are usually found concealed in cavities of the kelp's holdfast. Top left photograph, acquired with the help of Larry Friesen. **b**, The toxic and unpalatable nudibranches *Polycera elegans*, *Facelina auriculata*, *Trinchesia caerulea*, and *Felimare cantabrica* (from left to right) with similar blue features and overlapping habitats around the coast of Great Britain and Ireland. **c**, Overlapping geographical distribubutions of the blue rayed limpet, *Patella pellucida* and four toxic nudibranch species (*Polycera elegans* [red circle], *Trinchesia caerulea* [blue triangle], *Facelina auriculata* [green triangle], and *Felimare cantabrica* [yellow square]) which exhibit similar color patterns. Limpet and nudibranch photographs were kindly provided by Larry Friesen, Josep Lluis Peralta, Jim Anderson, and Joao Pedro Silva.

In summary, we show that a composite mineralized structure is responsible for the striking appearance of the blue iridescent stripes on the shell of the limpet *P. pellucida*. Our study clearly identifies various components of the complex photonic system and their role in creating a profound optical effect. We show that the blue color arises from the combination of a microscopic mineralized multilayer with regular lamella thickness and gap spacing that creates blue color by light interference, and a disordered array of absorbing colloidal particles underneath that provide enhanced contrast for the blue hue. The incorporation of this photonic architecture within the continuum of the mineralized shell offers visibility in a broad angular range, high conspicuity due to enhanced color contrast and the highest spectrally selective reflectivity observed in any marine animal so far. Prior to our work, a diverse range of biological photonic structures composed of organic materials has been reported. It is also well known that a number of species demonstrate high control over microstructure, crystallography, and macroscopic geometry in the formation of mineralized tissues thereby constructing materials with superior mechanical behavior. Our discovery of the mineralized hierarchical photonic system localized in the translucent shell of the blue-rayed limpet now shows for the first time that a species is capable of taking advantage of complex photonic design principles commonly realized with exclusively organic materials in other organisms while concurrently exploiting the

superior mechanical properties of inorganic materials employed for mechanical protection in many other mollusk shells. This structure likely has evolved to satisfy an optical purpose without compromising overly on the shell's mechanical performance. Our findings could inspire the design of transparent, mechanically robust optical surfaces with incorporated, controllable display capacity. A more detailed investigation of the morphogenesis of the limpet's photonic architecture could provide new ideas for the technological realization of inorganic photonic materials.

Chapter 7 Multifunctional design of a biomineralized armor with an integrated visual system

This chapter is based on a collaborative work and is now in submission for publication: Connors, M. J.*, Li, L.*, Kolle, M., England, G., Speiser, D., Xiao. X., Aizenberg, J. & Ortiz, C. Multifunctional design of a biomineralized armor with an integrated visual system. 2014 (* Equal contribution).

7.1 Introduction

The design of material systems with multiple functionalities is an emergent direction of materials research[1]. In particular, multifunctional structural materials with both improved mechanical performance and other functions, such as sensing[239], power generation and storage[1,240], and self-healing capabilities[241] holds great potential for a diversity of engineering applications. In Chapter 3-6, I have presented two biomineralized structural materials with optical transparency and photonic coloration in their protective armor systems. Photoreception is another important light-tissue interaction in nature, and there are a variety of visual designs from simple photoreceptive cells to complex eyes, as discussed in Chapter 2. Understanding of biological vision systems allows us to design better navigation systems, specialized detectors, and surveillance cameras[242,243].

As discussed in Chapter 2, the majority of animal eyes are organic-based tissues. Direct integration of visual systems with protective armor exoskeletons is rarely found in biological organisms. In this chapter, we select a unique mollusk species, the chiton *Acanthopleura granulata*, as the model system to explore the interplay between mechanical protection and vision, as it possesses hundreds of mineralized lens-based eyes directly integrated in its protective armor plates (**Figure 7-1**).

Chitons are a special group of mollusks which possess eight highly mineralized armor plates, providing mechanical protection and flexibility simultaneously[173]. Moreover, chitons are the only known extant mollusks which have living tissue integrated within the outermost layer of their mineralized shells[136]. The tissue fills a complex network of channels that open on the dorsal surface as sensory organs known as aesthetes. A variety of functions have been proposed for the aesthetes, although observations of the phototactive behavior of a number of species suggest that photoreception may be a predominant role[137]. Two lineages of chitons have evolved to make a another step further towards the sensory functionality by developing hundreds of single chambered lens eyes which have been shown to have spatial resolutions based on behavioral studies[122,138]. Less than 10 million years old, the eyes of chitons are likely one of the most recently evolved animal eyes[136]. Unlike the protein-based lenses of most animal eyes[139], the lenses of chitons, like their shells, are principally composed of aragonite[127]. In contrast to the few other known eyes with calcium carbonate-based lenses, including those of trilobites[140] and

podocopid ostracodes[141–143], the eyes of chitons are integrated with the entire dorsal surface rather than localized to a specific exoskeletal region. Although the calcitic lenses of brittlestars are also non-localized across many dorsal arm plates[121], it is unclear whether they enable spatial vision in a fashion similar to chiton.

The objective of this research include: 1) to to investigate how the nano/microstructure and morphology of aragonite is modified within the shell to achieve multifunctionality, 2) to understand the material and geometric origins of *A. granulata*'s ability to spatially resolve objects equally well in air and seawater environments, 3) to experimentally demonstrate that the lens is capable of forming images, and 4) to explore possible trade-offs between mechanical protection and sensation in local regions of integrated functionality.

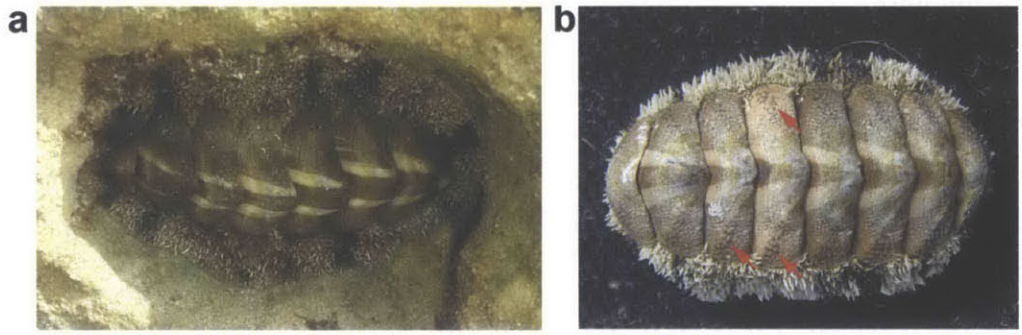

Figure 7-1| The model system: the chiton *A. granulata*. **a**, Photograph of *A. granulata* on the rocks of Macao Beach, Dominican Republic in May, 2013. **b**, Photograph of an *A. granulata* sample. Red arrows indicate regions of the shell that contain eyes, corresponding to the dark spots.

7.2 Materials and methods

7.2.1 Sample collection and preparation

A. granulata were collected from Tavernier, FL in August of 2011 and stored in a 70% ethanol solution until experimentation. To create samples for polarized light microscopy, nanoindentation, and electron backscattered diffraction, dried valves were first embedded in a room temperature curing epoxy. After curing for ~24 hours, the specimen was sectioned with a diamond saw (IsoMet 5000, Buehler, Lake Bluff, IL), polished (Model 920, South Bay Technology, CA) stepwise with aluminum oxide pads (15 μm, 5 μm, 3 μm, and 1 μm), and finely polished with 50 nm silica nanoparticles on cloth (MultiTex, South Bay Technology, CA).

7.2.2 Materials characterization

Micro-Computed Tomography (μCT) & Morphometric Measurements: Dried fractured pieces, approximately 1 mm^3 in size, of A. granulata valves were scanned with an energy of 18 keV and a resolution of 0.74 μm/voxel at beamline 2-BM of the Advanced Photon Source of Argonne National Laboratory. Mimics (Materialise, Belgium) was used for image segmentation and construction of three-dimensional triangulated surface meshes (binary STL format). Cross-sectional meshes were created using the cut function of the simulation module Mimics. For

figure creation, meshes were reduced in file size as needed via the smooth, reduce, and remesh functions of 3-matic (Materialise, Belgium) and rendered using Blender (www.blender.org). Open-source image analysis software ImageJ was used to make all morphometric measurements. The table in **Figure 7-5** represents the averages and standard deviations of measurements of 7 eyes. The curvatures of the top and bottom surfaces of the longitudinal and transverse cross sections of the lens region were fit from the aggregation of data from 7 lenses. 29 points were collected from each surface of each lens, for a total 203 points/surface.

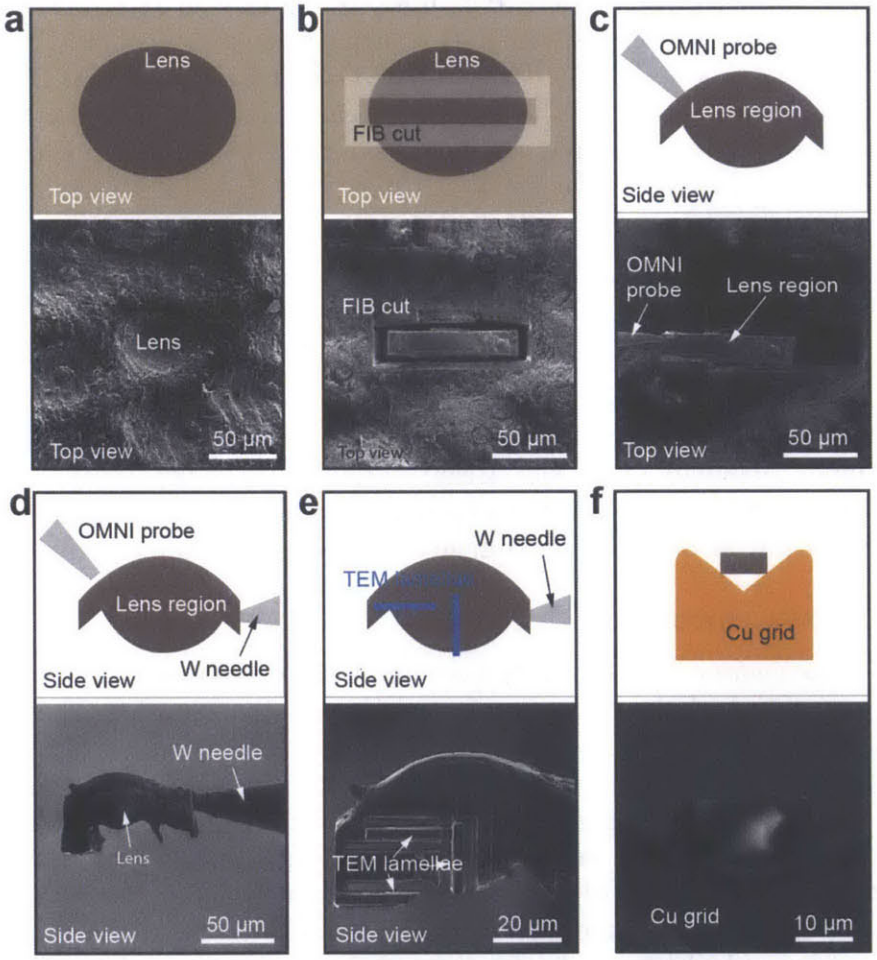

Figure 7-2| Preparation method of TEM samples from the lens region of eyes from the chiton *A. granulata*.

Focused Ion Beam (FIB) Milling & Electron Microscopy: Dried fractured pieces of A. granulata valves were fixed on a scanning electron microscopy (SEM) aluminum holder with carbon tape. Samples were coated with carbon to minimize charging effects. A Helios Nanolab 600 Dual Beam (FEI, OR) was used for SEM imaging at acceleration voltage of 2-4 kV and working distance of ~4 mm. Several cross-sectional and transmission electron microscopy (TEM) samples were prepared with focused ion beam (FIB) milling using the same system. Do to the large and complex geometry of the eyes, a protocol for preparing TEM samples (**Figure 7-2**) was developed: 1) A platinum protective layer (~0.5 µm) was first deposited on top of the lens region

of an individual eye; 2) A second platinum protective layer (~3 μm) was deposited on top of a rectangular region of interest (~20 μm × 100 μm), which was to be milled out; 3) Four trenches surrounding the rectangular region were milled by FIB (30 kV, 9.5 nA), creating a cross-sectional slab of the lens region (**Figure 7-2b**); 4) The slab was attached to an in situ OMNI probe via platinum deposition and lifted out (**Figure 7-2c**); 5) The slab transferred via FIB and platinum deposition from the OMNI probe to a tungsten needle that was fixed to an SEM holder with carbon tape (**Figure 7-2d**); 6) Multiple TEM samples of the lens region with a variety of orientations were prepared using the procedure (**Figure 7-2e,f**): 6.1) deposition of a protective platinum layer (~3 μm); 6.2) Stepwise FIB milling from 30 kV to 2kV; 6.3) Lift-out via an in situ OMNI probe via platinum deposition; 6.4) Attachment to a copper TEM grid and final FIB thinning and polishing (2 kV, 28 pA). Bright field TEM imaging and SAED were carried out using a JEOL 2011 operated at 120 kV to minimize beam damage. The image magnification and camera constants were calibrated using a standard sample (MAG*I*CAL, Electron Microscopy Sciences, PA, USA). A field emission JEOL 2010F, operated at 200 kV, was used for HRTEM imaging.

Energy-Dispersive X-ray Spectroscopy (EDX): EDX measurements of the lens region were conducted on FIB-polished cross sections with a Helios Nanolab 600 Dual Beam (FEI, OR) equipped with an INCA EDX system (Oxford Instruments) at an accelerating voltage of 20 kV.

Electron Backscattered Diffraction (EBSD): Finely polished cross-sectional samples were coated with an ultra-thin layer of carbon and mounted on 70° pre-tilted stage. EBSD was carried out using a Helios Nanolab 600 Dual Beam system (FEI, OR) equipped with the HKL Technology "Channel 5" system. EBSD patterns were generated using a working distance of 6 mm, a step size of 1 μm, an accelerating voltage of 20 kV, and a beam current of 2.7 nA.

7.2.3 Optical measurements

Valves of *A. granulata* were carefully fractured with tweezers to obtain small fragments of the outer shell layer in which the bottom surfaces of lenses were revealed. These fragments were mounted on a small needle on a 3-axis stage positioned underneath a 63× water immersion objective. A chrome mask containing printed objects of known size derived from the 1951 USAF resolution test chart (http://www.efg2.com/Lab/ImageProcessing/TestTargets/#USAF1951) was placed below each sample. Each sample was oriented such that the dorsal shell surface was facing and parallel to the surface of the underlying chrome mask. Next, a small drop of water was placed on the chrome mask, and then the sample was lowered into the water. To locate the ventral surface of individual lenses, the 63x immersion objective was brought into focus using illumination from the microscope. To create objects, the chrome mask was illuminated from below through a 10x objective using a ThorLabs (Newton, NJ) L2-1 source. Images of these objects formed by individual lenses were brought into focus using the 63x immersion objective. To calculate the focal length of each lens, the object distance was varied using the "z"-translation stage of the sample. At each object distance, the image size was measured independently by 3 authors, and an average image size was calculated. Since the object sizes were known, we were able to calculate the magnification, $M = (h_i/h_o)$, where h_i and h_o are the heights of the image and object, respectively. The object distance and magnification data were fit to the linear thick lens equation:

$$\frac{1}{M} = \frac{z}{f} + \left(\frac{z_o + P^*}{f} - 1\right)$$

where z_o is the initial object distance, z is the object distance away from z_o, and P^* is the front principal point distance. The focal length, f, was calculated from the slope.

7.2.4 Ray-trace simulations

The ray tracing program was written in IGOR Pro (WaveMetrics). As shown in **fig. S11**, each 2D simulation was repeated for each cross section of the lens region (longitudinal and transverse), refractive index of the lens (ordinary and extraordinary rays), and external environment (air and seawater). Thus, eight (2 × 2 × 2) measurements were made for each optical quantity.

The refractive indices used for air and seawater were 1 and 1.336, respectively. Since the cornea is continuous with granular microstructure of the non-sensory regions, which has a weak texture, it was given a refractive index of 1.632, the average of the three indices of aragonite. Although aragonite is a biaxial crystal, the pseudo-hexagonal symmetry about its c-axis allows it to be approximated as uniaxial with n_o = 1.683 and n_e = 1.530[244]. The optical properties of uniaxial crystals are only dependent on the polar angle θ that the incident wave vector forms with the optical axis, and not on the azimuthal angle[245]. While n_o does not vary with θ, n_e is given by:

$$n_e(\theta) = \left(\frac{n_o n_e}{\left[n_e^2 \cos^2(\theta) + n_o^2 \sin^2(\theta) \right]^{1/2}} \right)$$

Since the c-axis is oriented ~45° below the surface normal, the refractive indices of the lens were approximated as n_o = 1.683 and $n_e(45°)$ = 1.601, assuming normal incidence. The thin organic layer underneath the lens, *L1*, was modeled as chitin (n = 1.435[246]), a major component of the organic matrix of chiton shells. Since *L2* contains is calcified and amorphous, it was given a refractive index of 1.58, a value which lies in the experimentally determined range of ACC, 1.579-1.583[247], and has been used to calculate the focal lengths of ACC microlenses[248]. The photoreceptive region was given a refractive index of 1.36, which has been used to model the retinal receptors of jellyfish eyes[249].

7.2.5 Mechanical tests

Nanoindentation: Nanoindentation experiments on finely polished cross-sectional samples were conducted in ambient conditions using a TriboIndenter (Hysitron, MN, USA). Blunt Berkovich (trigonal pyramid, semi-angle = 65.3°) and sharp conospherical (tip radius ~1 μm, semi-angle = 30°) diamond probe tips were used to obtain quantitative material properties ($E_{O\text{-}P}$ and $H_{O\text{-}P}$) and investigate fracture behavior, respectively. Typical load functions included loading (10 s) to the maximum load (5 mN), holding (20 s), and unloading (10 s). The Oliver-Pharr (O-P) methodology was used to quantify material properties, i.e. indentation modulus ($E_{O\text{-}P}$) and hardness ($H_{O\text{-}P}$). The probe tip area function, $A(h_c)$, which is the projected area of the indentation tip as a function of contact depth, h_c, and frame compliance were calibrated prior to each set of experiments using a fused quartz sample.

Microindentation: Microindentation experiments on intact shell plates were conducted in ambient condition using an instrumented microindenter (MicroMaterials). A flat punch tip (diameter of bottom surface, ~80 μm) was used to compress the eyes, megalaesthetes, and protruding non-sensory regions. Typical load functions included loading (30 s) to a maximum

load (~1 N), holding (5 s), and unloading (30 s). The post-indentation residues were imaged via SEM using a Helios NanoLab 600 Dual Beam (FEI, OR).

7.3 Results

7.3.1 Geometrical features of the sensory system

The two main sensory structures of the shell of *A. granulata* appear on the surface as small bumps ~50 μm in diameter (**Figure 7-3**). The more numerous megalaesthetes, which are common to all chitons, are capped with a pore and maintain the same color as non-sensory regions, which are characterized with the large protrusions (~200-300 μm in diameter, **Figure 7-3a,b**). The eyes are distinguished by their circular translucent lens, which is encircled by a dark pigmented area (outer diameter 86 ± 3 μm**, Figure 7-3a**). Scanning electron microscopy (SEM) images revealed that the surfaces of the eyes are much smoother than those of the neighboring megalaesthetes and non-sensory protrusions (**Figure 7-3b,** inset). Both sensory structures are located within the valleys formed by non-sensory protrusions, as revealed by the 3D stereographic reconstruction of the shell surface (**Figure 7-3c,d**).

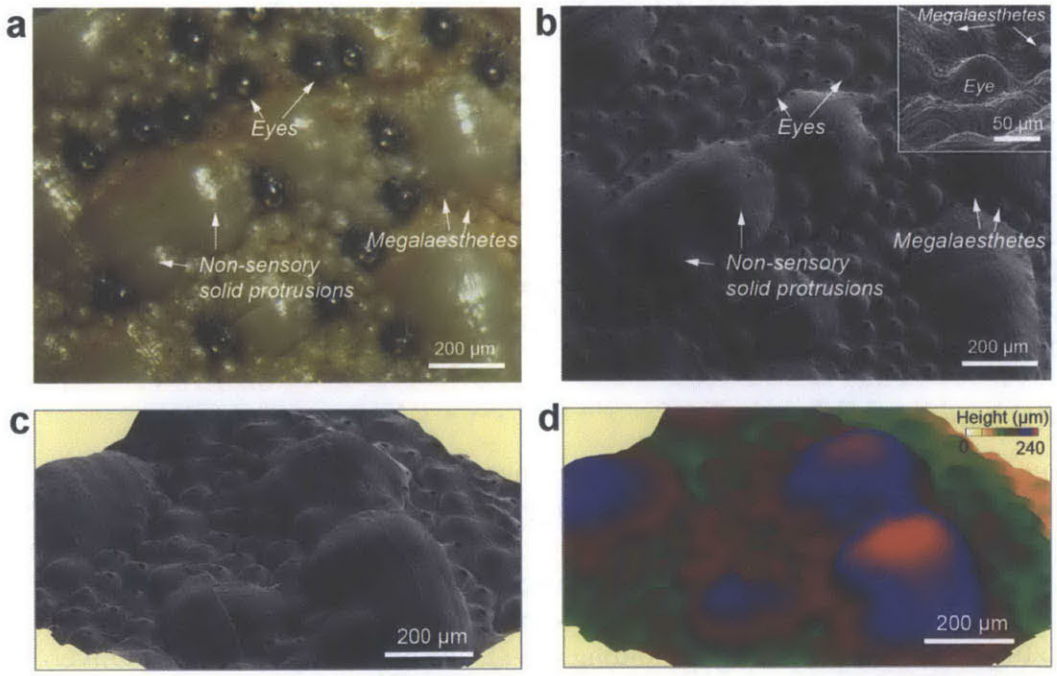

Figure 7-3| Surface morphology of the chiton *A. granulata*. a, Light micrograph of a region of the dorsal shell surface containing multiple sensory structures: eyes and megalaesthetes. Megalaesthetes are sensory organs common to all chitons. **b**, SEM image corresponding in position to (**b**). Inset, a high magnification SEM image of an eye, showing its much smoother surface as compared to surrounding megalaesthetes. **c,d**, 3D reconstructed topography of the dorsal shell surface using a stereographic pair of SEM images.

Synchrotron μCT was used to investigate the 3D morphology of the megalaesthetes and eyes, and the results are summarized in **Figure 7-4**. The megalaesthetes have cylindrical chamber with a relatively constant diameter of ~40 μm, although a reduction in chamber

diameter to ca. 20 μm towards to the dorsal surface (**Figure 7-4c**). In contrary, the specialized eye structure, in addition to the lens structure on the surface (will be discussed in detail later), has a much enlarged pear-shaped chamber, which has a depth and width of ~55 μm and 75 μm, respectively (**Figure 7-4a,b**). We have carried out a detailed morphometric measurements of the chamber, and results are summarized in **Figure 7-5**. This expansion results in an eye chamber volume that is ~5× greater than that of the megalaesthete. In addition to these two primary sensory structures, numerous small sensory channels, known as micraesthetes, were observed branching from the chambers of the eyes and megalaesthetes to the shell surface (**Figure 7-4f,g**). The diameter of these micraesthetes is 5 μm. Please see **Movie 3 and 4 in Appendix B** for the 3D visualization of the eye chamber and megalaesthete.

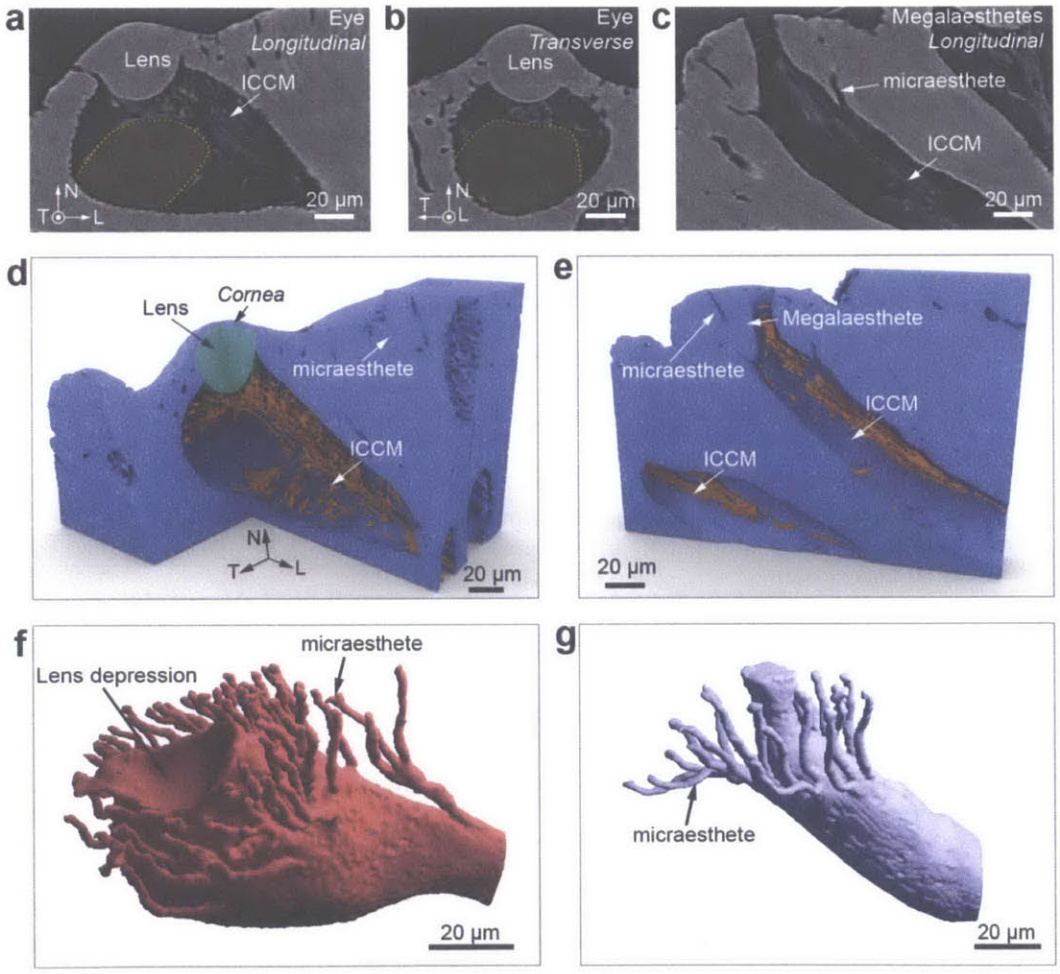

Figure 7-4| Synchrotron μCT reconstructions of the sensory structures integrated with the outer shell layer. a,b, Transverse and longitudinal, respectively, cross-sectional tomographic slices of an eye. **c**, Longitudinal cross-sectional slice of a megalaesthete. Highly X-ray absorbent material is clearly visible inside the chambers of both sensory structures. This material was found to be calcified, so we refer to it throughout this paper as intra-chamber calcified material (ICCM). **d,e**, 3D reconstructions of a megalaesthete and an eye, respectively. **f,g**, 3D reconstructions of the non-calcified (minimally X-ray absorbent) volumes of the megalaesthetes and eyes, respectively. These volumes represent the chambers which contain soft sensory tissues. Numerous small sensory structures, micraesthetes, branch from these chambers to the shell surface.

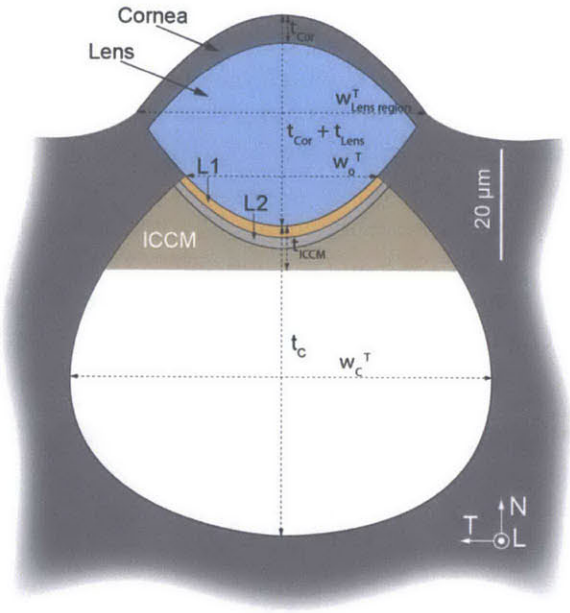

Symbol	Description	Measurement (µm)	Method
t_{Cor}	Thickness of Cornea	~5	OM
$t_{Cor} + t_{Lens}$	Thickness of Cornea and Lens	38 ± 2	µCT
t_{L1}	Thickness of Layer L1	~2	SEM
t_{L2}	Thickness of Layer L2	~2	SEM
t_{ICCM}	Depth of ICCM Below Lens	8 ± 1	µCT
d_C	Distance from Bottom of Lens to Back of Chamber	56 ± 7	µCT
w_C^L	Maximum Width of Chamber in "L" Cross Section	108 ± 7	µCT
w_C^T	Maximum Width of Chamber in "T" Cross Section	76 ± 5	µCT
w_o^T	Width of Bottom of Lens in "T" Cross Section	35 ± 2	µCT
$w_{Lens\ region}^T$	Width of Lens Region in "T" Cross Section	~52	µCT and fitting
$w_{Lens\ region}^L$	Width of Lens Region in "L" Cross Section	~56	µCT and fitting

Figure 7-5| Morphometric measurements of the eyes of the chiton *A. granulata*. **a**, Schematic diagram defining the morphometric dimensions. **b**, Table displaying the average (± standard deviation) values of measurements from 7 eyes. Abbreviations: T, Transverse; L, Longitudinal; ICCM, Intra-chamber calcified material.

Highly X-ray absorbent structures were discovered within the chambers of the megalaesthetes and eyes (**Figure 7-4a,b,d,e**). These structures were found contain calcium (**Figure 7-7b**), so we denote them as intra-chamber calcified material (ICCM). In megalaesthetes, the ICCM consist of rod-shaped structures. The long axes of the rods are approximately parallel to the long axis of the megalaesthete chamber (**Figure 7-4e**). In eyes, the ICCM forms a "c"-shaped pocket that likely encircles the retina (**Figure 7-4d**). ICCM was probably not uncovered earlier for two reasons. First, prior studies of the interior structure of megalaesthetes and eyes focused on living tissues, so samples were decalcified. Secondly, ICCM is easily destroyed by polishing (**Figure 7-8a**), and perhaps other common sample preparation techniques. SAED revealed that the ICCM is amorphous (**Figure 7-9f**, will be discussed in detail later). Therefore, we hypothesize that the ICCM is composed primarily of amorphous calcium

carbonate (ACC). Although to date the only mineral component found in chiton shell plates has been aragonite, ACC is an established precursor to crystalline $CaCO_3$ in other groups of mollusks[250].

The geometry of the lens was studied in detail by quantifying the μCT data. The lens region of each eye is ~38 μm thick and slightly elongated in the direction of the optic canal, which we denote as the longitudinal direction (**Figure 7-6a**). This anisotropic geometry was consistently observed, and hence we conducted measurements in both longitudinal and transverse directions. **Figure 7-6b,c** summarizes the average cross-sectional shapes of the lens region in the two orientations based on seven sets of μCT data. Both top and bottom surfaces were generally best fit with parabolic curves (**Figure 7-6c**), which may function to reduce spherical aberration.

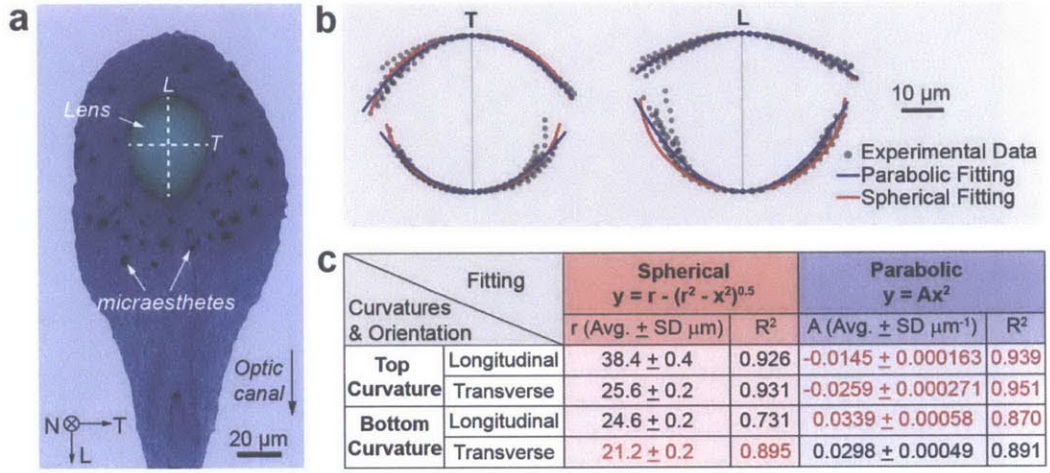

c

Curvatures & Orientation	Fitting	Spherical $y = r - (r^2 - x^2)^{0.5}$		Parabolic $y = Ax^2$	
		r (Avg. ± SD μm)	R^2	A (Avg. ± SD μm^{-1})	R^2
Top Curvature	Longitudinal	38.4 ± 0.4	0.926	-0.0145 ± 0.000163	0.939
	Transverse	25.6 ± 0.2	0.931	-0.0259 ± 0.000271	0.951
Bottom Curvature	Longitudinal	24.6 ± 0.2	0.731	0.0339 ± 0.00058	0.870
	Transverse	21.2 ± 0.2	0.895	0.0298 ± 0.00049	0.891

Figure 7-6| Geometry of the mineralized lens region of the eyes of the chiton in *A. granulata*. **a**, Bottom view of the lens region showing the axially asymmetric lens. **b**, Contours (dotted-lines, 29 points per line) of the top and bottom surfaces of the transverse (left) and longitudinal (right) cross sections of the lens regions from 7 eyes measured via synchrotron μCT. Parabolic and spherical fittings are superimposed with the dotted-contours. The encircled area includes the cornea and the lens. **c**, Spherical and parabolic fittings of the cross-sectional curvatures of the top and bottom surfaces of the lens region.

7.3.2 Ultrastructural, compositional, and crystallographic features

Having studied the geometrical features of the eyes and megalaesthetes, we next carefully compared the ultrastructures, chemical compositions, crystallographic textures of the lens region of the eyes to granular microstructure which comprises the bulk of calcified portion of the outer shell layer.

Sectioning an eye by focused ion beam (FIB) milling revealed the presence of additional two layers, *L1* and *L2*, underlying the lens (**Figure 7-7a**). In contrast to the smooth curved bottom surface of the lens, the boundaries between L1 and L2 and the bottom surface of L2 have local variation in curvatures. This feature is also consistent to the uneven thickness of these two layers, which are gradually thinned towards to the circumferential regions close to the side chamber walls. In addition, L1 had a much lower image contrast whereas the lens and L2 are

similar in greyscale, indicating that L1 may high amount of low atomic weight elements and L2 might be mineralized. Energy-dispersive X-ray spectroscopy (EDX) indicated that *L1* is indeed mainly composed of organic materials as indicated by its high carbon content, whereas calcium and oxygen contents are minimal (**Figure 7-7b**). In the contrary, L2 has similar chemical composition as the primary lens region.

In addition, strut-like structures were observed which dorsally branch from *L2* to the chamber walls (**Appendix A, Figure A-8**). This ICCM corresponds in size, shape, and location to the aforementioned X-ray absorbent structures observed in the chamber with μCT (**Figure 7-4d**).

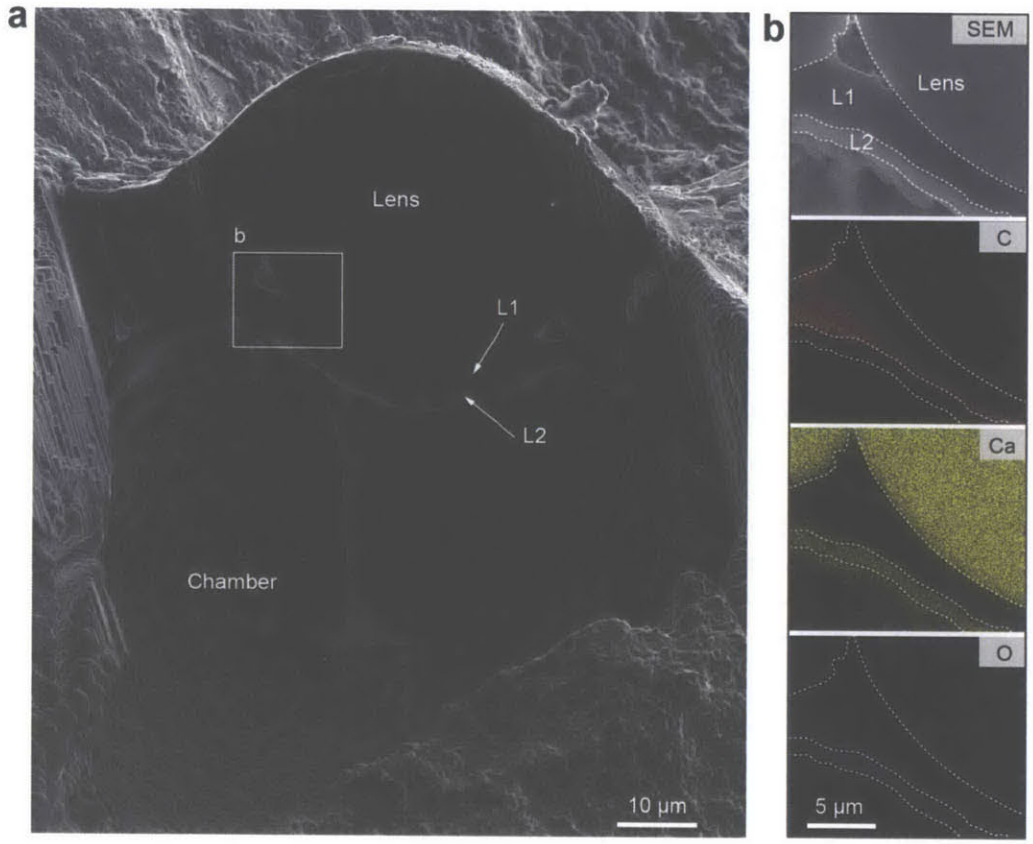

Figure 7-7| Fine structural features and chemical compositions of the lens region of the eyes of the chiton *A. granulata*. **a**, SEM image of a FIB-cut cross section of the lens region of a single eye, showing two additional layers underneath the lens, L1 and L2. **b**, EDX mapping of a FIB-polished cross section of the lens and underlying layers L1 and L2.

Crystallographic information is critical in understanding the optical performance of this mineralized lens structure. Viewing polished cross sections of eyes under cross-polarized light (**Figure 7-8a**) showed that the lenses have a relatively uniform grayscale level compared to the surrounding granular microstructure, which is known to have no preferred grain orientations in the chiton *Tonicella marmorea*[173]. This suggested that the lens is either a single crystal or is polycrystalline with highly aligned grains. The clear boundaries between the lens and granular microstructure in **Figure 7-8a** indicate a delicate control of crystallography in the lens region. A

thin (~5 μm thick) concavo-convex corneal layer covers the lens and is continuous with the surrounding granular microstructure.

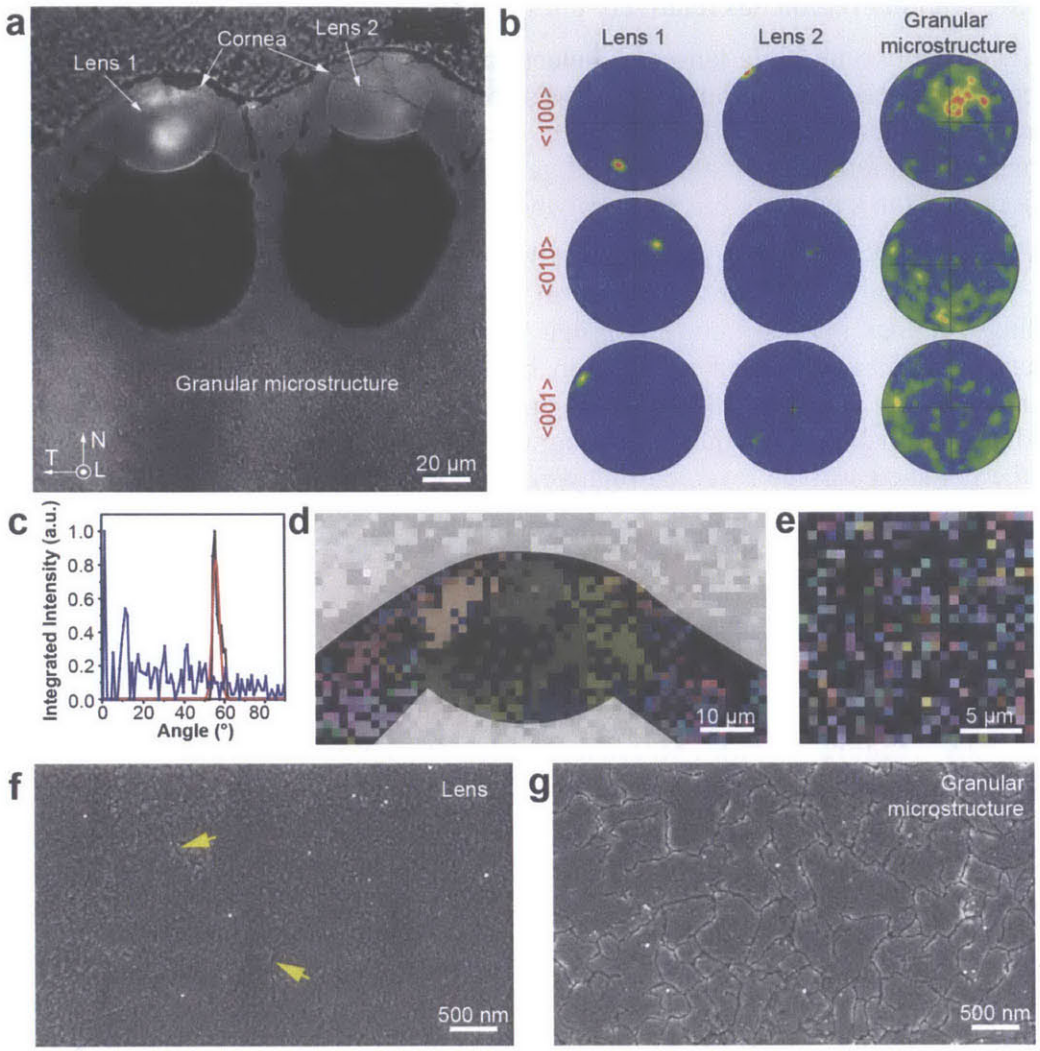

Figure 7-8| Crystallographic features of the lens and surrounding granular microstructure regions of the chiton *A. granulata*. **a**, Polarized light micrograph of a polished transverse cross section of the shell containing two adjacent single chamber lens eyes. **b**, EBSD pole figures of the lenses and granular microstructure of the non-sensory regions. **c**, Integration distribution of the tilt angle of the aragonite c-axis from the region of lens 1 (black) and adjacent non-sensory (blue) region with respect to the normal of the cross section The red curve represents a Gaussian fit of the data from the lens (average, 55.8°; SD, 1.7°; FWHM, 4.1°). **d**,**e**, EBSD maps from the lens and non-sensory regions the outer shell layer, showing large (~10 μm) and small (~1 μm) grains, respectively. **f**,**g**, SEM images from a polished cross section of the outer shell layer for the lens and granular microstructure region, respectively. Yellow arrows indicate the faint grain boundaries.

The crystallographic pole figures obtained with electron backscattered diffraction (EBSD) in **Figure 7-8b** confirmed that the lens has a strong crystallographic texture, indicated by the regions of localized intensity, which is in stark contrast to the weak texture of the surrounding

granular region. The good crystallographic alignment can be quantitatively measured by integrating the c-axis from the pole figure of the lens and granular region, as shown in **Figure 7-8c**. The result shows that the full width at half maximum is ~4° for the lens region, whereas the surrounding granular region has relatively uniform intensity across all the polar angles.

EBSD of the two multiple lenses and electron diffraction results demonstrated that the polar angle θ between the c-axis and optical axis was consistently ~45°, while the orientations of the a- and b-axes were inconsistent (**Figure 7-8b**). Since aragonite is a pseudo-uniaxial crystal, the non-normal orientation of the c-axis should generate double refraction, which is consistent with observations that the lenses are birefringent when viewed with polarized light.

In addition, EBSD mapping showed that the lens has an average grain size of roughly 10 μm (**Figure 7-8d**), which is approximately an order of magnitude greater than that of the surrounding granular microstructure (**Figure 7-8d**). High resolution SEM images of polished cross sections display faint and clear grain boundaries in the lens and surrounding granular regions, respectively (**Figure 7-8f,g**). These grain boundaries were produced by partial selective etching during polishing. As the crystallographic orientations in the lens region are highly aligned, the polished surface revealed relatively uniform roughness, and the boundaries between adjacent grains are not as obvious as those in the granular region. In addition, the size of grains in the granular region as revealed by SEM (**Figure 7-8f**) is on the order of ~1 μm. The likely function of the large grains is to reduce the number and area of grain boundaries in the lens region, which will minimize light scattering.

Further ultrastructural characteristics were revealed using transmission electron microscopy (TEM, **Figure 7-9**). High resolution TEM images easily revealed the atomic lattice planes of the aragonite lens (**Figure 7-9a**). Moreover, grain boundaries with small crystallographic misorientations were identified (**Figure 7-9b**). In the contrary, low magnification TEM images clearly showed the aragonite grains in the granular microstructure region, and the corresponding selective area electron diffraction pattern confirms the large crystal misorientations among the grains (**Figure 7-9c**). Moreover, inclusions with size of several tens of nanometers were observed within the individual grains in the granular region ((**Figure 7-9d**), which are believed to be intracrystalline organic materials trapped during biomineralization process. These organic inclusions are anisotropic in shape, and exhibit different preferred alignments in adjacent grains. This is probably due to the crystallographic misorientations in the grains. However, such organic inclusions were less observed in the lens region, as indicated by the continuous lattice fringes. This reduction in the amount of organic inclusions in the lens region may serve to reduce light scattering, as discussed in Chapter 2.

TEM imaging and corresponding electron diffraction indicate that both L1 and L2 are amorphous, despite some fine structural difference (**Figure 7-9e,f**). In contrast to the relatively uniform greyscale (suggesting its uniform chemical composition) in L1, L2 exhibits striations which follow the contours of the bottom boundaries (Error! Reference source not found.**f**). Moreover, SAED pattern in L2 revealed an amorphous diffraction ring corresponding to the lattice spacing of 0.296 nm, which was not observed in L1.

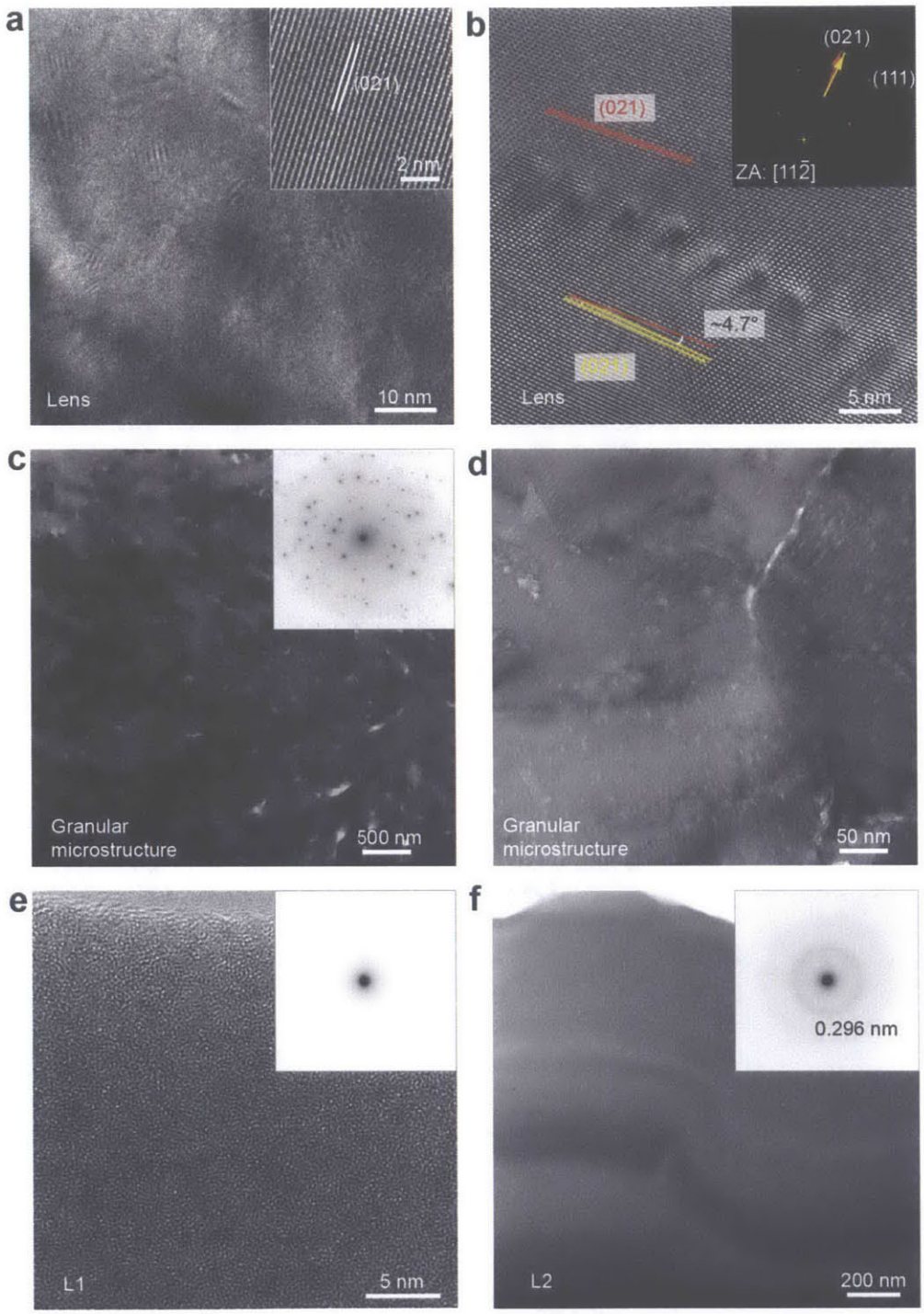

Figure 7-9| TEM analysis of the ultrastructural features of the lens and granular microstructures in *A. granulata*. **a**,**b**, HRTEM images of the lens region. (**b**) shows two aragonite grains with small misorientations (~4.7°). **Inset**, corresponding FFT pattern with zone axis of [11$\bar{2}$]. **c**, TEM image and (**inset**) corresponding SAED pattern of the granular microstructure of non-sensory regions. **d**, High magnification TEM image of the non-sensory region, which shows distributed nanoscopic inclusions within the crystalline grains. Notice that the orientations of the inclusions are different in adjacent grains, probably related to their crystallographic misorientation. **e**,**f**, TEM images of the two layers underneath the lens, L1 and L2, respectively, and their corresponding SAED patterns (**insets**).

7.3.3 Optical performance of the lenses

The optical performance of individual eyes of *A. granulata* was investigated via both theoretical modelling and experimental measurements. First, key elements of the geometry, composition, and crystallography of the lens were combined in 2D ray-trace simulations to investigate the locations of rear focal points, *F*. For each possible external environment, air and seawater, *F* of the ordinary and extraordinary rays were calculated in two orthogonal extremes, the transverse and longitudinal cross sections (**Figure 7-10**).

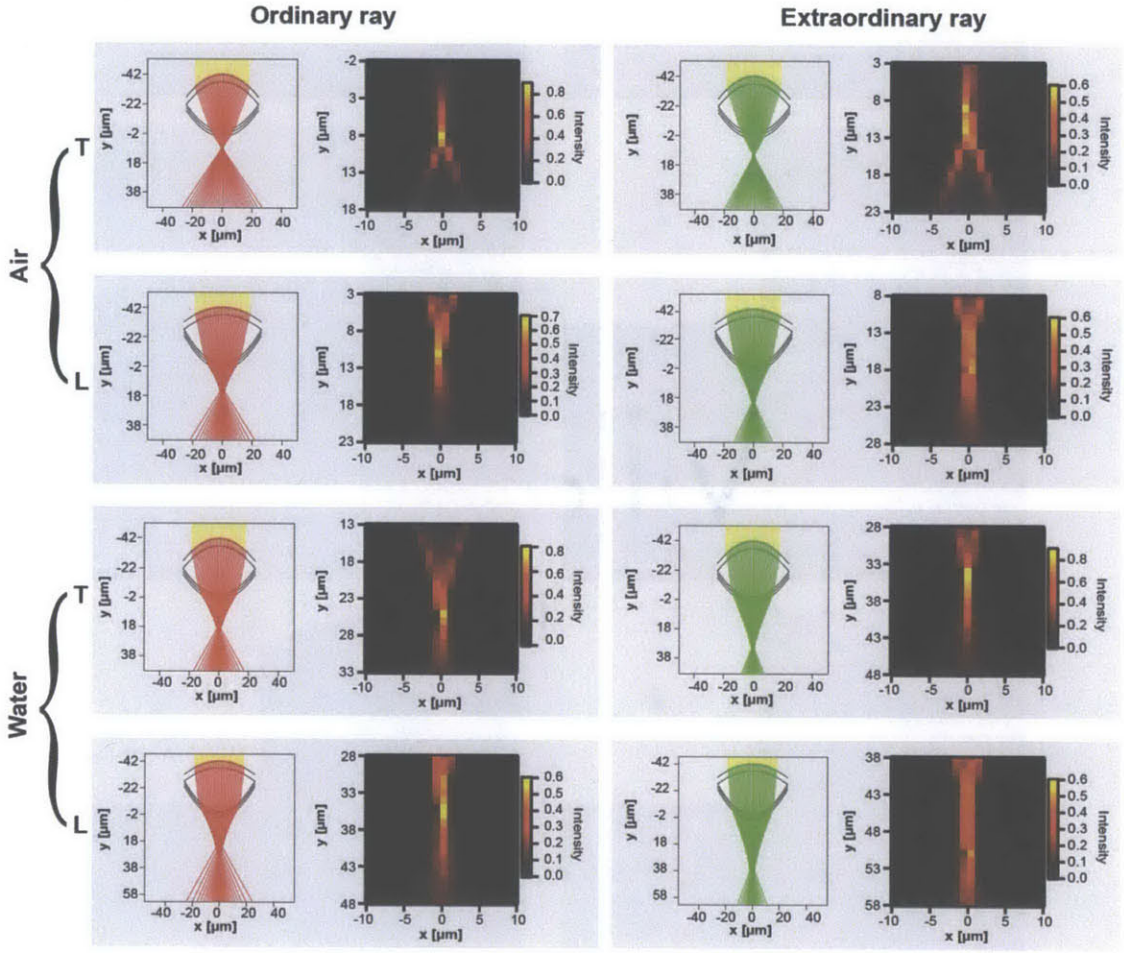

Figure 7-10| 2D ray-trace simulations of an eye of the chiton *A. granulata*. "Air" and "Water" indicate external environments of air and seawater, respectively. "T" and "L" indicate transverse and longitudinal cross-sectional geometries, respectively.

The key results of the ray-trace simulations are summarized in **Figure 7-11a**, which also includes the experimentally measured geometry of the eye chamber. The ranges of the *F* in air and seawater, 8-28 µm and 25-51 µm below *L2,* respectively, lie within the maximum allowed photoreceptor range, ~4-52 µm, which is constrained above by ICCM and below by the end of the chamber. Interestingly, if θ were 0° or 90° instead of 45°, the maximum values of *F* in seawater would be 35 µm or 71 µm, which means the chamber would be unnecessarily large or small, respectively. Thus, the geometry of the chamber is highly consistent with $\theta \approx 45°$. The

positions of F within the allowed range of photoreceptors suggests that chitons are not required to use different polarizations of light to form images in air and seawater as was previously hypothesized, unless the actual photoreceptor range is much smaller than that which is geometrically permitted. In this context, since birefringence would not increase functionality, it is puzzling why θ is not 0°, which would eliminate double refraction aberrations as in trilobites[140] and brittlestars[121].

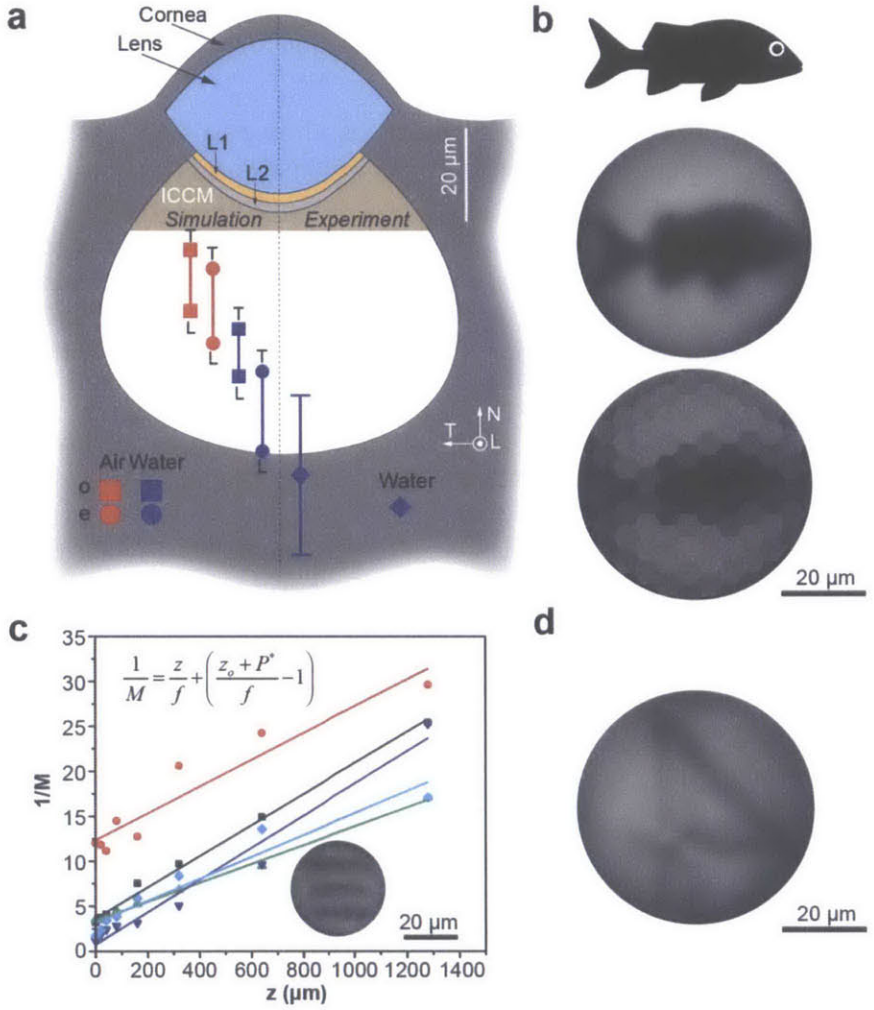

Figure 7-11| Focal length and image formation capacity of the lenses of the eyes the chiton *A. granulata*. **a**, Illustration of the positions of the rear focal points obtained from 2D ray-trace simulations (left) and experiments (right). The red or blue color of the points signifies an external environment of air or water, respectively. "T" and "L" indicate which cross-sectional geometry (transverse or longitudinal, respectively) was simulated. The square and circle symbols represent focal points formed by the ordinary and extraordinary rays, respectively, of the birefringent lens. **b**, Experimental measurements of the focal length, f, of five individual lenses derived from the inverse slope of inverse magnification, $1/M$, vs. object distance, z. **c**, Image formation ability of an individual eye. Top, the object used, which represents the side profile of a predatory fish. Middle, image formed by the lens region of an eye. Bottom, physiological image resolution in which each hexagonal pixel corresponds in size to a single photoreceptor. **d**, Double image of the number "4" produced by the birefringent lens of an eye of the chiton *A. granulata*.

Since the small size and perceived curvature[145] of the chiton lenses have cast doubt on their ability to form images, we decided to experimentally investigate the image formation capabilities of the eyes by projecting objects representative of potential predators through individual lenses (**Figure 7-11b**, top). The middle image of **Figure 7-11b** demonstrates that the lenses can indeed form clear images. This image is analogous to that which would be generated by a 20 cm long fish that is 30 cm away. However, the bottom pixelated image of **Figure 7-11b** represents what the eye is physiologically capable of resolving, since image quality is constrained by the size of the photoreceptors, s ~7 μm. This suggests the maximum distance at which *A. granulata* can spatially resolve a 20 cm object is ~2 m, since at this object distance the image will be approximately the size of a single photoreceptor.

The clear images produced by individual lenses allowed us to test the accuracy of our simulations. We determined f of individual eyes by measuring the dimensions of images produced from a known object at a number of object distances (**Figure 7-11c**). Submerging the lenses in water, we obtained $f = 72 \pm 17$ μm, which is comparable to maximum value of f, 65 μm, determined from ray-trace simulations (**Figure 7-11a**). This allowed us to quantify the resolution of an individual eye, $\Delta\varphi$, using $\Delta\varphi = \tan^{-1}(s/f)$[79]. We determined $\Delta\varphi$ to range between 8-13° in air and 6-9° in seawater. These results explain the outcome of behavioral experiments in which *A. granulata* responded to dark targets with angular size of 9° in both air and seawater.

Double refraction was clearly observed during image formation experiments (**Figure 7-11d; Appendix B, Movie 5**), but not consistently, which may be because the optical axes of the lens and microscope were not aligned parallel in each trial. Similarly, the extent of astigmatism observed was variable, presumably because we did not know the orientation of the transverse and longitudinal directions of each lens relative to the horizontal and vertical lines of our test objects (**Figure 7-11c**, inset). However, the maximum astigmatism observed, $\Delta F = 19$ μm, is consistent with the maximum, $\Delta F = 17$ μm, predicted by our ray-trace simulations.

7.3.4 Mechanical properties

As the mechanical protection is another function which clearly contributes to the chitons' survavibility, the mechanical properties of the mineralized plates are also important to investigate. In addition, relative to the solid non-sensory regions of the outer shell layer, the integration of sensory structures introduces large, localized volumes of soft sensory tissue, and modifies the aragonite-based microstructure at the intrinsic material level. We hypothesized these changes might affect the mechanical robustness of the shell, which is surely critical to survivability.

To test this hypothesis, we first investigated the intrinsic mechanical properties of the lens and surrounding granular region via instrumented nanoindentation (**Figure 7-12**). Indentation with a blunt Berkovich tip allows us to quantify the mechanical properties of the two regions. The two regions exhibit similar indentation hardness (lens: 4.87 ± 0.18 GPa; 5.08 ± 0.29 GPa), and the indentation modulus in the granular region is slightly higher than that in the lens region (lens: 66.41 ± 1.73 GPa; granular: 78.92 ± 1.84 GPa).

Moreover, we used a sharp conospherical indentation tip to probe their fracture behavior. As shown in **Figure 7-12c,d**, indentation induced radial cracking which originated from the indentation site in the lens region, while the damage in the granular region was very localized without any radial cracks. The more brittle fracture behavior in the lens region can be attributed

to its single crystal-like structure, where the large grains are highly aligned. In addition, less amount of organic inclusions within the lens region might also result less resistance to inelastic deformation, such as crack propagations.

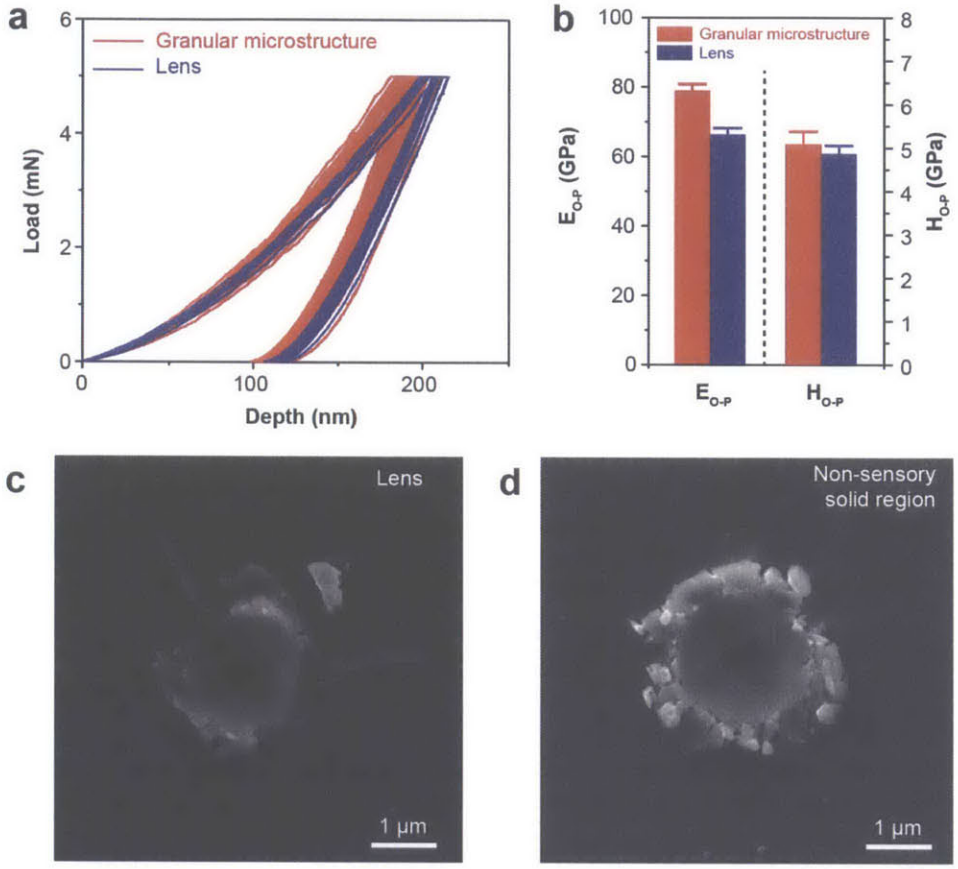

Figure 7-12| Nanomechanical properties of a lens and non-sensory region of the outer shell layer of the chiton *A. granulata*. **a**, Force-depth curves through nanoindentation tests using a Berkovich tip. **b**, Indentation modulus and hardness derived from the nanoindentation tests of (**c**) using the Oliver-Pharr method.,**d**, SEM images of residual indents in the non-sensory and lens regions, respectively, after nanoindentation with a sharp conospherical tip (semi-angle = 30°; tip radius = ~1 μm; maximum load = 4 mN).

To probe the mechanical behavior on the scale of the entire sensory structures, we used a flat punch tip to perform "crush" experiments on the eyes, megalaesthetes, and solid non-sensory regions (**Figure 7-13a**). As illustrated by the load-depth curves in **Figure 7-13b**, compression of eyes first induced gradual fracture of the protective corneal layer (**Figure 7-13b**, inset), and eventually led to catastrophic failure by pushing the entire lens into the chamber, as shown in the post-test SEM image (**Figure 7-13c**). The average load for the catastrophic fracture of lens is slightly less than 1 N (0.84 ± 0.11 N). With a maximum load of 1N, the megalaesthetes exhibited step-wise micro-fracture up to the maximum load without catastrophic failure (**Figure 7-13d**). Similar indentation on the solid non-sensory protrusions induced a relatively small amount of permanent deformation, demonstrating its greater mechanical integrity (**Figure 7-13e**).

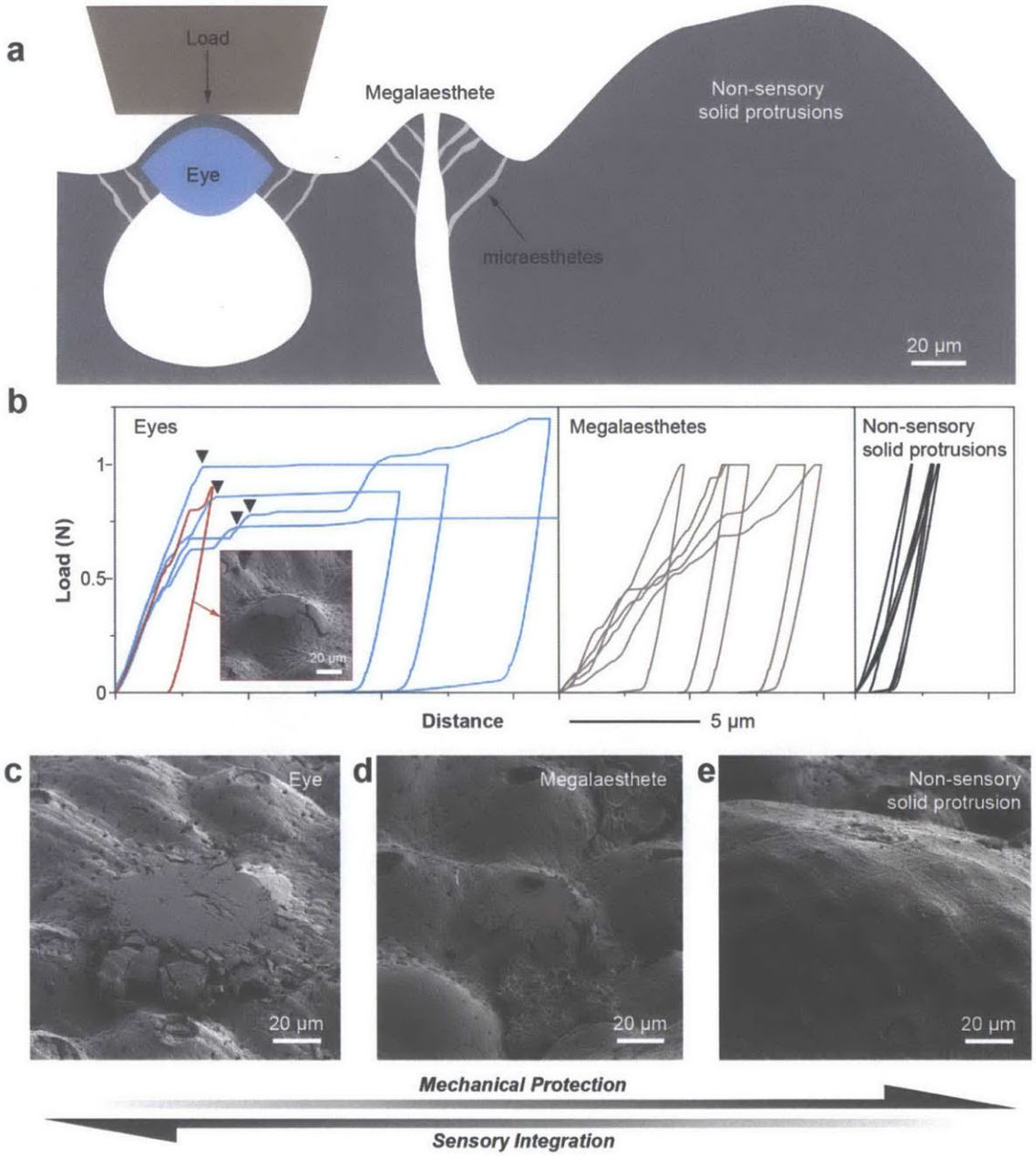

Figure 7-13| Trade-offs between mechanical protection and sensory integration. a, Schematic diagram of the three superficial areas of the outer shell layer: non-sensory regions, megalaesthetes, and eyes. **b**, Microindentation force vs. depth curves for the non-sensory, megalaesthete, and eye regions of the outer shell layer. The approximate size and geometry of the indenter relative to surface features is shown in (**a**). The SEM inset shows the onset of plastic deformation in the eye region, where the cornea fractures radially. **c-e**, SEM images of residual indents in the non-sensory, megalaesthete, and eye regions of the outer shell layer, respectively.

7.4 Discussion and conclusions

Organisms often need to perform multiple tasks that contribute to their fitness, resulting in trade-off situations[147]. These trade-offs have traditionally been discussed in the context of phenotype morphologies, e.g. the beak shape and size of Darwin's finches. Our study of the structure/property/performance relationships of the shell of *A. granulta* demonstrates that trade-offs are also fundamentally present at the materials level within a single organism. The shells of chitons have evolved to satisfy two conflicting design requirements, protection and sensation. Three design aspects are fundamental to the functional integration of the sensory structures within the armor, and trade-offs this integration creates: 1) the incorporation of soft sensory tissue (creation of a porous network), 2) modification of the geometry of the armor material, and 3) the material-level adjustment of the armor material.

Sensory integration necessitates the incorporation of a living tissue, which creates porosity. This degrades the mechanical robustness of the armor, which can be seen by comparing the mechanical performance of megalaesthetes to the solid non-sensory region. Depending on the species, megalaesthetes may serve a variety of functions including mechano-, chemo-, and/or photoreception. Increasing the integrated optical functionality from simple photoreception to spatial vision (in other words, advancing from megalaesthetes ("eyespots") to eyes) requires a much larger volume of sensory tissue per sensory unit, as well as the modification of the local geometry of the armor material to form a lens. Although the eyes provide distinct optical advantages over megalaesthetes, e.g. the ability distinguish dark objects from uniform decreases in illumination, they further degrade the penetration resistance of the armor. This is demonstrated by the microindentation experiments, in which the megalaesthetes exhibited step-wise micro-fractures while the eyes failed catastrophically at less than 1 N. Furthermore, at the material-level, increasing the grain size and alignment in the lens relative to the granular microstructure of non-sensory regions reduces scattering and improves its ability to focus light. However, this causes the lens the fracture radially upon nanoindentation, which is in stark contrast to the relatively isotropic, localized damage observed in the non-sensory regions. These mechanical disadvantages may constrain the size of the eyes, which could improve in both resolution and sensitivity if larger[79]. In summary, as the size, complexity, and functionality of the integrated sensory elements increases, the local penetration resistance decreases.

Although functional integration decreases the overall mechanical performance of the outer shell layer, *A. granulata* has developed strategies to compensate for its vulnerabilities. First, the mechanically weak sensory regions are strategically located in the valleys created by the protruding, robust non-sensory regions. This likely protects the delicate sensory structures from blunt impacts. These protrusions may also discourage fouling to make sure the sensory regions are not covered. Secondly, it's possible that chitons compensate for the mechanical weakness of the entire outer layer by having thick, hard underlying layers. This is consistent with observations of living chitons which had oyster-drill scars that penetrated the outer layer, but did not pierce the inner layers[251]. Lastly, the apparent redundancy of the eyes will help to reduce the impact of partial shell damage. Eyes in older parts of the shell are often damaged by erosion, and replacements are continually grown at the shell margin. From a visual performance perspective, redundancy also ensures that *A. granulata* can simultaneously monitor the entire hemisphere for threats, which is important since the eyes are static structures and chitons can take several minutes to turn around. Additionally, redundancy can improve sensitive, signal-to-noise ratio, and can help to distinguish false alarms from real threats[252].

Chapter 8 Summary and future directions

8.1 Summary

In this thesis, I studied three biomineralized structural material systems from three exotic mollusk species, each with unique functional optical properties: transparency, photonic coloration, and lens-mediated vision. The intimate interplay between mechanical and optical properties in relation to their distinctive multiscale structural features was elucidated through a combination of experimental and theoretical approaches. The purpose of this section is to summarize the key findings of each model system.

The first part of Chapter 3 investigated the hierarchical structure of the highly transparent bioceramic armor of the bivalve *Placuna placenta*. The heavily mineralized shell of *P. placenta* (~99 wt%) has a single foliated microstructure, which is composed of calcitic building blocks with elongated diamond geometries. The crystallographic orientations are generally aligned by tilting the *c*-axes by ~24° along the longitudinal directions of building blocks, despite the presence of crystallographic misorientations amongst adjacent building blocks. Both macroscopic and microscopic optical measurements indicate that the shell is able to transmit ~80% of total incident light, although more than half of the transmitted light is scattered. The structural and crystallographic information at the building block level were directly incorporated into a light scattering model to further investigate the optical properties of the shell, as discussed in the second part of the chapter. The predictions of the model were highly consistent with experimental results. Decoupling the major contributions to scattering suggests that the most important factor is birefringence scattering due to the crystallographic misorientations amongst the building blocks.

Chapter 4 presented a detailed study of the deformation behavior of the shell of *P. placenta* at the nanometer scale using primarily instrumented nanoindentation and electron microscopy. Quantitative mechanical measurements allowed a direct comparison of key mechanical parameters between the *P. placenta* shell and its abiotic counterpart, i.e. single-crystal calcite. The bioceramic armor of *P. placenta*, despite being 99% chemically similar to abiotic calcite, is superior in almost every mechanical aspect, including enhanced resistance to penetration, localized and isotropic deformation, graceful failure, small permanent damage zone, and high energy dissipation efficiency. With comprehensive electron microscopy analysis, we, for the first time, revealed that pervasive nanoscale deformation twinnings are produced surrounding indentation sites. These deformation twins not only provide damage localization with the twinning boundaries, but also catalyze a series of additional nanoscale energy dissipation mechanisms, such as organic interface opening, fragmentation, grain formation and reorientation, and amorphization. These nanoscale deformation mechanisms work synergistically to enhance the energy dissipation efficiency by almost of an order of magnitude in comparison to single-crystal calcite.

Chapter 5 further explored the deformation behavior of *P. placenta* on a larger length scale via a number of novel techniques. In the first section, I presented a detailed analysis of the distribution of a unique structural motif, i.e. screw dislocation-like connection centers, over large

cross-sectional areas of the shell. Quantitative structural analysis revealed that the density and signs of the connection centers play a critical role in controlling the fracture surface and orientation of building blocks, respectively. In the second part of this work, a customized macroindentation testing method was developed to investigate the mechanical response of this bioceramic armor under high loads. *P. placenta* shells exhibited localized deformation without catastrophic failure even when the shells were entirely penetrated with maximum loads of ~65 N. Similar indentation experiments on calcite plates with a similar thickness easily led to brittle fracture without noticeable inelastic deformation. The post-macroindentation sites were then visualized in 3D by means of synchrotron X-ray μCT analysis, which revealed the formation of a complex interconnecting network of microcracks within the damage zone. This network allows the generation of a large interfacial opening area for energy dissipation while still maintaining structural integrity. In addition, combined with high resolution electron microscopy studies, we provided direct evidence that the connection centers serve as structural holding points for crack deflection and bridging. Moreover, quantitative analysis of the interfacial opening area generated within the damage zone allowed us to estimate its contribution to total energy dissipation, which is consistent with a simple theoretical analysis based on the measured density of connection centers.

The work on the highly transparent shell of *P. placenta* presented in this thesis is the first systematic investigation of the structure-function relationships in a biomineralized armor system with a high optical transmission capability. As a bivalve shell, this bioceramic exoskeleton utilizes material designs similar to those of other common opaque mollusk shells, for example, a layered structure with mineralized building blocks. However, several key structural modifications emerge for achieving high optical transmittance, such as the extremely thin organic interfaces and small intracrystalline organic inclusions. Reducing the amount of secondary phase for high optical transparency is also a common effective design strategy in engineering transparent materials; however, this strategy inevitably compromises the mechanical integrity, especially for laminate-based transparent structural materials. In the bioceramic armor of *P. placenta*, we observe unique deformation mechanisms operating at different length scales in order to counteract these mechanical degradations, including nanoscale deformation twinning and macroscopic damage localization. Although the efficient energy dissipation through nanoscale deformation twinning is material specific, design strategies for facilitating effective activation of these processes, such as building block size, geometry and crystallographic orientation, may be applicable to engineering ceramic systems. Most notably, the remarkable capability of damage localization at the macroscopic level through crack bridging and deflection via the special structural motif of screw dislocation-like connection centers is material generic, which should be applicable to a variety of engineering materials. In particular, with the continuous development of additive manufacturing methods, the effects of this material-generic design strategy can be further explored and refined in order to produce specific structural materials for different loading conditions.

Chapter 6 focuses on the structural origin of another form of light-tissue interaction, i.e. photonic coloration, in the biomineralized shell of the blue-rayed limpet *Patella pellucida*. We, for the first time, described a composite mineralized photonic structure, which is responsible for the striking blue iridescent stripes on the limpet's shell. We showed that the blue color arises from the combination of a microscopic mineralized (calcite-based) multilayer with regular lamella thickness and gap spacing for constructive interference of light, and a disordered array of light-absorbing colloidal particles underneath for enhanced contrast. As discussed in Chapter 2, a

diverse range of biological photonic structures have been reported previously. However, our discovery of the hierarchical photonic system localized in the shell of *P. pellucida* shows for the first time that a mollusk species is able to utilize complex photonic design principles, commonly realized exclusively with organic materials, for producing special mineralized protective shells with functional optical properties. This structure has likely evolved to satisfy an optical purpose (possibly biomimicry) without negatively influencing the shell's mechanical performance, which could improve the organism's overall fitness. This study is an excellent example which shows that mollusks are able to tailor the local composition, structure, and crystallography of their mineralized shells to create and integrate optical elements into their protective shells.

In Chapter 7, I presented a comprehensive investigation of a biomineralized armor system with the third form of light-tissue interaction, i.e. photoreception via a biomineralized lens, in the chiton *Acanthopleura granulata*. Despite some authors' doubts concerning the size and curvature of the lenses, we experimentally demonstrated that the lenses are capable of forming images. These images were used to measure the focal length of the lens, which is consistent with 2D ray-trace simulations in which most of the modelling parameters, including the geometry and crystallography of the lens, were experimentally determined. Finally, microindentation experiments revealed that as the size, complexity, and functionality of the integrated sensory elements within the armor increases, the local mechanical performance of the armor decreases. This type of materials-level trade-off may be fundamental to natural multifunctional materials.

This thesis research explored the material designs for achieving optical effects (transparency, color, and vision) with biomineralized materials in three biological systems Although similar optical phenomena are predominately achieved with organic-based materials in nature, the biological species described in this thesis are able to engineer mineralized materials at multiple length scales in order to achieve desired optical properties. These three systems utilize the same set of design parameters, including the size/geometry of building blocks, interfaces, and composition and crystallography. These parameters are the exactly same ones used for controlling the mechanical properties of biomineralized armor materials. With the same tools in the toolbox, biological systems use them in different ways for mechanical and optical purposes. For example, slight crystallographic misorientations are present in the *P. placenta* shell for enhanced penetration resistance, while highly aligned crystal orientation is preferred in the lens of *A. granulata* to minimize aberrations. The intricate multilayered structure is necessary for photonic coloration in the shell of *P. pellucida*, while well-controlled parabolic surface curvatures of the lens are extremely valuable to achieve focused images in *A. granulata*. I observed that the integration of optical functions degrades mechanical performance to a certain extent. However, each system develops its own unique measures to counteract these degradations, such as the interconnection structure in *P. placenta* to reduce interface delamination, effective integration of the photonic multilayer in *P. pellucida* to reduce interfacial stress concentrations, and strategic placement and redundancy of the lens in *A. granulata* to avoid and compensate for damage.

In addition to elucidating the structure-function relationships and providing material design strategies, this thesis research also paints a relatively more complete picture for this special group of multifunctional biomineralized materials by considering both mechanical and optical properties. These systems might have been evolved under multiple selection pressures (not limited to mechanics and optics as discussed in this thesis) during the hundreds of millions of years of evolution. Identifying the primary biological functions might be the first task for

biomimetic materials research, as it is often assumed that the structure is "*optimized*" through evolution to achieve one presumed function. If we fail to identify the correct or complete set of biological functions, the material design strategies that we find in biological systems might not work effectively to achieve desired properties.

8.2 Future directions

8.2.1 Theoretical study of deformation twinning at building block level of *P. placenta*

Pervasive nanoscale deformation twinning has been shown to be the primary mechanism leading to efficient energy dissipation in the shell of *P. placenta* by activating a number of additional nanoscale processes. Experimental approaches with instrumented nanoindentation and electron microscopy are excellent tools to collect direct evidence of these underlying nanoscale mechanisms. However, several limitations of this approach are obvious. Firstly, it is difficult to study the mechanical behavior in a parametric and systematic manner. For example, we cannot vary the mineral layer thickness of *P. placenta* to investigate its effect on the deformation mechanisms. Secondly, it is challenging to infer direct dynamic in-situ information during deformation from post-indentation analysis.

Recently, there have been significant development in computational simulations of the mechanical deformation behavior of engineering materials due to the improvement of algorithms and computing power[189,253–255]. In particular, simulations at the atomic level are capable of providing direct information of the dynamic deformation mechanisms. Using atomistic simulations to investigate the deformation twining in *P. placenta* could provide a more in-depth understanding of the system. For example, by parametrically varying the thickness of the calcite layers, it is possible to explore the effect on twining and potentially answer the question of whether or not the thickness is optimized for twinning. Moreover, a parametric study on the crystallographic misorientation among calcite layers may provide insights on its effect on the progression of activation deformation twinning. These simulations will all provide the temporal information of the entire deformation process. This approach will be able to provide us further design strategies to apply to advanced engineering structural materials.

8.2.2 3D structural characterizations of photonic multi-layer in *P. pellucida*

In this thesis, the biomineralized photonic multi-layer structure in *P. pellucida* was investigated primarily with electron microscopy techniques. These methods provide 2D information of the nanoscopic structure; however, detailed information about the 3D architecture is still lacking. Special reinforcing structures, such as dislocation-like connections and mineral bridges, were observed and are believed to enhance the structural integrity. However, their 3D architecture and distribution is not clear. Since this photonic multilayer is also an integrated structure within the armor, mechanical protection should also be a major design constraint of this multifunctional material system.

Conventional X-ray μCT does not provide enough resolution to resolve such nanoscopic structures; therefore, other techniques should be considered. For example, two approaches might be appropriate: focused ion beam-based tomography using a slice and view technique, and synchrotron X-ray based nanotomography. Once the detailed 3D information is obtained, their

mechanical properties can be investigated through finite element analysis by directly using the reconstructed 3D structure.

REFERENCES

1. Nemat-nasser, S., Plaisted, T., Starr, A. & Amirkhizi, A. V. in *Biomimetics Biol. Inspired Technol.* (Bar-Cohen, Y.) (2005).

2. Fratzl, P., Dunlop, J. & Weinkamer, R. *Materials Design Inspired by Nature.* (Royal Society of Chemistry, 2013).

3. Bhushan, B. Biomimetics: lessons from nature--an overview. *Philos. Trans. A. Math. Phys. Eng. Sci.* **367,** 1445–86 (2009).

4. Dunlop, J. W. C. & Fratzl, P. Biological Composites. *Annu. Rev. Mater. Res.* **40,** 1–24 (2010).

5. Wegst, U. G. K. & Ashby, M. F. The mechanical efficiency of natural materials. *Philos. Mag.* **84,** 2167–2186 (2004).

6. Ortiz, C. & Boyce, M. C. Bioinspired Structural Materials. *Science (80-.).* **319,** 1053–1054 (2008).

7. Studart, A. R. Towards high-performance bioinspired composites. *Adv. Mater.* **24,** 5024–44 (2012).

8. Grujicic, M., Bell, W. C. & Pandurangan, B. Design and material selection guidelines and strategies for transparent armor systems. *Mater. Des.* **34,** 808–819 (2012).

9. Nicol, D. The number of living species of molluscs. *Syst. Zool.* **18,** 251–254 (1969).

10. Vermeij, G. J. *A natural history of shells.* 207 (Princeton University Press, 1993).

11. Caner, C. J. G., Bandel, K., Buffrenil, V. De & Carlson, S. in *Skelet. Biomineral. Patterns, Process. Evol. Trends* (Carter, J. G.) 337–352 (2013).

12. Currey, J. D. & Taylor, J. D. The mechanical behavior of some molluscan hard tissues. *J. Zool., Lond.* **173,** 395–406 (1974).

13. Bruet, B. J. F. Multiscale Structural and Mechanical Design of Mineralized Biocomposites. 222 (2008).

14. Lowenstam, H. A. & Weiner, S. *On biomineralization.* (Oxford University Press, 1989).

15. Yao, H. *et al.* Protection mechanisms of the iron-plated armor of a deep-sea hydrothermal vent gastropod. *PNAS* **107,** 987–92 (2010).

16. Williams, A., Cusack, M. & Mackay, S. Collagenous Chitinophosphatic Shell of the Brachiopod Lingula. *Philos. Trans. R. Soc. B Biol. Sci.* **346,** 223–266 (1994).

17. Merkel, C. *et al.* Micromechanical properties and structural characterization of modern inarticulated brachiopod shells. *J. Geophys. Res.* **112,** G02008 (2007).

18. Nudelman, F. *et al.* Forming nacreous layer of the shells of the bivalves Atrina rigida and Pinctada margaritifera: an environmental- and cryo-scanning electron microscopy study. *J. Struct. Biol.* **162,** 290–300 (2008).

19. Younis, S., Kauffmann, Y., Bloch, L., Zolotoyabko, E. & Kau, Y. Inhomogeneity of Nacre Lamellae on the Nanometer Length Scale. *Cryst. Growth Des.* **12,** 4574–4579 (2012).

20. Li, H. *et al.* Calcite Prisms from Mollusk Shells (Atrina Rigida): Swiss-cheese-like Organic-Inorganic Single-crystal Composites. *Adv. Funct. Mater.* **21,** 2028–2034 (2011).

21. Weiner, S. & Dover, P. M. in *Biomineralization* (Dove, P. M., De Yoreo, J. J. & Weiner, S.) 1–29 (2003).

22. Belcher, A. M. *et al.* Control of crystal phase switching and orientation by soluble mollusc-shell proteins. *Nature* **381,** 56–58 (1996).

23. Addadi, L. & Weiner, S. Interactions between acidic proteins and crystals: stereochemical requirements in biomineralization. *PNAS* **82,** 4110–4 (1985).

24. Weiner, S. & Addadi, L. Crystallization Pathways in Biomineralization. *Annu. Rev. Mater. Res.* **41,** 21–40 (2011).

25. Fratzl, P. & Weinkamer, R. Nature's hierarchical materials. *Prog. Mater. Sci.* **52,** 1263–1334 (2007).

26. Aizenberg, J. *et al.* Skeleton of Euplectella sp.: structural hierarchy from the nanoscale to the macroscale. *Science (80-.).* **309,** 275–278 (2005).

27. Weaver, J. C. *et al.* The stomatopod dactyl club: a formidable damage-tolerant biological hammer. *Science* **336,** 1275–1280 (2012).

28. Bruet, B. J. F., Song, J., Boyce, M. C. & Ortiz, C. Materials design principles of ancient fish armour. *Nat. Mater.* **7,** 748–56 (2008).

29. Kamat, S., Su, X., Ballarini, R. & Heuer, A. H. Structural basis for the fracture toughness of the shell of the conch Strombus gigas. *Nature* **405,** 1036–1040 (2000).

30. Lin, A. & Meyers, M. A. Growth and structure in abalone shell. *Mater. Sci. Eng. A* **390,** 27–41 (2005).

31. Lopez, M. I., Meza Martinez, P. E. & Meyers, M. A. Organic interlamellar layers, mesolayers and mineral nanobridges: Contribution to strength in abalone (Haliotis rufescence) nacre. *Acta Biomater.* **10,** 2056–2064 (2013).

32. Bruet, B. J. F. *et al.* Nanoscale morphology and indentation of individual nacre tablets from the gastropod mollusc Trochus niloticus. *J. Mater. Res.* **20,** 2400–2419 (2005).

33. Checa, A. G., Cartwright, J. H. E. & Willinger, M.-G. Mineral bridges in nacre. *J. Struct. Biol.* **176,** 330–339 (2011).

34. Gries, K., Kröger, R., Kübel, C., Fritz, M. & Rosenauer, A. Investigations of voids in the aragonite platelets of nacre. *Acta Biomater.* **5,** 3038–3044 (2009).

35. Gries, K. *et al.* Correlation of the orientation of stacked aragonite platelets in nacre and their connection via mineral bridges. *Ultramicroscopy* **109,** 230–236 (2009).

36. Pokroy, B. *et al.* Atomic Structure of Biogenic Aragonite. *Chem. Mater.* **19,** 3244–3251 (2007).

37. Pokroy, B., Quintana, J. P., Caspi, E. N., Berner, A. & Zolotoyabko, E. Anisotropic lattice distortions in biogenic aragonite. *Nat. Mater.* **3,** 900–902 (2004).

38. Kim, Y.-Y. *et al.* An artificial biomineral formed by incorporation of copolymer micelles in calcite crystals. *Nat. Mater.* **10,** 890–896 (2011).

39. Chateigner, D., Hedegaard, C. & Wenk, H. Mollusc shell microstructures and crystallographic textures. *J. Structrual Geol.* **22,** 1723–1735 (2000).

40. Checa, A. G., Esteban-Delgado, F. J. & Rodríguez-Navarro, A. B. Crystallographic structure of the foliated calcite of bivalves. *J. Struct. Biol.* **157,** 393–402 (2007).

41. Pérez-Huerta, A., Dauphin, Y., Cuif, J. P. & Cusack, M. High resolution electron backscatter diffraction (EBSD) data from calcite biominerals in recent gastropod shells. *Micron* **42,** 246–251 (2011).

42. Checa, A. G. *et al.* Crystallographic control on the substructure of nacre tablets. *J. Struct. Biol.* **183,** 368–76 (2013).

43. Gilbert, P. U. P. a *et al.* Gradual ordering in red abalone nacre. *J. Am. Chem. Soc.* **130,** 17519–17527 (2008).

44. Ma, Y. *et al.* The grinding tip of the sea urchin tooth exhibits exquisite control over calcite crystal orientation and Mg distribution. *PNAS* **106,** 6048–6053 (2009).

45. Currey, J. D. Mechanical Properties of Mother of Pearl in Tension. *Proc. R. Soc. Lond. B* **196,** 443–463 (1977).

46. Jackson, a. P., Vincent, J. F. V. & Turner, R. M. The Mechanical Design of Nacre. *Proc. R. Soc. B Biol. Sci.* **234,** 415–440 (1988).

47. Wang, R. Z., Suo, Z., Evans, A. G., Yao, N. & Aksay, I. A. Deformation mechanisms in nacre. *J. Mater. Res.* **16,** 2485–2493 (2011).

48. Menig, R., Meyers, M. H., Meyers, M. A. & Vecchio, K. S. Quasi-static and dynamic mechanical response of Haliotis Rufescens (Abalone) shells. *Acta Mater.* **48,** 2383–2398 (2000).

49. Barthelat, F., Tang, H., Zavattieri, P., Li, C. & Espinosa, H. On the mechanics of mother-of-pearl: A key feature in the material hierarchical structure. *J. Mech. Phys. Solids* **55,** 306–337 (2007).

50. Barthelat, F. & Espinosa, H. D. An Experimental Investigation of Deformation and Fracture of Nacre–Mother of Pearl. *Exp. Mech.* **47,** 311–324 (2007).

51. Pokroy, B., Demensky, V. & Zolotoyabko, E. Inhomogeneous Strain/Stress Profiles in the Nacre Layer of Mollusk Shells. *Metall. Mater. Trans. A* **42,** 554–558 (2010).

52. Barthelat, F. & Rabiei, R. Toughness amplification in natural composites. *J. Mech. Phys. Solids* **59,** 829–840 (2011).

53. Rabiei, R., Bekah, S. & Barthelat, F. Failure mode transition in nacre and bone-like materials. *Acta Biomater.* **6,** 4081–9 (2010).

54. Mayer, G. Rigid biological systems as models for synthetic composites. *Science* **310,** 1144–1147 (2005).

55. Sumitomo, T., Kakisawa, H., Owaki, Y. & Kagawa, Y. In situ transmission electron microscopy observation of reversible deformation in nacre organic matrix. *J. Mater. Res.* **23,** 1466–1471 (2011).

56. Smith, B. L. *et al.* Molecular mechanistic origin of the toughness of natural adhesives , fibres and composites. *Nature* **399,** 761–763 (1999).

57. Song, F., Soh, a. K. & Bai, Y. L. Structural and mechanical properties of the organic matrix layers of nacre. *Biomaterials* **24,** 3623–3631 (2003).

58. Evans, A. G. *et al.* Model for the robust mechanical behavior of nacre. *J. Mater. Res.* **16,** 2475–2484 (2001).

59. Espinosa, H. D. *et al.* Tablet-level origin of toughening in abalone shells and translation to synthetic composite materials. *Nat. Commun.* **2,** 173 doi: 10.1038/ncomms1172 (2011).

60. Fleischli, F. D., Dietiker, M., Borgia, C. & Spolenak, R. The influence of internal length scales on mechanical properties in natural nanocomposites: a comparative study on inner layers of seashells. *Acta Biomater.* **4,** 1694–706 (2008).

61. Bonderer, L. J., Studart, A. R. & Gauckler, L. J. Bioinspired design and assembly of platelet reinforced polymer films. *Science* **319,** 1069–73 (2008).

62. Gao, H., Ji, B., Ja, I. L., Arzt, E. & Fratzl, P. Materials become insensitive to flaws at nanoscale. *PNAS* **100,** 5597–5600 (2003).

63. Ji, B. & Gao, H. Mechanical properties of nanostructure of biological materials. *J. Mech. Phys. Solids* **52,** 1963–1990 (2004).

64. Ballarini, R., Kayacan, R., Ulm, F.-J., Belytschko, T. & Heuer, A. H. Biological Structures Mitigate Catastrophic Fracture Through Various Strategies. *Int. J. Fract.* **135,** 187–197 (2005).

65. Li, X., Chang, W.-C., Chao, Y. J., Wang, R. & Chang, M. Nanoscale Structural and Mechanical Characterization of a Natural Nanocomposite Material: The Shell of Red Abalone. *Nano Lett.* **4,** 613–617 (2004).

66. Li, X., Xu, Z.-H. & Wang, R. In situ observation of nanograin rotation and deformation in nacre. *Nano Lett.* **6,** 2301–2304 (2006).

67. Li, X. & Huang, Z. Unveiling the Formation Mechanism of Pseudo-Single-Crystal Aragonite Platelets in Nacre. *Phys. Rev. Lett.* **102,** 1–4 (2009).

68. Fratzl, P., Gupta, H. S., Fischer, F. D. & Kolednik, O. Hindered Crack Propagation in Materials with Periodically Varying Young's Modulus—Lessons from Biological Materials. *Adv. Mater.* **19,** 2657–2661 (2007).

69. Pokroy, B. *et al.* Anisotropic lattice distortions in the mollusk-made aragonite: a widespread phenomenon. *J. Struct. Biol.* **153,** 145–150 (2006).

70. Kamat, S., Kessler, H., Ballarini, R., Nassirou, M. & Heuer, A. H. Fracture mechanisms of the Strombus gigas conch shell: II-micromechanics analyses of multiple cracking and large-scale crack bridging. *Acta Mater.* **52,** 2395–2406 (2004).

71. Kessler, H., Ballarini, R., Mullen, R. L., Kuhn, L. T. & Heuer, A. H. A biomimetic example of brittle toughening: (I) steady state multiple cracking. *Comput. Mater. Sci.* **5,** 157–166 (1996).

72. Kessler, H. *et al.* Correction to "A biomimetic example of brittle toughening. I. Steady state multiple cracking."*Comput. Mater. Sci.* **5,** 353–355 (1996).

73. Wang, R. & Gupta, H. S. Deformation and Fracture Mechanisms of Bone and Nacre. *Annu. Rev. Mater. Res.* **41,** 41–73 (2011).

74. Delgado-Vargas, F., Jiménez, a R. & Paredes-López, O. Natural pigments: carotenoids, anthocyanins, and betalains--characteristics, biosynthesis, processing, and stability. *Crit. Rev. Food Sci. Nutr.* **40,** 173–289 (2000).

75. Slabaugh, R., Alkema, J. & Seagerl, S. L. The Chemical Pigments of Plants. **59,** 183–186 (1982).

76. Haddock, S. H. D., Moline, M. a & Case, J. F. Bioluminescence in the sea. *Ann. Rev. Mar. Sci.* **2,** 443–493 (2010).

77. Kolle, M. Photonic structures inspired by nature. *Philosophy* 151 (2010).

78. Johnsen, S. Hidden in plain sight: the ecology and physiology of organismal transparency. *Biol. Bull.* **201,** 301–318 (2001).

79. Land, M. F. & Nilsson, D. E. *Animal eyes*. 271 (2012).

80. Alfonsopazphoto. Picture of Flamingo rubro-Phoenicopterus ruber ruber. (2005). at <http://en.wikipedia.org/wiki/File:Flamingo_rubro-Phoenicopterus_ruber_ruber.jpg>

81. Nagata, T. *et al.* Depth Perception from Image Defocus in a Jumping Spider. *Science (80-.).* **335,** 469–471 (2012).

82. Riley, P. A. Melanin. *Int. J. Biochem. Cell Biol.* **29,** 1235–1239 (1997).

83. Harvey, N. Studies on bioluminescence. IX. Chemical nature of Cypridina luciferin and Cypridina luciferase. *J. Gen. Physiol.* 269–293 (1919).

84. Brown, F. A., Burtt, E. H., Fox, D. L. & Losey, G. S. Coloration. *Encycl. Br. Online Acad. Ed.* (2014). at <http://www.britannica.com/EBchecked/topic/126546/coloration>

85. Pouya, C., Stavenga, D. G. & Vukusic, P. Discovery of ordered and quasi-ordered photonic crystal structures in the scales of the beetle Eupholus magnificus. *Opt. Express* **19,** 11355–11364 (2011).

86. Welch, V. L. & Vigneron, J.-P. Beyond butterflies—the diversity of biological photonic crystals. *Opt. Quantum Electron.* **39,** 295–303 (2007).

87. Jordan, T. M., Partridge, J. C. & Roberts, N. W. Non-polarizing broadband multilayer reflectors in fish. *Nat. Photonics* **6,** 759–763 (2012).

88. Prum, R. O. Structural colouration of mammalian skin: convergent evolution of coherently scattering dermal collagen arrays. *J. Exp. Biol.* **207,** 2157–2172 (2004).

89. Prum, R. O., Torres, R. H., Williamson, S. & Dyck, J. Coherent light scattering by blue feather barbs. *Nature* **396,** 28–29 (1998).

90. D'Alba, L. *et al.* Colour-producing β-keratin nanofibres in blue penguin (Eudyptula minor) feathers. *Biol. Lett.* **7,** 543–546 (2011).

91. Kramer, R. M., Crookes-Goodson, W. J. & Naik, R. R. The self-organizing properties of squid reflectin protein. *Nat. Mater.* **6,** 533–8 (2007).

92. Johnsen, S. Transparent Animals. *Sci. Am.* 81–89 (2000).

93. Johnsen, S. & Widder, E. The physical basis of transparency in biological tissue: ultrastructure and the minimization of light scattering. *J. Theor. Biol.* **199,** 181–198 (1999).

94. Shi, Y. *et al.* The stratified syncytium of the vertebrate lens. *J. Cell Sci.* **122,** 1607–1615 (2009).

95. Bassnett, S., Shi, Y. & Vrensen, G. F. J. M. Biological glass: structural determinants of eye lens transparency. *Philos. Trans. R. Soc. Lond. B. Biol. Sci.* **366,** 1250–64 (2011).

96. Dahm, R. Nuclear degradation in the lens, circa 1897-1899. *Sci.* **23,** 84 (2009).

97. Wallin, M. Nature's palette: How animals, including humans, produce colours. *Biosci. Explain.* **1,** 1–12 (2002).

98. Fujii, R. in *Fish Physiol.* (Hoar, W. S. & Randall, D. J.) (Academic Press Inc., 1969).

99. Fox, D. L. *Animal biochromes and structural colours: Chemical, Distributional & Physiological Features of Coloured Bodies in the Animal World.* 433 (University of California Press, 1976).

100. Shawkey, M. D., Morehouse, N. I. & Vukusic, P. A protean palette: colour materials and mixing in birds and butterflies. *J. R. Soc. Interface* **6,** S221–S231 (2009).

101. Mäthger, L. M., Denton, E. J., Marshall, N. J. & Hanlon, R. T. Mechanisms and behavioural functions of structural coloration in cephalopods. *J. R. Soc. Interface* **6,** S149–S163 (2009).

102. Parker, A. R. The diversity and implications of animal structural colours. *J. Exp. Biol.* **201,** 2343–2347 (1998).

103. Crowson, R. A. in *Biol. Coleopt.* (Crowson, R. A.) 292–321 (Elsevier Ltd, 1981).

104. Zi, J. *et al.* Coloration strategies in peacock feathers. *PNAS* **100,** 12576–12578 (2003).

105. Yoshioka, S. & Kinoshita, S. Effect of Macroscopic Structure in Iridescent Color of the Peacock Feathers. *Forma* **17,** 169–181 (2002).

106. Stavenga, D. G., Tinbergen, J., Leertouwer, H. L. & Wilts, B. D. Kingfisher feathers-colouration by pigments, spongy nanostructures and thin films. *J. Exp. Biol.* **214,** 3960–3967 (2011).

107. Vukusic, P. & Sambles, J. R. Photonic structures in biology. *Nature* **424,** 852–855 (2003).

108. Parker, A. R. & Martini, N. Structural colour in animals—simple to complex optics. *Opt. Laser Technol.* **38,** 315–322 (2006).

109. Kinoshita, S. *Structural Colors in the Realm of Nature*. 368 (World Scientific Publishing Company, 2008).

110. Simonis, P. & Vigneron, J. P. Structural color produced by a three-dimensional photonic polycrystal in the scales of a longhorn beetle: Pseudomyagrus waterhousei (Coleoptera: Cerambicidae). *Phys. Rev. E* **83,** 011908 (2011).

111. Kinoshita, S., Yoshioka, S. & Miyazaki, J. Physics of structural colors. *Reports Prog. Phys.* **71,** 076401 (2008).

112. Kinoshita, S. & Yoshioka, S. Structural colors in nature: the role of regularity and irregularity in the structure. *Chemphyschem* **6,** 1442–1459 (2005).

113. Johnsen, S. & Widder, E. A. Transparency and Visibility of Gelatinous Zooplankton from ihe Northwestern Atlantic and Gulf of Mexico. *Biol. Bull.* **195,** 337–348 (1998).

114. Johnsen, S. & Widder, E. A. Ultraviolet absorption in transparent zooplankton and its implications for depth distribution and visual predation. *Mar. Biol.* **138,** 717–730 (2001).

115. Bassnett, S., Wilmarth, P. A. & David, L. L. The membrane proteome of the mouse lens fiber cell. *Mol. Vis.* **15,** 2448–2463 (2009).

116. Blankenship, T., Bradshaw, L., Shibata, B. & Fitzgerald, P. Structural specializations emerging late in mouse lens fiber cell differentiation. *Invest. Ophthalmol. Vis. Sci.* **48,** 3269–3276 (2007).

117. Clarkson, E. N. K. The visual system of trilobites. *Palaeontology* **22,** 1–22 (1979).

118. Clarkson, E., Levi-Setti, R. & Horváth, G. The eyes of trilobites: The oldest preserved visual system. *Arthropod Struct. Dev.* **35,** 247–259 (2006).

119. Schoenemann, B. & Clarkson, E. N. K. Light guide lenses in trilobites? *Earth Environ. Sci. Trans. R. Soc. Edinburgh* **102,** 17–23 (2011).

120. Lee, M. R., Torney, C. & Owen, A. W. Biomineralisation in the Palaeozoic oceans: Evidence for simultaneous crystallisation of high and low magnesium calcite by phacopine trilobites. *Chem. Geol.* **314-317,** 33–44 (2012).

121. Aizenberg, J., Tkachenko, A., Weiner, S., Addadi, L. & Hendler, G. Calcitic microlenses as part of the photoreceptor system in brittlestars. *Nature* **412,** 819–822 (2001).

122. Moseley, H. N. On the Presence of Eyes in the Shells of Certain Chitonidae, and on the Structure of These Organs. *Q. J. Microsc. Sci.* **25,** 37–60 (1885).

123. Krell, a., Klimke, J. & Hutzler, T. Transparent compact ceramics: Inherent physical issues. *Opt. Mater. (Amst).* **31,** 1144–1150 (2009).

124. Launey, M. E. & Ritchie, R. O. On the Fracture Toughness of Advanced Materials. *Adv. Mater.* **21,** 2103–2110 (2009).

125. Wakaki, M., Kudo, K. & Shibuya, T. *Physical Properties and Data of OPtical Materials. CRC Press* 89–96 (2007).

126. Winchell, A. N. *Elements of Optical Mineralogy*. 117–118 (Wiley, 1967).

127. Speiser, D. I., Eernisse, D. J. & Johnsen, S. A chiton uses aragonite lenses to form images. *Curr. Biol.* **21,** 665–670 (2011).

128. Poutiers, J. M. in *Living Mar. Resour. West. Cent. Pacific* 124–141 (1998).

129. Deheyn, D. D. & Wilson, N. G. Bioluminescent signals spatially amplified by wavelength-specific diffusion through the shell of a marine snail. *Proc. R. Soc. B* **278,** 2112–2121 (2011).

130. Hedegaard, C. Molluscan shell pigments: an in situ resonance raman study. *J. Molluscan Stud.* **72,** 157–162 (2006).

131. Brink, D. J., van der Berg, N. G. & Botha, A. J. Iridescent colors on seashells: an optical and structural investigation of Helcion pruinosus. *Appl. Opt.* **41,** 717–722 (2002).

132. Brink, D. J. & van der Berg, N. G. An investigation of green iridescence on the mollusc Patella granatina. *J. Phys. D. Appl. Phys.* **38,** 338–343 (2005).

133. Hayward, P. J. & Ryland, J. S. *Handbook of the marine fauna of North-West Europe.* (Oxford University Press, 1995).

134. Nordsieck, F. & Garcia-Talavera, F. *Moluscos Marinos de Canarias y Madera (Gastropoda).* (1979).

135. Graham, A. & Fretter, V. The life history of Patina pellucida. *J. Mar. Biol. Assoc. UK* **26,** (1974).

136. Serb, J. M. & Eernisse, D. J. Charting Evolution's Trajectory: Using Molluscan Eye Diversity to Understand Parallel and Convergent Evolution. *Evol. Educ. Outreach* **1,** 439–447 (2008).

137. Vendrasco, M. J., Fernandez, C. Z., Eernisse, D. J. & Runnegar, B. Aesthete canal morphology in the Mopaliidae (Polyplacophora). *Am. Malacol. Bull.* **25,** 51–69 (2008).

138. Boyle, P. R. Rhabdomeric Ocellus in a Chiton. *Nature* **222,** 895–896 (1969).

139. Wistow, G. J. & Piatigorsky, J. Lens crystallins: the evolution and expression of proteins for a highly specialized tissue. *Ann. Rev. Biochem.* **57,** 479–504 (1988).

140. Towe, K. M. Trilobite eyes: calcified lenses in vivo. *Science (80-.).* **179,** 1007–1009 (1973).

141. Tanaka, G. Functional morphology and light-gathering ability of podocopid ostracod eyes and the palaeontological implications. *Zool. J. Linn. Soc.* **147,** 97–108 (2006).

142. Tanaka, G. Morphological design and fossil record of the podocopid ostracod naupliar eye. *Hydrobiologia* **538,** 231–242 (2005).

143. Andersson, A. & Nilsson, D. E. Fine Structure and Optical Properties of an Ostracode (Crustacea) Nauplius Eye. *Protoplasma* **107,** 361–374 (1981).

144. Brooker, L. R. Revision of Acanthopleura Guilding, 1829 Mollusca: Polyplacophora) based on light and electron microscopy. *Murdoch Univ.* **1,** (2003).

145. Boyle, P. R. Fine structure of the eyes of Onithochiton neglectus (Mollusca: Polyplacophora). *Zeitschrift für Zellforsch. und mikroskopische Anat.* **102,** 313–332 (1969).

146. Li, L. & Ortiz, C. Biological design for simultaneous optical transparency and mechanical robustness in the shell of Placuna placenta. *Adv. Mater.* **25,** 2344–2350 (2013).

147. Shoval, O. *et al.* Evolutionary trade-offs, Pareto optimality, and the geometry of phenotype space. *Science* **336,** 1157–1160 (2012).

148. Lauder, G. V. & Reilly, S. M. in *Phylogenies Comp. method Anim. Behav.* (Martins, E. P.) 104–137 (Oxford University Press, 1996).

149. Swanson, B. O., Blackledge, T. A., Summers, A. P. & Hayashi, C. Y. Spider dragline silk : correlated and mosaic evolution in high-performance biological materials. *Evolution (N. Y).* **60,** 2539–2551 (2012).

150. Aizenberg, J., Sundar, V. C., Yablon, A. D., Weaver, J. C. & Chen, G. Biological glass fibers: correlation between optical and structural properties. *PNAS* **101,** 3358–3363 (2004).

151. Song, J. *et al.* Quantitative microstructural studies of the armor of the marine threespine stickleback (Gasterosteus aculeatus). *J. Struct. Biol.* **171,** 318–331 (2010).

152. Sands, J. M. *et al.* Transparent armour materials. *J. Eur. Ceram. Soc.* **12,** 82–91 (2008).

153. Patel, P. J., Gilde, G. A., Dehmer, P. G., McCauley, J. W. & Armor, T. Transparent Armor. *AMPTIAC Newsl.* **4,** 1 (2000).

154. Patel, P. J., Gilde, G. A., Dehmer, P. G. & Mccauley, J. W. Transparent ceramics for armor and EM window applications. *Proc. SPIE* **4102,** 1–14 (2000).

155. Peelen, J. G. J. & Metselaar, R. Light scattering by pores in polycrystalline materials: transmission properties of alumina. *J. Appl. Phys.* **45,** 216–220 (1974).

156. Apetz, R. & Bruggen, M. P. B. Van. Transparent Alumina : A Light-Scattering Model. *Measurement* **86,** 480–486 (2003).

157. Yamashita, I., Nagayama, H. & Tsukuma, K. Transmission Properties of Translucent Polycrystalline Alumina. *J. Am. Ceram. Soc.* **91,** 2611–2616 (2008).

158. Mätzler, C. *MATLAB Functions for Mie Scattering and Absorption Version 2. Unversity Bern* (2002).

159. Sweeney, A. M., Des Marais, D. L., Ban, Y.-E. A. & Johnsen, S. Evolution of graded refractive index in squid lenses. *J. R. Soc. Interface* **4,** 685–698 (2007).

160. Vörös, J. The density and refractive index of adsorbing protein layers. *Biophys. J.* **87,** 553–561 (2004).

161. Taylor, J. D. The structural evolution of the bivalve shells. *Palaeontology* **16,** 519–534 (1973).

162. Carter, J. G. *Skeletal biomineralization: patterns, processes and evolutionary trends. Skelet. Biominer. patterns, Process. Evol. trends* (1990).

163. Robach, J. S., Stock, S. R. & Veis, a. Transmission electron microscopy characterization of macromolecular domain cavities and microstructure of single-crystal calcite tooth plates of the sea urchin Lytechinus variegatus. *J. Struct. Biol.* **151,** 18–29 (2005).

164. Su, X., Kamat, S. & Heuer, A. H. The structure of sea urchin spines, large biogenic single crystal of calcite. *J. Mater. Sci.* **5,** 5545–5551 (2000).

165. Heinemann, F., Launspach, M., Gries, K. & Fritz, M. Gastropod nacre: structure, properties and growth--biological, chemical and physical basics. *Biophys. Chem.* **153,** 126–153 (2011).

166. Jensen, D. G. Estimation of the size distribution of spherical, disc-like or ellipsoidal particles in thin foils. *J. Phys. D Appl. Phys.* **28,** 549–558 (1995).

167. Zhao, J., Zhou, B., Liu, B. & Guo, W. Elasticity of single-crystal calcite by first-principles calculations. *J. Comput. Theor. Nanosci.* **6,** 1181–1188 (2009).

168. Krell, A., Hutzler, T. & Klimke, J. Transmission physics and consequences for materials selection, manufacturing, and applications. *J. Eur. Ceram. Soc.* **29,** 207–221 (2009).

169. Checa, A. A new model for periostracum and shell formation in Unionidae (Bivalvia, Mollusca). *Tissue Cell* **32,** 405–416 (2000).

170. Hillman, R. E. Formation of the periostracum in Mercenaria mercenaria. *Science (80-.).* **134,** 1754–1755 (1961).

171. Greer, J. R. & De Hosson, J. T. M. Plasticity in small-sized metallic systems: Intrinsic versus extrinsic size effect. *Prog. Mater. Sci.* **56,** 654–724 (2011).

172. Ma, Y., Cohen, S. R., Addadi, L. & Weiner, S. Sea urchin tooth design: an "all-calcite" polycrystalline reinforced fiber composite for grinding rocks. *Adv. Mater.* **20,** 1555–1559 (2008).

173. Connors, M. J. *et al.* Three-dimensional structure of the shell plate assembly of the chiton Tonicella marmorea and its biomechanical consequences. *J. Struct. Biol.* **177,** 314–328 (2012).

174. Li, L. & Ortiz, C. Pervasive nanoscale deformation twinning as a catalyst for efficient energy dissipation in a bioceramic armour. *Nat. Mater.* **13,** 501–507 (2014).

175. Yang, W. *et al.* Natural flexible dermal armor. *Adv. Mater.* **25,** 31–48 (2013).

176. Huang, Z. *et al.* Uncovering high-strain rate protection mechanism in nacre. *Sci. Rep.* **1,** 148 (2011).

177. Tai, K., Dao, M., Suresh, S., Palazoglu, A. & Ortiz, C. Nanoscale heterogeneity promotes energy dissipation in bone. *Nat. Mater.* **6,** 454–462 (2007).

178. Arciszewski, T. & Cornell, J. in *Intell. Comput. Eng. Archit.* (Springer, 2006).

179. Oliver, W. C. & Pharr, G. M. An improved technique for determining hardness and elastic modulus using load and displacement sensing indentation experiments. *J. Mater. Res.* **7,** 1564–1583 (1992).

180. Song, J., Ortiz, C. & Boyce, M. C. Threat-protection mechanics of an armored fish. *J. Mech. Behav. Biomed. Mater.* **4,** 699–712 (2011).

181. Kunitake, M. E., Mangano, L. M., Peloquin, J. M., Baker, S. P. & Estroff, L. A. Evaluation of strengthening mechanisms in calcite single crystals from mollusk shells. *Acta Biomater.* **9,** 5353–5359 (2013).

182. He, L. H. & Swain, M. V. Energy absorption characterization of human enamel using nanoindentation. *J. Biomed. Mater. Res. A* **81,** 482–492 (2007).

183. Turner, F. J., Griggs, D. T. & Heard, H. Experimental deformation of calcite crystals. *Bull. Geol. Soc. Am.* **66,** 883–934 (1964).

184. Barber, D. J. & Wenk, H.-R. Deformation twinning in calcite, dolomite, and other rhombohedral carbonates. *Phys. Chem. Miner.* **5,** 141–165 (1979).

185. Chen, M. *et al.* Deformation twinning in nanocrystalline aluminum. *Science* **300,** 1275–1277 (2003).

186. Oyen, M. L. & Cook, R. F. A practical guide for analysis of nanoindentation data. *J. Mech. Behav. Biomed. Mater.* **2,** 396–407 (2009).

187. Yu, Q. *et al.* Strong crystal size effect on deformation twinning. *Nature* **463,** 335–338 (2010).

188. Zhu, Y. T., Liao, X. Z. & Wu, X. L. Deformation twinning in nanocrystalline materials. *Prog. Mater. Sci.* **57,** 1–62 (2012).

189. Szlufarska, I., Nakano, A. & Vashishta, P. A crossover in the mechanical response of nanocrystalline ceramics. *Science* **309,** 911–914 (2005).

190. Li, Y. S., Tao, N. R. & Lu, K. Microstructural evolution and nanostructure formation in copper during dynamic plastic deformation at cryogenic temperatures. *Acta Mater.* **56,** 230–241 (2008).

191. Lu, K., Lu, L. & Suresh, S. Strengthening materials by engineering coherent internal boundaries at the nanoscale. *Science* **324,** 349–352 (2009).

192. Goetz, A. J. *et al.* Interdigitating biocalcite dendrites form a 3-D jigsaw structure in brachiopod shells. *Acta Biomater.* **7,** 2237–2243 (2011).

193. O'neill, P. L. Polycrystalline echinoderm calcite and its fracture mechanics. *Science* **213,** 646–648 (1981).

194. Wang, R. Z., Addadi, L. & Weiner, S. Design strategies of sea urchin teeth: structure, composition and micromechanical relations to function. *Philos. Trans. R. Soc. Lond. B. Biol. Sci.* **352,** 469–480 (1997).

195. Suzuki, M., Kim, H., Mukai, H., Nagasawa, H. & Kogure, T. Quantitative XRD analysis of {110} twin density in biotic aragonites. *J. Struct. Biol.* **180,** 458–468 (2012).

196. Younis, S., Kauffmann, Y., Pokroy, B. & Zolotoyabko, E. Atomic structure and ultrastructure of the Murex troscheli shell. *J. Struct. Biol.* **180,** 539–45 (2012).

197. Meyers, M. A., Chen, P.-Y., Lin, A. Y.-M. & Seki, Y. Biological materials: Structure and mechanical properties. *Prog. Mater. Sci.* **53,** 1–206 (2008).

198. Meyers, M. a, Chen, P.-Y., Lopez, M. I., Seki, Y. & Lin, A. Y. M. Biological materials: a materials science approach. *J. Mech. Behav. Biomed. Mater.* **4,** 626–657 (2011).

199. Chen, P.-Y. *et al.* Structure and mechanical properties of selected biological materials. *J. Mech. Behav. Biomed. Mater.* **1,** 2082–26 (2008).

200. Mayer, G. & Sarikaya, M. Rigid Biological Composite Materials: Structural Examples for Biomimetic Design. *Exp. Mech.* **42,** 395–403 (2002).

201. Shyr, T.-W. & Pan, Y.-H. Impact resistance and damage characteristics of composite laminates. *Compos. Struct.* **62,** 193–203 (2003).

202. Kim, J.-K. & Mai, Y.-W. High strength, high fracture toughness fibre composites with interface control-A review. *Compos. Sci. Technol.* **41,** 333–378 (2006).

203. Dastjerdi, A. K., Rabiei, R. & Barthelat, F. The weak interfaces within tough natural composites: experiments on three types of nacre. *J. Mech. Behav. Biomed. Mater.* **19,** 50–60 (2013).

204. Bruno, M., Massaro, F. R. & Prencipe, M. Theoretical structure and surface energy of the reconstructed {01.2} form of calcite (CaCO3) crystal. *Surf. Sci.* **602,** 2774–2782 (2008).

205. Bruno, M., Massaro, F. R., Rubbo, M., Prencipe, M. & Aquilano, D. (10.4), (01.8), (01.2), and (00.1) Twin laws of calcite (CaCO3): equilibrium geometry of the twin boundary interfaces and twinning energy. *Cryst. Growth Des.* **10,** 3102–3109 (2010).

206. Wise, S. W. & DeVilliers, J. Scanning Electron Microscopy of Molluscan Shell Ultrastructures: Screw Dislocations in Pelecypod Nacre. *Trans. Am. Microsc. Soc.* **90,** 376–380 (1971).

207. Yao, N., Epstein, A. & Akey, A. Crystal growth via spiral motion in abalone shell nacre. *J. Mater. Res.* **21,** 1939–1946 (2006).

208. Yao, N., Epstein, A. K., Liu, W. W., Sauer, F. & Yang, N. Organic-inorganic interfaces and spiral growth in nacre. *J. R. Soc. Interface* **6,** 367–76 (2009).

209. Katti, K. S., Katti, D. R., Pradhan, S. M. & Bhosle, A. Platelet interlocks are the key to toughness and strength in nacre. *J. Mater. Res.* **20,** 1097–1100 (2011).

210. Chen, P. *et al.* Failure mechanisms of laminated composites subjected to static indentation. *Compos. Struct.* **75,** 489–495 (2006).

211. Sela, N. & Ishai, O. Interlaminar fracture toughness and toughening of laminated composite materials: a review. *Composites* **20,** 423–435 (1989).

212. Dransfield, K., Baillie, C. & Mai, Y. Improving the delamination resistance of CFRP by stitching-A review. *Compos. Sci. Technol.* **50,** 305–317 (2006).

213. Guenon, V. A., Cho, T.-W. & Cilliespie Jr, J. W. Toughness properties of a three-dimensional carbon-epoxy composite. *J. Mater. Sci.* **24,** 4168–4175 (1989).

214. Chung, W. C., Jang, B. Z., Hwang, L. R. & Wilcox, R. C. Fracture behavior in stitched multidirectional Composites. *Mater. Sci. Eng. A* **112,** 157–173 (1989).

215. Balint, D. S. & Hutchinson, J. W. Mode II Edge Delamination of Compressed Thin Films. *J. Appl. Mech.* **68,** 725–730 (2001).

216. Land, M. F. The physics and biology of animal reflectors. *Prog Biophys Mol Biol* **24,** 75–106 (1972).

217. Seago, A. E., Brady, P., Vigneron, J.-P. & Schultz, T. D. Gold bugs and beyond: a review of iridescence and structural colour mechanisms in beetles (Coleoptera). *J. R. Soc. Interface* **6,** S165–S184 (2009).

218. Denton, E. J. On the organization of reflecting surfaces in some marine animals. *Aphil. Trans. Roy. Soc. Lond. B.* **258,** 285–313 (1970).

219. Levy-Lior, A. *et al.* Guanine-Based Biogenic Photonic-Crystal Arrays in Fish and Spiders. *Adv. Funct. Mater.* **20,** 320–329 (2010).

220. Parker, A. R. 515 million years of structural colour. *J. Opt. A Pure Appl. Opt.* **2,** R15–R28 (2000).

221. Parker, A. R. & Mcphedran, R. C. Aphrodite's iridescence. **409,** 36–37 (2001).

222. Trzeciak, T. M. & Vukusic, P. Photonic crystal fiber in the polychaete worm Pherusa sp. *Phys. Rev. E* **80,** 061908 (2009).

223. Mäthger, L. M. & Hanlon, R. T. Malleable skin coloration in cephalopods: selective reflectance, transmission and absorbance of light by chromatophores and iridophores. *Cell Tissue Res.* **329,** 179–186 (2007).

224. Mäthger, L. M. *et al.* Bright White Scattering from Protein Spheres in Color Changing, Flexible Cuttlefish Skin. *Adv. Funct. Mater.* **23,** 3980–3989 (2013).

225. Heavens, O. *Optical properties of thin solid films.* (Dover Publications, 1965).

226. Onslow, H. On a Periodic Structure in Many Insect Scales, and the Cause of Their Iridescent Colours. *Philos. Trans. R. Soc. London. Ser. B* **211,** 1–74 (1921).

227. Stavenga, D. G., Wilts, B. D., Leertouwer, H. L. & Hariyama, T. Polarized iridescence of the multilayered elytra of the Japanese jewel beetle, Chrysochroa fulgidissima. *Philos. Trans. R. Soc. Lond. B. Biol. Sci.* **366,** 709–23 (2011).

228. Mason, C. W. Structural colors in insects. III. *J. Phys. Chem* **31,** 1856–1872 (1927).

229. Hariyama, T. *et al.* The Origin of the Iridescent Colors in Coleopteran Elytron. *Forma* **17,** 123–132 (2002).

230. Suzuki, M. *et al.* Characterization of the multilayered shell of a limpet, Lottia kogamogai (Mollusca: Patellogastropoda), using SEM-EBSD and FIB-TEM techniques. *J. Struct. Biol.* **171,** 223–230 (2010).

231. Suzuki, M., Kogure, T., Weiner, S. & Addadi, L. Formation of Aragonite Crystals in the Crossed Lamellar Microstructure of Limpet Shells. *Cryst. Growth Des.* **11,** 4850–4859 (2011).

232. Van de Hulst, H. C. *Light scattering by small particles.* (Dover Publications, 1981).

233. Bohren, C. F. Multiple scattering of light and some of its observable consequences. *Am. J. Phys.* **55,** 524–533 (1987).

234. Shawkey, M. D. & Hill, G. E. Significance of a basal melanin layer to production of non-iridescent structural plumage color: evidence from an amelanotic Steller's jay (Cyanocitta stelleri). *J. Exp. Biol.* **209,** 1245–1250 (2006).

235. Hale, G. M. & Querry, M. R. Optical Constants of Water in the 200-nm to 200-microm Wavelength Region. *Appl. Opt.* **12,** 555–563 (1973).

236. Salvini-Plawen, L. & Mizzaro-Wimmer, M. *Praktische Malakologi (Practical Malacology).* (Springer-Verlag, 2001).

237. Bates, H. W. Contributions to an insect fauna of the Amazon valley (Lepidoptera: Heliconidae). *Biol. J. hte Linn. Soc.* **16,** 41–54 (1981).

238. Stevens, M., Cuthill, I. C., Windsor, A. M. M. & Walker, H. J. Disruptive contrast in animal camouflage. *Proc. Biol. Sci.* **273,** 2433–2438 (2006).

239. Liu, J. *et al.* Multifunctional three-dimensional macroporous nanoelectronic networks for smart materials. *PNAS* **110,** 6694–6699 (2013).

240. Thomas, J. P. & Qidwai, M. A. The Design and Application of multifunctional structure-battery materials systems. *J. Mater.* 18–24 (2005).

241. Hager, M. D., Greil, P., Leyens, C., van der Zwaag, S. & Schubert, U. S. Self-healing materials. *Adv. Mater.* **22,** 5424–5430 (2010).

242. Lee, L. P. & Szema, R. Inspirations from biological optics for advanced photonic systems. *Science* **310,** 1148–1150 (2005).

243. Szema, R. & Lee, L. P. in *Biomimetics Biol. inspired Technol.* 291–308 (CRC Press, 2006).

244. Bragg, W. L. The Refractive Indices of Calcite and Aragonite. *Proc. R. Soc. London. Ser. A* **105,** 370–386 (1924).

245. Davis, C. C. *Lasers and electro-optics: fundamentals and engineering.* (Cambridge University Press, 1996).

246. De Carvalho, H. F. & Vidal, B. C. Polarized Microscopy Study of an Antennal Sensillum of Triatoma Infestans: An Ordered Distribution of Chitin Fibrils and Associated Components. *Comptes Rendus l'Académie Des Sci. Série III* **319,** 33–38 (1996).

247. Bachman, G. L. & Merten, H. L. Stabilized amorphous calcium carbonate. (1980).

248. Lee, K. *et al.* Self-assembly of amorphous calcium carbonate microlens arrays. *Nat. Commun.* **3,** 725 doi: 10.1038/ncomms1720 (2012).

249. Nilsson, D.-E., Gislen, L., Coates, M., Skogh, C. & Garm, A. Advanced optics in a jellyfish eye. *Nature* **435,** 201–205 (2005).

250. Cartwright, J. H. E., Checa, A. G., Gale, J. D., Gebauer, D. & Sainz-Díaz, C. I. Calcium carbonate polyamorphism and its role in biomineralization: how many amorphous calcium carbonates are there? *Angew. Chem. Int. Ed. Engl.* **51,** 11960–70 (2012).

251. Arey, L. & Grozier, W. The Sensory Response of Chiton. *J. Exp. Zool.* **29,** 157–260 (1919).

252. Nilsson, D.-E. Eyes as Optical Alarm Systems in Fan Worms and Ark Clams. *Phil. Trans. R. Soc. Lond. B* **346,** 195–212 (1994).

253. Li, X., Wei, Y., Yang, W. & Gao, H. Competing grain-boundary- and dislocation-mediated mechanisms in plastic strain recovery in nanocrystalline aluminum. *PNAS* **106,** 16108–16113 (2009).

254. Li, X., Wei, Y., Lu, L., Lu, K. & Gao, H. Dislocation nucleation governed softening and maximum strength in nano-twinned metals. *Nature* **464,** 877–880 (2010).

255. Wang, Y. M. *et al.* Defective twin boundaries in nanotwinned metals. *Nat. Mater.* **12,** 697–702 (2013).

Appendix A. Additional supporting figures

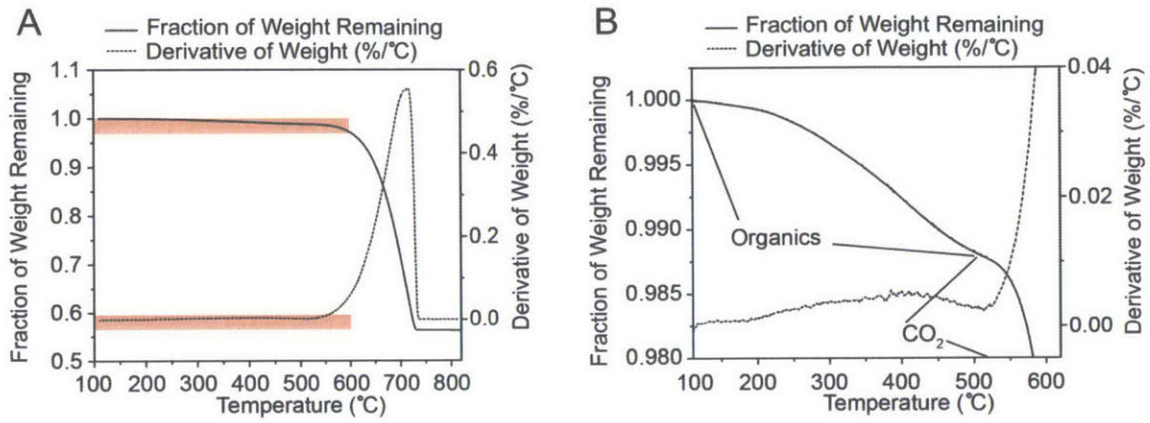

Figure A-1| Thermogravimetric analysis of *P. placenta* shell. A) Full scan and **B**) enlarged portion from 100-600°C. Organic content is calculated using two methods: 1) weight loss below 500°C (1.07 ± 0.09 wt%); 2) the final weight of CaO at 850°C (1.10 ± 0.19 wt%).

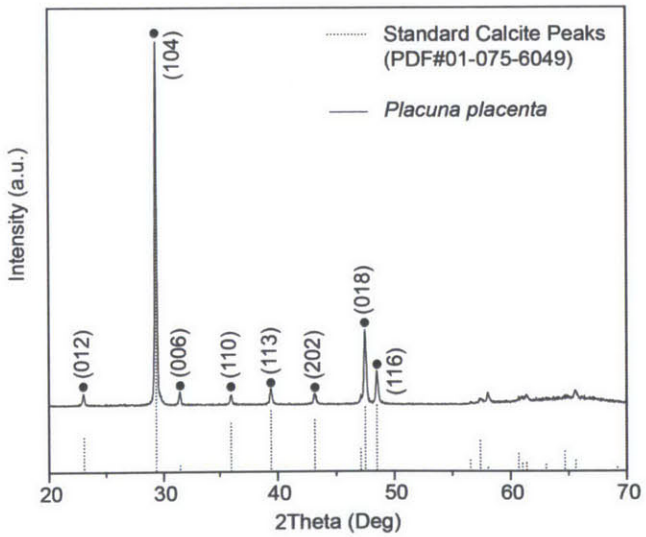

Figure A-2| Powder X-ray diffraction spectrum of *P. placenta* with standard calcite peaks (PDF #01-075-6049).

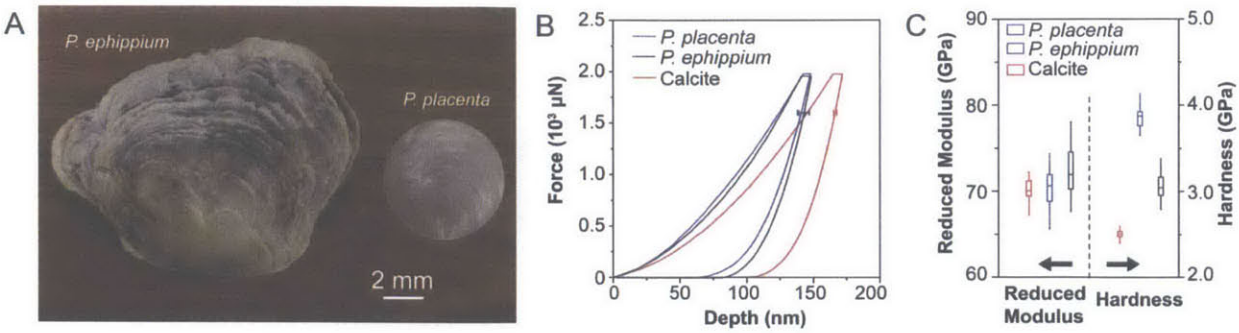

Figure A-3| A) Picture of transparent *P. placenta* and its cogeneric species, non-transparent *P. ephippium.* **B)** Averaged load-depth curves for *P. placenta* and *P. ephippium*. **C)** Distribution of reduced modulus and hardness.

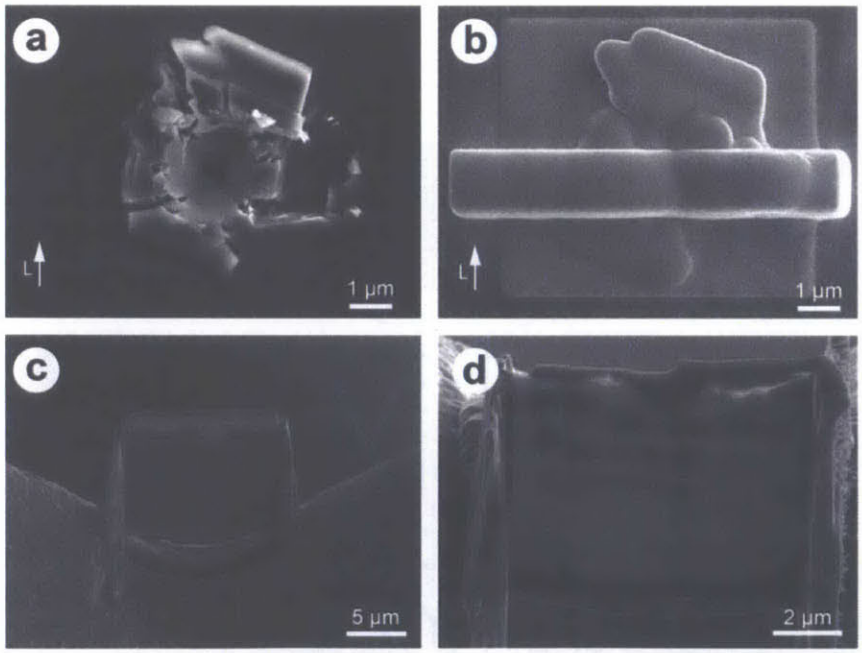

Figure A-4| SEM images showing TEM sample preparation of the indentation residue by FIB. a, An indentation residue before FIB-milling. **b,** An overall platinum protective layer was deposited first (thickness ~ 0.5 μm); another thick protective platinum layer was then deposited (thickness ~ 1.5 μm). The orientations were chosen either parallel or perpendicular to the longitudinal direction of the laths. **c,** In-situ pick-up and transfer the slab to a TEM copper grid using the OMNI probe after FIB milling. **d**, The slab was ion milled step-wisely to final electron transparent.

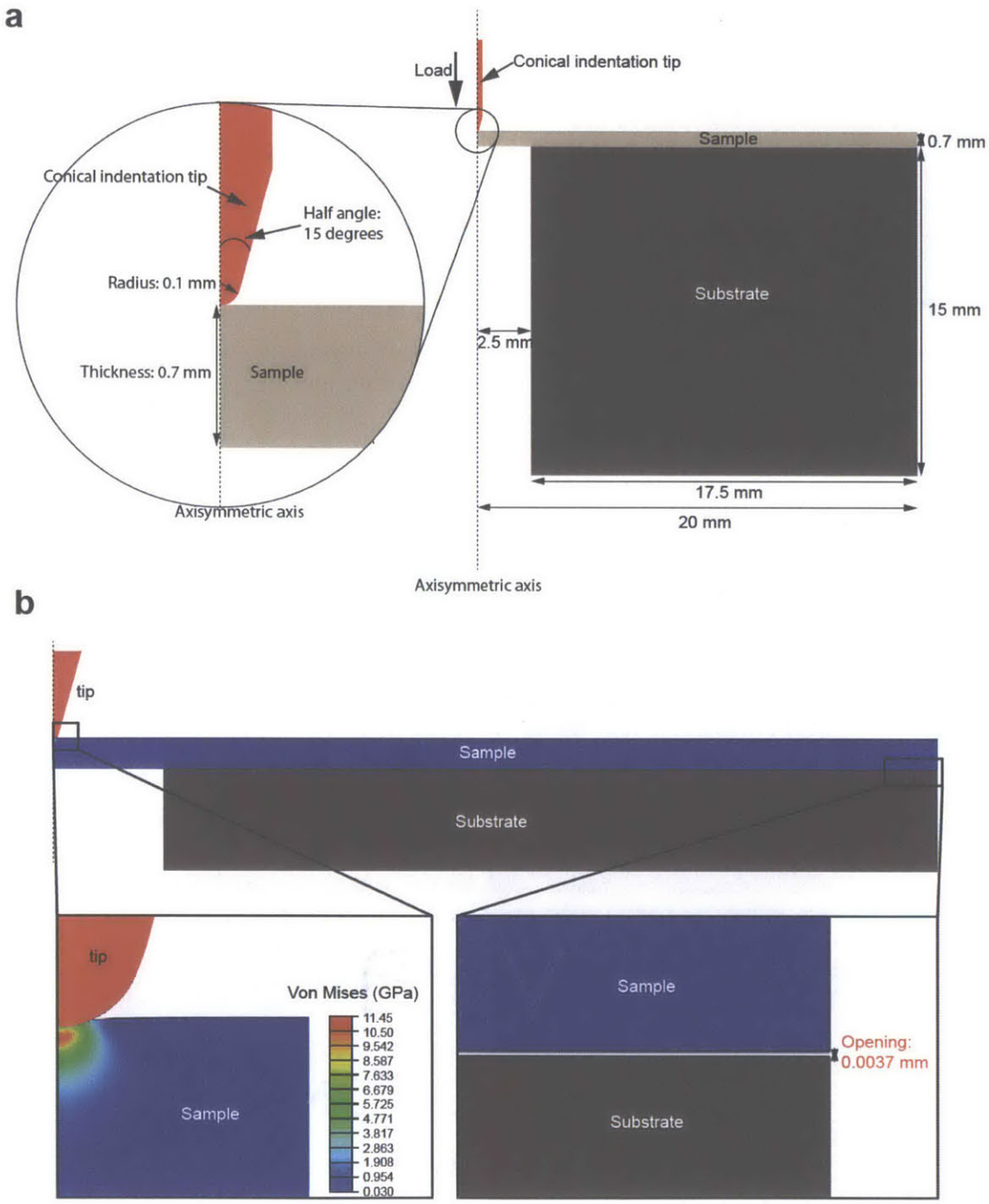

Figure A-5| Finite element simulation to investigate the bending effects during a macroindentation test. a, The axisymmetric simulation model. The indentation tip and substrate were modeled as rigid, and the sample is elastic with modulus of 71 GPa (based on nanoindentation results). All interfaces are frictionless. **b,** Simulation result at maximum load of 65 N, the maximum load to fracture determined experimentally. Bottom left, Von Mises stress field close to the indentation tip. Bottom right, opening (0.0037 mm) between sample and substrate resulted from bending at the maximum load. The magnitude of opening is only ~0.5% of the sample thickness, and was neglected in the discussion.

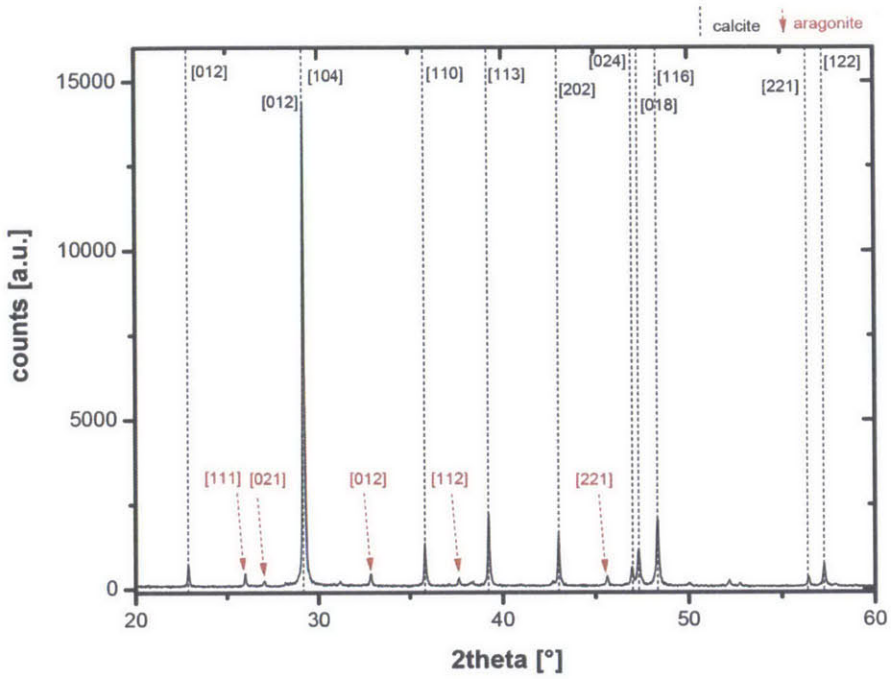

Figure A-6| X-ray powder diffraction spectrum of a hand-ground limpet shell, showing the characteristic signatures of calcite and aragonite. *Experiment by Mathias Kolle.*

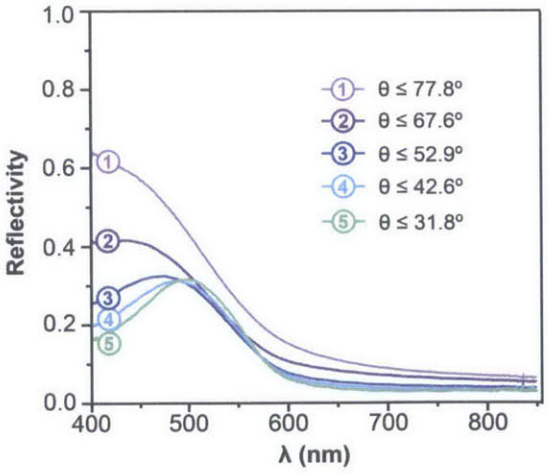

Figure A-7| Spectrally resolved reflectivity of a stripe for successively increasing light incidence and collection cone angles, referenced against a >97% reflective silver mirror. Measurements were taken with a Leica 100x oil immersion objective with variable aperture. θ signifies the corresponding maximum collection angle for each curve, if measurements would have been taken in water instead of oil.

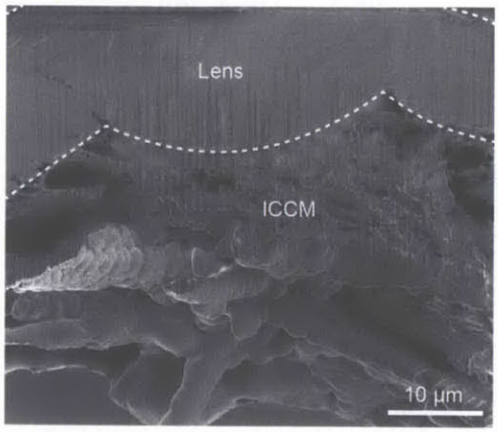

Figure A-8| SEM image of a FIB-prepared cross section of the lens region of an eye of the chiton *A. granulata*. Intra-chamber calcified material ("ICCM") is abundant below the lens.

Appendix B. List of supporting movies

1. 3D visualization of damage zone after macroindentation test.
2. Multiscale structures of the biomineralized photonic structure in the blue-rayed limpet Patella pellucida.
3. 3D visualization of the eye chamber of the chiton *Acanthopleura granulata.*
4. 3D visualization of the megalaesthetes of the chiton *Acanthopleura granulata.*
5. Astigmatism in the image formation of the chiton *Acanthopleura granulata.*

The above movies are available upon request (lingli@mit.edu or lingli1985@gmail.com).